Summer 1992

Laminar and Turbulent Natural Convection Heat Transfer in Trombe Wall Channels

Tony D. T. Chen
Old Dominion University

Recommended Citation

Chen, Tony D.. "Laminar and Turbulent Natural Convection Heat Transfer in Trombe Wall Channels" (1992). Doctor of Philosophy (PhD), Dissertation, Mechanical & Aerospace Engineering, Old Dominion University, DOI: 10.25777/fn85-nm72
https://digitalcommons.odu.edu/mae_etds/225

LAMINAR AND TURBULENT NATURAL CONVECTION HEAT TRANSFER IN TROMBE WALL CHANNELS

by

Tony D. T. Chen
M.S. Mechanical Engineering
May 1983, The University of Iowa

A Dissertation Submitted to the Faculty of
Old Dominion University in Partial Fulfillment of the
Requirements for the Degree of

DOCTOR OF PHILOSOPHY
IN
MECHANICAL ENGINEERING

OLD DOMINION UNIVERSITY
July 1992

Approved by:

Dr. S. K. Chaturvedi (Director)

Dr. A. S. Roberts

Dr. J. J. Singh

Dr. S. N. Tiwari

ABSTRACT

LAMINAR AND TURBULENT NATURAL CONVECTION HEAT TRANSFER IN TROMBE WALL CHANNELS

Tony D. T. Chen
Old Dominion University
Director: Dr. S. K. Chaturvedi

The natural convective heat transfer and air movement in a Trombe wall solar passive system has been studied analytically and numerically. Three Trombe wall channel geometries including the parallel channel with axial inlet and exit, parallel channel with side vents and Trombe wall channel coupled to the room have been considered. Several models representing these Trombe wall geometries have been formulated. For the parallel channel with axial inlet and exit geometry, a momentum-integral method has been used to solve parabolic governing equations for two-dimensional laminar flow. This formulation leads to a second order ordinary differential equation for pressure defect in the Trombe wall channel. The solution of this equation leads to prediction of velocity, temperature and pressure fields, and Nusselt number correlations that are in good agreement with previously reported finite difference solution of natural convection boundary layer equations.

For the side-vented channel case, results are obtained for both two-dimensional laminar and turbulent natural convective flow regimes. Due to presence of recirculating flow patterns in this geometry, full Navier-Stokes equations in two-dimensions are employed. The turbulent flow characteristics are modeled by a two-equation (k-ϵ) model. The governing equations for steady laminar as well as turbulent flows are solved by a finite volume technique that uses the quadratic upwind differencing scheme to discretize non-linear governing equations to form algebraic equations which govern physical variables at the various numerical grid points. The coupled algebraic equations are solved by a semi-implicit algorithm known as SIMPLER. Flow patterns, isotherms and heat transfer characteristics are obtained for aspect ratios of 10 and 20, and Grashof number ranging from 1.4×10^3 to 1.4×10^8. The effect of the free pressure boundary location of flow characteristics is also analyzed. Results show that the mass flow rates induced and net energy delivered by the system is governed by the channel Grashof number and the channel vent size. Numerical results also indicate a transitional regime as indicated with number of iterations. Correlations for average Nusselt number as a function of Grashof number and vent size are also obtained based on numerical results. The inlet and exit pressure losses for the geometry have also calculated. Results show that the total vent loss coefficient for the side-vented cavity shows a minimum at $Gr = 1.4 \times 10^4$ for which the dimensionless mass flow rate also shows a maximum value.

Results are also obtained for a more comprehensive geometry in which the Trombe wall channel is coupled to the room. Both heating and ventilation modes are investigated. In the heating mode, the natural convective mass flow rate and energy delivery rate are predicted as a function of the channel width and the cooled wall temperature. Several truncated Trombe wall passive system geometries are also considered in an attempt to reduce the computational time. Results indicate that for these truncated configurations, the heat delivery rate and convective mass flow rate are within nine percent of the values obtained for the more comprehensive and full size geometry. For the ventilation mode, the effect of ventilation port position on mass flow rate and energy delivery rate is investigated.

ACKNOWLEDGEMENT

I would like to thank Dr. S. K. Chaturvedi for his valuable advice, encouragement and helpful discussions throughout this work. I also wish to thank my dissertation guidance committee members, Drs. A. S. Roberts, S. N. Tiwari and J. J. Singh for their active interest in the project. I also would like to thank my wife Cheryl Lin for her uncompromising support and taking good care of our daughter Rebecca Chen during the entire period of this work.

TABLE OF CONTENTS

Page

Chapter

APPENDICES

LIST OF TABLES

LIST OF FIGURES

LIST OF SYMBOLS

A	Convection-diffusion coefficient; also used to denote area
Ar	Aspect ratio
a	Coefficient in the discretization equation
b	Constant term in the discretization equation
c	Speed of sound
ck	Von Karman constant
D	Diffusion conductance
Ec	Eckert number
e	Internal energy
F	Flow rate through a control-volume face
f	A body force
h	Grid size
H	Channel height
g	Acceleration due to gravity
J	Total (convection + diffusion) flux
k	Turbulent kinetic energy
K	Thermal conductivity, pressure loss coefficient
L	Channel length
$\dot{m}$	Mass flow rate
$\dot{M}$	Mass flux
Nu	Nusselt number

P	Pressure
Pe	Peclet number
Pst	Hydrostatic pressure
Pt	Pressure (P_o+Pst)
P'	Pressure correction
Pr	Prandtl number
Q	Net energy rate
q	Heat flux
R	Gas constant
Ra	Rayleigh number
Re	Reynolds number
Ri	Richardson number
S	General source term
Sc	Constant part of the linearized source term
Sp	Coefficient of Φ_p in the linearized source expression
T	Temperature
T_c^*	Dimensionless cooled wall temperature
t	Time
u	x-direction velocity
u	Pseudo-velocity in the x direction
u*	Velocity based on the guessed pressure P*
$\vec{u}$	Velocity vector
v	y-direction velocity
$\hat{v}$	Pseudo-velocity in the y direction
v*	Velocity based on the guessed pressure P*
Vs*	Dimensionless vent size
x,y	Coordinates

Greek Letters

α	Thermal diffusivity, also relaxation parameters, and correlation factor
β	Coefficient of thermal expansion
Δx	Grid spacing in the x direction
Δy	Gruid spacing in the y direction
μ	Dynamic viscosity
ρ	Density
τ	General diffusion coefficient
Φ	General dependent variable
∇	The gradient operator

Subscripts

c	Cooled wall
E	Neighbor in the positive x direction
e	Control-volume face between P and E, channel exit
f	Floor temperature
h	Heated wall
i	Channel inlet
N	Neighbor in the positive y direction
n	Control-volume face between P and N
nb	General neighbor grid point
o	Subscript for scaling parameters
P	General grid point under consideration
r	Room wall temperature
S	Neighbor in the negative y direction
s	Control-volume face between P and S
T, t	Total (inlet + exit)
u,v	Subscripts for x,y-momentum source terms

W	Neighbor in the negative x direction
w	Control-volume face between P and W
∞	Free stream condition

Chapter 1

INTRODUCTION

Rapid depletion of fossil-fuel resources on a worldwide basis has necessitated an urgent search for alternative energy sources to meet the global energy demand. Several energy sources are currently being considered as alternatives to the fossil-fuels such as oil, coal and natural gas. These include wind, solar and ocean thermal systems amongst others. All these sources are virtually inexhaustible and relatively pollution free. Recent concerns about global warming due to carbon dioxide emissions from fossil-fuel energy converters have further enhanced the attractiveness of these systems. Of the three alternative energy sources mentioned earlier, wind power and ocean thermal systems are more localized and site specific. On the other hand, solar energy conversion systems are more appealing from the point of view of more widespread resource availability and the versatility of applications. The major disadvantages of these systems are primarily attributable to the fluctuating nature of the solar resource and due to their high capital cost. The fluctuating nature of the resource requires that the solar energy be stored during sunny days so that stored energy can be utilized during periods of extended cloudiness. The high capital cost of solar systems have been a major impediment to commercialization of solar technologies.

In recent years, there has been a growing realization that solar energy systems may not be suitable for all kinds of applications, and as a result there has been a trend towards identifying those solar technologies that have the best chance of substituting for the fossil-fuels. Solar passive systems have been identified as being attractive for residential and commercial space heating applications. It is to be noted that solar energy systems are classified as active or passive depending on the agency that motivates the absorption and transport of energy. In a passive system, solar radiation is admitted directly into the building through large transparent openings, and massive building structures are relied on for the collection, storage and distribution of energy. In an active system, solar radiation is collected by specially designed collectors. Thermal energy is stored in a storage device, and transportation of energy via a fluid medium is done by mechanical means such as fans, blowers and pumps.

The passive systems are becoming more popular for two reasons. First of all they do not have mechanical parts and as a result mechanical failure problems are altogether eliminated. Secondly, many of the passive solar energy systems are easily integrated in residential and commercial buildings, and this reduces the cost of solar energy collection substantially. For example, simple steps such as orienting the building with greater south facing exposure or providing more glass windows can substantially result in greater solar energy collection during the space heating season. Most of these systems lack an identifiable storage system, and consequently they suffer from lack of control of comfort conditions due to under or overheating of buildings in winter months. A more advanced passive solar system is known as the Trombe wall collector-storage system [1], the subject of present study. In this system, a thick south facing wall made of concrete, brick, adobe, or stone, located directly behind a single or double glazing is used, with an air gap between the glass and the black painted outer face of the wall. Heat is transferred to the wall and to the conditioned space by both conduction through the wall and natural convection in the air gap, sustained by ventilation openings at the top and bottom of the wall. On a sunny day, about half of the solar energy gain by the absorber wall is transferred by the airstream for immediate daytime heating of the interior space, while the remainder portion of the energy is stored in the wall for supplying the night-time energy requirements. The fluid flow in the Trombe wall gap and in the adjoining room is set up by buoyancy forces due to temperature gradient in the fluid. In this sense, the flow initiation and sustenance processes are similar to those encountered in the fields of thermo-syphon technology, electronic equipment and material processing to name the few.

The purpose of the present study is to investigate analytically and numerically various aspects concerning the natural convection phenomenon in a Trombe wall channel. In a typical Trombe wall system, the convective flow may be either laminar or turbulent, depending on the magnitude of the buoyancy force. For natural convection flows, Grashof number determines whether the flow patterns are laminar or turbulent. At low Grashof number the flow is typically laminar, while at higher values of Grashof number the flow is typically laminar, while at higher values of Grashof number, exceeding a critical value dependent on the geometrical features of the channel, the flow becomes turbulent due to instabilities of the fluid motion.

Although Trombe wall solar passive systems have been investigated by others [2–6][*] since the pioneering paper of Felix Trombe [1], several aspects of the problem are still not covered in the literature. A review of previous studies indicates that most of these studies adopt a very simplified geometry for analysis. These studies can be classified primarily into two classes where the buoyancy force driven mass flux is determined either by parabolic boundary layer equations or the full Navier-Stokes equations. In the first approach a parallel wall geometry with differentially heated walls is considered [7]. The flow set up by the buoyancy force leads to thermal and velocity boundary layers on the channel walls. These boundary layers, developing over the channel walls, are analyzed by

---

[*] The numbers in brackets indicate references.

incorporating the simplifications arising from the parabolic nature of governing equations. This is done by extending the boundary layer analysis to natural convective flows. The classical analysis in Ref. 7 is an example of this approach. More recently, the work of Akbari and Borgers [8], and Borgers and Akbari [9] explore the parallel wall geometry case further for both laminar and turbulent flows. In the turbulent case, they use the mixing length model to characterize turbulence properties of natural convective flow in the Trombe wall channel.

The problem of the parallel channel, considered by these previous authors, has two drawbacks. First of all, it does not simulate the actual Trombe wall geometry, in which the incoming flow makes a 90 degree turn. The parallel channel geometry considered by earlier studies has no such turns. Secondly, two boundary conditions for pressure are required at the channel inlet. These involve the specification of pressure and pressure gradient in the dominant flow direction at the inlet section. Unfortunately, both these values are usually unknown in the framework of boundary layer analysis. In many previous boundary layer analyses, the entrance and exit pressure losses are neglected, and the value of pressure at inlet is determined by applying the Bernoulli equation along streamline [8,9]. Also, a value of pressure gradient is assumed at the inlet. For example, Akbari and Borgers [8], following Aihara [10], assumed a non-dimensional pressure gradient value at the inlet. This problem, requiring above boundary conditions at channel inlet, arises as a result of neglect of second order gradients of flow properties in the boundary layer analysis.

An approach alleviating this problem considers the full Navier-Stokes equations to describe the natural convective phenomenon. Kettleborough [11] and Nakamura et al. [12] have considered this approach. They have analyzed the problem of free convection between two parallel plates numerically by using the Navier-Stokes equations.

Nakamura et al. [12] proposed a method that takes the entrance pressure drop into consideration, and their results show that the stream function and average Nusselt number values are closer to Aihara's solution but are somewhat different from Kettleborough's result for an identical problem. both Nakamura et al. and Kettleborough combine the inlet and exit vent pressure losses and lump them into a single equivalent pressure loss at the inlet. Due to this apparent simplification, their analysis cannot predict inlet and exit vent losses separately. In addition, their results are applicable to a parallel wall geometry with axial air entry.

To simulate the Trombe wall channel geometry properly, Chaturvedi et al. [13] added the inlet and exit horizontal segments to the vertical channel to analyze the fundamental nature of the fluid dynamical and heat transfer mechanisms inside the channel for the laminar mixed convective regime. The present study, an extension of Chaturvedi et al.'s work, considers convection in the Trombe wall channel attached to a room. It also differs from the work in Ref. 13 since the study considered only mixed laminar convection whereas the present study considers both laminar and turbulent natural convection phenomenon in more complex geometrical configurations.

Since the problems of flow in a parallel channel or in a Trombe wall channel coupled to the room are closely related to the widely analyzed closed rectangular cavity problem, a brief review of literature in this area is also presented here. Wilkes and Churchill [14], in their pioneering work, applied the Alternating Direction Implicit (ADI) finite difference scheme to solve the coupled mass, momentum and energy equations for a differentially heated closed square cavity. They obtained convective flow patterns for steady and transient flows in a square cavity for Grashof number up to 1.0×10^5. A detailed comparison of various numerical techniques applied to this classical natural convection problem is also presented by de Vahl davis [15]. Fraikin et al. [16] also applied ADI scheme with finite difference approximations of second order accuracy to study this problem in the range of Grashof numbers of 1.0×10^7 to 1.0×10^8. Markatows and Pericleous [17] used a semi-implicit finite volume technique to obtain the laminar and turbulent heat transfer characteristics in a square cavity with Raleigh number varying from 1.0×10^3 to 1.0×10^6. Nicolette and Yang [18] have used a fully transient semi-implicit upwind differencing scheme with a global pressure correction of air and water in a two-dimensional enclosure with Grashof number ranging from 1.0×10^5 to 1.0×10^7. Berkovsky and Polevikov [19] used a higher order scheme to analyze the laminar natural convection phenomenon in rectangular cavity for Prandtl number ranging from 1.0 to 1.0×10^5.

From the review of literature, it is evident that little information exists for the realistic Trombe wall channel configurations. The coupling of convection and energy transport processes between channel and the room has not been investigated. The present study analyzes the natural convective motion in the Trombe wall geometry in two dimensions by solving the Navier-Stokes, continuity and energy equations. Three different geometries have been considered, namely parallel wall channel with axial entry and exit of flow, parallel wall channel with side entry and side exit, and a comprehensive model employing Trombe wall channel coupled to the room. Both laminar and turbulent regimes are investigated in the present study. The laminar convective flow in parallel channel with axial entry and exit geometry is analyzed by a momentum-integral approach, using the boundary layer approximation. This formulation leads to a second order ordinary differential equation for pressure. Mass flux and heat transfer coefficients are predicted as a function of channel height and cold wall temperature. The second geometry, with side entry and exit is analyzed for both laminar and turbulent flows for an aspect ratio of 20. The flow field, mass flow rate, heat transfer and entrance and exit vent loss characteristics are predicted as a function of Grashof number and different wall temperatures by solving the Navier-Stokes equations numerically. For the third case, a realistic geometry simulating coupling of the Trombe wall channel to the room is employed. The flow patterns, mass flow rate, heat transfer and entrance and exit pressure loss characteristics are predicted as a function of different wall temperatures. Finally, the operation of Trombe wall for summer cooling case is also simulated, where ventilation of air, caused by the buoyancy action, is analyzed.

In this work, efforts have been directed towards analyzing numerically and analytically the laminar and turbulent natural convection heat transfer between the vertical channel surfaces. To achieve this objective, a numerical code based on the "SIMPLER" algorithm of Patankar [20] has been developed for the two-dimensional laminar and turbulent flows. The developed code has been validated by first considering a two-dimensional closed cavity with unity aspect ratio, and comparing its results with those available in the literature. The "FLUENT" code [21] using "SIMPLE" as well as "SIMPLER" algorithms [22] for solution of coupled non-linear equations has also been used in predict flow in side vent geometry and the flow in Trombe wall channel coupled to the room. The flow and temperature patterns, and turbulence properties for Grashof number ranging from 1.4×10^3 to 1.4×10^8 have been predicted for channel aspect ratios of 10 and 20. The nature of the fluid dynamical and heat transfer mechanisms is investigated by predicting temperature, velocity, stream function, pressure, local heat transfer coefficient, average Nusselt number, the net energy delivery rat and the dimensionless mass flow rate.

The work is organized as follows. The physical configurations, governing equations and turbulence models are introduced in Chap. 2. Chapter 3 describes the momentum-integral and numerical marching method for boundary layer type equations. The numerical solution procedure for the full Navier-Stokes elliptic equations is also presented.

Chapters 4, 5 and 6 pertain to discussion of the results obtained for parallel channel with parallel entry and exit or air, parallel channel with side entrance and exit of flow, and Trombe wall channel coupled to the room, respectively.

Chapter 2

PHYSICAL MODELS AND GOVERNING EQUATIONS

2.1 Introduction

Analysis of flow and energy transport processes in the Trombe wall channel coupled to the room, presents a challenge due to geometrical and physical complexities. Different characteristic length scales in the channel and in the room makes the comprehensive analysis of the system difficult. The Grashof number based on channel width can range from 1.0×10^3 to 1.0×10^8, depending on the chosen channel width and applied temperature difference between the walls. Since transition to turbulence occurs around Grashof number of 1.0×10^6, flow in the channel needs to be modeled either as laminar or turbulent, depending on the channel width and wall temperature conditions. The flow in the room is typically turbulent since Grashof number value based on room dimensions is typically of the order of 1.0×10^8 or greater. In view of geometric and flow complexities, many previous researchers have considered simplified geometric configurations for studying the Trombe wall channel natural convection phenomenon.

In the present study, three different geometric configurations have been analyzed to study the natural convection phenomenon in the Trombe wall channel and the adjoining room. These physical configurations are described in the next section.

2.2 Physical Configurations

2.2.1 Trombe Wall Channel Coupled to the Room

The schematic of the Trombe wall channel coupled to the room is depicted in Fig. 2.1. The operation is illustrated for the heating mode. The left surface of the room is a clear glass surface that allows solar radiation into the air gap, resulting in temperature rise of the black painted face of the storage wall. The differential heating of the concrete wall face and the glass window causes a buoyance driven flow in the channel. The low pressure created inside the channel draws in cooler air from the room. The heated air is then discharged to the room to meet the heating load demands. This constitutes the operation of the Trombe wall system in the heating mode.

The cooling or ventilation mode operation is shown in Fig. 2.2. The vent or top of the channel and the one in the room are both open during the operation. The surface of the storage wall, facing the room, is insulated. The heated air in the channel rises due to the buoyancy action, and is ejected from the channel vent. The cooler air from outside is drawn into the conditioned space from the room vent to provide the cooling and ventilation. It should be noted that the Trombe wall system has normally been used for meeting the heating load demand only. In this study, the potential of Trombe wall for providing ventilation is also investigated. This may be of interest in tropical regions where ventilation requirements outweigh heating requirements.

2.2.2 Parallel Wall Channel with Parallel Entry and Exit

This represents the simplest geometry since the channel flow is fully decoupled from the natural convection phenomenon in the room. The flow is initiated and maintained by buoyancy force in the channel and its interaction with room air convection is neglected.

The geometry of this configuration is shown in Fig. 2.3. Two parallel vertical plates have their bases in contact with air at rest at ambient temperature T_o. The temperature of the plates are constant and uniform at values T_c and T_h, different from the ambient temperature. This is the classical geometry that has been considered by many previous investigators [7, 9]. Most previous studies have used boundary layer approximation to determine the mass flow rate induced by differentially heated plates. Kettleborough [11] and Nakamura et al. [12] have also studied the same physical geometry but they have extended the domain of analysis at the inlet section to include a portion of ambient atmosphere. Application of undisturbed pressure boundary conditions on the boundaries of the extended inlet domain, as will be explained subsequently, enables one to avoid arbitrary specification of boundary conditions for pressure at the channel inlet in Fig. 2.3. In the present study, the configuration in Fig. 2.3 is analyzed for laminar flow by applying numerical as well as momentum integral techniques.

2.2.3 Parallel Channel with Side Inlet and Exit

Figure 2.4 shows a side-vented cavity with two same size openings on the heated wall, one near the upper wall and the other close to the lower wall. The upper and lower walls are insulated, and the vertical walls are maintained at constant temperatures T_c and T_h. This is fundamental geometry that models the Trombe wall channel more closely compared to the previously discussed geometry in Fig. 2.3. A review of literature indicates that natural convection characteristics of this differentially heated and vented channel has not been reported in the literature. The present study considers both laminar and turbulent natural convection in this basic configuration in some detail.

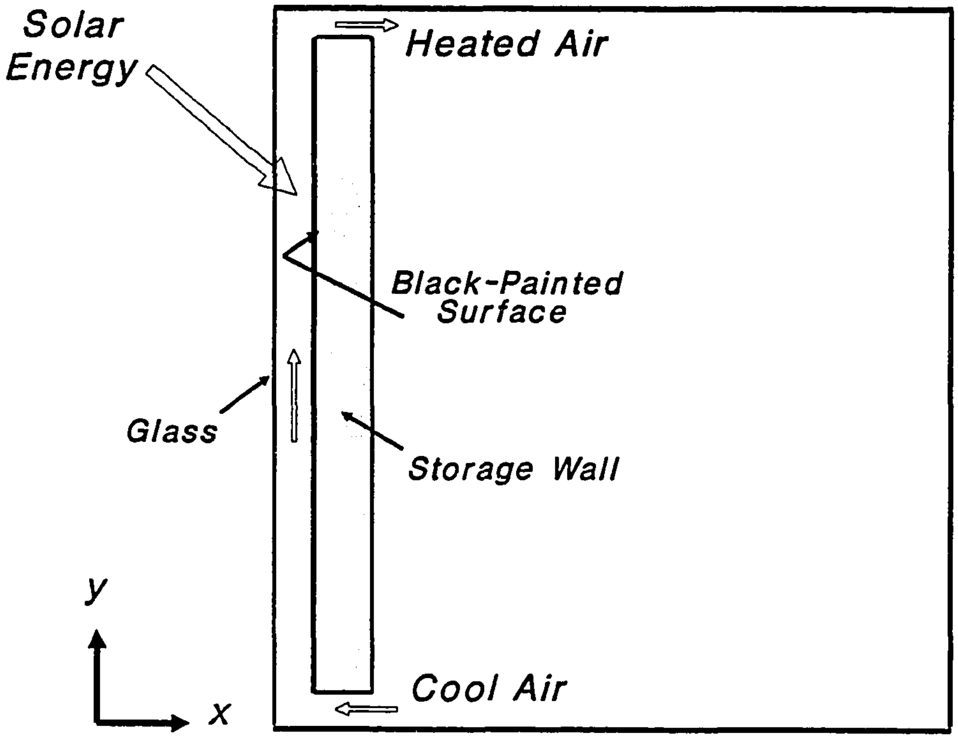

Fig. 2.1 Schematic of Trombe wall channel coupled to the room operating in heating mode

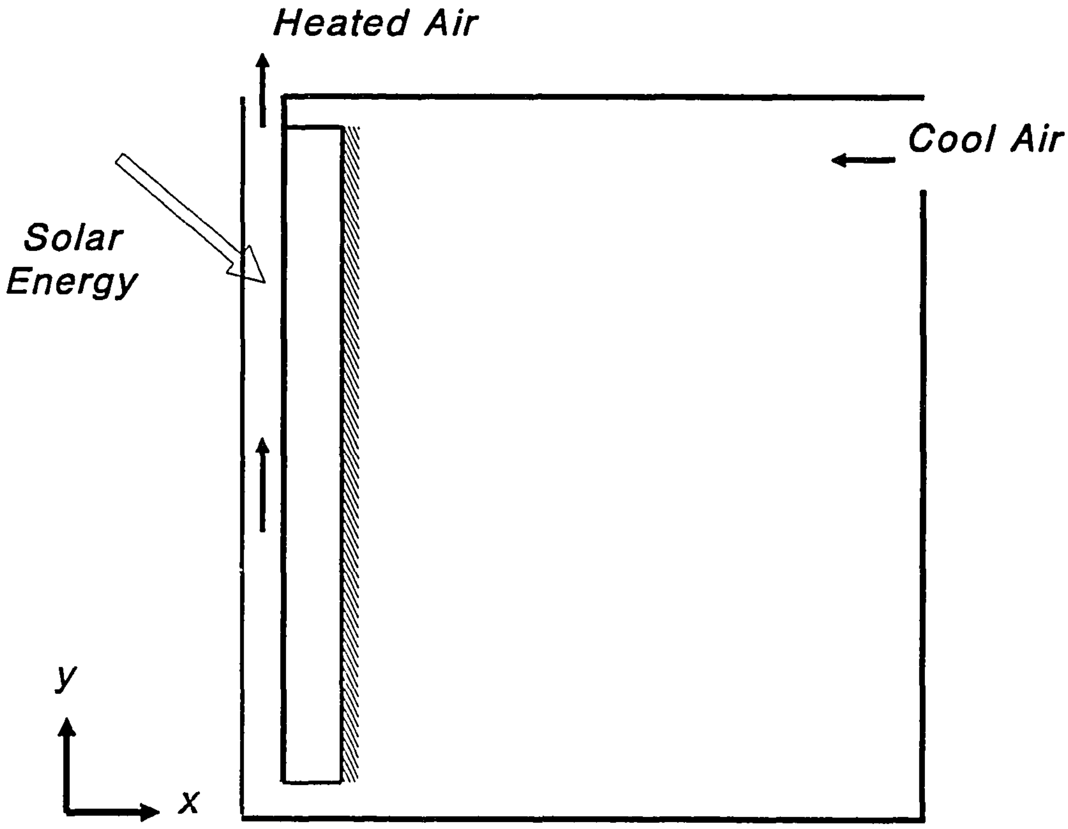

Fig. 2.2 Flow in a Trombe wall channel coupled to the room operating in cooling mode

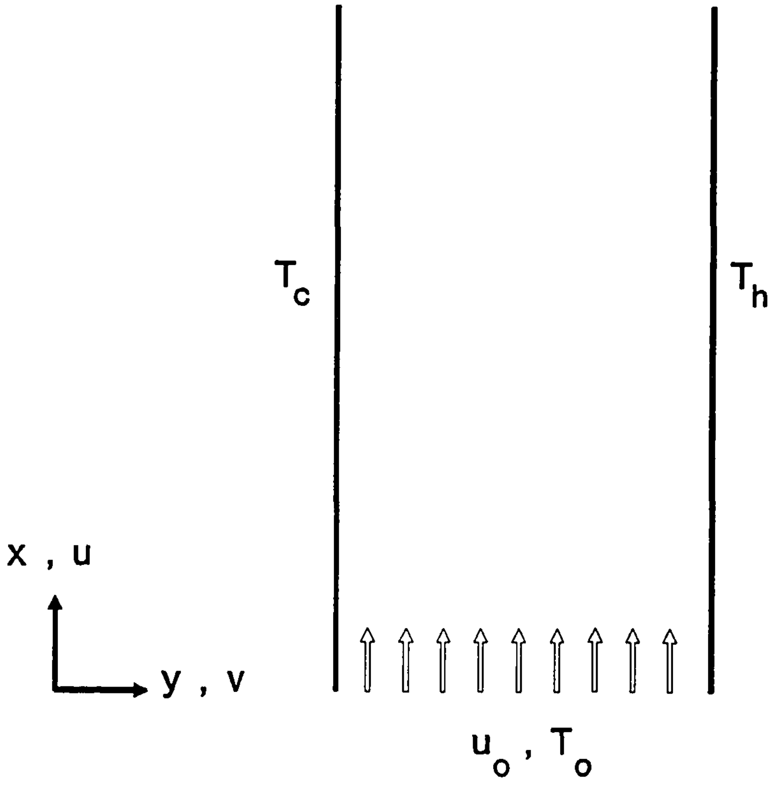

Fig. 2.3 Flow in a parallel channel with parallel entry and exit

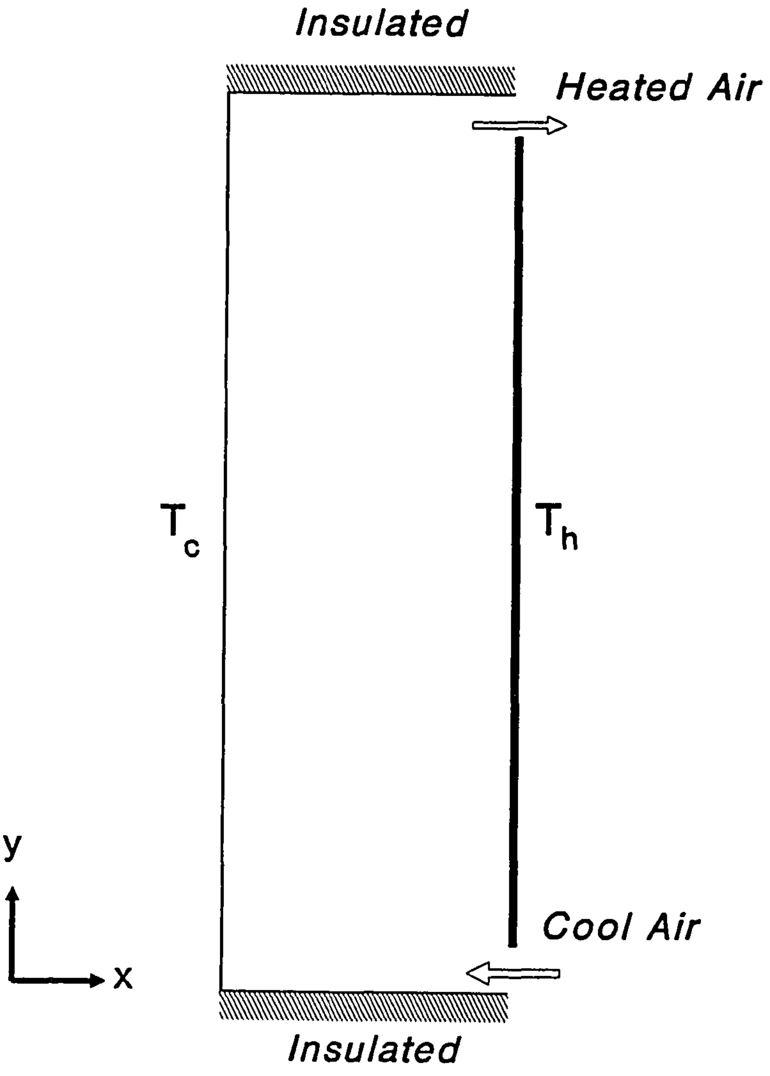

Fig. 2.4 Flow in a parallel channel with side vents

2.3 Governing Equations

The problem of determining the Trombe wall natural convection characteristics, as posed earlier, can be addressed by three different approaches, namely analytical, numerical and experimental. In the present study the first two approaches namely, the analytical and numerical are adopted to deal with the present problem. The fluid motion and heat transfer characteristics are governed by conservation laws for mass, momentum and energy transport, the equation of state, and turbulence models if the flow is turbulent. The next section describes these conservation laws.

2.3.1 Conservation Laws

Governing equations for laminar, constant property, steady and low speed flows with no heat and mass sources or sinks can be expressed as follows:

Conservation of mass:

$$\nabla \cdot (\rho \vec{u}) = 0 \tag{2.1}$$

Conservation of momentum:

$$\nabla \cdot (\rho \vec{u} u) = -\frac{\partial p}{\partial x} + \mu \nabla^2 u + B_x \tag{2.2}$$

$$\nabla \cdot (\rho \vec{u} v) = -\frac{\partial p}{\partial y} + \mu \nabla^2 v + B_y \tag{2.3}$$

Conservation of energy:

$$\nabla \cdot (\rho \vec{u} h) = k \nabla^2 T + S_h \tag{2.4}$$

Equation of state:

$$p = \rho RT \tag{2.5}$$

where, symbol ρ is the density, $\vec{u} = u\hat{i} + v\hat{j}$; μ is the dynamic viscosity, P is the pressure, B_x is the x-direction body force per unit volume, h is the specific enthalpy, k is the thermal conductivity, T is the temperature, and S_h is the volumetric rate of heat generation. The term $k\nabla^2 T$ represents the influence of conduction heat transfer within the fluid, according to the Fourier law of heat conduction. The internal heat source term S_h will be neglected from the energy equation since the present analysis focuses only on the influence of solar radiation on natural convection characteristics, through heated storage wall surfaces.

2.3.2 Governing Equations for Buoyancy Driven Flow

In problems where temperature changes bring about changes in density, it is necessary to include buoyancy forces in the equations of motion. They are treated as body forces imposed on the liquid or gas, and can be expressed as

$$\begin{aligned} B_x &= \rho g_x \\ B_y &= \rho g_y \end{aligned} \tag{2.6}$$

Generally speaking, $\rho = f(P, T)$. If P and T do not derivate too much from their reference values P_o and T_o, one can express density as

$$\rho = \rho_o + \left(\frac{\partial \rho}{\partial T}\right)_p (T - T_o) + \left(\frac{\partial \rho}{\partial p}\right)_T (p - p_o) + \;----- \tag{2.7}$$

$$\rho = \rho_o - \rho_o \beta (T - T_o) + \frac{\gamma}{C_o^2}(p - p_o) \tag{2.8}$$

where, $\beta = -\frac{1}{\rho_o}\left(\frac{\partial \rho}{\partial T}\right)_p$ is the coefficient of thermal expansion at temperature T_o, and C_o is the speed of sound in the fluid. The last term in Eq. (2.8) can usually be neglected in low speed flows that are dominated by large temperature but small pressure changes. This means that the dependence of density on pressure can be ignored, i.e.,

$$\rho\vec{g} = \rho_o\vec{g} - \rho_o\vec{g}\beta(T - T_o) \tag{2.9}$$

$$\rho_o\vec{g} = \nabla p_{st} \tag{2.10}$$

$$\bar{P} = P_o + P_{ST} \tag{2.11}$$

where P_{ST} is the hydrostatic pressure.

Substituting the above equations into the general equations, one gets:

$$\nabla \cdot (\rho\vec{u}) = 0 \tag{2.12}$$

$$\nabla \cdot (\rho\vec{u}u) = -\frac{\partial p}{\partial x} + \mu\nabla^2 u - \rho_o\beta g_x(T - T_o) \tag{2.13}$$

$$\nabla \cdot (\rho\vec{u}v) = -\frac{\partial p}{\partial y} + \mu\nabla^2 v - \rho_o\beta g_y(T - T_o) \tag{2.14}$$

$$\nabla \cdot (\rho\vec{u}h) = k\nabla^2 T \tag{2.15}$$

$$\beta = -\frac{1}{\rho}\left(\frac{\partial \rho}{\partial T}\right)_p \tag{2.16}$$

2.3.3 Governing Equation in Cartesian Coordinates

Since the geometrical configurations considered in the present study are all rectangular in nature, the governing equations for the two-dimensional, laminar, steady, natural convection flow, generated by the force of gravity along the negative y direction, can be described by the following conservation equations in Cartesian coordinates:

$$\frac{\partial}{\partial x}(\rho u) + \frac{\partial}{\partial y}(\rho v) = 0 \tag{2.17}$$

$$\frac{\partial}{\partial x}(\rho u u) + \frac{\partial}{\partial y}(\rho u v) = -\frac{\partial p}{\partial x} + \mu\left(\frac{\partial^2 u}{\partial x^2} + \frac{\partial^2 u}{\partial y^2}\right) \tag{2.18}$$

$$\frac{\partial}{\partial x}(\rho v u) + \frac{\partial}{\partial y}(\rho v v) = -\frac{\partial p}{\partial y} + \mu\left(\frac{\partial^2 v}{\partial x^2} + \frac{\partial^2 v}{\partial y^2}\right) - \rho g \tag{2.19}$$

$$\frac{\partial}{\partial x}(\rho T u) + \frac{\partial}{\partial y}(\rho T v) = \frac{k}{C_p}\left(\frac{\partial^2 T}{\partial x^2} + \frac{\partial^2 T}{\partial y^2}\right) \tag{2.20}$$

We note that the property variation is neglected except for density which is treated as variable in both inertia and buoyancy terms.

2.3.4 Turbulence Models

In turbulent flows, the instantaneous field variables, such as the flow velocity, density, pressure and temperature, fluctuate with time in a random manner. In many engineering applications, only time averaged values of flow variables are of interest. To obtain the spatial distribution of time-averaged flow properties, a procedure known as Reynolds averaging is often performed to obtain time averaged conservation equations. Conservation equations are integrated over a time period t, which is large enough to include all time scales of turbulence. The averaging procedure, however, gives rise to additional terms, namely Reynolds stresses and fluxes [22]. As a result, the number of governing equations are usually less than the number of variables in the equations. This situation is described in turbulence literature as the closure problem.

There are many different ways of addressing the closure problem, and this has given rise to a variety of turbulence models ranging from simple mixing length models to more sophisticated Reynolds stress transport models [23]. Many of these models combine analysis with empiricism to predict the turbulent flow characteristics. The mixing length models do not consider transport of turbulence properties and they are simply based on a localized balance of generation and dissipation of turbulence kinetic energy. These models are generally suited for boundary layer type flows. For flows with recirculation, transport of turbulence properties such as turbulence kinetic energy and dissipation must be taken into account. The more popular model for these situation is the two-equation (k-ϵ) model [24]. For many engineering calculations, this model provides satisfactory results. It should be emphasized that computational effort increases significantly as one shifts from relatively easy to program mixing length models to more advanced Reynolds stress transport models.

In the present study, two turbulence models have been used namely a mixing length model [25], and a two-equation (k-ϵ) model [24]. Both these models compute turbulent viscosity and turbulent thermal conductivity that occur in time-averaged momentum and energy equations.

2.3.5 Simple Algebraic Turbulence Model

The zero-equation turbulence models, also known as the algebraic turbulence model, have been developed mainly for the investigation of flows in which turbulent transport is significant only along a direction transverse to the flow direction. They are called "zero-equation" because no additional differential equation is needed to close the set of equations. It has been proposed that the effective turbulence viscosity and thermal conductivity can be written as follows [26]:

$$\frac{\mu_{eff}}{\mu} = 1 + \frac{\left[\left(\frac{\partial u}{\partial y}\right)^2 + \left(\frac{\partial v}{\partial x}\right)^2\right]^{1/2} \cdot l}{2 + \frac{g\left(\frac{\partial T}{\partial y}\right)}{\left(\frac{\partial u}{\partial y}\right)^2}} \tag{2.21}$$

$$\frac{K_{eff}}{\mu C_p} = \frac{1}{Pr} + \frac{1}{Pr_t}\left(\frac{\mu_{eff}}{\mu} - 1\right) \tag{2.22}$$

where, μ is the molecular viscosity, k_{eff} is the effective turbulent conductivity, and Pr_t is the turbulent Prandtl number. The symbol l, the mixing length, is expressed as

$$l = C_k\left(\frac{A1}{A2} + \frac{A3}{A4}\right)$$

$$C_k = von\ Karman\ consant \tag{2.23}$$

where,

$$\begin{aligned}
A1 &= \left(u^2 + v^2\right)^{1/2} \\
A2 &= \left(\frac{\partial u}{\partial x} + \frac{\partial u}{\partial y} + \frac{\partial v}{\partial x} + \frac{\partial v}{\partial y}\right)^{1/2} \\
A3 &= \left[\left(\frac{\partial u}{\partial x}\right)^2 + \left(\frac{\partial u}{\partial y}\right)^2 + \left(\frac{\partial v}{\partial x}\right)^2 + \left(\frac{\partial v}{\partial y}\right)^2\right]^{1/2} \\
A4 &= \left[\left(\frac{\partial^2 u}{\partial x^2}\right)^2 + \left(\frac{\partial^2 u}{\partial y^2}\right)^2 + \left(\frac{\partial^2 v}{\partial x^2}\right)^2 + \left(\frac{\partial^2 v}{\partial y^2}\right)^2\right]^{1/2}
\end{aligned} \tag{2.24}$$

2.3.6 The Two-Equation (k-ϵ) Turbulence Model

The zero-equation turbulence model described in the previous section greatly simplifies the analysis of turbulent flows. For predictions of the frictional coefficient and the Nusselt number for turbulent flows in pipes or over flat walls, this model serves as a useful approximation. If the flow patterns show recirculation, such that turbulent transport is important in both the x and y directions, the mixing length model is no longer valid. A typical example is turbulent natural convective flow in a two-dimensional enclosure. Before the analysis of this flow, information on the mixing length distribution $l(x,y)$ is not available. Under such circumstances the zero-equation turbulence model must be replaced by other more sophisticated models, such as the two-equation turbulent model described below.

The two equation (k-ϵ) turbulence model requires transport equations for k and ϵ which can be written in Cartesian coordinates as follows:

k-equation:

$$\frac{\partial}{\partial x}(\rho u k) + \frac{\partial}{\partial y}(\rho v k) = \frac{\partial}{\partial x}\left(\frac{\mu_t}{\sigma_k}\frac{\partial k}{\partial x}\right) + \frac{\partial}{\partial y}\left(\frac{\mu_t}{\sigma_k}\frac{\partial k}{\partial y}\right) + G - \epsilon \qquad (2.25)$$

ϵ-equation:

$$\frac{\partial}{\partial x}(\rho u \epsilon) + \frac{\partial}{\partial y}(\rho v \epsilon) = \frac{\partial}{\partial x}\left(\frac{\mu_t}{\sigma_\epsilon}\frac{\partial \epsilon}{\partial x}\right) + \frac{\partial}{\partial y}\left(\frac{\mu_t}{\sigma_\epsilon}\frac{\partial \epsilon}{\partial y}\right) + C_1\frac{G\epsilon}{k} - C_2\frac{\epsilon^2}{k^2} \qquad (2.26)$$

where,

$$G = \mu_t\left[2\left(\frac{\partial u}{\partial x}\right)^2 + 2\left(\frac{\partial v}{\partial y}\right)^2 + \left(\frac{\partial u}{\partial y} + \frac{\partial v}{\partial x}\right)^2\right] \qquad (2.27)$$

The effective turbulent viscosity μ_{eff} and the effective turbulent conductivity K_{eff} can be written as

$$\mu_{eff} = \mu + C_\mu\frac{k^2}{\epsilon} \qquad (2.28)$$

$$k_{eff} = \frac{C_p\mu}{Pr} + \frac{C_p\mu_t}{Pr_t} \tag{2.29}$$

where,

$$\begin{aligned} &Pr_t \simeq 0.9 && C_\mu = 0.09 \\ &C_1 = 1.45 && C_2 = 2.0 \\ &\sigma_k = 1.0 && \sigma_\epsilon = 1.3 \end{aligned} \tag{2.30}$$

where, k is the time-averaged turbulent kinetic energy, ϵ is the time-averaged rate of dissipation of turbulence energy, Pr_t is the turbulent Prandtl number and μ is the molecular viscosity. With the calculated values of k and one can compute the effective turbulent viscosity by using Eq. (2.28). Initial values of k and ϵ are needed for starting this calculation of effective turbulent viscosity. This iterative procedure is described in some detail in Chapter 3.

2.3.7 Governing Equations in Generalized Form

The governing equations stated above can be written in following generalized form:

$$\nabla \cdot \left(\rho u \Phi - \tau_\phi \nabla \Phi\right) = S_\phi \tag{2.31}$$

where, Φ is a general variable; τ_ϕ is the exchange coefficient for the property Φ; S_ϕ is the "source" expression for Φ, which, in the most general form may consist of a term for the rate of generation of Φ per unit volume together with other terms that cannot be included in the term on the left-hand side of the equation. With Φ representing respectively for u, v and T, Eq. (2.31) represents the conservation equations for mass, x-momentum, y-momentum and energy in a generalized form. Also, the transport equations for k and ϵ

can be represented by the same generalized form. For these equations τ_ϕ and S_ϕ assume the following forms:

$$
\begin{aligned}
S_u &= -\frac{\partial p}{\partial x} & S_v &= -\frac{\partial p}{\partial y} - \rho g \\
S_T &= 0 & & \\
S_k &= G - \epsilon & S_\epsilon &= C_1 \frac{G\epsilon}{k} - C_2 \frac{\epsilon^2}{k}
\end{aligned}
\tag{2.32}
$$

and

$$
\begin{aligned}
\tau_u &= \tau_v = \mu & \tau_T &= \frac{k}{C_p} \\
\tau_k &= \frac{\mu_t}{\sigma_k} & \tau_\epsilon &= \frac{\mu_t}{\sigma_\epsilon}
\end{aligned}
\tag{2.33}
$$

where subscripts u, v, T, k and ϵ represent the convection equations for u, v, T, k and ϵ.

The expression of all the governing differential equations for heat transfer, fluid flow, turbulence, and other related phenomena in generalized form is an important computational time-saving step. As a consequence, we need to concern ourselves with the numerical solution of the equation in the general conservation form. In the next chapter, the generalized equation has been used to develop the computer program for solving the proposed problem.

Chapter 3

BOUNDARY LAYER AND NAVIER-STOKES SOLUTION PROCEDURES

3.1 Introduction

In the present study, three different geometries, namely, the parallel channel with axial openings, the parallel channel with side vents and the Trombe wall channel coupled to the room are considered. The governing equations for steady natural convection in these geometries are coupled since temperature gradients are responsible for buoyancy driven flows. Since Navier-Stokes equations are quite difficult to solve even numerically, previous researchers have frequently made the boundary layer approximation to make the problem tractable. Using this approximation, a space marching procedure in the dominant flow direction can be used. This procedure in the dominant flow direction can be used. This procedure, used in Ref. 8, leads to correlations between mass flow rate and heat fluxes as a function of channel height and channel wall temperature difference. However, boundary layer approximation also requires a priori assumptions regarding the values of pressure and axial pressure gradient at inlet section [27]. It is also noted that the parallel wall channel geometry lends itself naturally to analysis by boundary layer approximation since recirculating regions do not appear under normal conditions, and as a result boundary layer analysis is quite appropriate. However, for channels with side entry and exit, and for the more comprehensive case of channel flow coupled to the room flow, the boundary layer analysis becomes invalid due to appearance of recirculating flows in different corners. In view of above discussion, the solution procedure is divided into two parts. The first part describes the parallel channel with axial entry. The laminar natural convective flow is analyzed by the boundary layer approximation. Both momentum integral approach, resulting in analytical solution, and numerical technique involving a marching procedure are discussed. The full Navier-Stokes procedure is discussed in the second part for both side entry/exit and comprehensive geometries. Solutions for these cases are obtained numerically.

3.2 Boundary Layer Solution Procedure

First, the momentum integral method [28] for the case of flow in a parallel channel with axial inlet and exit is presented. The temperature distribution in this case is obtained from the Oseen approximation [29]. The details of this method are given in the next section.

3.2.1 Boundary Layer Equations in the Non-Dimensional Form

In the case of flow within the vertical parallel plates, fluid properties, except density, are assumed to be independent of temperature. The decrease in fluid density due to heating is solely responsible for buoyancy forces which induce upward flow in the channel. By invoking boundary layer approximation, the governing equations for momentum and energy transport are reduced to the standard boundary layer form. In the present coordinate system, this amounts to neglecting $\frac{\partial^2 T}{\partial y^2}$, $\frac{\partial^2 u}{\partial x^2}$ and $\frac{\partial^2 v}{\partial x^2}$ in comparison to $\frac{\partial^2 T}{\partial y^2}$, $\frac{\partial^2 u}{\partial y^2}$ and $\frac{\partial^2 v}{\partial y^2}$. Additionally, the y-momentum equation reduces to the trivial form, $\frac{\partial p}{\partial y} = 0$. The resulting governing equations for mass, x-momentum and energy can be expressed as

$$\frac{\partial}{\partial x}(\rho u) + \frac{\partial}{\partial y}(\rho v) = 0 \tag{3.1}$$

$$\frac{\partial}{\partial x}(\rho u u) + \frac{\partial}{\partial y}(\rho u v) = -\frac{\partial p}{\partial x} + \frac{\partial}{\partial y}\left(\mu \frac{\partial u}{\partial y}\right) + \rho g \tag{3.2}$$

$$0 = -\frac{\partial p}{\partial y} \tag{3.3}$$

$$\rho C_p\left(u\frac{\partial T}{\partial x} + v\frac{\partial T}{\partial y}\right) = \frac{\partial}{\partial y}\left(K'\frac{\partial T}{\partial y}\right) \tag{3.4}$$

The boundary conditions are:

$$x = 0,\ 0 \le y \le b,\ \ u = U_o,\ v = 0,\ T = T_o,\ p = p_\infty \tag{3.5}$$

$$0 \le x \le L,\ y = 0,\ \ u = 0,\ v = 0,\ T = T_c \tag{3.6}$$

$$0 \le x \le L,\ y = b,\ \ u = 0,\ v = 0,\ T = T_h \tag{3.7}$$

$$x = L,\quad p = p_e \tag{3.8}$$

The pressure within the channel, P, is less than the hydrostatic pressure, P_∞, outside the channel at the same elevation. The difference, $(P - P_\infty)$, is the pressure defect. By using dimensionless parameters as

$$\begin{aligned} u^* &= \frac{ub}{vGr}, & T^* &= \frac{T - T_o}{T_h - T_o} \\ L &= \frac{l}{Grb}, & P^* &= \frac{b^2(p - p_\infty)}{\rho\nu^2 Gr^2} \\ v^* &= \frac{vb}{\nu}, & Gr &\equiv \frac{g\beta(T_h - T_o)b^3}{\nu^2} \\ y^* &= \frac{y}{b}, \end{aligned} \tag{3.9}$$

one can recast the governing equations in the following dimensionless form [8],

$$\frac{\partial u^*}{\partial x^*} + \frac{\partial v^*}{\partial y^*} = 0 \tag{3.10}$$

$$u^*\frac{\partial u^*}{\partial x^*}+v^*\frac{\partial u^*}{\partial y^*}=-\frac{\partial p^*}{\partial x^*}+\frac{\partial^2 u^*}{\partial y^{*^2}}+T^* \tag{3.11}$$

$$\frac{\partial p^*}{\partial y^*}=0 \tag{3.12}$$

and

$$u^*\frac{\partial T^*}{\partial x^*}+v^*\frac{\partial T^*}{\partial y^*}=\frac{1}{Pr}\frac{\partial^2 T^*}{\partial y^{*^2}} \tag{3.13}$$

It is noted that in non-dimensional form, the governing equations contain only one non-dimensional variable namely Pr. The other parameter, Gr, is eliminated from the equations due to stretching of dependent and independent variables, as given by Eq. (3.9). The boundary conditions in non-dimensional variables are:

$$x^*=0,\ 0\le y^*\le 1;\quad u^*=u_i^*,\ v^*=0,\ T^*=0, p^*=p_i^* \tag{3.14}$$

$$0\le x^*\le L,\ y^*=0;\quad u^*=0,\ v^*=0,\ T^*=T_c^* \tag{3.15}$$

$$0\le x^*\le L,\ y^*=1;\quad u^*=0,\ v^*=0,\ T^*=T_h^* \tag{3.16}$$

and, at

$$x^*=L;\quad p^*=p_e^* \tag{3.17}$$

where P_i^*, the pressure-defect at the inlet, is a function of u_i^*, the inlet velocity profile, which would be determined by the analysis of the "free-boundary" problem. Unfortunately P_i^* is an unknown in the boundary layer analysis since u_i^* is unknown. The pressure boundary condition at exit also requires further explanation. Let us consider

Fig. 3.1 for further elaboration. As the fluid accelerates along a stream line AB, there is a pressure loss associated with frictional forces acting in the ambient air before the inlet section. This is termed as the inlet pressure or vent loss $(\Delta P)_i$. The pressure at inlet in dimensional form (P_i) can be expressed as

$$P_\infty + \frac{U_\infty^2}{2} = P_i + \frac{U_i^2}{2} + (\Delta P)_i \tag{3.18}$$

therefore,

$$P_i = P_\infty - \frac{U_i^2}{2} - (\Delta P)_i \tag{3.19}$$

or

$$P_i - P_\infty = -\frac{U_i^2}{2} - (\Delta P)_i \tag{3.20}$$

Similar equation applied at the exit section results in

$$P_e + \frac{U_e^2}{2} = P_\infty + \frac{U_\infty^2}{2} + (\Delta P)_e \tag{3.21}$$

Therefore,

$$P_e - P_\infty = -\frac{U_e^2}{2} + (\Delta P)_e \tag{3.22}$$

Since $(\Delta P)_i$ and $(\Delta P)_e$ occur outside the channel, the boundary layer analysis can not account for them. As a result, many studies have either neglected $(\Delta P)_i$ and $(\Delta P)_e$ [7] or they have assumed their values [11]. It can also be shown that $(\Delta P)_i$ and $(\Delta P)_e$ can be combined into a single $(\Delta P)_t$, and can be lumped, and an equivalent problem with an equivalent inlet vent loss of $(\Delta P)_t$, and $(\Delta P)_e$ equal to zero can be formulated. This can be done by defining a new variable P_{new} as

$$P_{new} = P - P_\infty - (\Delta P)_e \tag{3.23}$$

therefore,

$$(P_{new})_e = P_e - P_\infty - (\Delta P)_e = 0 \tag{3.24}$$

Also,

$$(P_{new})_i = P_i - P_\infty - (\Delta P)_e \tag{3.25}$$

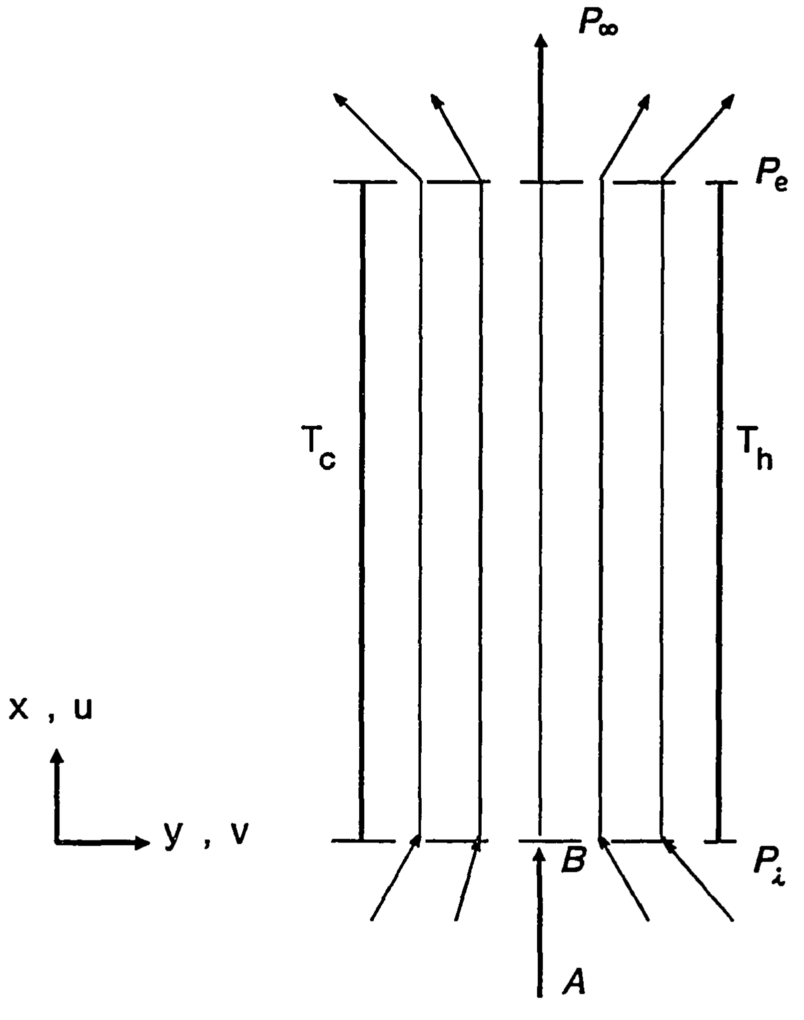

Fig. 3.1 Schematic of pressure losses at channel inlet and exit

Using Eq. (3.19), above equation be rewritten in dimensional form as,

$$\begin{aligned}(P_{new})_i &= P_\infty - \frac{U_i^2}{2} - (\Delta P)_i - P_\infty - (\Delta P)_e \\ &= -\frac{U_i^2}{2} - [(\Delta P)_i + (\Delta P)_e] \\ &= -\frac{U_i^2}{2} - (\Delta P)_t \end{aligned} \tag{3.26}$$

In non-dimensional form, this equation can be expressed as

$$(P^*_{new})_i = -\frac{{U_i^*}^2}{2} - (\Delta P^*)_t \tag{3.27}$$

Since boundary condition on pressure at exit is simplified, many boundary layer analyses have considered this equivalent formulation.

3.2.2 Momentum Integral Method

The dimensionless x-momentum equation for boundary layer formulation can be written as

$$\frac{\partial}{\partial x^*}(u^* u^*) + \frac{\partial}{\partial y^*}(u^* v^*) = -\frac{\partial p^*}{\partial x^*} + \frac{\partial^2 u^*}{\partial {y^*}^2} + T^* \tag{3.28}$$

The momentum integral form of the above equation is obtained by integrating it with respect to y^* from the left wall $(y^* = 0)$ to the right wall $(y^* = 1)$. The boundary conditions $u^* = 0$, at $y^* = 0$ and $u^* = 0$ at $y^* = 1$ are also applied. After simplification the integrated x-momentum equation becomes:

$$\underbrace{\frac{d}{dx^*}\left[\int_0^1 {u^*}^2 dy^*\right]}_{\substack{Rate\ of\ change \\ of\ integrated \\ x-momentum}} = \underbrace{-\frac{dp^*}{dx^*}}_{\substack{Pressure \\ Force}} + \underbrace{\left[\left.\frac{\partial u^*}{\partial y^*}\right|_{y^*=1} - \left.\frac{\partial u^*}{\partial y^*}\right|_{y^*=0}\right]}_{\substack{Wall\ shear \\ stress}} + \underbrace{\int_0^1 T^* dy^*}_{\substack{Buoyancy \\ Force}} \tag{3.29}$$

To solve the above equation, one needs to have some idea about the temperature and velocity profiles. In the present study, two velocity profiles were assumed, namely the

4th order and the quadratic type. The procedure here will be illustrated by considering the 4th order u^*-velocity profile. Results for the second order profile are illustrated in Appendix A. The momentum integral procedure leads to a second order ordinary differential equation for pressure, which can be solved numerically or analytically.

The u^*-velocity profile is assumed to be of the following fourth order form.

$$u^* = u_o + u_1 y^* + u_2 {y^*}^2 + u_3 {y^*}^3 + u_4 {y^*}^4 \tag{3.30}$$

The equation has five constants, and thus the procedure requires five boundary conditions or associated relations to solve for these constants. First two boundary conditions can be expressed as follows:

$$y^* = 0; \qquad u^* = 0 \tag{3.31}$$

$$y^* = 1; \qquad u^* = 0 \tag{3.32}$$

Other two boundary conditions are derived from Eq. (3.28) by evaluating the governing equation on the two walls. If one substitutes $u^* = 0$, $v^* = 0$ at $y^* = 0$ and $y^* = 1$, one obtains two associated relations

$$y^* = 0; \qquad -\frac{dp^*}{dx^*} + \frac{\partial^2 u^*}{\partial {y^*}^2} + T_c^* = 0 \tag{3.33}$$

$$y^* = 1; \qquad -\frac{dp^*}{dx^*} + \frac{\partial^2 u^*}{\partial {y^*}^2} + T_h^* = 0 \tag{3.34}$$

The final condition comes from the constancy of integrated volumetric flowrate for the incompressible flow, namely

$$Q = \int_0^1 u^* dy^* = constant \tag{3.35}$$

Using these five conditions, the five constants can be determined and expressed as

$$u_o = 0 \tag{3.36}$$

$$u_1 = \frac{1}{12}\left(\frac{dp^*}{dx^*} - T_c^*\right) + 5Q - \frac{1}{24}(T_h^* - T_c^*) \tag{3.37}$$

$$u_2 = \frac{1}{2}\left(\frac{dp^*}{dx^*} - T_c^*\right) \tag{3.38}$$

$$u_3 = \frac{1}{4}(T_h^* - T_c^*) - 10Q - \frac{5}{6}\left(\frac{dp^*}{dx^*} - T_c^*\right) \tag{3.39}$$

$$u_4 = 5Q - \frac{5}{24}(T_h^* - T_c^*) + \frac{5}{12}\left(\frac{dp^*}{dx^*} - T_c^*\right) \tag{3.40}$$

It is noted that the velocity profile is a function of pressure gradient $\frac{dp^*}{dx^*}$, and thus changing $\frac{dp^*}{dx^*}$ brings about a change of shape of the velocity profile at different section of the channel. Substituting the u-velocity profile of Eq. (3.30), along with Eqs. (3.36)-(3.40) in momentum integral Eq. (3.29) leads to the following equation

$$\begin{aligned} \frac{d}{dx^*}\left[F\left(\frac{dp^*}{dx^*}, Q\right)\right] = &- \frac{dp^*}{dx^*} + 2u_2\left(\frac{dp^*}{dx^*}, Q\right) + 3u_3\left(\frac{dp^*}{dx^*}, Q\right) \\ &+ 4u_4\left(\frac{dp^*}{dx^*}, Q\right) + \int_0^1 T^*(x^*, y^*, Q)dy^* \end{aligned} \tag{3.41}$$

where

$$F\left(\frac{dp^*}{dx^*}, Q\right) \equiv \int_0^1 u^{*^2}\left(\frac{dp^*}{dx^*}, Q\right)dy^* \tag{3.42}$$

Equation (3.41) represents a second order differential equation for P^* since Eq. (3.41) can be written as

$$\begin{aligned} \frac{dF\left(\frac{dp^*}{dx^*}, Q\right)}{d\left(\frac{dp^*}{dx^*}\right)} \frac{d^2p^*}{dx^{*^2}} = &- \frac{dp^*}{dx^*} + 2u_2\left(\frac{dp^*}{dx^*}, Q\right) + 3u_3\left(\frac{dp^*}{dx^*}, Q\right) \\ &+ 4u_4\left(\frac{dp^*}{dx^*}, Q\right) + \int T^*(x^*, y^*, Q)dy^* \end{aligned} \tag{3.43}$$

The second order equation for P^* requires two boundary conditions. They are

$$x^* = 0; \qquad P_i^* = -\frac{1}{2}Q^2 \tag{3.44}$$

$$x^* = L; \qquad P_e^* = 0 \tag{3.45}$$

Here, $(\Delta P)_t = 0$ has been assumed.

It is noted that the basic problem is to determine, for a given value of Q, a channel length (L) that will produce $P^* = 0$ at the exit. Thus, one can assume Q to be known and attempt to find L. This poses a problem since L is not known and, as a result two fully known boundary conditions are not available for this second order problem.

The momentum integral method discussed earlier is an approximation and the exact solution of boundary layer equations can be obtained by a marching technique. Realizing this limitation of boundary layer approximation and following other previous authors [8,9], we assumed in this procedure a value of $\left(\frac{dp^*}{dx^*}\right) = -3Q$ as the additional boundary condition. Use of $\left(\frac{dp^*}{dx^*}\right) = -3Q$ and $P_i^* = -\frac{1}{2}Q^2$ boundary condition, facilitates numerical procedure since both boundary conditions are then at $x^* = 0$. The assumption $\left(\frac{dp^*}{dx^*}\right) = -3Q$, represents the basic limitation of this procedure like those of other previous authors [8,9]. The effect of initial $\frac{dp^*}{dx^*}$ on natural convection problem has also been investigated in this study, and will be reported subsequently.

Since the momentum integral method has been used in the present study, the solution of Eq. (3.29) is obtained by assuming a polynomial profile of u^* as a function of y^*. A quadratic and fourth order profiles were employed. They result in a second order and first order differential equations for p, respectively. It is noted that the inertia term on the left-hand side of Eq. (3.29) leads to non-linear terms for $\frac{dp^*}{dx^*}$, and also raises the order of P^* equation to second order. This in turn requires an extra pressure boundary condition. It is taken here as $\frac{dp^*}{dx^*} = -3Q$ as suggested in Ref. 8. Dropping the inertia term in Eq. (3.29) leads to lowering of the order of the differential equation. Since the finite difference marching technique has been used in the present study, we found that by neglecting the relatively strong inertia term compare to the stress and buoyancy terms at the channel entrance, will solve the difficulty of the convergence of the calculation of $\frac{dp^*}{dx^*}$ at the first x-location. However, this inertia term, the effect of convection heat transfer, can not be totally neglected.

It is noted that Eq. (3.43) can not be solved unless T^* is known. The value of T^* is obtained by the Oseen approximation described below.

In the momentum integral Eq. (3.43), the integral of buoyancy or temperature term is still unknown. In this study, we have used the Oseen approximation [29] to get a closed form approximation to the temperature profile. In the Oseen approximation as described by Oseen [29], and applied by Tichy [27] to natural convection problem, the governing equations are expressed as

$$\frac{\partial u^*}{\partial x^*} + \frac{\partial v^*}{\partial y^*} = 0 \tag{3.46}$$

$$\alpha Q \frac{\partial u^*}{\partial x^*} = -\frac{\partial p^*}{dx^*} + \frac{\partial^2 u^*}{\partial y^{*2}} + T^* \tag{3.47}$$

$$\alpha Q \frac{\partial T^*}{\partial x^*} = \frac{1}{Pr} \frac{\partial^2 T^*}{\partial y^{*2}} \tag{3.48}$$

We note that in the Oseen approximation, the non-linear terms such as $u^* \frac{\partial u^*}{\partial x^*} + v^* \frac{\partial u^*}{\partial y^*}$ are replaced by a linear term $\alpha Q \frac{\partial u^*}{\partial x^*}$ for modeling. The value of constant α is between 1 and 2. The parameter Q represents the uniform flow velocity at the inlet. The boundary conditions for Eq. (3.48) can be expressed as

$$x^* = 0, \quad 0 \leq y^* \leq 1; \quad T^* = 0 \tag{3.49}$$

$$
\begin{aligned}
0 \le x^* \le L, \quad y^* = 0; \quad & T^* = T_c^* \\
y^* = 1; \quad & T^* = T_h^*
\end{aligned}
\tag{3.50}
$$

The solution to Eq. (3.48), subject to the boundary conditions expressed by Eqs. (3.49) and (3.50), is found by the standard methods of separation of variables and Fourier series analysis [27].

$$T^*(x^*, y^*, Q) = T_c^* + (1 - T_c^*)y^* + \sum A_n e^{-\frac{n^2\pi^2 x^*}{Pr\alpha Q}} \sin(n\pi y^*)$$

where

$$A_n = \frac{2}{n\pi}\left[(-1)^n - T_c^*\right] \tag{3.51}$$

where the empirical constant α has been found to have an optimal value of 1.3 in the present study, to account for variation of convective terms of Eqs. (3.47) and (3.48). Some results are presented in Chapter 4 to justify the above value of α.

3.2.3 The Solution Procedure

A computer program (Appendix C) was written to solve for pressure and velocity profile by using the momentum-integral method in conjunction with the Oseen model.

The steps for solving the u, v, P fields are:

1. Choose the volumetric flowrate Q, and wall temperatures T_c^* and T_h^*.
2. Use an initially guessed value of $\frac{dp^*}{dx^*}$, usually taken from the previous step.
3. Find u and v based on assumed value of $\frac{dp^*}{dx^*}$.
4. Solve for new $\frac{dp^*}{dx^*}$ from Eq. (3.41).
5. Compare calculated $\left(\frac{dp^*}{dx^*}\right)_{new}$ value with the guessed value.

6. Update guess value of $\frac{dp^*}{dx^*}$ with previous calculated value, until it converges.
7. Use the converged $\frac{dp^*}{dx^*}$ value and calculate the u-velocity field by using Eq. (3.30).
8. Solve v-velocity through the continuity equation.
9. March in x-direction until the boundary condition $P^* = 0$ of Eq. (3.45) is satisfied at $x^* = L$.
10. The length of the channel L represents the final outcome of the solution procedure for a given value of Q. Different values of Q are selected and steps 1 to 10 are repeated to obtain a relationship between L and Q.

3.3 Calculation of Boundary Layer Flow Using Finite Difference Scheme

The dimensionless governing equations, Eqs. (3.10) to (3.13), for boundary layer flow have also been solved by a forward-marching line-by-line implicit finite-difference technique in the present study [8].

A rectangular grid, across the channel width as shown in Fig. 3.2, is used to establish the increments of the finite-difference approximations to the dimensionless Eqs. (3.10) to (3.13) stated in the previous section. In general, the expressions are of the form

$$u^* \frac{\partial u^*}{\partial x^*} = \frac{u^*_{M+1,N}\left(u^*_{M+1,N} - u^*_{M,N}\right)}{\Delta x^*} \tag{3.52}$$

$$v^* \frac{\partial u^*}{\partial y^*} = \frac{v^*_{M+1,N}\left(u^*_{M+1,N+1} - u^*_{M+1,N-1}\right)}{2(\Delta y^*)} \tag{3.53}$$

$$\frac{\partial^2 u^*}{\partial y^{*2}} = \frac{\left(u^*_{M+1,N+1} - 2u^*_{M+1,N} + u^*_{M+1,N-1}\right)}{(\Delta y^*)^2} \tag{3.54}$$

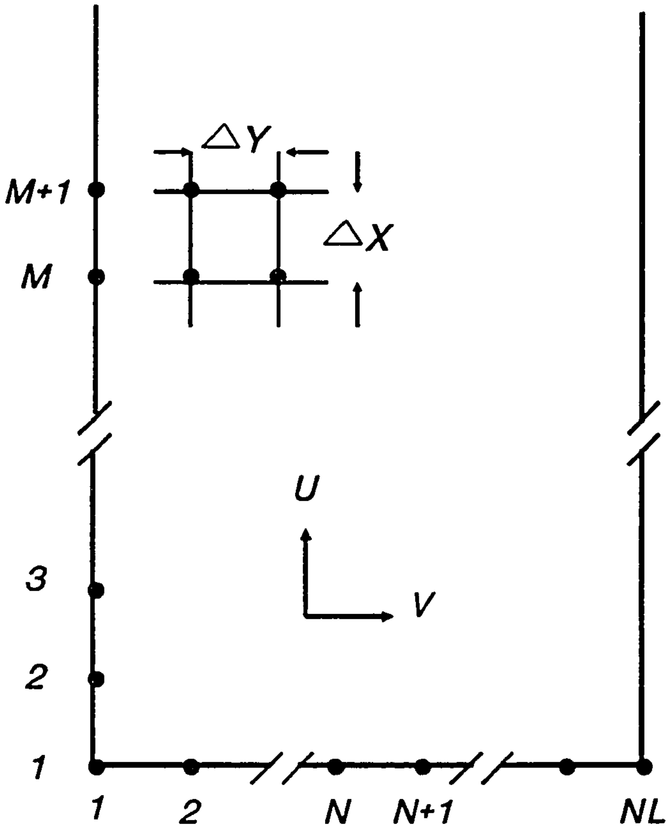

Fig. 3.2 Grid for difference representation

Upon substituting the finite-difference approximations into Eqs. (3.10), (3.11) and (3.13), and applying the boundary conditions of Eqs. (3.14) to (3.17), a set of $(N-2)$ linear equations for $u^*_{M+1,N}$ and $T^*_{M+1,N}$ and $v^*_{M+1,N}$ are obtained. First the energy equation is solved, providing a temperature $T^*_{M+1,N}$, which is then used in the momentum equation. The u^* velocity which results is used to calculate a new v^* velocity based on the continuity equation.

The results pertaining to prediction of channel height, L, for given volumetric flow rate, Q, obtained from the momentum integral and finite difference methods are presented in Chapter 4.

3.4 Navier-Stokes Solutions for Complex Geometries

Boundary layer approximation, as discussed earlier, breaks down for more complex Trombe wall geometries due to recirculating flow regions in the channel as well as in the room. Since analytical solutions of full Navier-Stokes are not feasible, one must use numerical methods to obtain solution of the governing conservation equations. A review of literature reveals that researchers have used primarily three methods namely finite difference, control volume and finite element. We have adopted the control volume approach in the present study. This approach assures that the conservation laws are satisfied even for very coarse grid and control volumes. This approach also lends itself to better interpretation of physical mechanisms.

3.4.1 Control-Volume Approach

The physical domain is discretized by using a numerical grid in the Cartesian coordinate. This is illustrated for the square cavity geometry shown in Fig. 3.3. A non-uniform grid with more points located near solid walls, for resolving the boundary layers on the walls, is considered. The half control volume around point P is considered

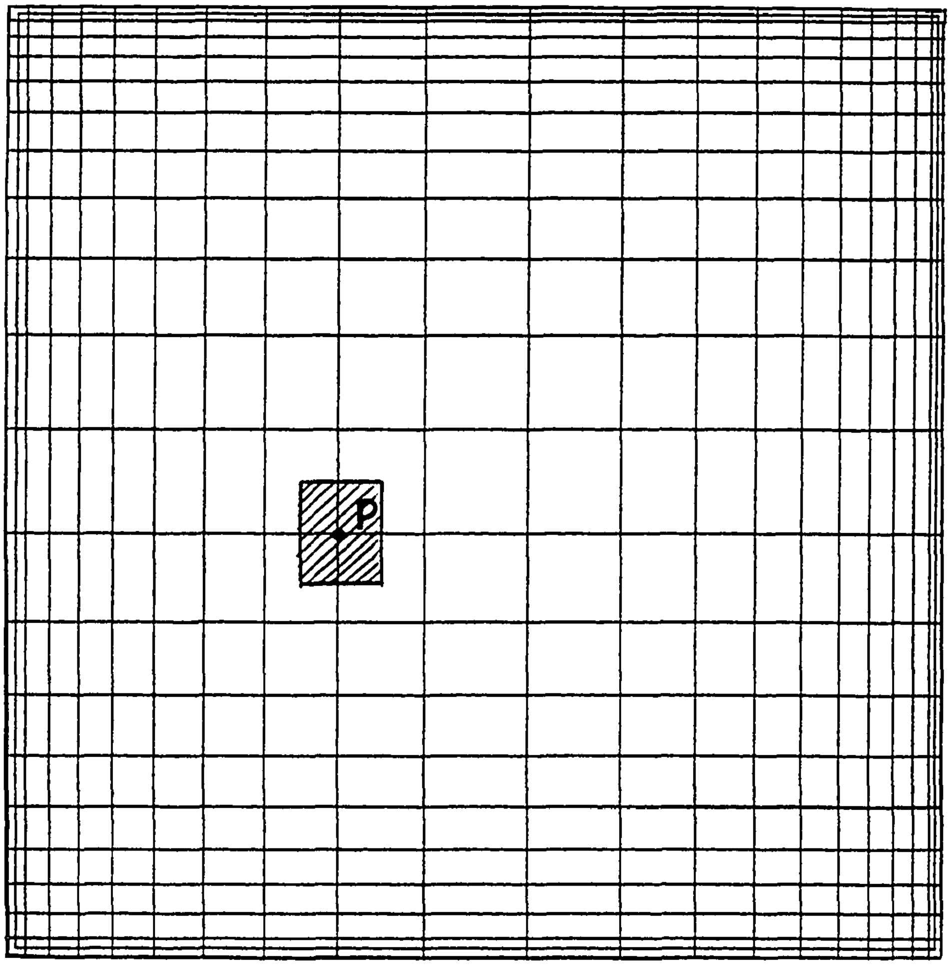

Fig. 3.3 Grid illustration of a square cavity

for determining the discretized equations. The differential equation, representing a conservation law, is integrated over each control-volume by assuming certain profiles expressing the variation of the general variable Φ, between the grid point, to obtain the integrals that need to be evaluated during the integration process. This results in the discretization equations for various variable at grid points. The next section gives details of the discretization procedure.

3.4.2 Discretization Equations

The objective is to select a control-volume and integrate the generalized equation which represents conservation equations for mass, momentum and energy, as described in Chapter 2. For the two-dimensional case, the general governing equation can be written as [20]

$$\frac{\partial J_x}{\partial x} + \frac{\partial J_y}{\partial y} = S \tag{3.55}$$

where, J_x and J_y are called the total (convection plus diffusion) fluxes defined by

$$J_x = \rho u \Phi - \tau \frac{\partial \Phi}{\partial x} \tag{3.56}$$

$$J_y = \rho v \Phi - \tau \frac{\partial \Phi}{\partial y} \tag{3.57}$$

where u and v denote the velocity components in the x and y directions. Since details of numerical procedure follows Patankar [20], only important features of the numerical procedure are described here.

An enlarged view of the control-volume employed for illustration of discretization procedure is shown in Fig. 3.4. A staggered grid is employed. All variables except velocity are stored at grid points while velocity components are stored at locations midway between the grid points.

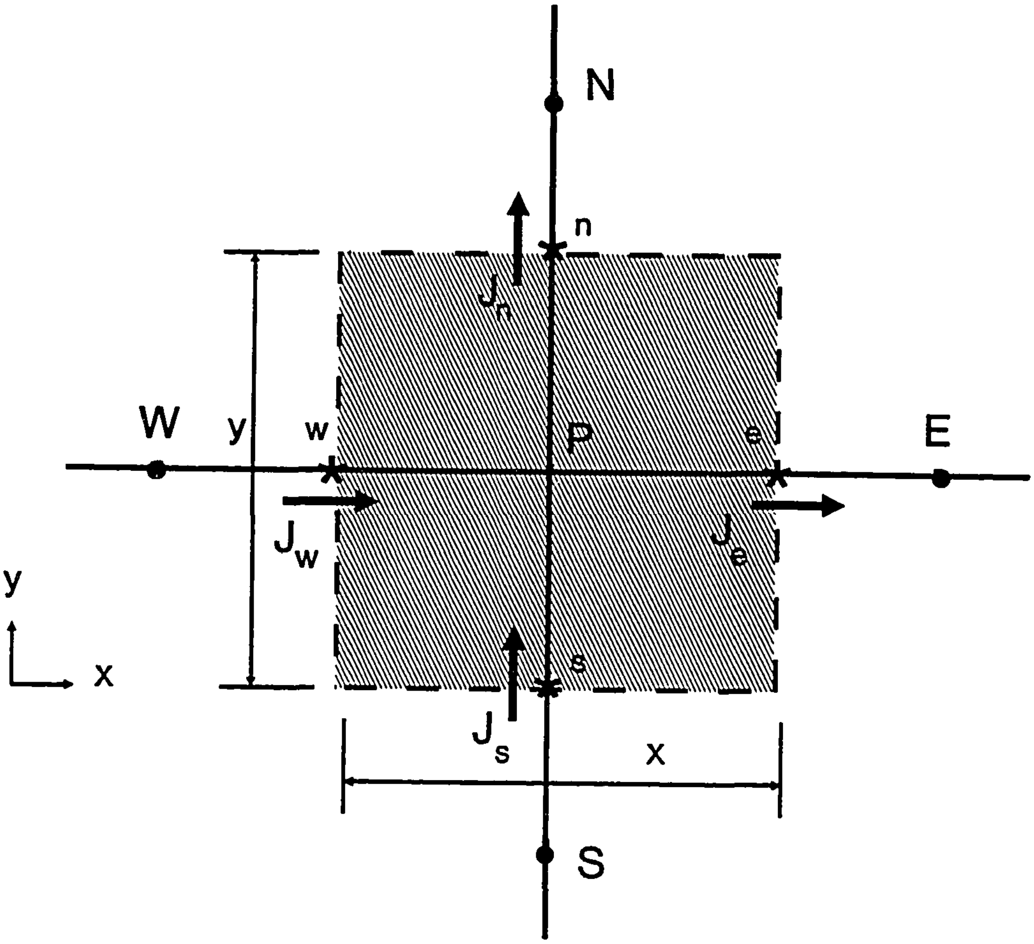

Fig. 3.4 Control-volume for the two-dimensional situation

The integration of Eq. (3.55) over the control-volume shown in Fig. 3.4 gives

$$(J_e - F_e\Phi_p) - (J_w - F_w\Phi_p) + (J_n - F_n\Phi_p) - (J_s - F_s\Phi_p) = \bar{S}\Delta x\Delta y \qquad (3.58)$$

The quantities J_e, J_w, J_n and J_s are the integrated total fluxes over the control-volume faces. F_e, F_w, F_n and F_s are the mass flow rates through the faces of the control-volume.

In the present study, we have used the hybrid scheme, power-law scheme and the quadratic upwind differencing scheme. In hybrid and power-law schemes, the variation of function Φ between grid points is represented by piece-wise linear functions. At low values of a cell Peclet number, $-2 \leq Pe \leq 2$, the hybrid scheme reduces to central differencing scheme. At value of $|Pe|$ greater 2.0, the upwind-differencing scheme is used to discretize the non-linear convective terms. The upwind-differencing scheme is first order accurate, and consequently it can lead to significant artificial diffusion as high Peclet numbers. The power-law scheme, avoids an abrupt change from central to upwind differencing at $|Pe| = 2.0$. At low values of Pe, it reduces to central differencing scheme. For $|Pe| > 10$, it becomes identical to the upwind differencing scheme, while providing a smooth transition between the two schemes in the Peclet number ranging from $2 \leq |Pe| \leq 10$. The quadratic upwind differencing scheme represents improvement over power-law and hybrid schemes since it uses a quadratic function to interpolate the value of function Φ between nodal points. This scheme is second order accurate, and it minimizes artificial diffusion inherent in power-low and quadratic interpolation schemes. The numerical procedure here is illustrated by using the power-law scheme.

It is noted that the departure of the hybrid scheme from the exact solution is rather larger at $Pe = \pm 2$; also, it seems rather premature to set the diffusion effects equal to zero as soon as absolute value of Pe exceeds 2. A better approximation to the exact solution is given by the power-law scheme [20]. In turns out that for absolute value of Pe greater than 10, the power-law becomes identical with the hybrid scheme.

By using the power-law scheme, the two-dimensional discretization equation can be written as

$$a_p\Phi_p = a_E\Phi_E + a_W\Phi_W + a_N\Phi_N + a_S\Phi_S + b_\phi \tag{3.59}$$

where,

$$a_p = a_E + a_W + a_N + a_S - S_p\Delta x\Delta y \tag{3.60}$$

$$b_\phi = S_c\Delta x\Delta y \tag{3.61}$$

The quantities S_c and S_p arise from the source term linearization of the form

$$S = S_c + S_p\Phi_p \tag{3.62}$$

3.4.3 Calculation of the Flow Field

The major problem of using the primitive variables namely u, v and p is that the pressure field is unknown. If the pressure field was known, the momentum equation can be quickly solved to yield u and v values. However, this will leave an unsatisfied mass conservation equation. The procedure adopted here is due to Patankar [20], and it uses the mass conservation equation to generate an additional equation for unknown pressure field.

A staggered grid, as shown in Fig. 3.5, is used for solution of u, v, p and Φ variables. Harlow and Welch [31] were the first to use staggered grid in which u, v and values are stored at different points. The approach was also used subsequently by Patankar and Spalding [32]. The treatment of the momentum equation is essentially the same as that

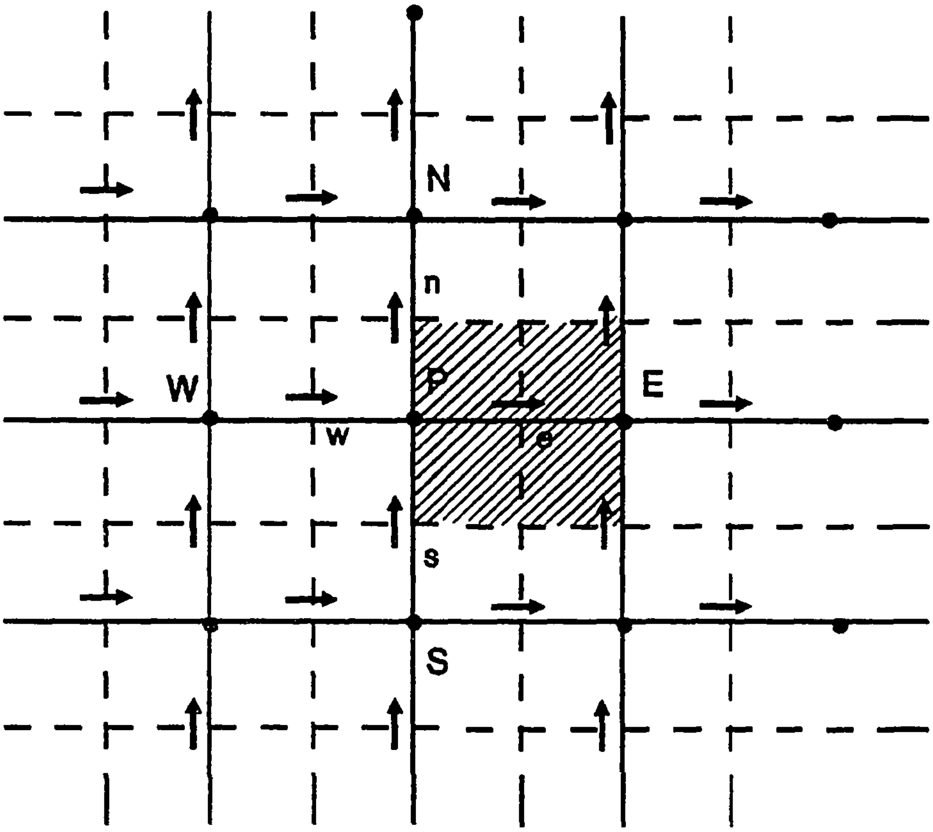

Fig. 3.5 Staggered location for u and v

for the general variable Φ. The resulting discretization equations for u and v components can be written as

$$a_e u_e = \sum a_{nb} u_{nb} + b_u + (P_P - P_E) A_e \tag{3.63}$$

$$a_n v_n = \sum a_{nb} v_{nb} + b_v + (P_p - P_N) A_n \tag{3.64}$$

In the above equations, the neighbor coefficients account for the combined convection-diffusion influence at the control-volume faces. The term b is defined in the same manner as in the previous section of this chapter, but the pressure gradient is not included in the source-term quantities S_c and S_p. Symbols A_e and A_n are the area on which the pressure difference acts.

3.4.4 The Pressure Equation

In the present study, we have used the SIMPLER [32] procedure to calculate the flow field. This algorithm consists of solving the pressure equation to obtain the pressure field and solving the pressure-correction equation to only correct the velocities. An equation for obtaining the pressure field can be derived as follows: The momentum equations (3.63) and (3.64) is first written as

$$u_e = \frac{\sum a_{nb} u_{nb} + b_u}{a_e} + \frac{A_e}{a_e}(P_P - P_E) \tag{3.65}$$

Following Patankar [20], we define a pseudo-velocity

$$\hat{u}_e = \frac{\sum a_{nb} u_{nb} + b_u}{a_e} \tag{3.66}$$

Equation (3.65) the becomes

$$u_e = \hat{u}_e + \frac{A_e}{a_e}(P_P - P_E) \tag{3.67}$$

Similarly, one can write

$$v_n = \hat{v}_n + \frac{A_n}{a_n}(P_p - P_N) \tag{3.68}$$

If one constructs a control-volume in Fig. 3.5 for the continuity equation and integrates it over the control volume, the continuity equation becomes

$$[(\rho u)_e - (\rho u)_w]\Delta y + [(\rho v)_n - (\rho v)_s]\Delta x = 0 \tag{3.69}$$

Substitution of all the velocity components, in mass conservation equation results in the following equation for pressure

$$a_P P_P = a_E P_E + a_W P_W + a_N P_N + a_S P_S + b \tag{3.70}$$

$$b = [(\rho u)_w - (\rho u)_e]\Delta y + [(\rho v)_s - (\rho v)_n]\Delta x \tag{3.71}$$

where,

$$\begin{aligned} a_E &= \rho_e \frac{A_e}{a_e}\Delta y \\ a_W &= \rho_w \frac{A_w}{a_w}\Delta y \\ a_N &= \rho_n \frac{A_n}{a_n}\Delta x \\ a_S &= \rho_s \frac{A_s}{a_s}\Delta x \end{aligned} \tag{3.72}$$

3.4.5 The Velocity-Correction Equation

The pressure field determined from Eq. (3.70) is not the right solution since it is based on guessed velocity components $\hat{u}$ and $\hat{v}$. The velocity field obtained from momentum equations and the uncorrected pressure field will not satisfy the mass conservation equation. As a result, the velocity field needs to be corrected so that the corrected field is closer to satisfying the mass conservation equation. This is done by deriving a pressure correction equation by first expressing the velocity field as [20]

$$u_c = u_c^* + \frac{A_e}{a_e}(P_P - P_E) \tag{3.73}$$

where, u_e^* is the velocity calculated by using the pressure field P, based on $\hat{v}$.

Similarly, we can express velocity in y-direction as

$$v_n = v_n^* + \frac{A_n}{a_n}(P_P - P_N) \tag{3.74}$$

Substituting for velocity components in the continuity equation, one gets

$$a_P P'_P = a_E P'_E + a_W P'_W + a_N P'_N + a_S P'_S + b' \tag{3.75}$$

where

$$b' = [(\rho u^*)_w - (\rho u^*)_c]\Delta y + [(\rho v^*)_s - (\rho v^*)_n]\Delta x \tag{3.76}$$

After, solving the above equation for P', one can use the results to correct the velocity field by Eqs. (3.73) and (3.74).

3.4.6 The Solution Procedure

The difference equations to be solved can be summarized as follows:

The pressure P equation

$$a_P P_P = a_E P_E + a_W P_W + a_N P_N + a_S P_S + b \tag{3.77}$$

The velocity-field equations

$$a_e u_e = \sum a_{nb} u_{nb} + b_u + (P_P - P_E) A_e \tag{3.78}$$

$$a_n u_n = \sum a_{nb} v_{nb} + b_v + (P_P - P_N) A_n \tag{3.79}$$

The pressure-P' equation

$$a_P P'_P = a_E P'_E + a_W P'_W + a_N P'_N + a_S P'_S + b' \tag{3.80}$$

The Eq. (3.59) can be reduced to the following tridiagonal matrix form by making sweeps in x and y directions:

$$a_\xi \Phi_\xi = b_\xi \Phi_{\xi+1} + c_\xi \Phi_{\xi-1} + d_\xi \tag{3.81}$$

The tridiagonal matrix inversion algorithm (Thomas algorithm) is employed for the solution of the algebraic finite-difference equation, with suitable boundary conditions for the type of problems considered.

The unknown variables along each grid line are calculated by application of the tridiagonal matrix, on the assumption that values on neighboring lines are known. This operation is performed in turn on the sets of lines lying in x and y directions (for 2D flow).

A computer program was developed that incorporated the SIMPLER algorithm [20]. The sequence of operations can be stated as follows:

1. Initiate the procedure with the guessed velocity field (u, v).
2. Calculate the coefficients a_{nb} for the momentum equations.
3. Calculate $\hat{u}$ and $\hat{v}$.
4. Calculate the coefficients for the pressure Eq. (3.72) and solve Eq. (3.70) to obtain the pressure field P,
5. Using the pressure field P, solve the momentum Eqs. (3.63) and (3.64) to obtain u and v.
6. Calculate the mass source b of Eq. (3.76) and hence solve for P' from Eq. (3.75).
7. Solve for Φ from Eq. (3.59).
8. Return to step 2 and repeat until convergence.

Chapter 4

RESULTS FOR PARALLEL CHANNEL USING BOUNDARY LAYER MODEL

4.1 Introduction

In this chapter, we present results that have been obtained from the boundary layer model for laminar flow in parallel wall channel geometry with axial entry and exit (Fig. 2.3). Both plates are maintained at temperature T_c^* and T_h^* respectively. All results, using the momentum-integral method, have been obtained by assuming a fourth-order fit to the velocity profile. Results have also been obtained for various values of Prandtl number. First, results obtained for air flow through the parallel wall geometry are presented, and compared with results of Akbari and Borger [8]. The present work then extends the theory to high and low Prandtl number fluids.

4.2 Convective Constant (α)

The role of three factors namely thermal convective constant (α) in Oseen Model, initial pressure gradient, $\left(\frac{dp^*}{dx^*}\right)_i$, an the inertia term on the left-hand side of the momentum-integral equation were analyzed before calculating the flow and temperature fields. The optimum value of α was determined by considering several values of α and comparing the results with those of Akbari and Borger [8]. The $\alpha = 1.3$ value yielded the best comparison as seen from Fig. 4.1 for a wide range of volumetric flow rate and cooled wall temperatures. Consequently, $\alpha = 1.3$ was adopted for all subsequent calculations.

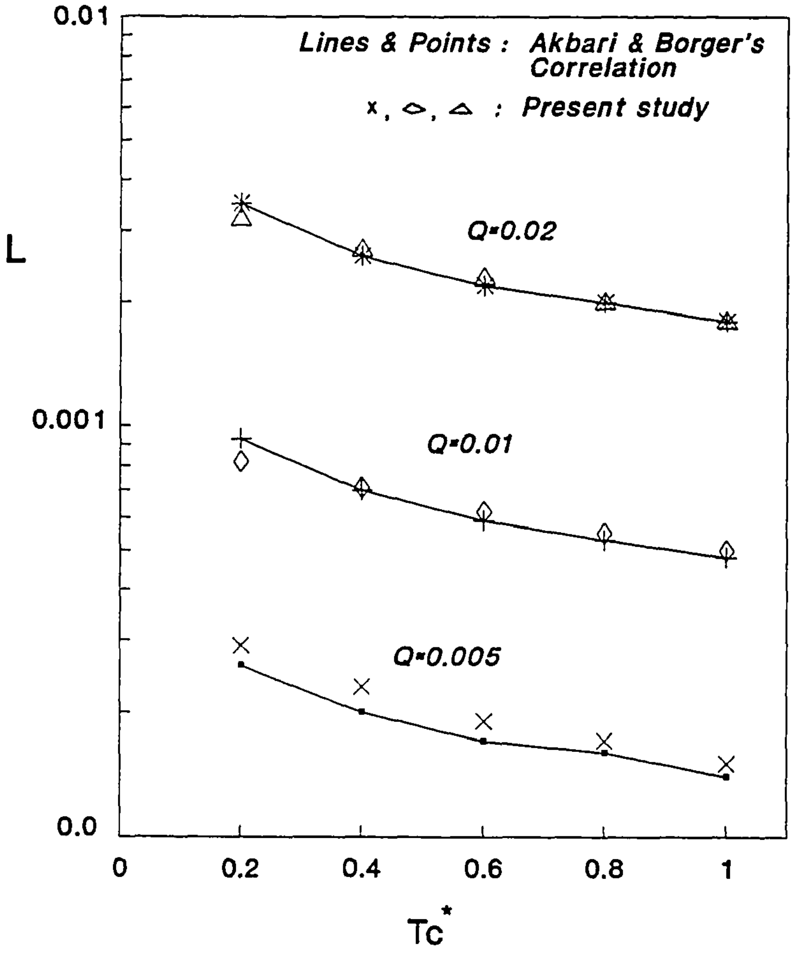

Fig. 4.1 Comparison of the prediction of channel height between Akbari's correlations and present study with $\alpha = 1.3$

As noted earlier, the boundary layer approximation requires specification of pressure gradient value $\frac{dp^*}{dx^*}$ at the inlet section. Previous researchers have used the boundary condition $\left(\frac{dp^*}{dx^*}\right) = -3Q$ at the inlet section of the channel [8]. In the present study, the inlet pressure gradient was varied from $-3Q$ to $-30Q$ to determine the sensitivity of results to the inlet pressure gradient. Results of the present study show that the prediction of channel height differ by about 2 percent from Akbari and Borger's results when a value of $-30Q$ is used instead of $-3Q$ value. This indicated that the results are not very sensitive to the inlet value of pressure gradient. In subsequent calculations, we used the pressure gradient condition $\left(\frac{dp^*}{dx^*}\right) = -3Q$ at the inlet.

Figure 4.2 shows the comparison of the prediction of channel height for two cases namely, with inertia term and without inertia term in the momentum-integral equation. As we discussed earlier in Chapter 3, the neglect of inertia term leads to simplification of the solution procedure of momentum-integral equation as it reduces from a second order equation to a first order equation for pressure. Results show that by dropping the inertial term can still predict the channel height with reasonable accuracy, specially in the mid-to-high flow rate regimes. However, as seen from Fig. 4.2, the accuracy of this inertia less procedure deteriorates significantly for flow rates lower than $Q = 0.005$.

4.3 Temperature and Velocity Profiles for Air

In this section, the temperature and velocity profiles are calculated and compared with existing results for parallel channel geometry. As discussed in Chapter 3, the procedure first involves choosing a flow rate Q. Using boundary conditions $P_i^* = -\frac{1}{2}Q^2$, and $\left(\frac{dp^*}{dx^*}\right) = -3Q$, the governing Eq. (3.29) is integrated along the flow direction. The procedure is continued until the location $x = L^*$ is reached, where the pressure value becomes zero, thus satisfying the exit pressure boundary condition. After $\frac{dp^*}{dx^*}$ and p^*

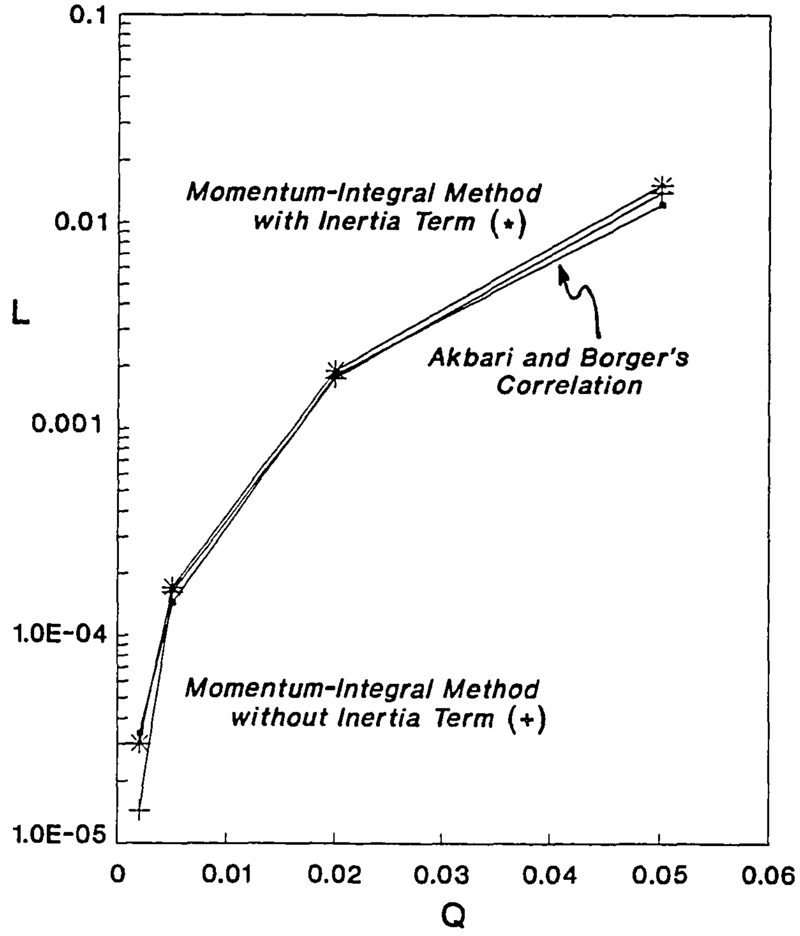

Fig. 4.2 Comparison of Q vs. L for cases with and without inertia term in the momentum-integral equation

values are determined, the u-velocity profiles at different x-locations are determined from Eq. (3.40). The v-velocity is determined from the mass conservation equation, and temperature profiles are obtained from Eq. (3.51).

Figure 4.3 shows the comparison of u-velocity profiles at two x locations, obtained from Akbari and Borger's calculation and present study. It is noted that they are in good agreement with one another. Figures 4.4–4.9 show details of the temperature profiles, T^*, and the x and y velocity components labeled as u^* and v^* for two flow rates respectively. The first case discusses the high flow rate of $Q = 0.02$ with symmetric wall temperature boundary condition expressed as $T_c^* = 1.0$ and $T_h^* = 1.0$. The second case considers lower flow rate of $Q = 0.0005$ with asymmetric wall temperature boundary condition expressed as $T_c^* = 0.15$ and $T_h^* = 1.0$. Each figure shows the temperature and velocity profiles at four relative wall elevations, namely, x/L = 0.01, 0.1, 0.5 and 1.0.

At high flow rates, the u-velocity profiles in Fig. 4.5 shows rapid development to parabolic shape soon after entry. The v-velocity component as expected shows anti-symmetry about the mid-plane of the channel. As the flow near the wall in inlet section slows due to fluid friction, a rapid movement of flow towards the channel axis develops. This is evident by sharp peaks in v-velocity in the entrance region. As the axial flow velocity reaches the nearly fully developed shape, the v-velocity peaks decrease sharply, and eventually v-velocity becomes very small across the channel section. This is consistent with rapid development of velocity profile to its asymptotic parabolic shape. For high flow rate case $Q = 0.02$) and symmetric temperature boundary conditions ($T_c^* = T_h^* = 1.0$), the fluid temperature (T^*) in the core region of the fluid gradually acquires higher and higher values as the flow proceeds up the channel (Fig. 4.4).

For the lower flow rate ($Q = 0.0005$) and unsymmetric heating case, frictional forces are still largely responsible for the initial acceleration of the fluid. The axial velocity

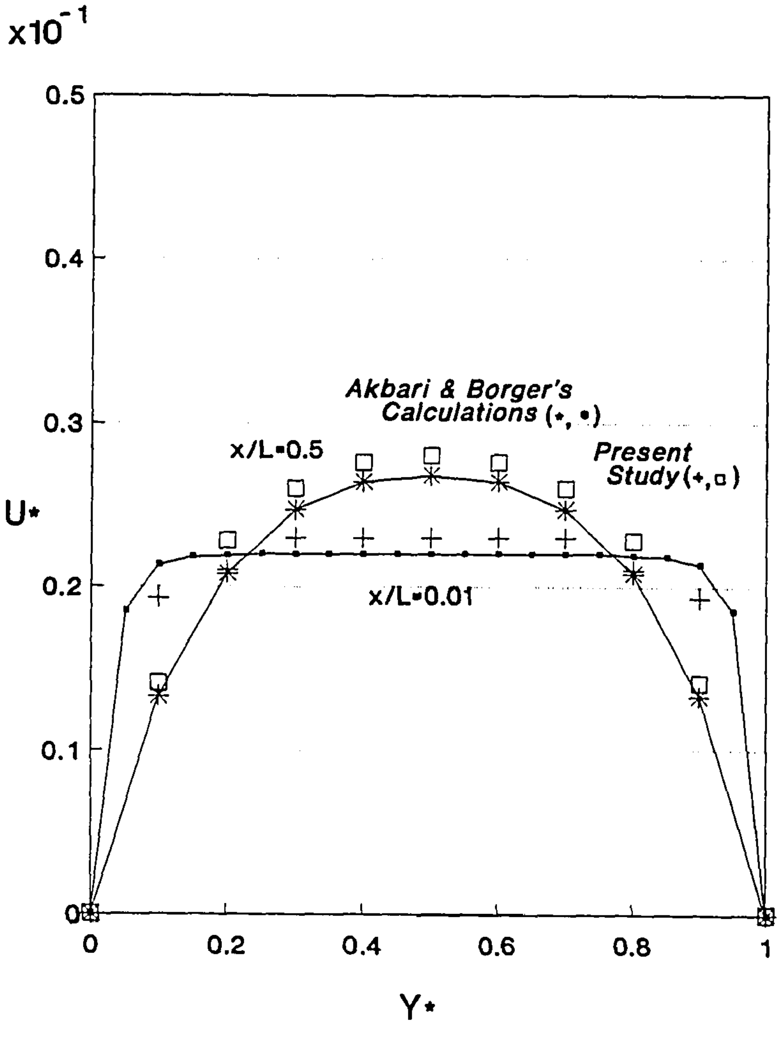

Fig. 4.3 Comparison of the prediction of channel height between Akbari's correlations and present study with $\alpha = 1.3$

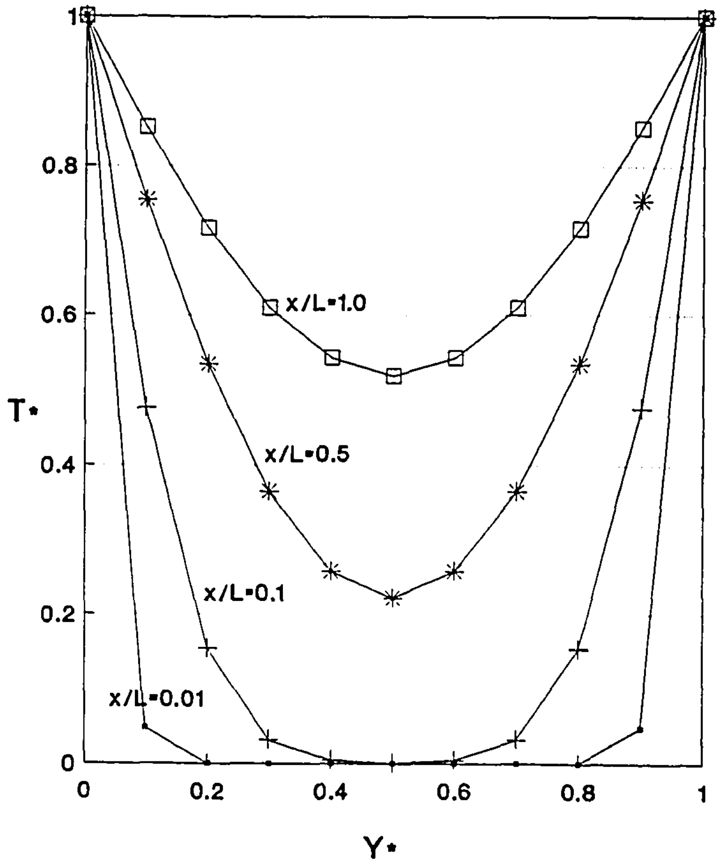

Fig. 4.4 Temperature profiles at four stages of development for Q = 0.02, $T_c^* = 1.0$

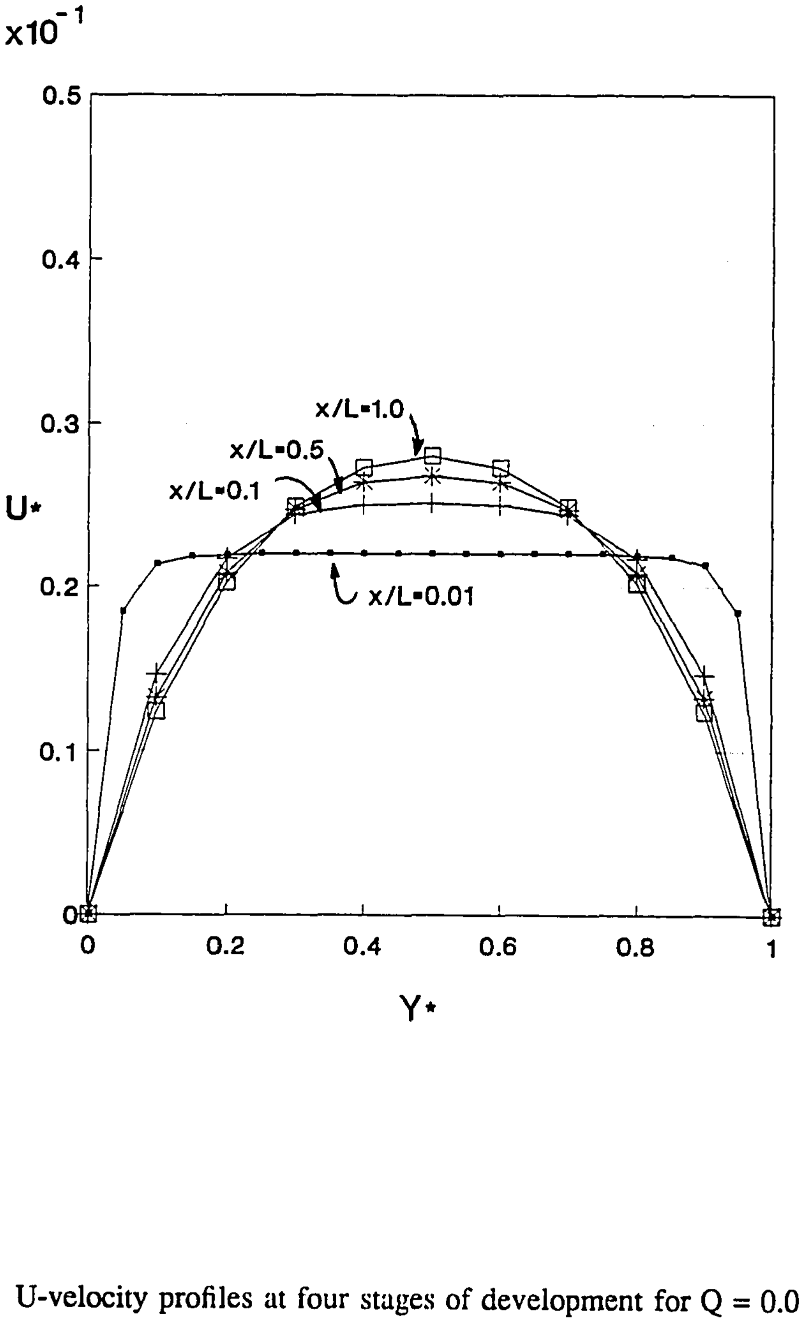

Fig. 4.5 U-velocity profiles at four stages of development for Q = 0.02, $T_c^* = 1.0$

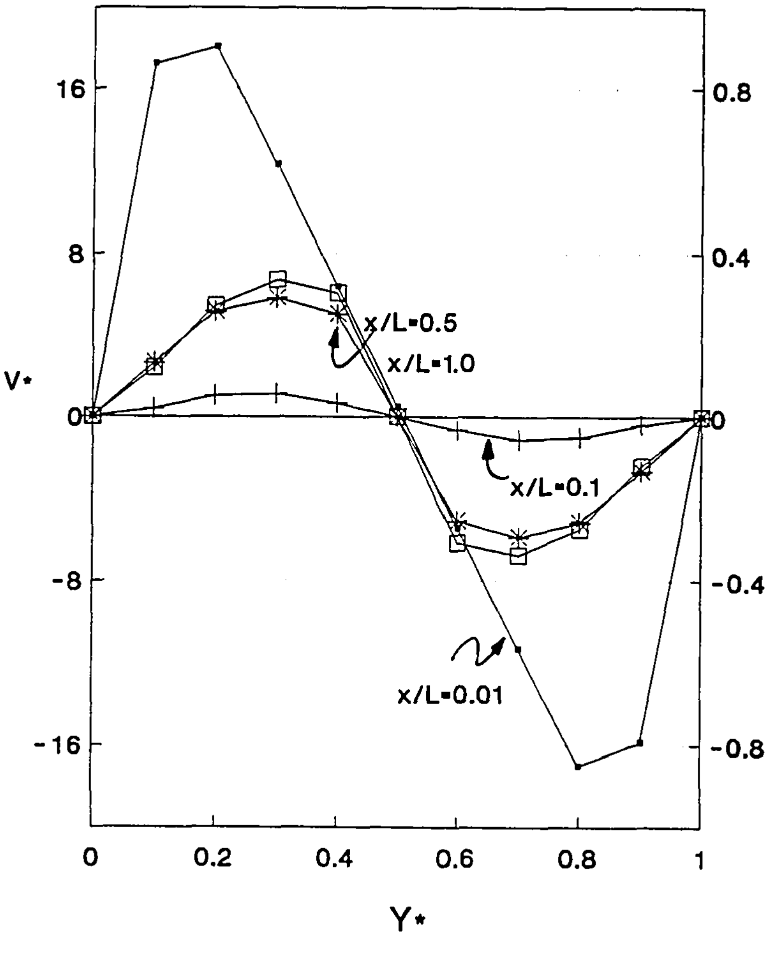

Fig. 4.6 V-velocity profiles at four stages of development for Q = 0.02, $T_c^* = 1.0$

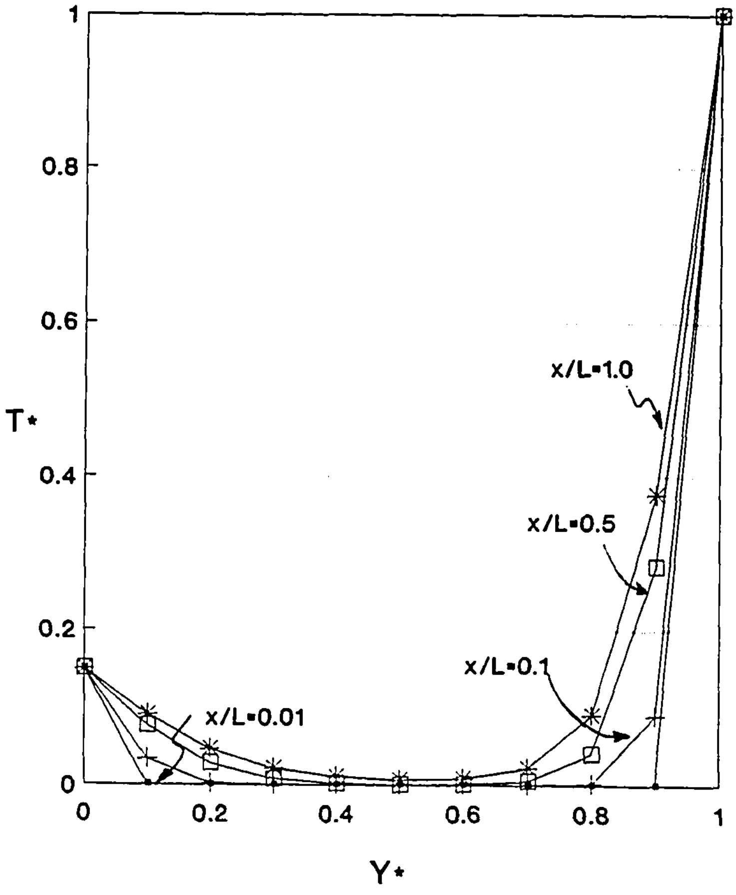

Fig. 4.7 Temperature profiles at four stages of development for Q = 0.0005, $T_c^* = 0.15$

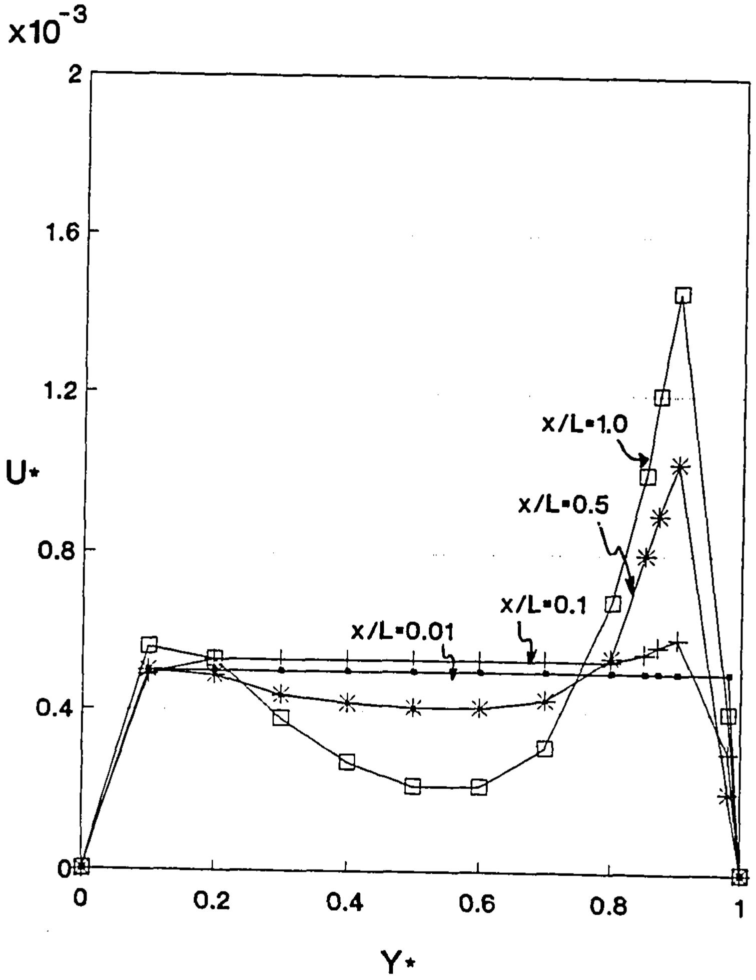

Fig. 4.8 U-velocity profiles at four stages of development for $Q = 0.0005$, $T_c^* = 0.15$

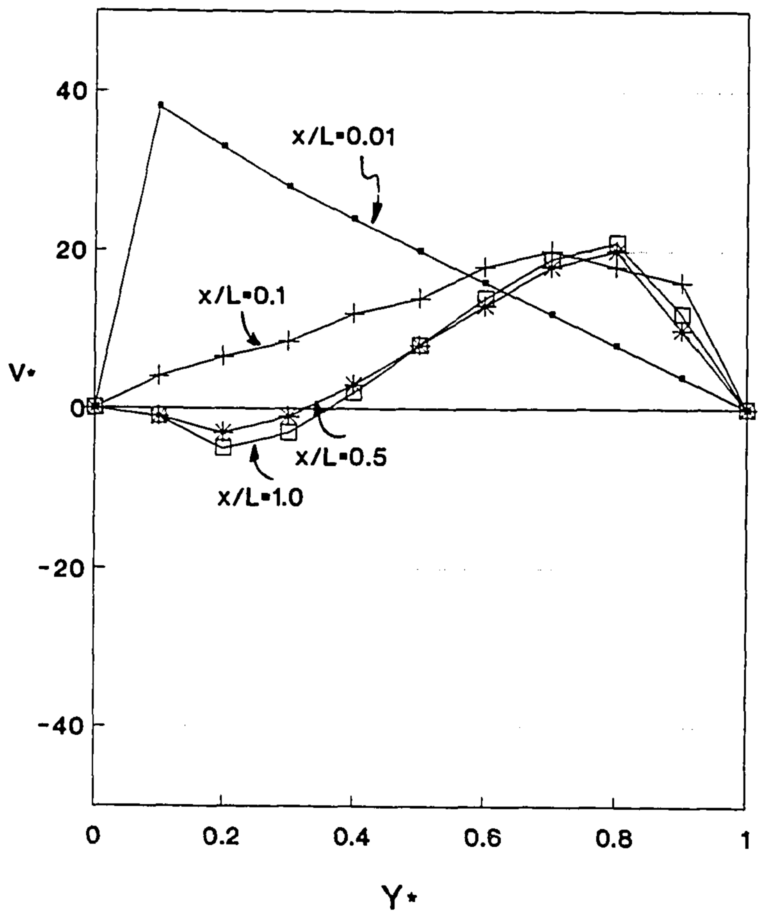

Fig. 4.9 V-velocity profiles at four stages of development for Q = 0.0005, $T_c^* = 0.15$

in Fig. 4.8 clearly indicates the asymmetry by major and minor peaks in the vicinity of the heated and cooled walls respectively. This is due to higher buoyancy force near the heated wall. As the development of profile in flow direction proceeds, the velocity of the heated layer increases substantially while the velocity in the cooler central region decreases. The velocity component, v^*, for the lower flow rate at $Q = 0.0005$ initially shows behavior similar to that of high flow rate. However, contrary to the higher flow rate, the cooler fluid from the core region moves towards both the walls.

It should be noted that all results including velocity profiles and temperature distributions are in good agreement to Akbari and Borger's calculations, as indicated in the previous section of this chapter.

4.4 Pressure Defect and Heat Removal

The comparison of pressure defect as a function of the channel height between the present study and Akbari and Borger's calculations are shown in Figs. 4.10 and 4.11 for high flow rate of $Q = 0.02$ and low flow rate of $Q = 0.0005$, respectively. Figure 4.10 shows that for high flow rate, the pressure defect rapidly becomes negative and shows a minimum near the one-tenth portion of the channel, and then reverses and gradually reaches zero at the channel exit. The initial decrease is due primarily to the strong buoyancy force and tremendous adjustment of the flow profiles as a result of large fluid friction near the leading edge of the two walls. At very low flow rate of $Q = 0.0005$, the pressure defect variation quickly becomes nearly linear after showing a small minimum near the inlet (Fig. 4.11).

Figures 4.12 and 4.13 illustrate the comparison of present results and Akbari and Borger's results correlated for local heat extracted and the total average Nusselt number.

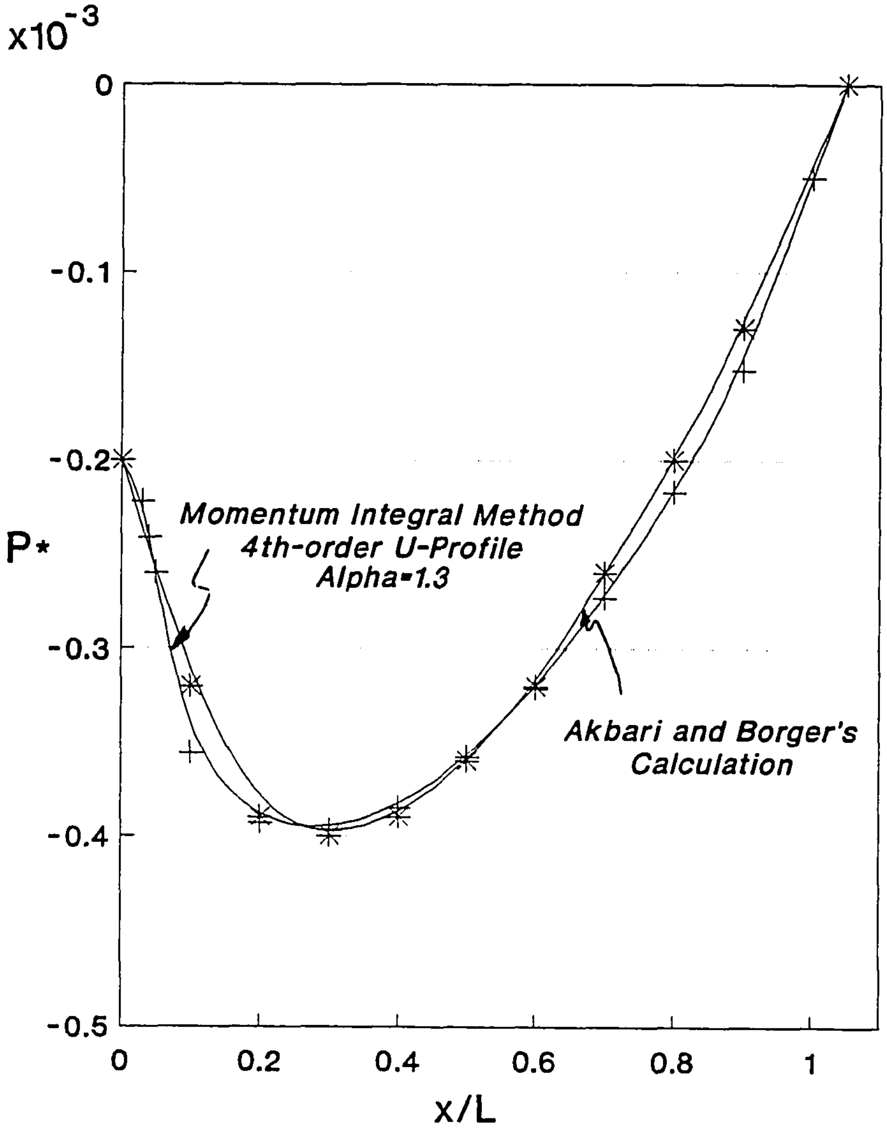

Fig. 4.10 Pressure defect as a function of channel height at Q = 0.02, $T_c^* = 1.0$

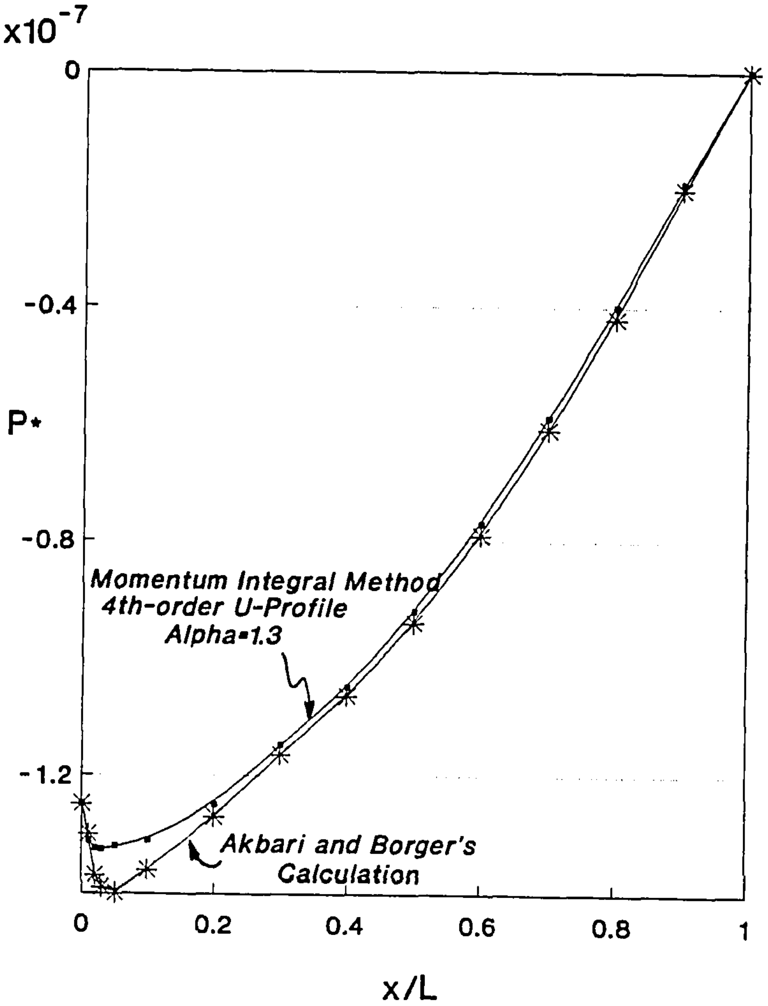

Fig. 4.11 Pressure defect as a function of channel height at Q = 0.0005, $T_c^* = 0.15$

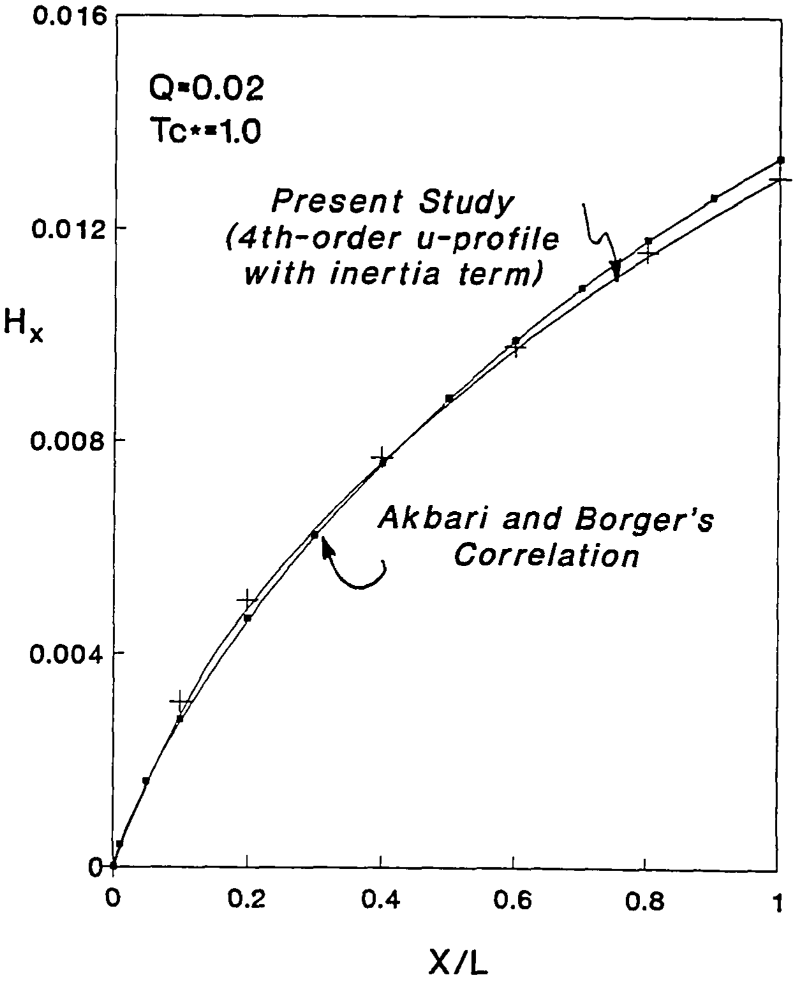

Fig. 4.12 Comparison of total heat extraction as a function of height

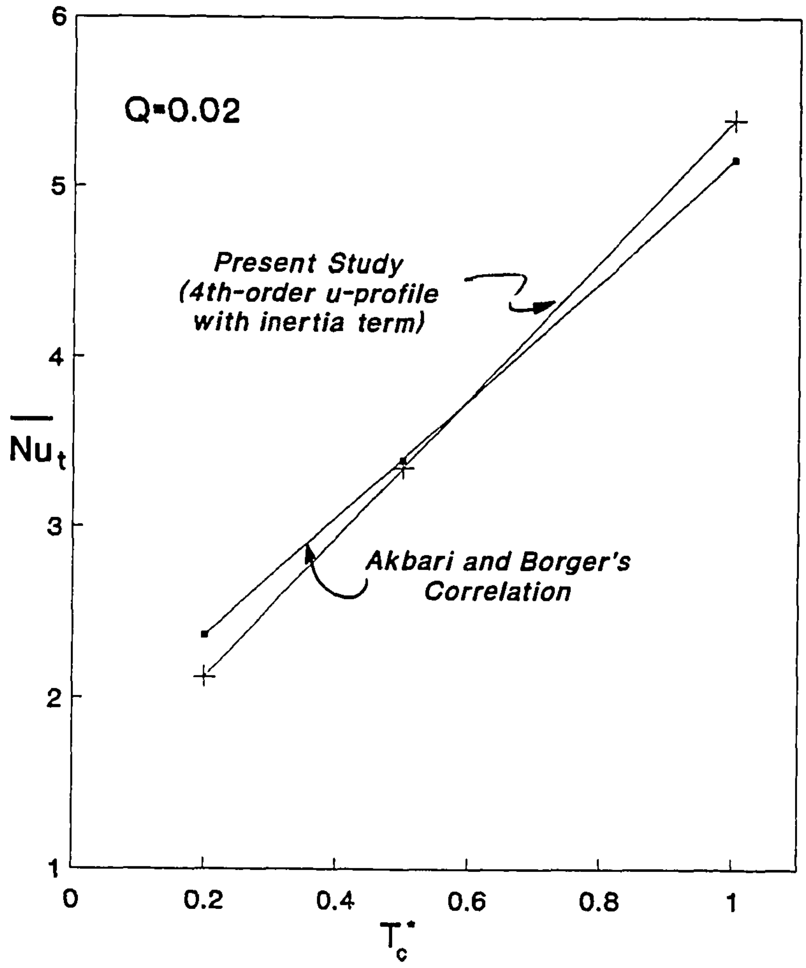

Fig. 4.13 Comparison of total average Nusselt number as the function of cooled wall temperature

These quantities are respectively defined as

$$H_L = \int_0^1 u^* T^* dy^* \tag{4.1}$$

and,

$$Nu_L = \frac{H_L Pr}{L} \tag{4.2}$$

where, L is the total height of the channel and H_L is the total heat extracted from heated walls.

The amount of heat extracted from the fluid increases along the channel as indicated in Fig. 4.12. The total average Nusselt number as a function of the cooled wall temperature, T_c^* is shown in Fig. 4.13. Both of these figures exhibit good agreement between present study and Akbari and Borger's calculations.

4.5 A Closed Form Solution

The solution of problem of flow in a parallel channel can also be determined analytically in closed form. This is done by adopting a second order velocity profile in the momentum-integral method. The temperature profile is obtained from the Oseen's model. In the present study, the following second order expression for axial velocity profile is used

$$u^* = A\left(y^* - y^{*^2}\right) \tag{4.3}$$

Equation (4.3) satisfies the no slip condition at both walls. The constant A in the above equation can be found by satisfying the integral mass conservation constraint, namely Eq. (3.60).

$$Q = \int_0^1 u^* dy^* \tag{3.60}$$

Using the value of $A = 6Q$, as obtained from Eq. (3.60), the Eq. (4.3) becomes

$$u^* = 6Q\left(y^* - y^{*^2}\right) \tag{4.5}$$

It is noted that, unlike the fourth order u-profile case, the second order u-velocity profile does not depend on the local pressure gradient. In other words, u^* as calculated from Eq. (4.4) is independent of x-coordinate. This would represent the fully developed case since inertia term, represented by the left hand side of Eq. (3.29) vanishes identically. This in turn implies a linear profile for pressure defect variation as a function of axial coordinate.

One can apply this second-order u-velocity profile to the momentum-integral equation, Eq.(3.29), and find a closed form solution by integrating it from 0 to L. The details of the derivation of this closed form solution are given in Appendix A. However, a brief discussion is presented here, in order to compare the results with those of boundary layer calculation and 4th-order u-velocity profile in the present study and Akbari and Borger's calculations.

If one substitutes Eq. (4.4) into Eq. (3.29) and integrates from 0 to L and from 0 to 1, one gets

$$\int_0^1 u^{*^2} dy^* \bigg|_{x^*=L} - \int_0^1 u^{*^2} dy^* \bigg|_{x^*=0} = [P_L - P_o] - 12QL + \int_0^L \int_0^1 T^* dy^* dx^* \tag{4.6}$$

Since, as noted earlier, $P_L = 0$ and $P_o = -\frac{1}{2}Q^2$ boundary conditions have been used, the Eq. (4.5) can be rewritten as

$$\frac{7}{10}Q^2 = -12QL + \int_0^L \int_0^1 T^* dy^* dx^* \tag{4.7}$$

Using Eq. (3.40) for T^*, one gets

$$\frac{7}{10}Q^2 = \left[-12Q + \frac{(T_c^* + 1)}{2}\right]L + \sum \frac{a_n PrQ}{n^3\pi^3}\left[(-1)^n - 1\right]\left(e^{\frac{-n^2\pi^2 L}{PrQ}} - 1\right) \tag{4.8}$$

or,

$$L = \frac{\frac{7}{10}Q^2 - \left[-\left(\frac{2}{\pi^4}\right)(-2)(1 + T_c^*)PrQ\left(e^{\frac{-\pi^2 L}{PrQ}} - 1\right)\right]}{-12Q + \frac{(1+T_c^*)}{2}} \tag{4.9}$$

Equation (4.8) is an implicit equation for L, and it can be solved by Newton's method to produce a graphical or functional relationship between Q and L. The results of this closed form solution designated as "present study withy 2nd-order u-velocity profile" are shown in the next section where they are compared with the 4th-order u-velocity profile results and the numerical boundary layer calculation of the present study, as well as Akbari and Borger's calculations. Results show that this closed form solution can predict the channel height at high flow rates with fairly good accuracy. But the department from other more comprehensive models becomes significant at low flow rates specially for Q values less than 0.005.

4.6 Comparison of Q vs L Relationship as Predicted by Models

The usefulness of present study for the Trombe wall system is that a simulation program can be developed, which requires as input, the wall height, the distance between glazing and wall, and the glazing type. Wall and inside glazing (cooled wall) surface temperatures can be calculated iteratively by the program at regular time intervals using ambient temperature and solar radiation data from a weather tape. The output would be in the form of an air volumetric flow rate at an average fluid temperature, or simply a heat flux.

Table 4.1 shows not only the calculation results for air, but also for high Prandtl number fluid (water) and a typical low Prandtl number fluid (sodium). The results for air are predicted in Figs. 4.14 to 4.16 for different dimensionless cooled wall temperature with the flow rate ranging from $Q = 0.002$ to $Q = 0.05$. Results show that the calculations in the present study, using the momentum-integral method, are in good agreement with Akbari and Borger's correlations as well as the calculations based on the numerical solution of boundary layer equation in the present study.

4.7 Effect of Prandtl Number

Different medium such as water and sodium representing high and low Prandtl number have also been considered in the present study for natural convective flows in a parallel channel with axial inlet and exit sections. Figures 4.17 to 4.19 show the comparison of temperature, u-velocity and v-velocity profiles respectively, between water and sodium at four axial locations for Q = 0.02, $T_c^* = 1.0$. These figures illustrate the effect of Prandtl number of flow and temperature fields development. In the case of water, the temperature profile develops slowly due to its low thermal diffusivity. On the contrary, the temperature distribution of sodium develops very fast due to its high value of thermal diffusivity. The profile reaches the nearly fully developed stage soon after the mid-section of the channel. The flow patterns of these two different medium have exactly opposite trends of development, as shown in Figs. 4.18 and 4.19. As expected, the sodium velocity profiles develops much more slowly as compared to water velocity profile development.

Table 4.1 The prediction of channel height as a function of Q and T_c^* for air, water and sodium

Q	$T_c^* = 1.0$	$T_c^* = 0.55$	$T_c^* = 0.15$
Air, Pr=0.71 (Present Study)			
.050 (4th-order with	1.40×10^{-2}	2.12×10^{-2}	–
.020 inertia term)	1.75×10^{-3}	1.95×10^{-3}	2.22×10^{-3}
.005	1.62×10^{-4}	1.51×10^{-4}	1.38×10^{-4}
.002	4.16×10^{-5}	3.40×10^{-5}	2.72×10^{-5}
Air, Pr=0.71 (Akbari's Correlation)			
.050	1.40×10^{-2}	2.12×10^{-2}	–
.020	1.78×10^{-3}	1.91×10^{-3}	2.22×10^{-3}
.005	1.60×10^{-4}	1.53×10^{-4}	1.38×10^{-4}
.002	4.04×10^{-5}	3.60×10^{-5}	2.678×10^{-5}
Water, Pr=6.78			
.050	1.01×10^{-1}	1.54×10^{-1}	–
.020	1.12×10^{-2}	1.20×10^{-2}	1.35×10^{-2}
.005	1.00×10^{-3}	7.70×10^{-3}	5.40×10^{-4}
.002	2.80×10^{-4}	1.86×10^{-4}	9.30×10^{-5}
Sodium, Pr=0.0072			
.050	3.25×10^{-3}	6.00×10^{-3}	–
.020	2.80×10^{-4}	3.60×10^{-4}	5.00×10^{-4}
.005	1.80×10^{-5}	2.10×10^{-5}	2.60×10^{-5}
.002	3.60×10^{-6}	4.20×10^{-6}	4.60×10^{-6}

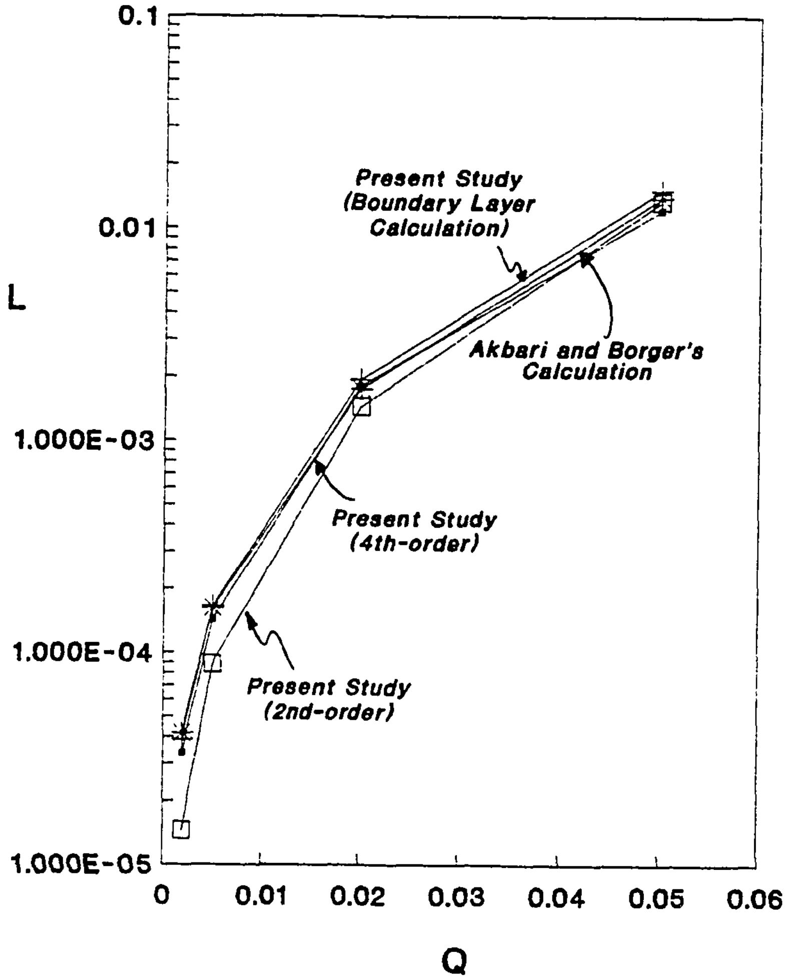

Fig. 4.14 Comparison of Q vs. L among models for air at 23C and $T_c^* = 1.0$

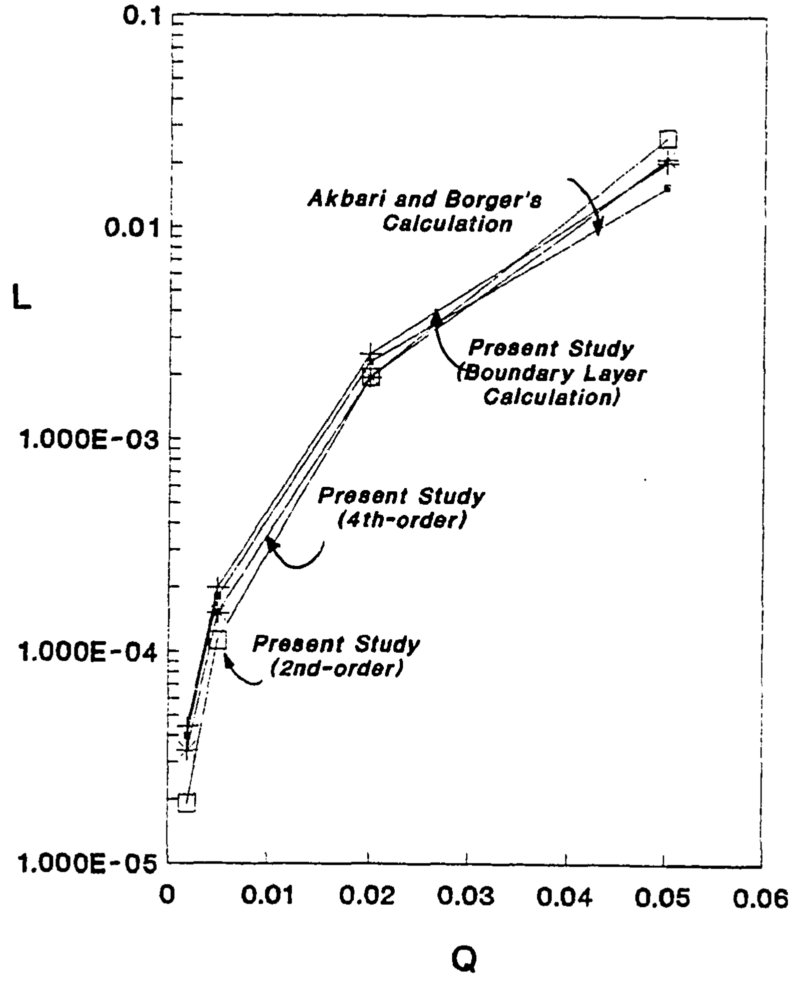

Fig. 4.15 Comparison of Q vs. L among models for air at 23C and $T_c^* = 0.55$

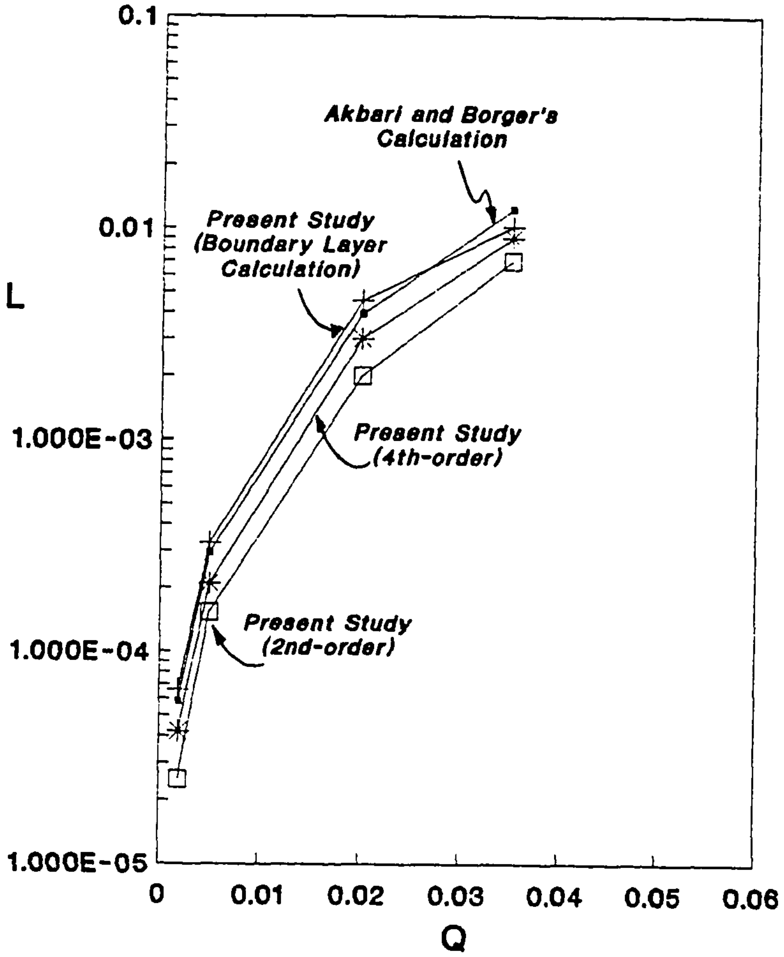

Fig. 4.16 Comparison of Q vs. L among models for air at 23C and $T_c^* = 0.15$

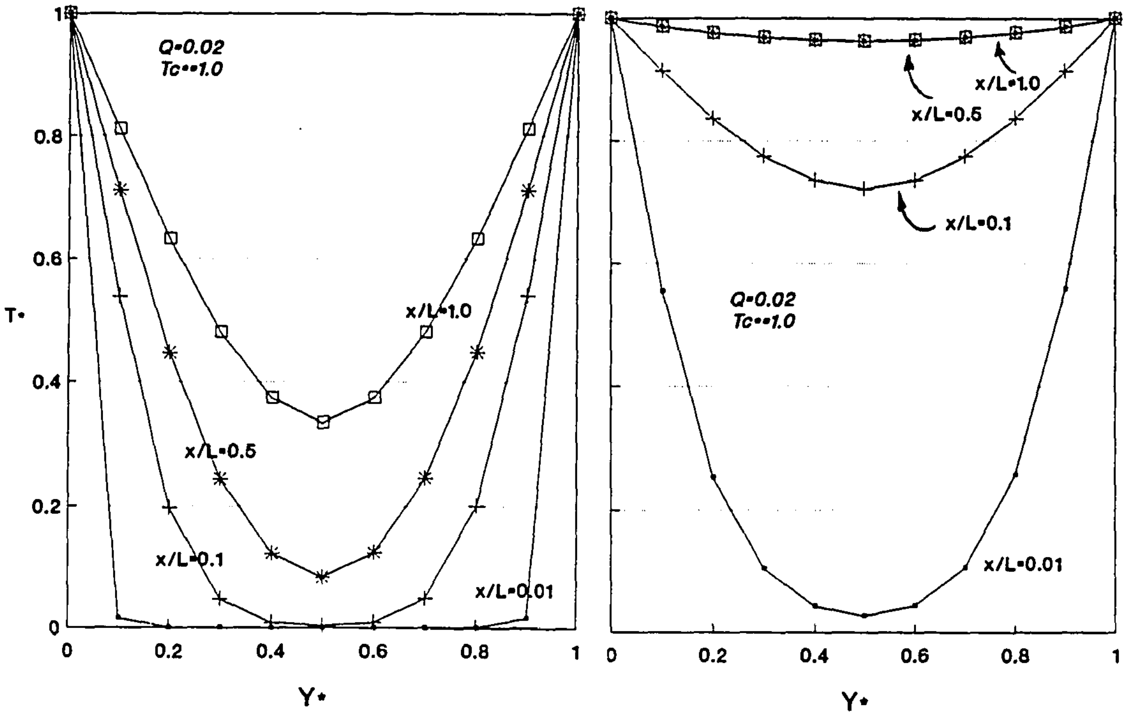

(a). Water (Pr=6.78) *(b). Sodium (Pr=0.0072)*

Fig. 4.17 Comparison of temperature profiles at four stages of development for Q = 0.02, T_c^* = 1.0 between water and sodium

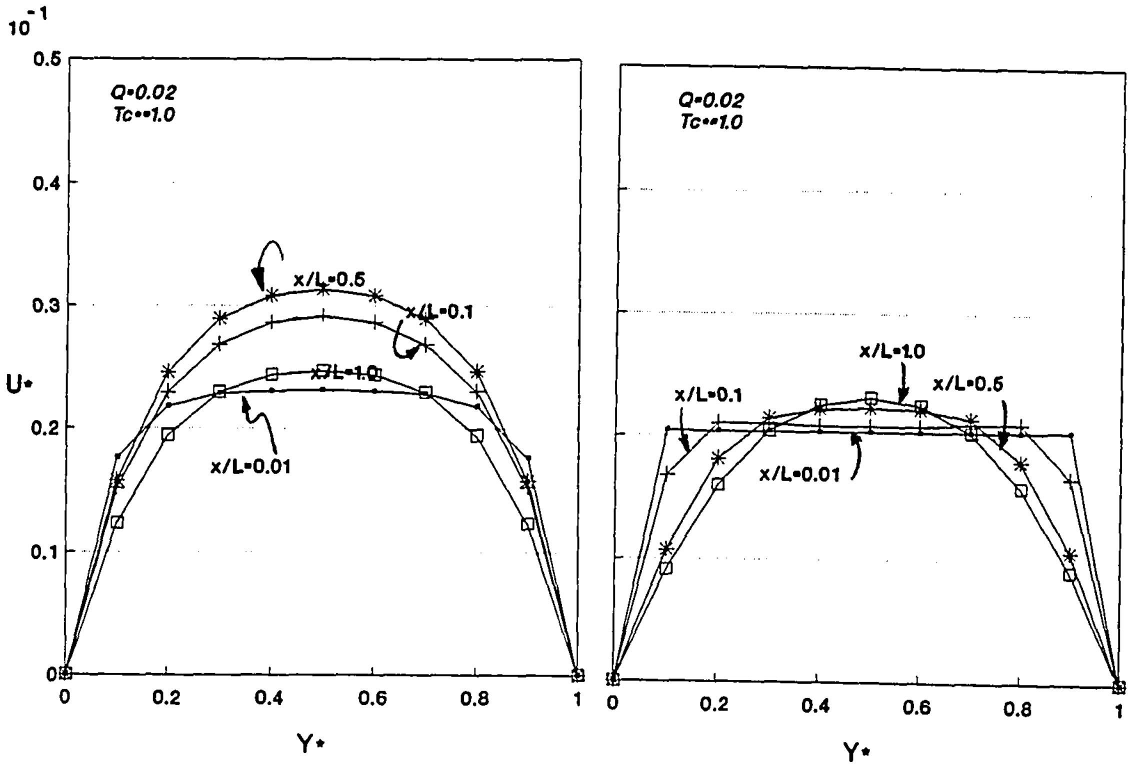

(a). Water (Pr=6.78)

(b). Sodium (Pr=0.0072)

Fig. 4.18 Comparison of U-velocity profiles at four stages of development for Q = 0.02, $T_c^* = 1.0$ between water and sodium

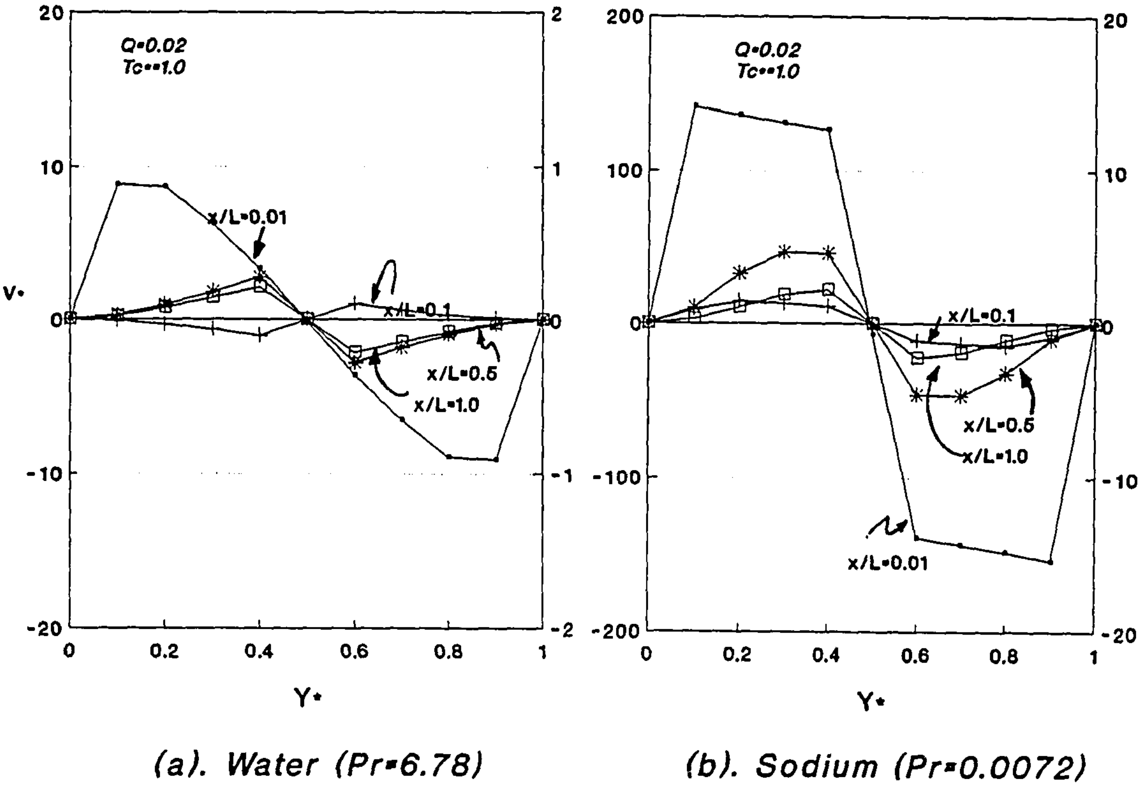

(a). Water (Pr=6.78)

(b). Sodium (Pr=0.0072)

Fig. 4.19 Comparison of V-velocity profiles at four stages of development for Q = 0.02, $T_c^* = 1.0$ between water and sodium

Figure 4.20 show the comparison of pressure defect for different Prandtl numbers, namely water, air and sodium as a function of dimensionless x along the channel axis. The higher the Prandtl number the later is the recovery of the pressure defect and the more negative is its minimum value.

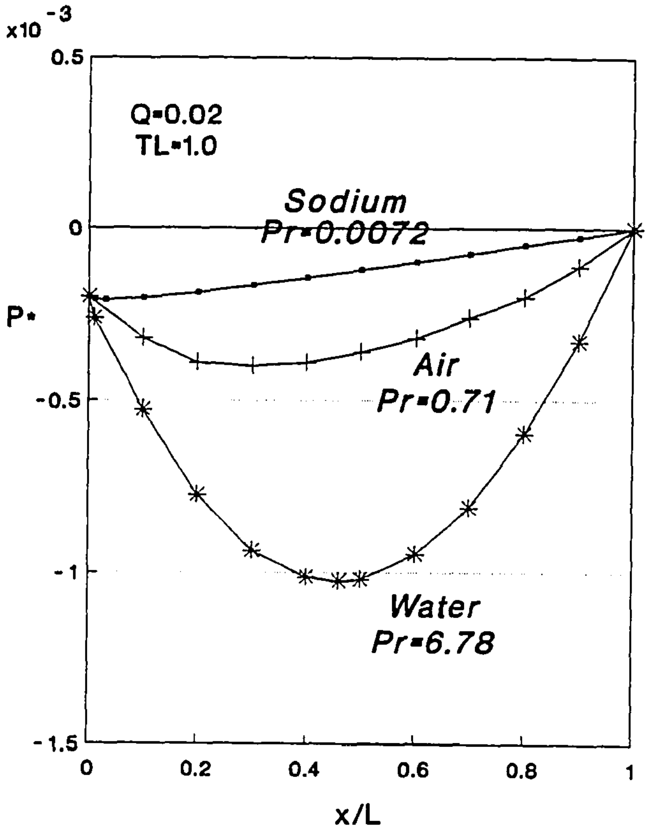

Fig. 4.20 Pressure defect as the function of x^* for various of fluids with Pr = 0.0072 (Sodium), Pr = 0.71 (Air), Pr = 6.78 (Water)

Chapter 5

RESULTS FOR SIDE VENT GEOMETRY

5.1 Physical Model

Figure 5.1 shows a side-vented cavity configuration with two same size gaps CD and AB on the heated wall. The upper and lower walls are insulated, and the vertical sides are maintained at constant temperatures T_c and T_h. This is a very basic geometry that in many ways models the heat transfer and ventilation characteristics of an actual Trombe wall geometry. Natural convection characteristics of this geometry have not been reported in the literature.

As noted earlier, the velocity and pressure values at inlet and exit sections are not known a priori. For numerical procedure, either velocity or pressure must be known at the inlet section AB. To overcome this dilemma of two unknown quantities, the computational domain is extended well beyond the geometric configuration. We take advantage of the fact that the differentially heated channel is attached to a constant pressure reservoir namely atmosphere. The boundary $EJIHGF$ in Fig. 5.1 is the extended boundary, located far away from heated surfaces, where known atmospheric pressure condition can be applied. The computational domain has been extended three times of the channel width, L, in x-direction, and five times of the channel width from both upper and lower boundaries ED and FA of the channel. The first derivative of

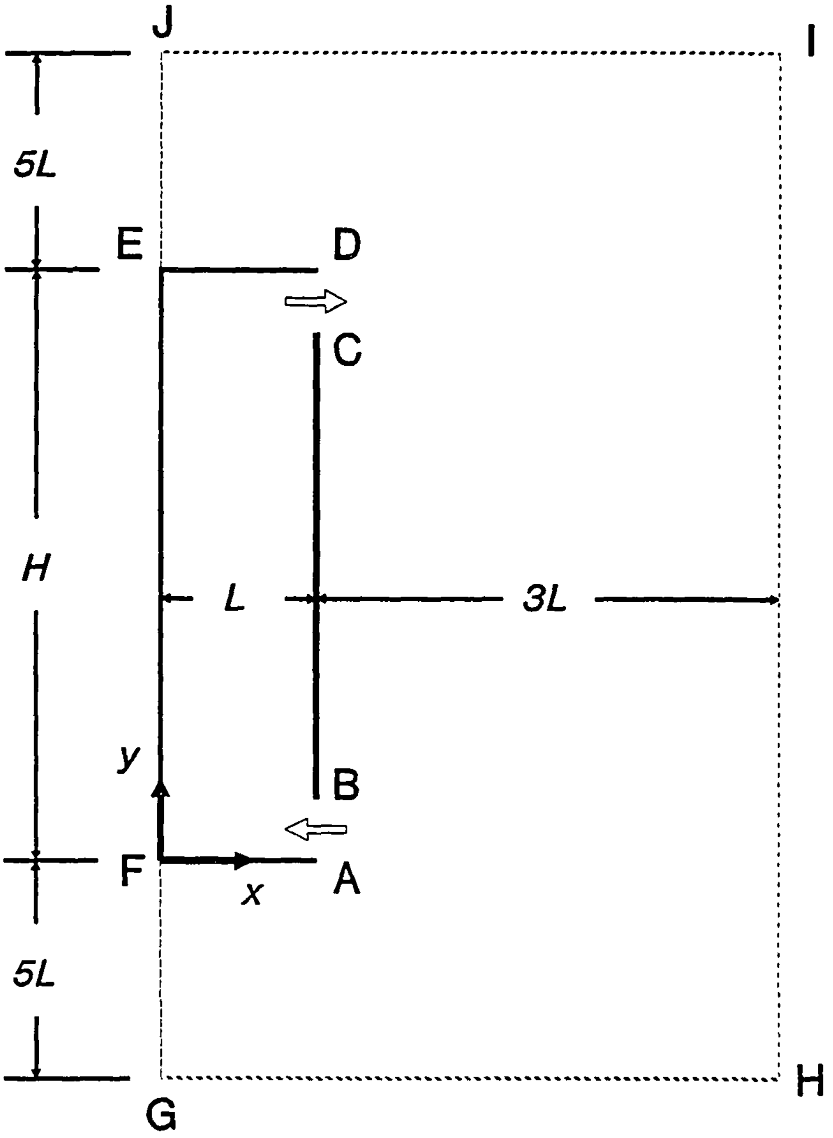

Fig. 5.1 Schematic of the side-vented cavity

temperature normal to the boundaries is set as zero and the pressure is fixed and assumed to be equal to the atmospheric pressure on the boundary $EJIHGF$.

5.2 Numerical Codes

5.2.1 The Present Computational Code

The numerical code developed here is the modification of the code developed by Mohieldin [36] for laminar flows. The present code extends the previous code to include the effect of turbulence. It also features variable step size grid. In its present form, it is capable of solving two-dimensional turbulent natural convective flows. The power law scheme has been used to discretize the governing transport equations, using the finite volume approach [20]. The two-equation (k-ϵ) turbulence model has been used to predict effects of turbulence [24]. Validation of the code for the square cavity at Grashof number 1.4×10^8 has been conducted, and compared to results from the "FLUENT" code [21] and Markatos's results [17] shown in Table 5.1. Fairly good agreement has been achieved for the averaged Nusselt number.

5.2.2 The "FLUENT" Code

The drawback of the present code is that it uses the power law scheme which essentially reduces to the first order accurate upwind differencing scheme at high cell Peclet numbers. This invariably leads to high artificial diffusion and errors in solution. In order to avoid this problem, one must use a very refined grid. This is not always possible in many complex geometries, such as the one considered in the present study. A very high number of grid points, required to resolve the flow in the inlet/exit sections and flow near the wall, gradually causes the computational effort to escalate. The alternative is to use a second order accurate scheme such as QUICK [32] that employs quadratic interpolation of functions between grid points. Since this scheme and other features of

Table 5.1 Comparison of Nusselt number between present study and Markato's calculation

Average Nusselt Number	Present Study		
	Present Code k-ϵ Model	FLUENT Code	Markato's Calculation
Laminar $Gr=1.4\times 10^5$			
$\overline{Nu}$	4.516	4.524	4.470
Turbulence $Gr=1.4\times 10^8$			
$\overline{Nu}$	35.948	38.784	35.140

the present code are incorporated in the "FLUENT" code [21], it was decided to use the "FLUENT" code instead of incorporating the "QUICK" scheme in the present code. This code has options that enables one to use either power law or the second order "QUICK" scheme. It also features two options for turbulence modeling. One can use either the two-equation (k-ϵ) turbulence model or the algebraic stress model. The code uses both "SIMPLE" and "SIMPLER" algorithms to solve the non-linear algebraic equations resulting from the finite volume procedure. The "FLUENT" program also provides a very good graphical capability which proved to be an asset in the present investigation. Since simulation of flow phenomenon in the channel requires large number of grid points, a second order procedure that minimizes artificial diffusion is more desirable. It is for this reason the "FLUENT" code was used in the present study. The validation of the "FLUENT" code has been reported in the literature [37]. An independent validation of the code was done by Mohieldin [38]. The present study also carried out an independent validation of "FLUENT" for natural convective flows. Table 5.1 shows typical results from the code and comparison with results from other sources. All subsequent results in the present study have been obtained from the "FLUENT" code.

5.3 Numerical Aspects

5.3.1 Grid Independence of Results

A typical variable grid pattern for the entire calculation domain is shown in Fig. 5.2. More grid points have been placed near all physical walls to resolve boundary layers. Figure 5.3 shows the comparison of the local Nusselt number on the heated wall for turbulent flow for three grids, namely 33×41, 53×61 and 73×81. One observes that results are practically grid independent except for a minimum near the entrance region, predicted by the finer 73×81 grid. All three grids show a developing entrance region,

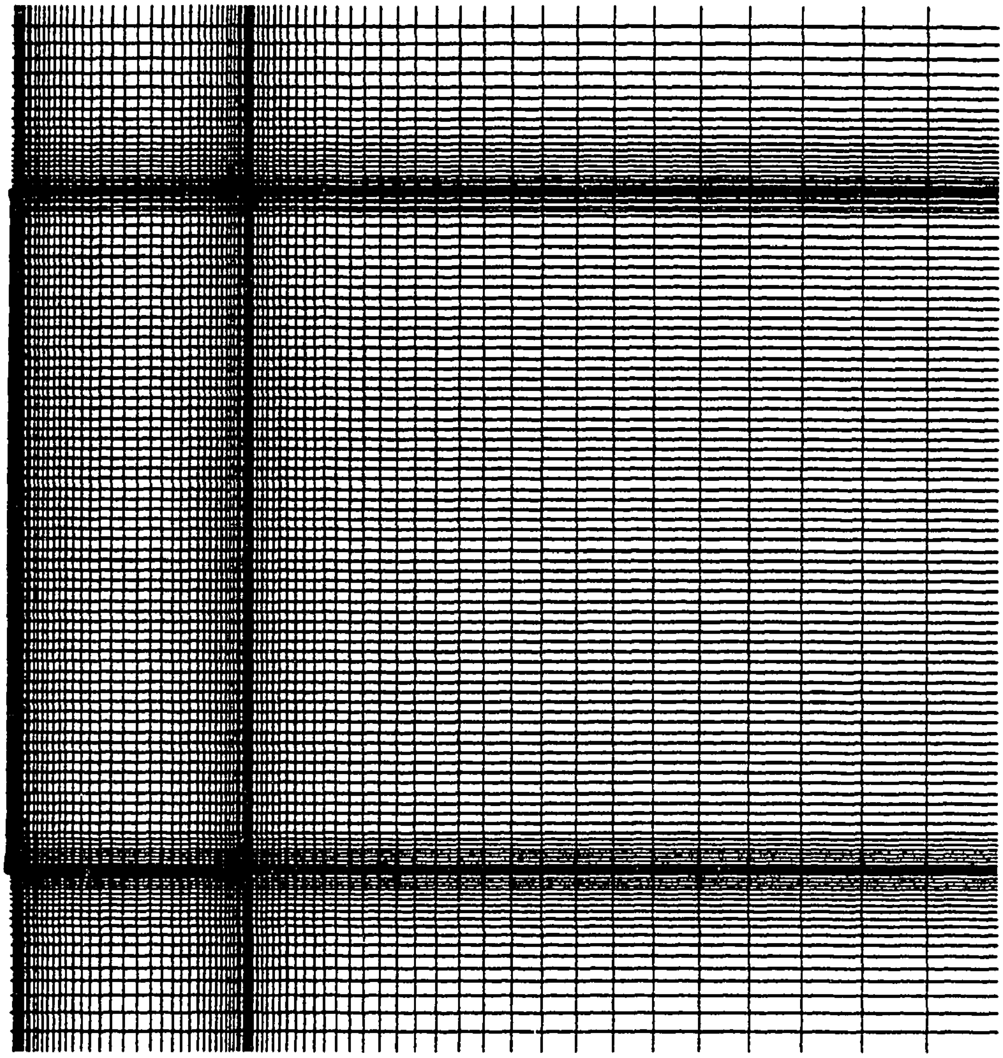

Fig. 5.2 Grid illustration of a side-vented cavity

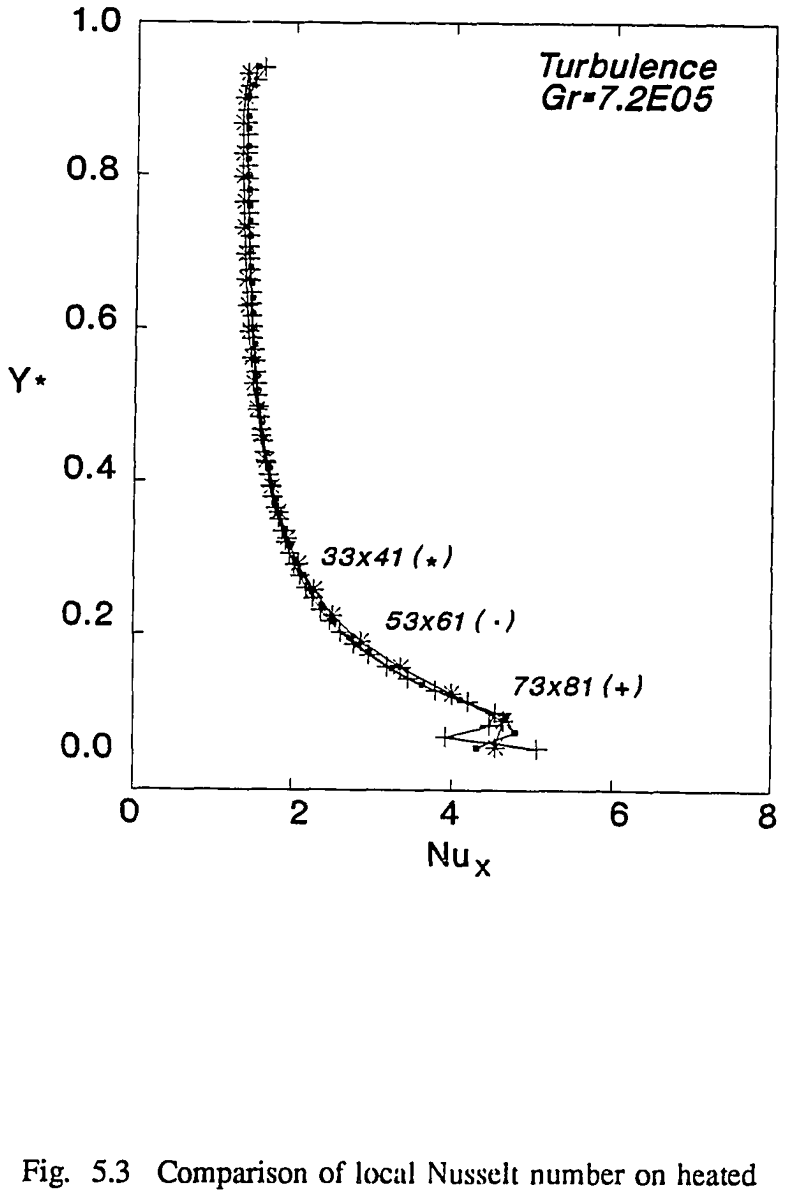

Fig. 5.3 Comparison of local Nusselt number on heated wall for 33×41, 53×61 and 73×81 grids.

followed by a nearly fully developed thermal region. The 73×81 grid has been used for all cases in the present study of flows in the side-vented cavity configuration.

5.3.2 Location of the Free Boundary

The effect of location of the free boundary was a major concern in early stages of the present study. The basic objective in this regard is to establish the free boundary at a location far removed from the heated surface of the channel. From the computational point of view, farthest location will increase the computational effort. Conversely, nearest free boundary location will reduce computational effort, but results may be dependent on the location of the boundary. As a result, an optimal location needs to be found from numerical experimentation.

Initially, two types of free boundaries shown in Figs 5.4 and 5.5 were tried in the present study. The first type of free boundary is also shown in Fig. 5.1. The second type of free boundary is constructed by extended the physical boundaries ED and FA in Fig. 5.1 all the way to the free boundary III. Figures 5.4 and 5.5 show the streamline contours of a side-vented cavity, using these two different types of free boundary. Although the mass flow rate and the Nusselt number characteristics are almost same for these two cases, results from parallel boundary case in Fig. 5.5 shows that there is a returning flow from exit to inlet near the outside surface of the heated wall. This appears physically unreasonable behavior since it indicates that the flow has been restricted by using this type of free boundary. Consequently, the more comprehensive boundary of Fig. 5.1 has been used throughout this study since it does not predict the returning flow pattern, and it generally yields results that are physically reasonable.

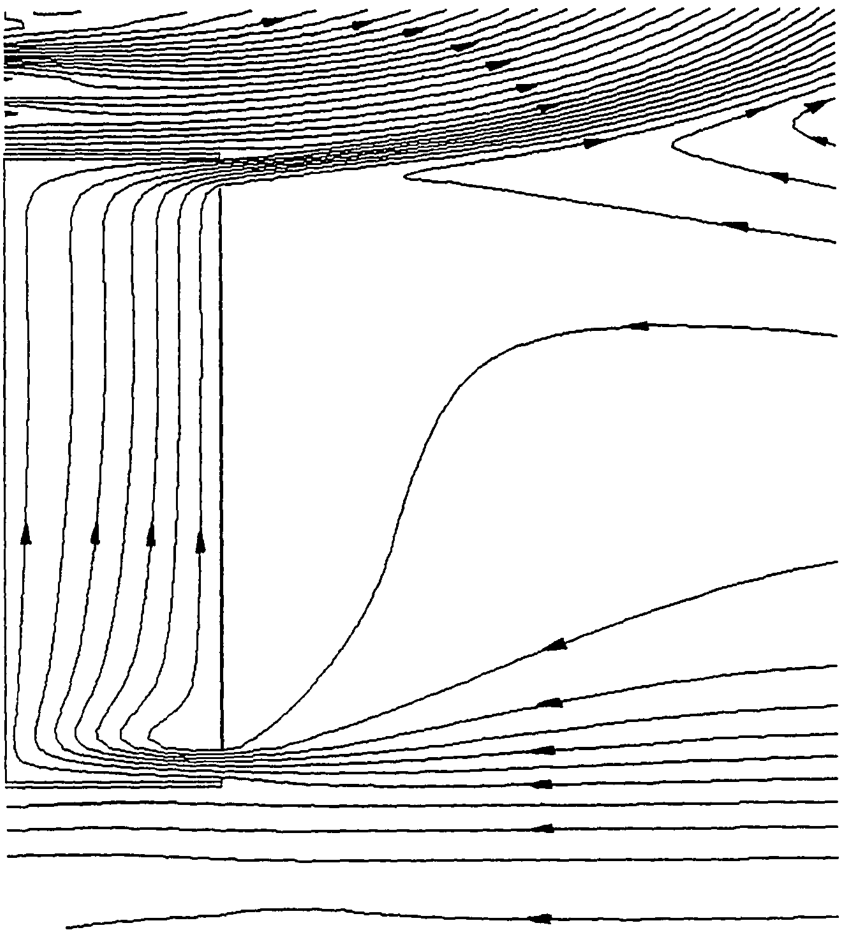

Fig. 5.4 Streamline contours for $Gr = 7.2\times10^5$, $Pr = 0.71$, $Ar = 20$, $Vs^* =$ 1.0 turbulent case (The first type of free boundary)

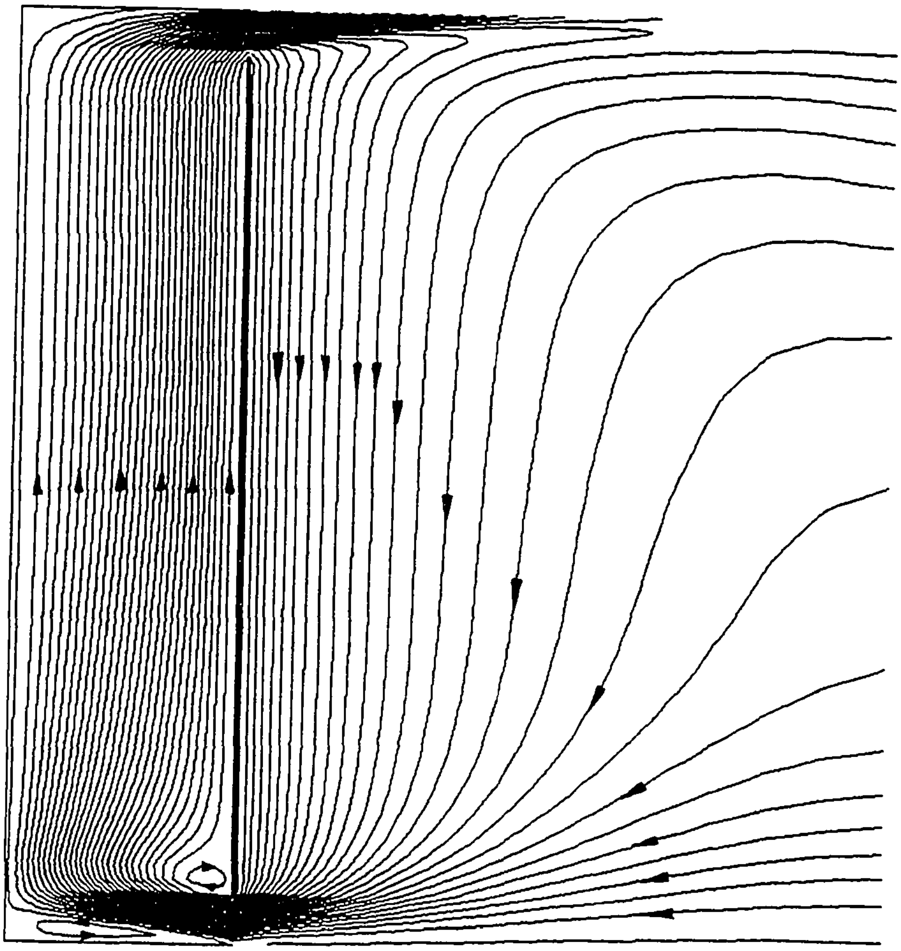

Fig. 5.5 Streamline contours for $Gr = 7.2\times10^{-5}$, $Pr = 0.71$, $Ar = 20$, $Vs^* = 1.0$ turbulent case (The second type of free boundary)

The study of the effect of location of the free boundary on the computational results has been conducted by choosing four locations of the vertical boundary IH (in Fig. 5.1) in the x-direction, namely at $x = L$, $x = 2L$, $x = 3L$ and $x = 4L$. Figure 5.6 shows the comparison of local Nusselt number on the heated wall of four different locations of the free boundary IH. In the case of free boundary located right at the inlet and exit sections of the cavity, the local Nusselt number shows an oscillatory behavior. The cases of $x = 3L$ and $x = 4L$, predict nearly identical local Nusselt number values where as the location of boundary at $x = 2L$ shows a marked departure from these two cases near the inlet section. In the present study, the free boundary has been located at $x = 4L$ for all subsequent results in this study. This ensures that the results obtained in the present study are independent of IH boundary location.

5.4 Streamline and Temperature Contours

Results were obtained for side-vented cavities of aspect ratios of $Ar = 10$ and $Ar = 20$. The non-dimensional vent size, Vs^*, was varied from 1.0 to 0.25 for Grashof number, Gr, ranging from 1.4×10^3 in the laminar regime to 1.4×10^8 for the turbulent cases. The value of $Gr = 1.0\times10^6$ is used for distinguishing laminar regime from turbulent regime. We note that if numerical results were obtained for $Gr > 1.0\times10^6$, using laminar flow assumption, the flow and heat transfer characteristics would show marked oscillations, indicating numerically the onset of transition to turbulence. As a result, all cases with Gr less than 1.0×10^6 or greater were calculated using the turbulent flow assumption. The turbulent flow results are shown in Figs. 5.11–5.13. The convergence of solution was said to be achieved when the residuals for variables u, v, h and p became less than 1.0×10^{-6}, 1.0×10^{-6}, 1.0×10^{-6} and 1.0×10^{-3} respectively.

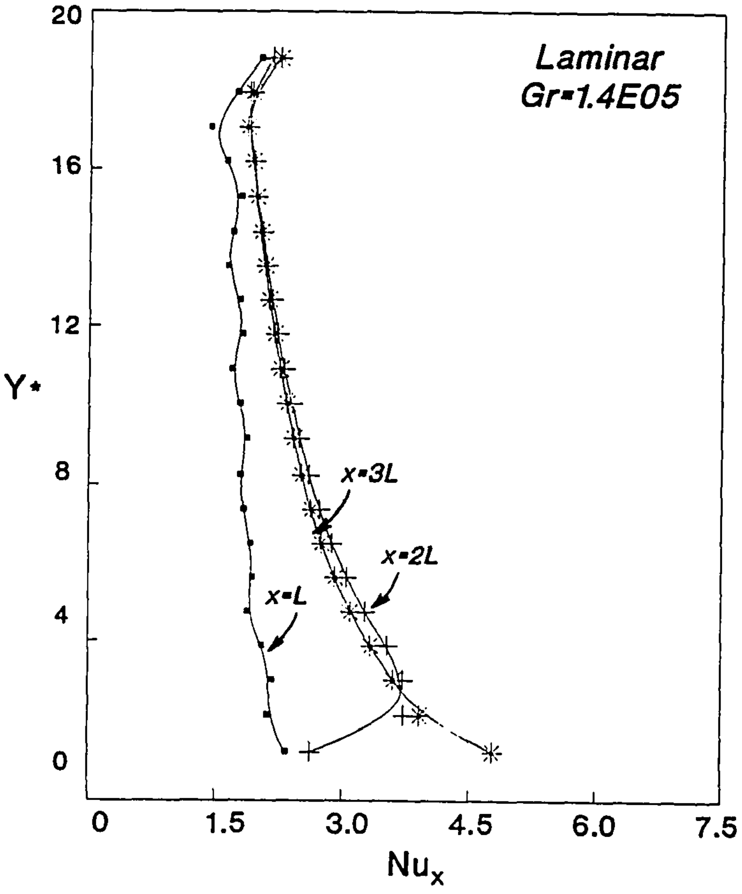

Fig. 5.6 Comparison of local Nusselt number on heated wall for $x = L$, $2L$, $3L$ and $4L$ locations

The streamline contours for vent size Vs^*, = 1.0 for all laminar and turbulence flow cases are shown in Figs. 5.7–5.13. For the case of $Gr = 1.4\times10^3$, the buoyancy effect is small, and the flow in the channel is essentially uni-directional. As the Grashof number increases from 1.4×10^3 to 1.4×10^4, a small recirculating region appears at the top left corner of the cavity. In addition, a small recirculating flow region appears on the leading edge of the heated wall. As Grashof number is increased to 1.4×10^6, the convective flow pattern changes, indicating larger recirculating flow patterns in the channel. For all cases except $Gr = 1.0\times10^6$ (laminar calculation), converged solutions were obtained in about 2000 iterations. For laminar calculation with $Gr = 1.0\times10^6$ (Fig. 5.10), oscillatory solutions were observed even after 2000 iterations, and this indicated that steady laminar solutions were not feasible for $Ar = 20$ and Grashof number equal to and greater than 1.0×10^6. After incorporating the two-equation (k-ϵ) turbulence model in the calculation for the same case of $Gr = 1.0\times10^6$, no oscillatory solutions were observed as indicated in Fig. 5.11. This indicated that the turbulence assumption should be used for all cases of Gr greater than or equal to 1.0×10^6.

For the case of dimensionless vent size equals to 0.5, the streamline contours exhibit patterns similar to those of Vs^*, = 1.0. However, when the vent size is reduced, the flow velocities became smaller compared to those for the bigger vent sizes. This causes a large secondary flow region near the upper left corner and near the leading edge of the warmer wall. Figures 5.14 to 5.19 show the streamline contours for Vs^*, = 0.5 as Grashof number is varied from 1.4×10^3 to 1.4×10^8.

Figures 5.20 to 5.30 show the temperature distributions for the dimensionless vent size, Vs^*, of 1.0 and 0.5, and for Grashof number ranging from 1.4×10^3 in the laminar regime to 1.4×10^8 in the turbulent regime. A thermal boundary layer region on the heated wall, and a large thermal plume of hot air, exiting from the top vent, are evident

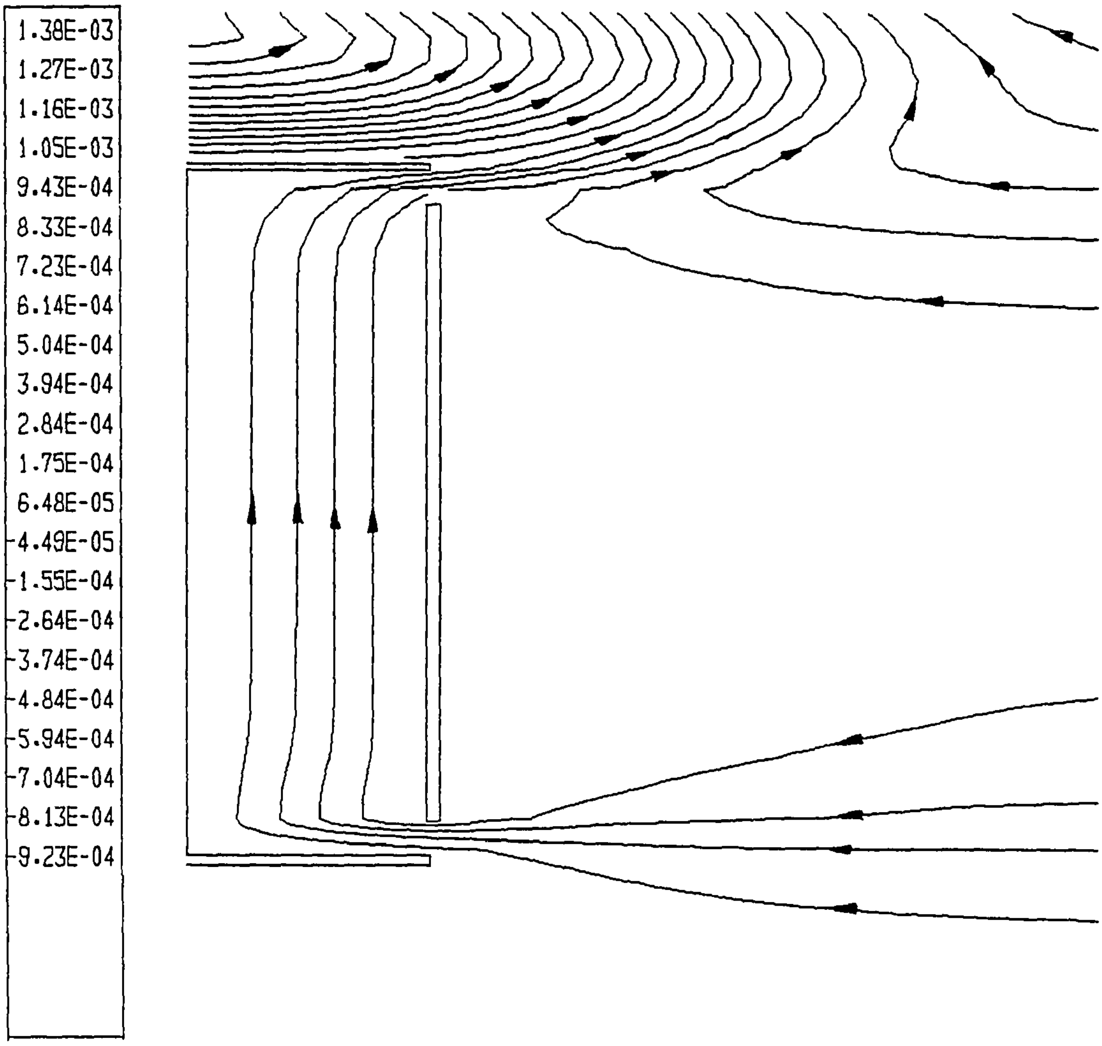

Fig. 5.7 Streamline contours for laminar case with $Gr = 1.4\times10^3$, $Pr = 0.71$, $Ar = 20$ and $Vs^* = 1.0$

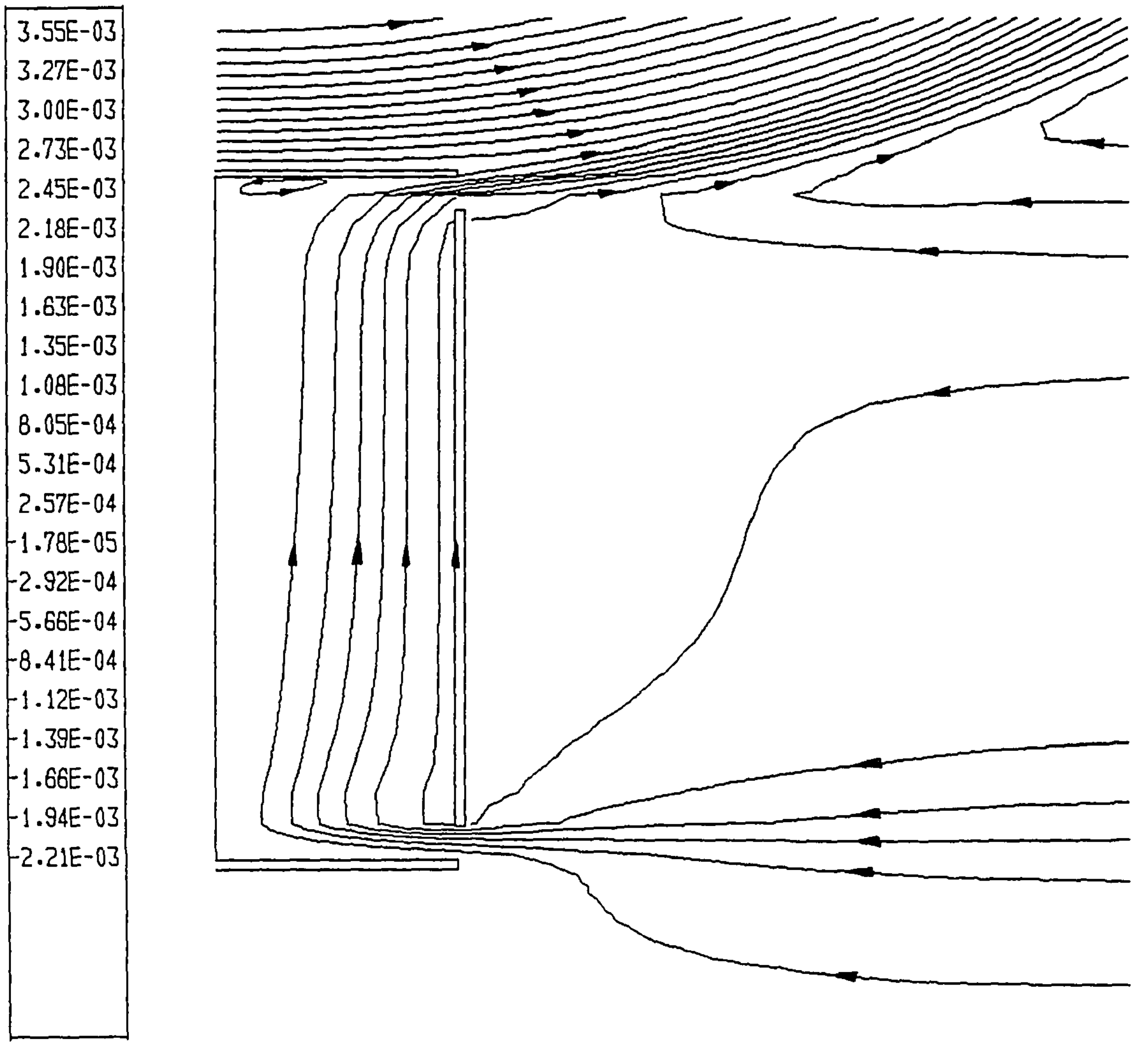

Fig. 5.8 Streamline contours for laminar case with $Gr = 1.4\times10^4$, $Pr = 0.71$, $Ar = 20$ and $Vs^* = 1.0$

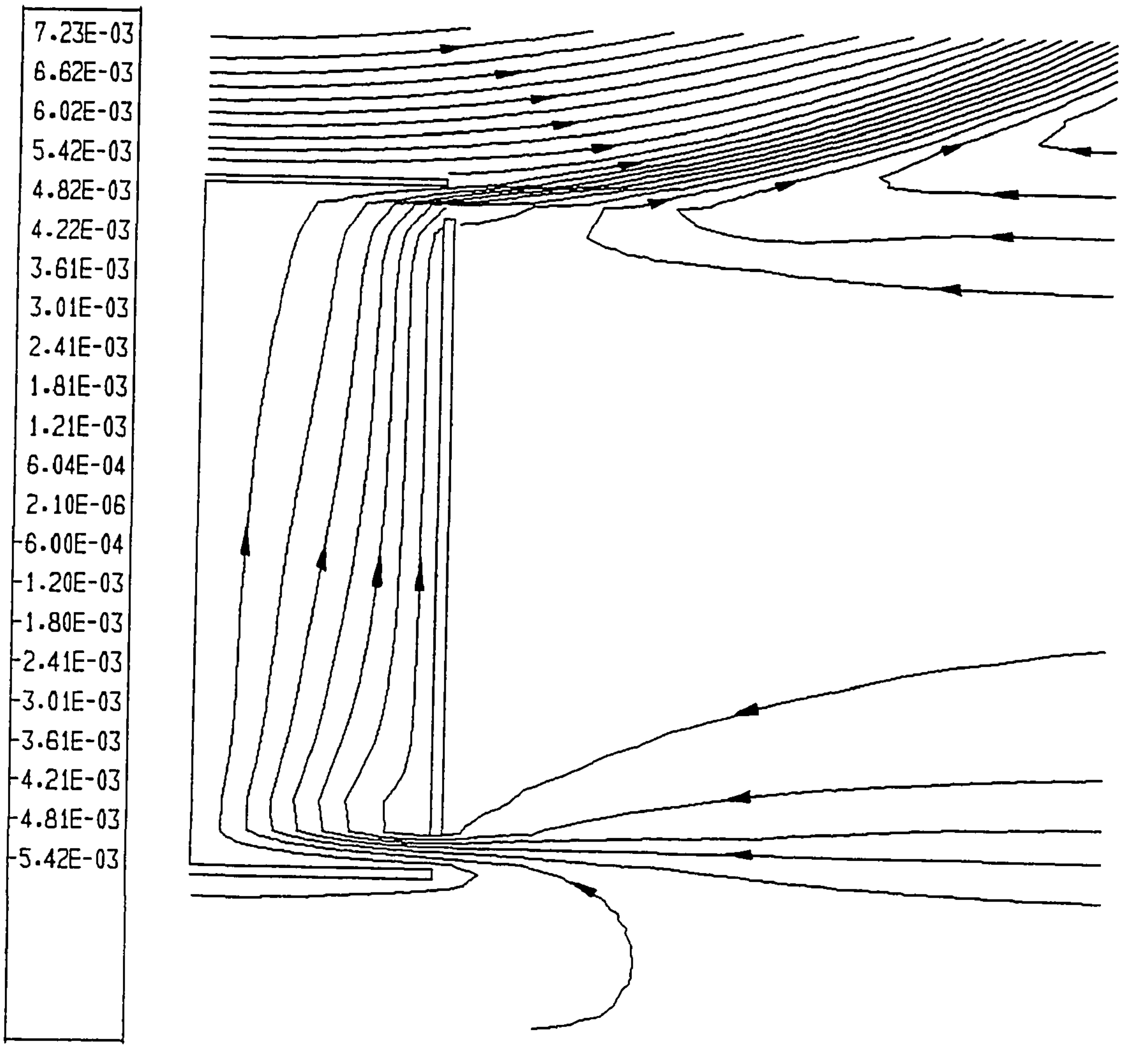

Fig. 5.9 Streamline contours for laminar case with $Gr = 1.4\times10^5$, $Pr = 0.71$, $Ar = 20$ and $Vs^* = 1.0$

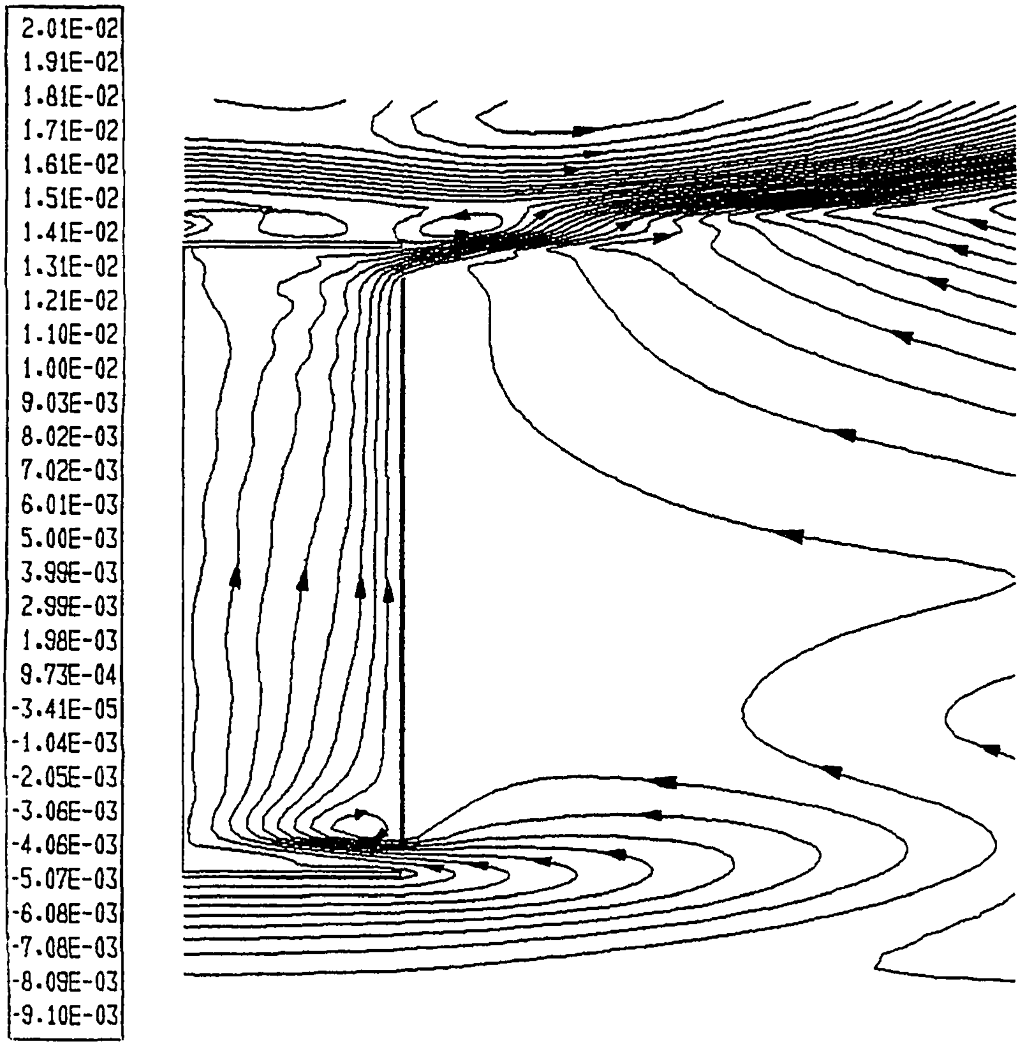

Fig. 5.10 Streamline contours for laminar case with $Gr = 1.0 \times 10^6$, $Pr = 0.71$, $Ar = 20$ and $Vs^* = 1.0$

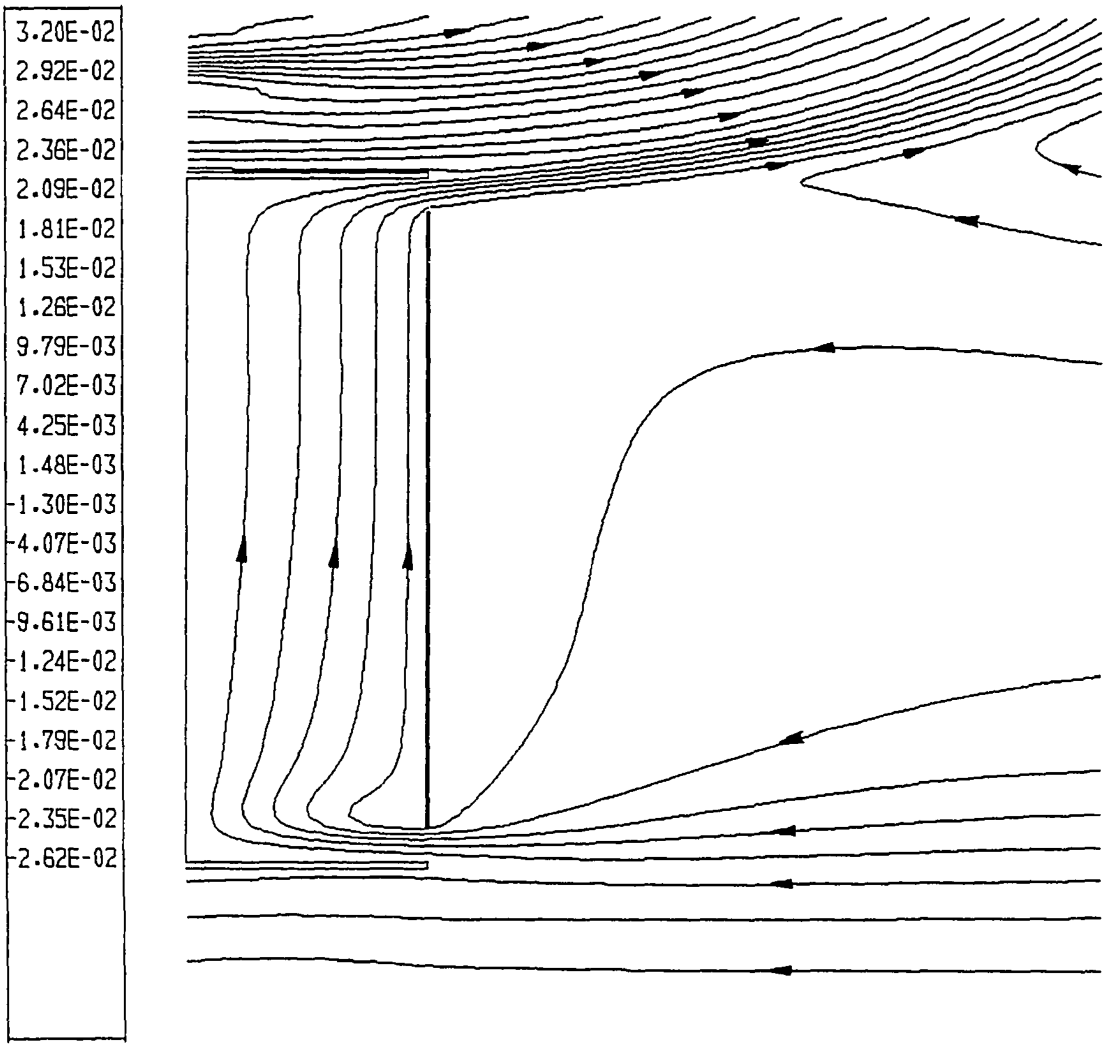

Fig. 5.11 Streamline contours for turbulent case with $Gr = 1.0 \times 10^6$, $Pr = 0.71$, $Ar = 20$ and $Vs^* = 1.0$

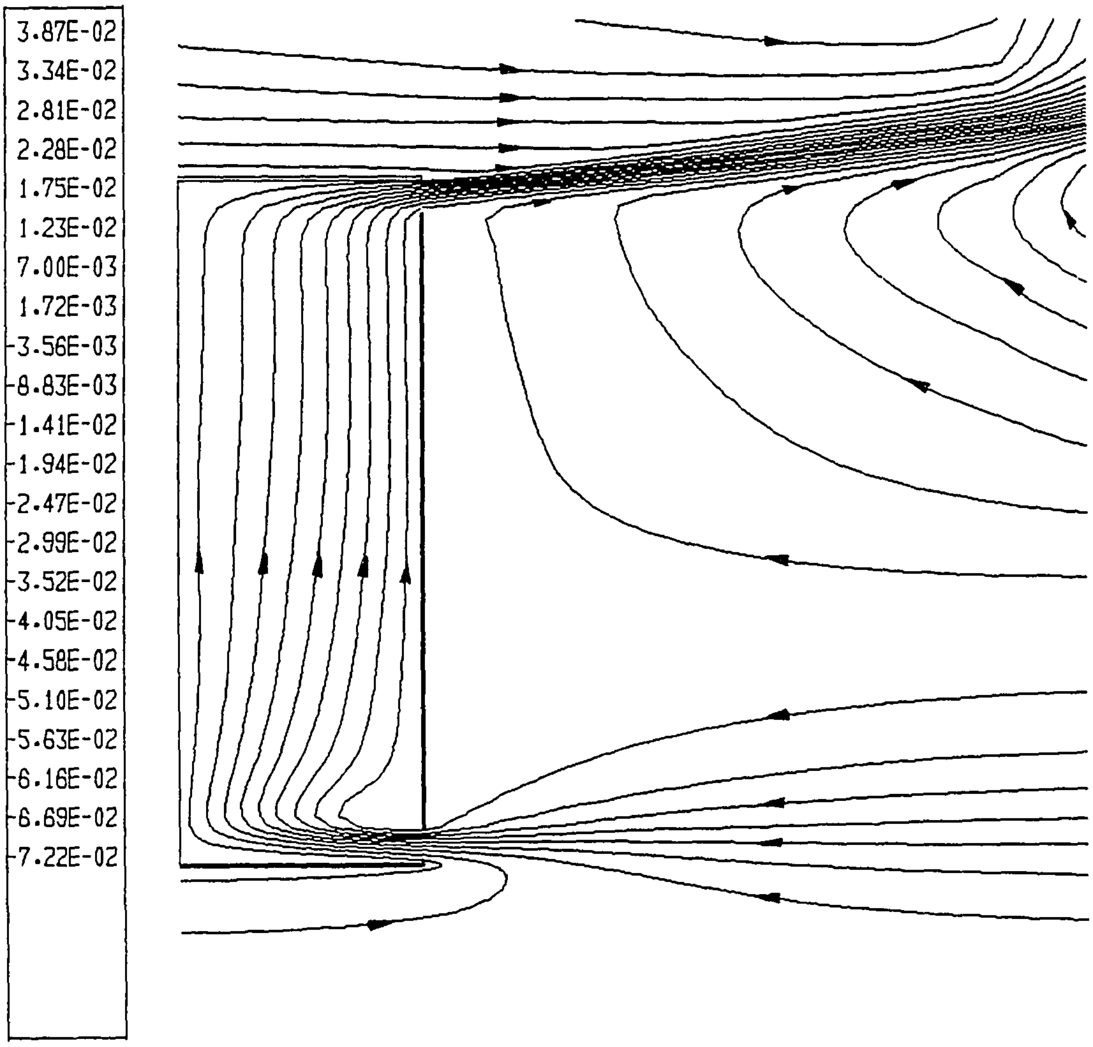

Fig. 5.12 Streamline contours for turbulent case with $Gr = 1.4\times10^7$, $Pr = 0.71$, $Ar = 20$ and $Vs^* = 1.0$

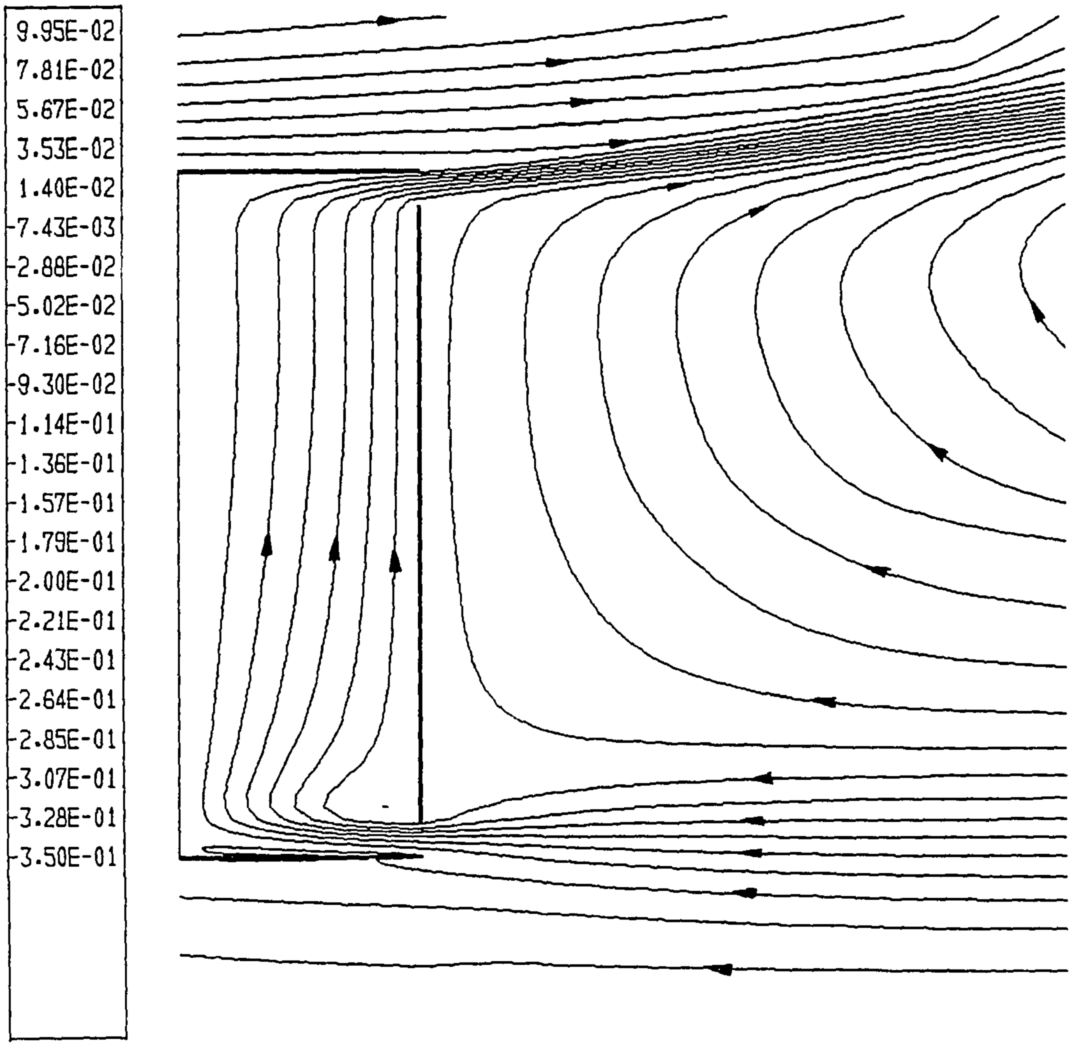

Fig. 5.13 Streamline contours for turbulent case with $Gr = 1.4\times10^8$, $Pr = 0.71$, $Ar = 20$ and $Vs^* = 1.0$

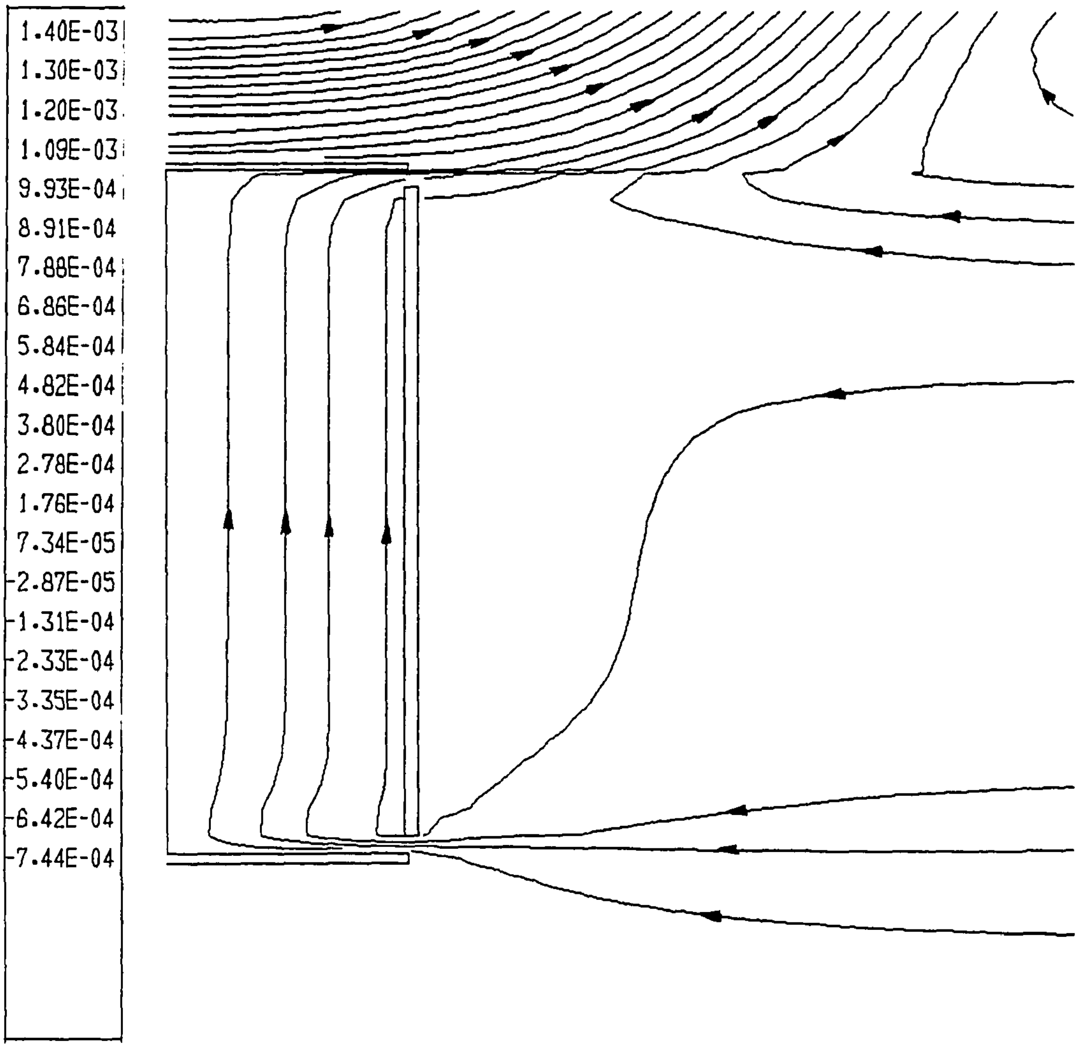

Fig. 5.14 Streamline contours for laminar case with $Gr = 1.4\times10^3$, $Pr = 0.71$, $Ar = 20$ and $Vs^* = 0.5$

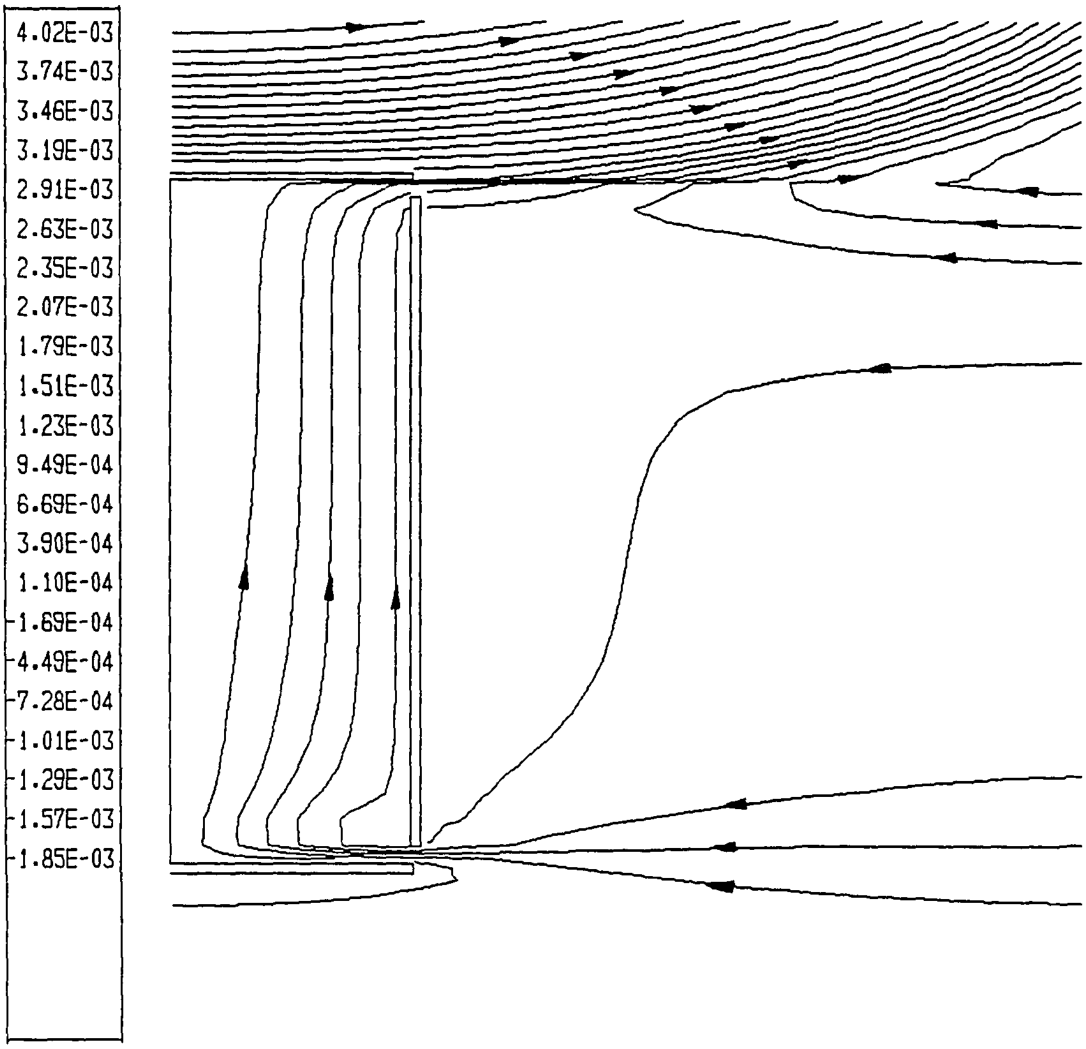

Fig. 5.15 Streamline contours for laminar case with $Gr = 1.4\times10^4$, $Pr = 0.71$, $Ar = 20$ and $Vs^* = 0.5$

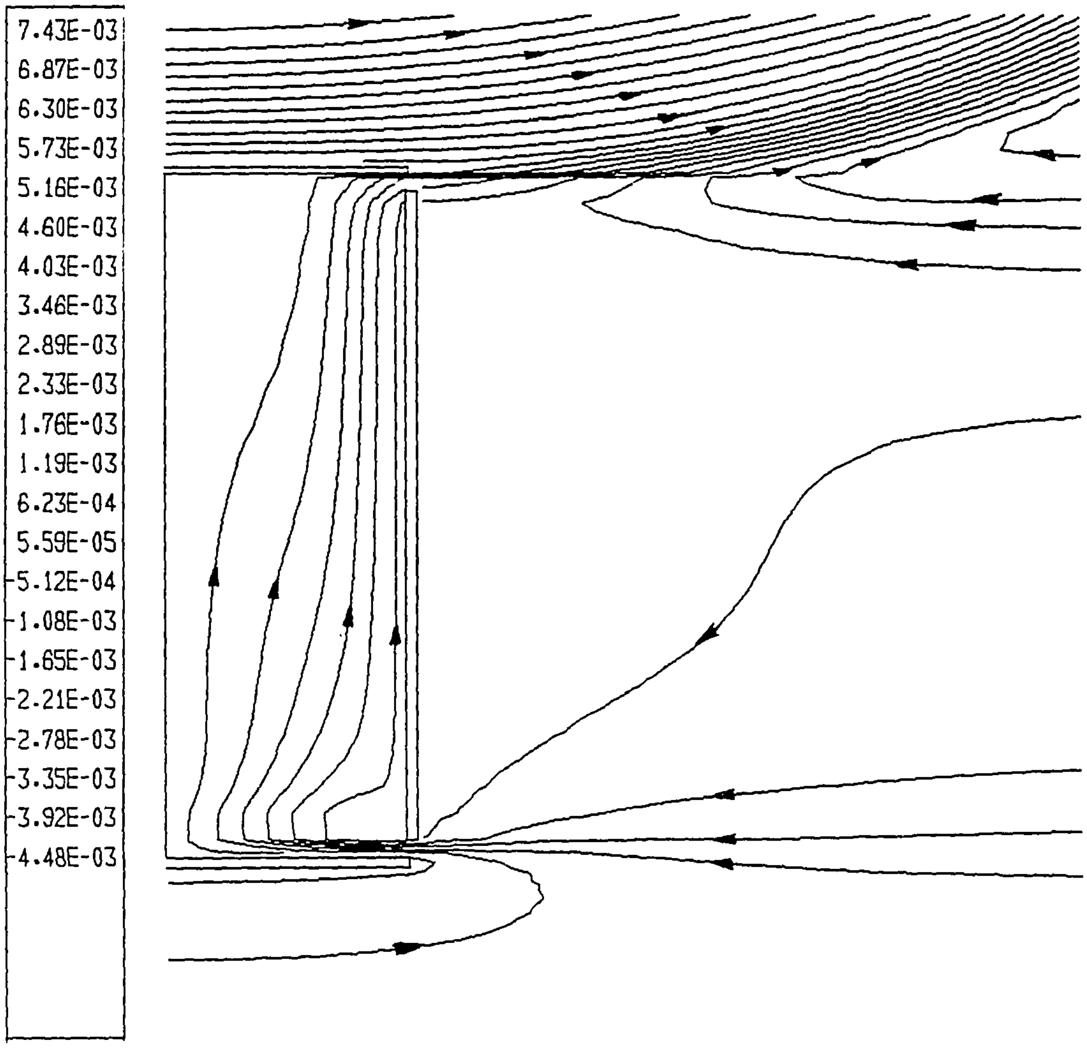

Fig. 5.16 Sreamline contours for laminar case with $Gr = 1.4\times10^5$, $Pr = 0.71$, $Ar = 20$ and $Vs^* = 0.5$

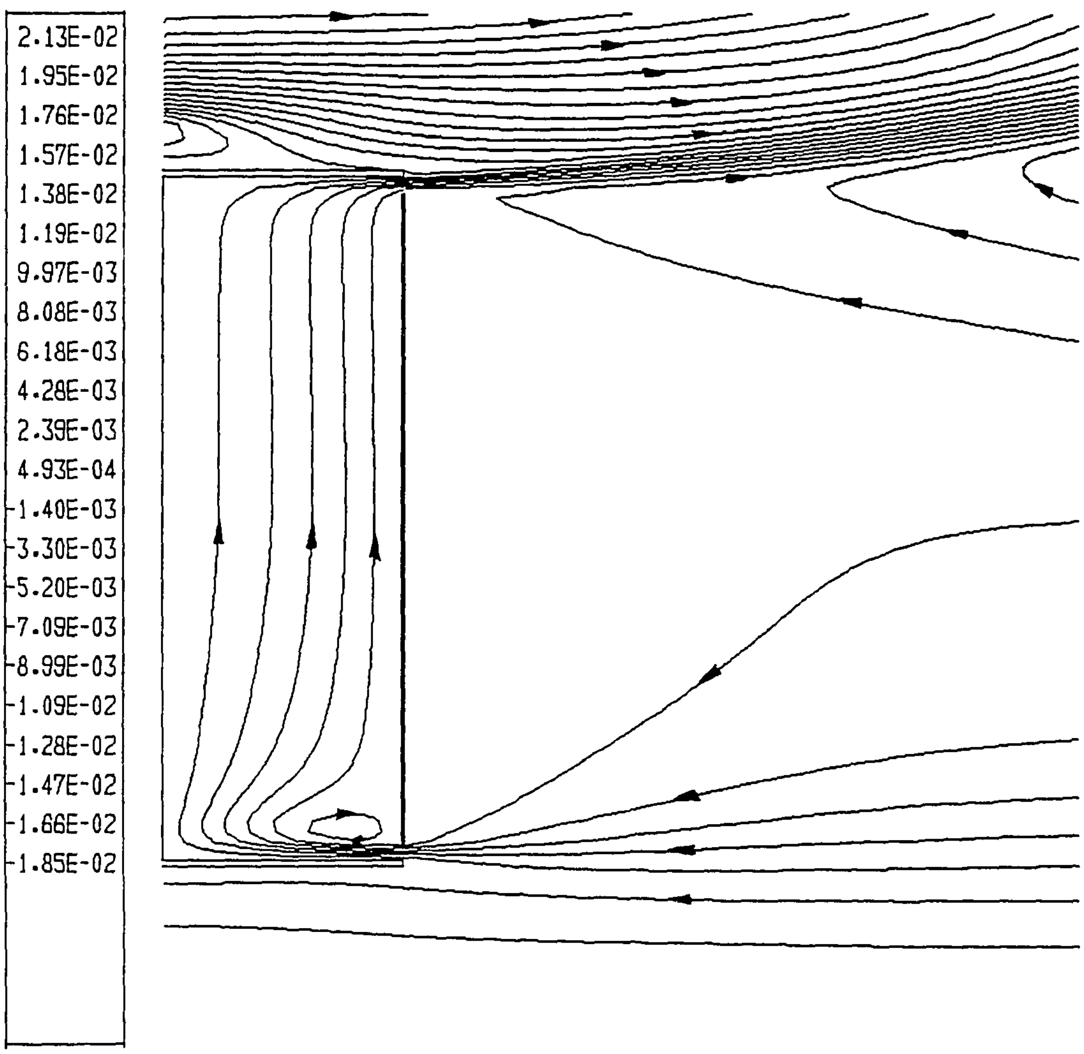

Fig. 5.17 Streamline contours for turbulent case with $Gr = 1.0\times10^6$, $Pr = 0.71$, $Ar = 20$ and $Vs^* = 0.5$

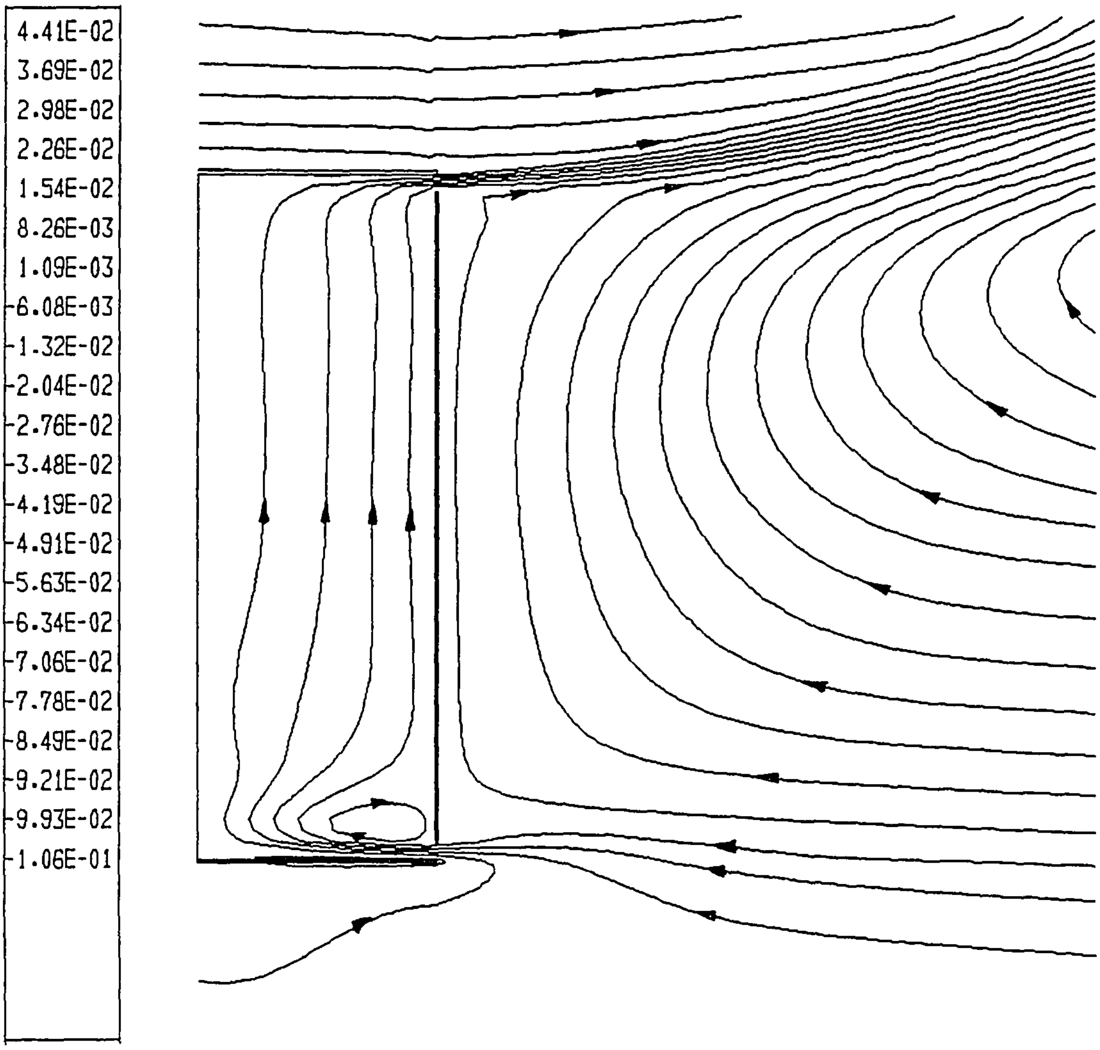

Fig. 5.18 Streamline contours for laminar case with $Gr = 1.4 \times 10^7$, $Pr = 0.71$, $Ar = 20$ and $Vs^* = 0.5$

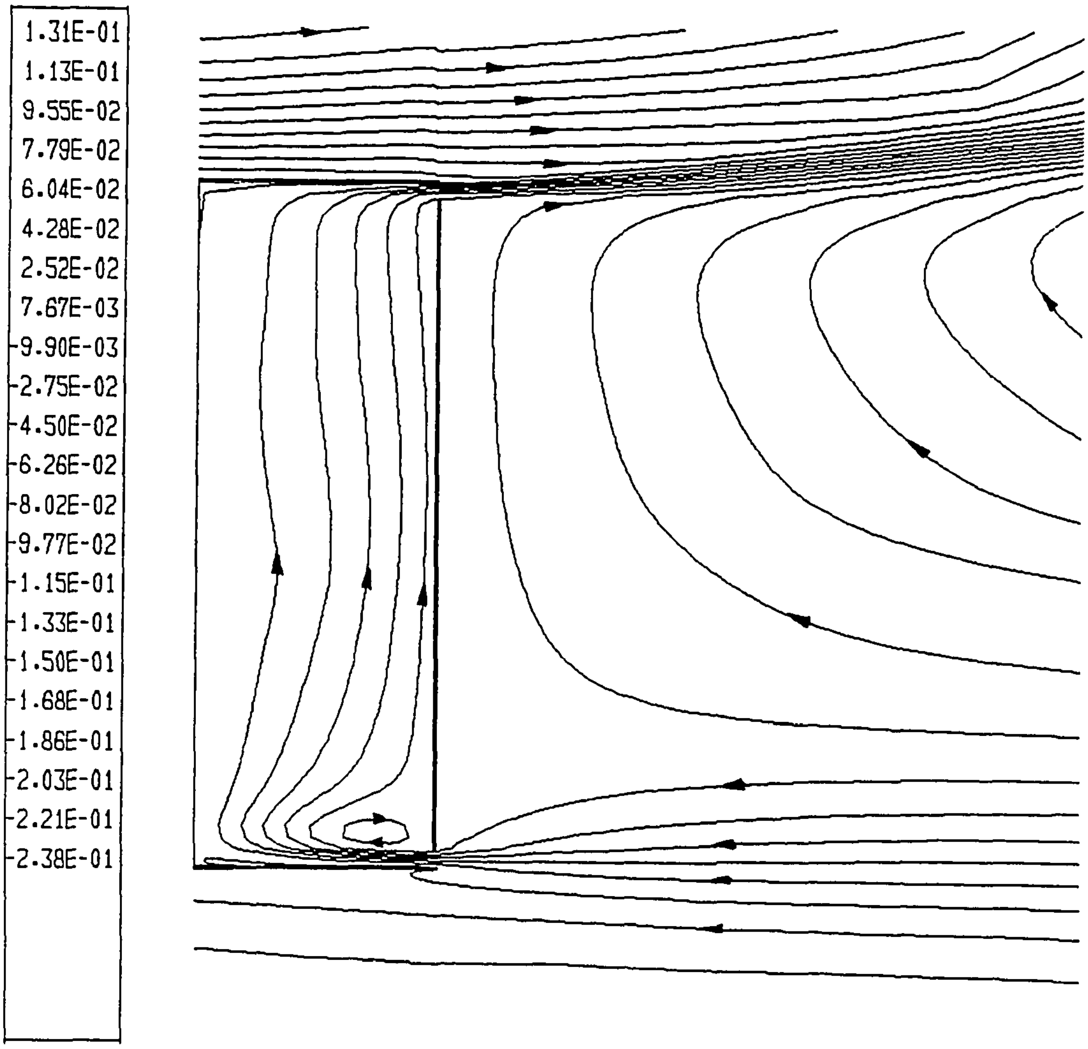

Fig. 5.19 Streamline contours for turbulent case with $Gr = 1.4 \times 10^8$, $Pr = 0.71$, $Ar = 20$ and $Vs^* = 0.5$

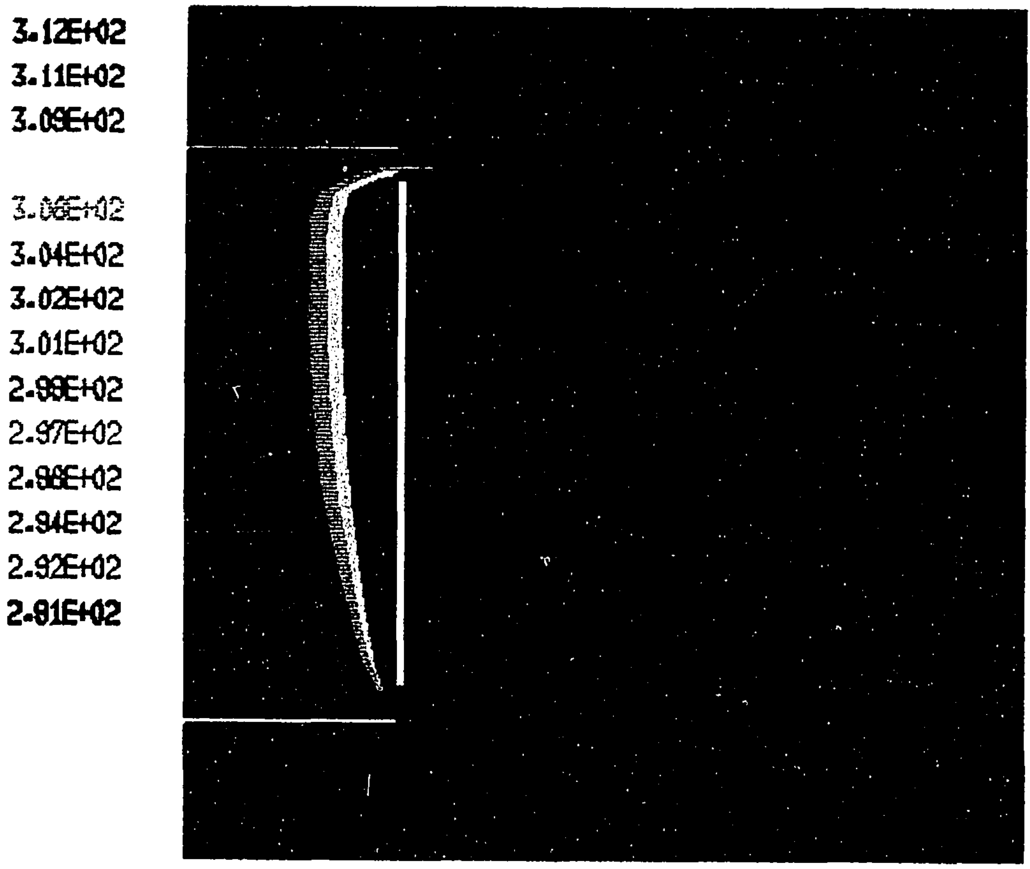

Fig. 5.20 Temperature distribution for laminar case with $Gr = 1.4\times10^3$, $Pr = 0.71$, $Ar = 20$ and $Vs^* = 1.0$

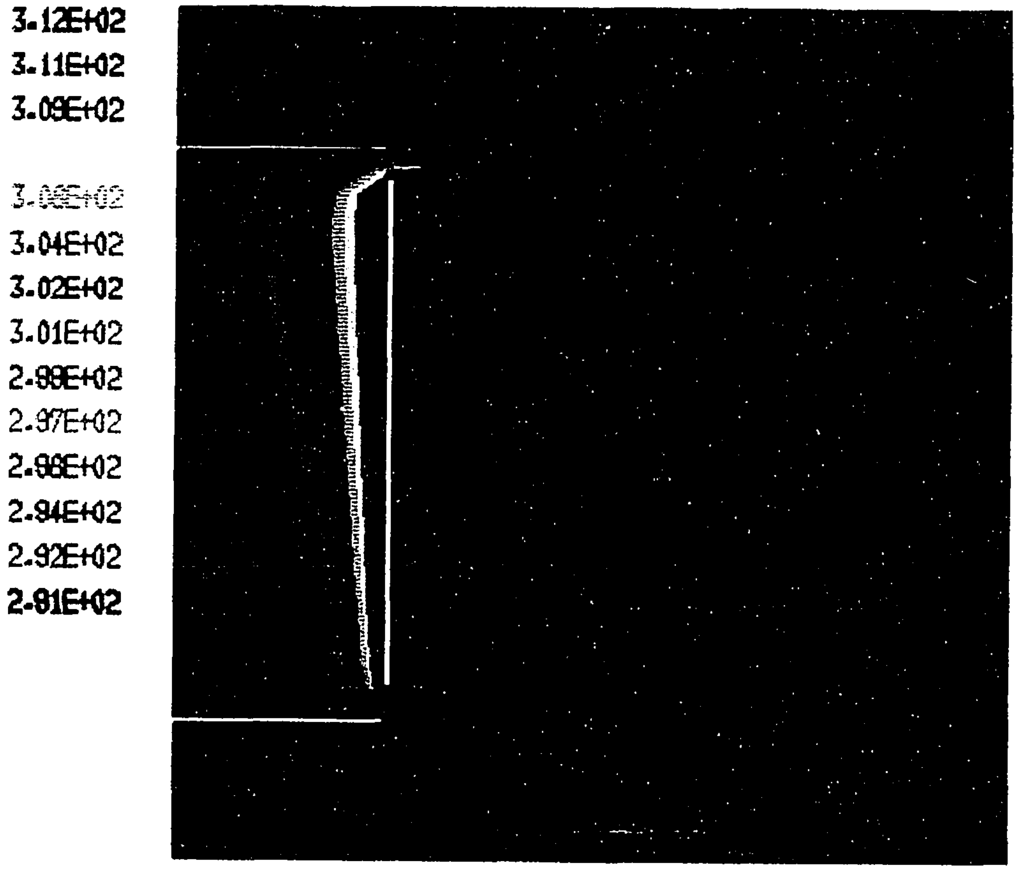

Fig. 5.21 Temperature distribution for laminar case with $Gr = 1.4\times10^4$, $Pr = 0.71$, $Ar = 20$ and $Vs^* = 1.0$

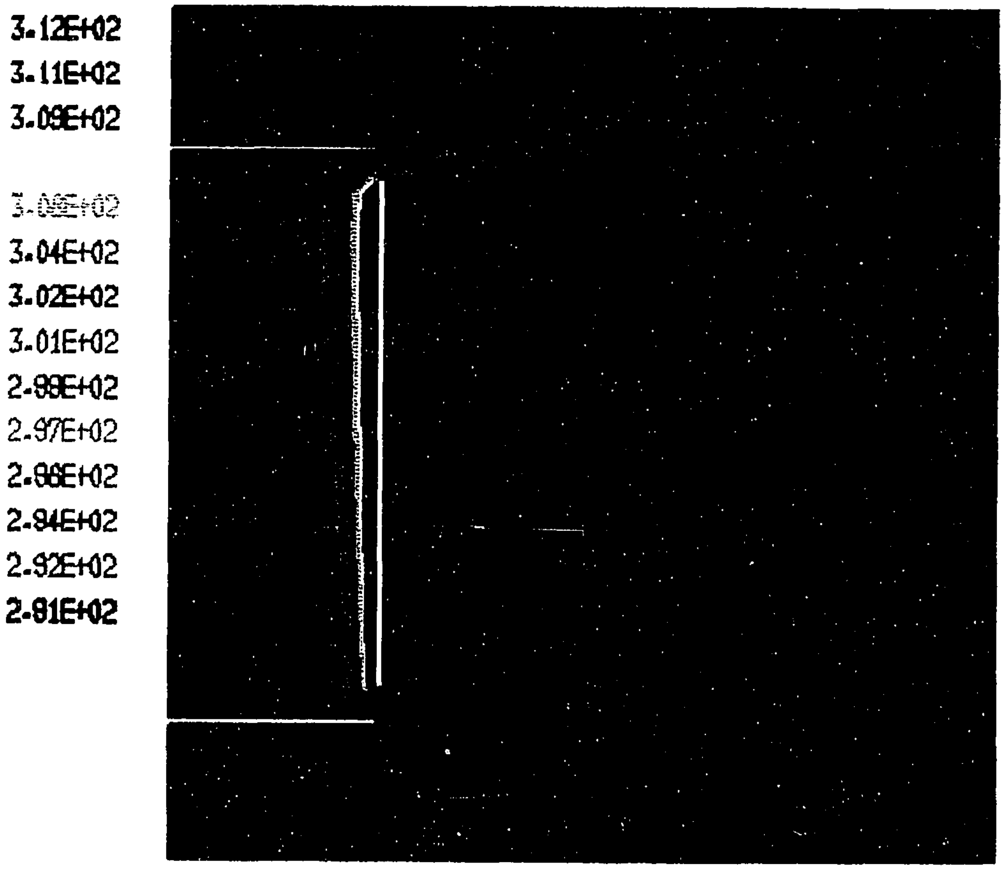

Fig. 5.22 Temperature distribution for laminar case with $Gr = 1.4\times10^5$, $Pr = 0.71$, $Ar = 20$ and $Vs^* = 1.0$

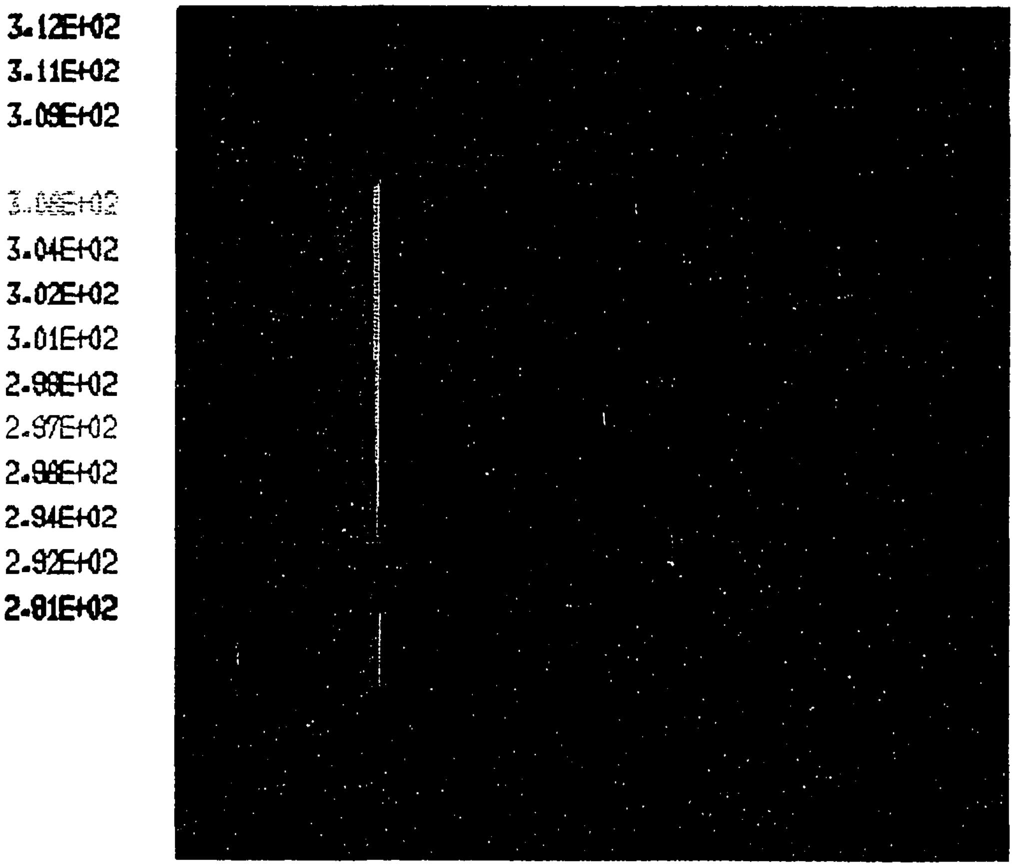

Fig. 5.23 Temperature distribution for turbulent case with Gr = 1.4×10^7, Pr = 0.71, Ar = 20 and Vs^* = 1.0

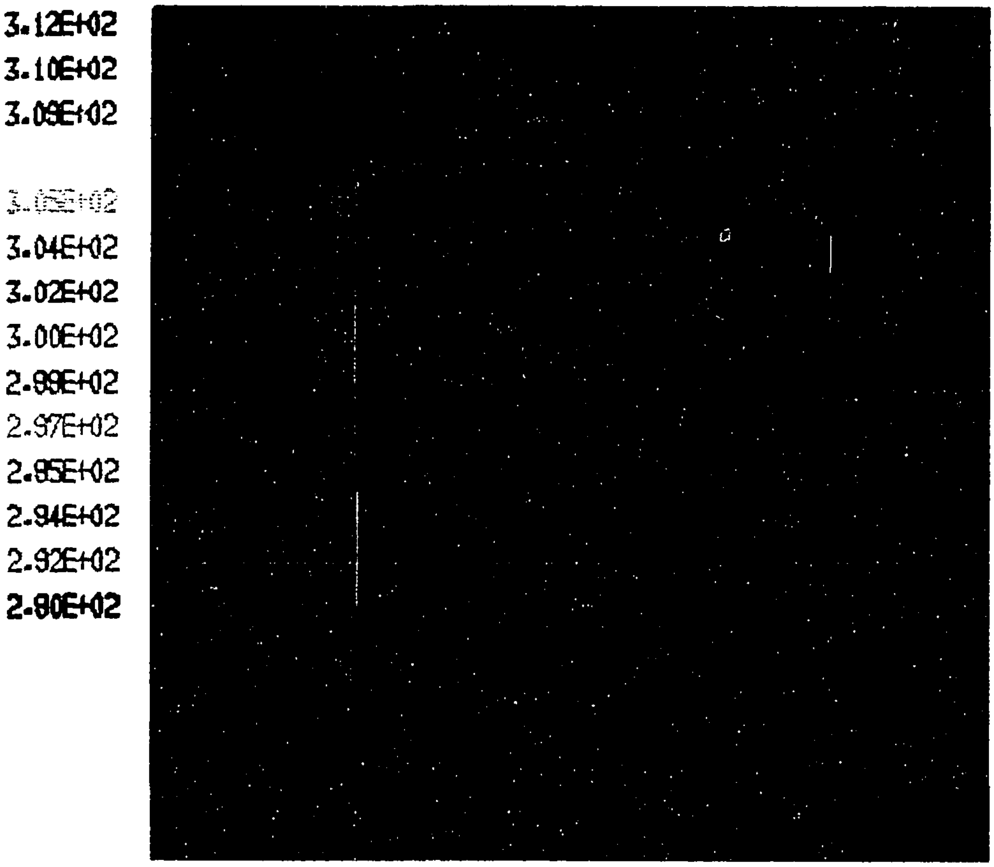

Fig. 5.24 Temperature distribution for turbulent case with Gr = 1.4×10^8, Pr = 0.71, Ar = 20 and Vs^* = 1.0

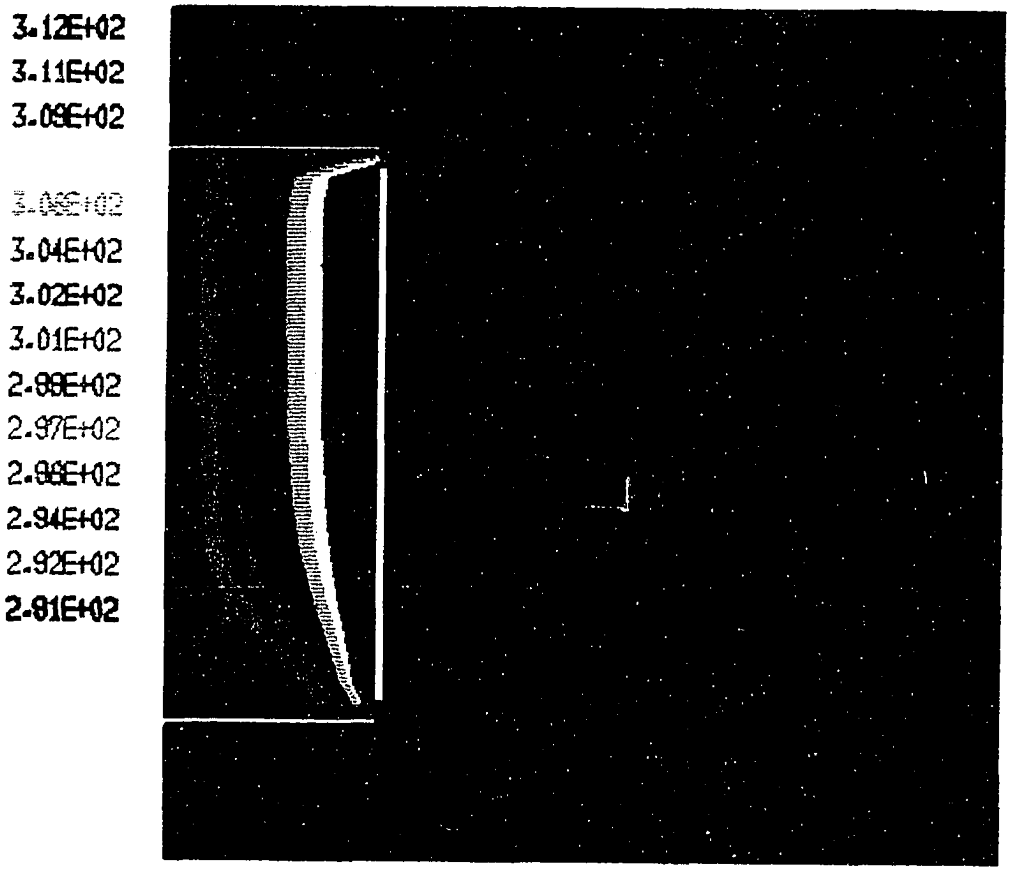

Fig. 5.25 Temperature distribution for laminar case with $Gr = 1.4\times10^3$, $Pr = 0.71$, $Ar = 20$ and $Vs^* = 0.5$

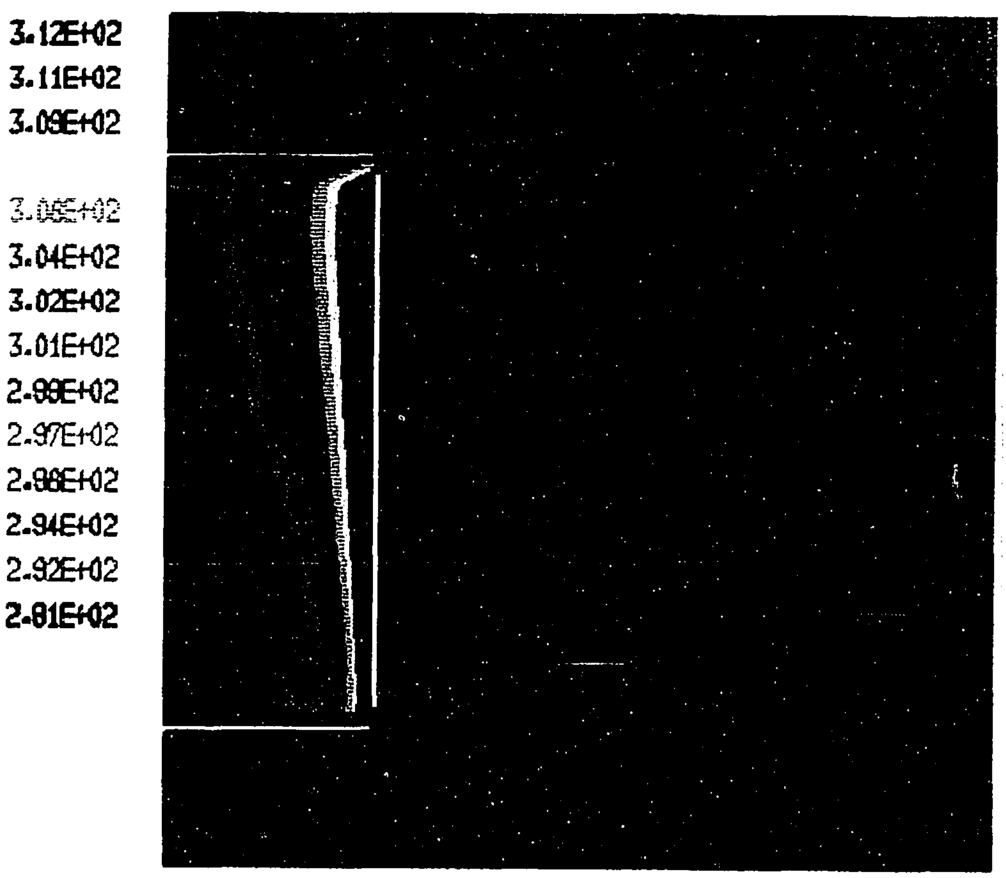

Fig. 5.26 Temperature distribution for laminar case with $Gr = 1.4\times10^4$, $Pr = 0.71$, $Ar = 20$ and $Vs^* = 0.5$

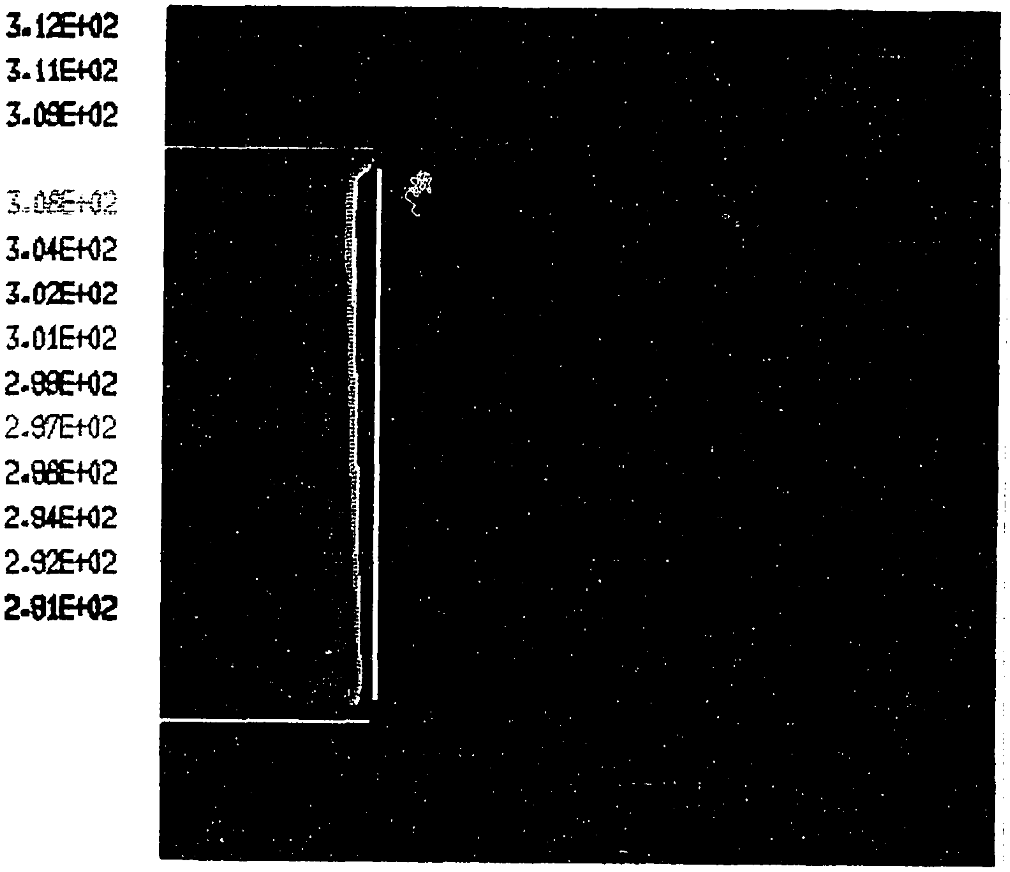

Fig. 5.27 Temperature distribution for laminar case with $Gr = 1.4\times10^5$, $Pr = 0.71$, $Ar = 20$ and $Vs^* = 0.5$

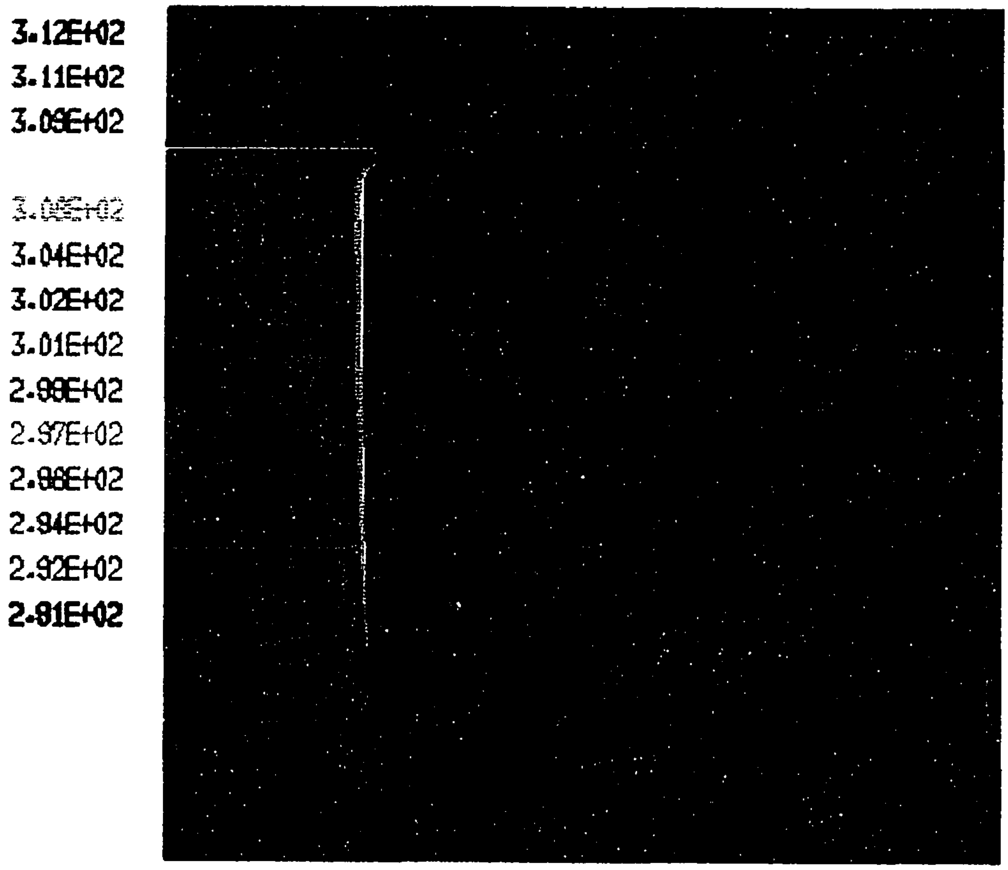

Fig. 5.28 Temperature distribution for turbulent case with $Gr = 1.0 \times 10^6$, $Pr = 0.71$, $Ar = 20$ and $Vs^* = 0.5$

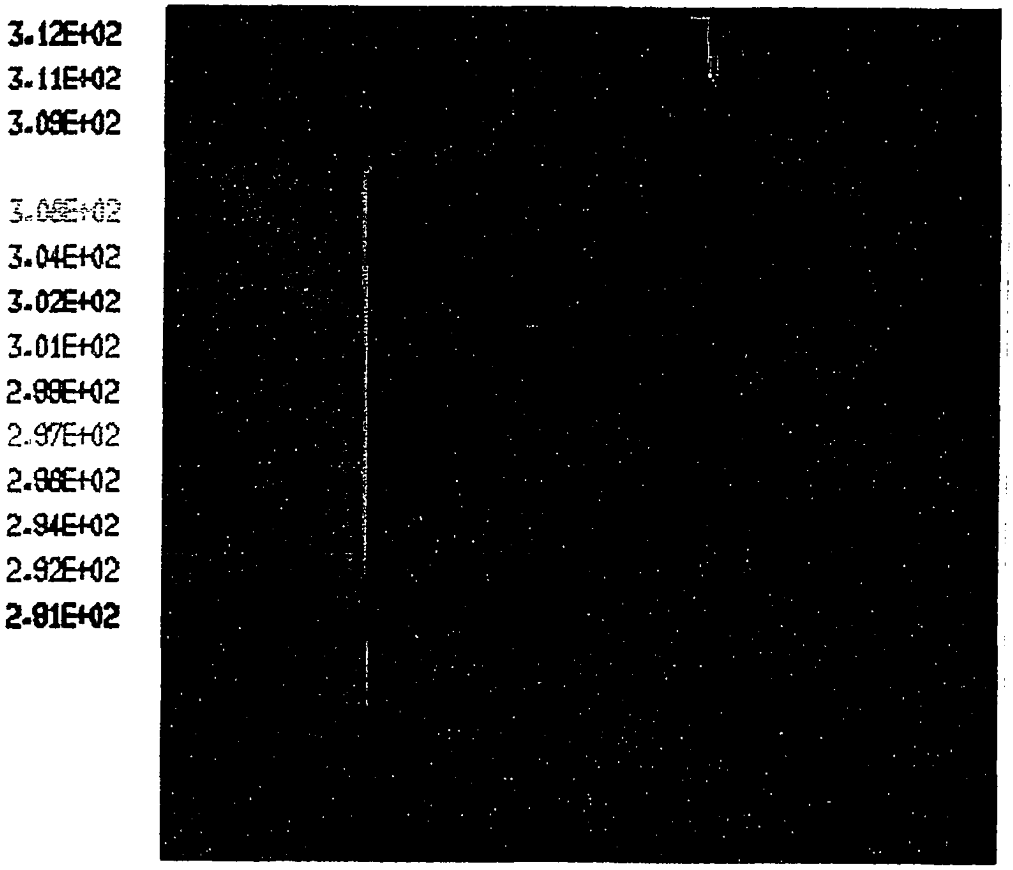

Fig. 5.29 Temperature distribution for turbulent case with $Gr = 1.4\times 10^7$, $Pr = 0.71$, $Ar = 20$ and $Vs^* = 0.5$

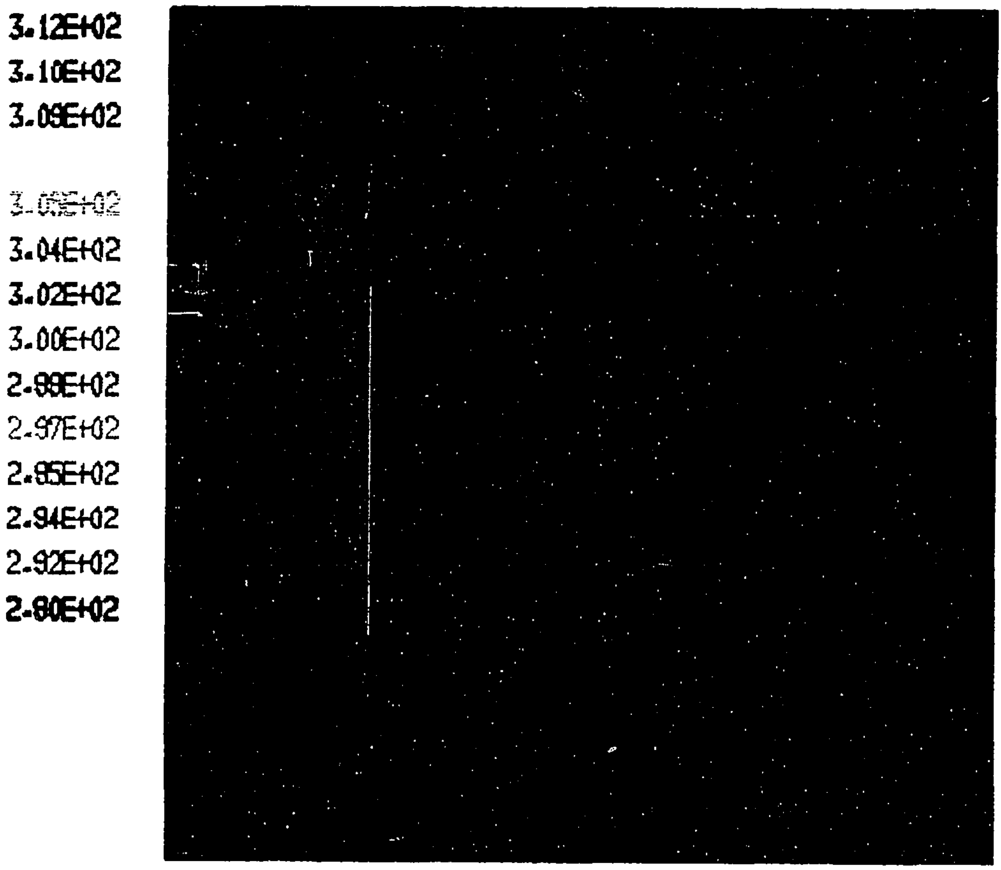

Fig. 5.30 Temperature distribution for turbulent case with $Gr = 1.4\times10^8$, $Pr = 0.71$, $Ar = 20$ and $Vs^* = 0.5$

from these figures. The higher the Grashof number, the thinner the thermal boundary layer on the heated wall becomes, and the more strongly the thermal plume discharges hot air into the atmosphere.

5.5 Heat Transfer and Mass Flow Rate Characteristics

Figure 5.31 shows the variation of non-dimensional mass flow rate induced through the cavity as a function of Grashof number for the channel aspect ratio of 20. Here, the non-dimensional mass flow rate, $\dot{m}^*$, is defined as

$$\dot{m}^* = \frac{\dot{m}}{\rho_\infty L u^*} = \frac{\dot{m}}{\rho_\infty L(\beta g \Delta T L)^{1/2}} = \frac{\dot{m}}{\left(\frac{\rho_\infty^2 \beta g \Delta T L^3}{\mu^2}\mu^2\right)^{1/2}}$$
$$= \frac{\dot{m}}{\mu (Gr)^{1/2}} \qquad (5.1)$$

where

$$u^* = (\beta g \Delta T L)^{1/2} \qquad (5.2)$$

show that this quantity is governed by Grashof number as well as dimensionless vent size. The mass flow rate, for a given vent size, first increases and then decreases with Grashof number in laminar regime, indicating a maximum around $Gr = 1.4\times10^4$. As the vent size is reduced for a fixed Grashof number, the mass flow rate is reduced substantially due to increased throttling effect of the reduced vent size. For the turbulent flow regime, the mass flow rate decreases slightly with increasing Grashof number.

The average horizontal velocity at the channel inlet and outlet is depicted in Fig. 5.32 for several vent sizes and Grashof numbers. For constant Grashof number, the average horizontal velocity at inlet increases as the vent size decreases. However, increase in velocity magnitude is not proportional to the decrease in vent size due to higher inlet and exit vent losses for smaller size vents. As expected, the velocity values at the channel exit are mirror images of incoming velocity values in Fig. 5.32.

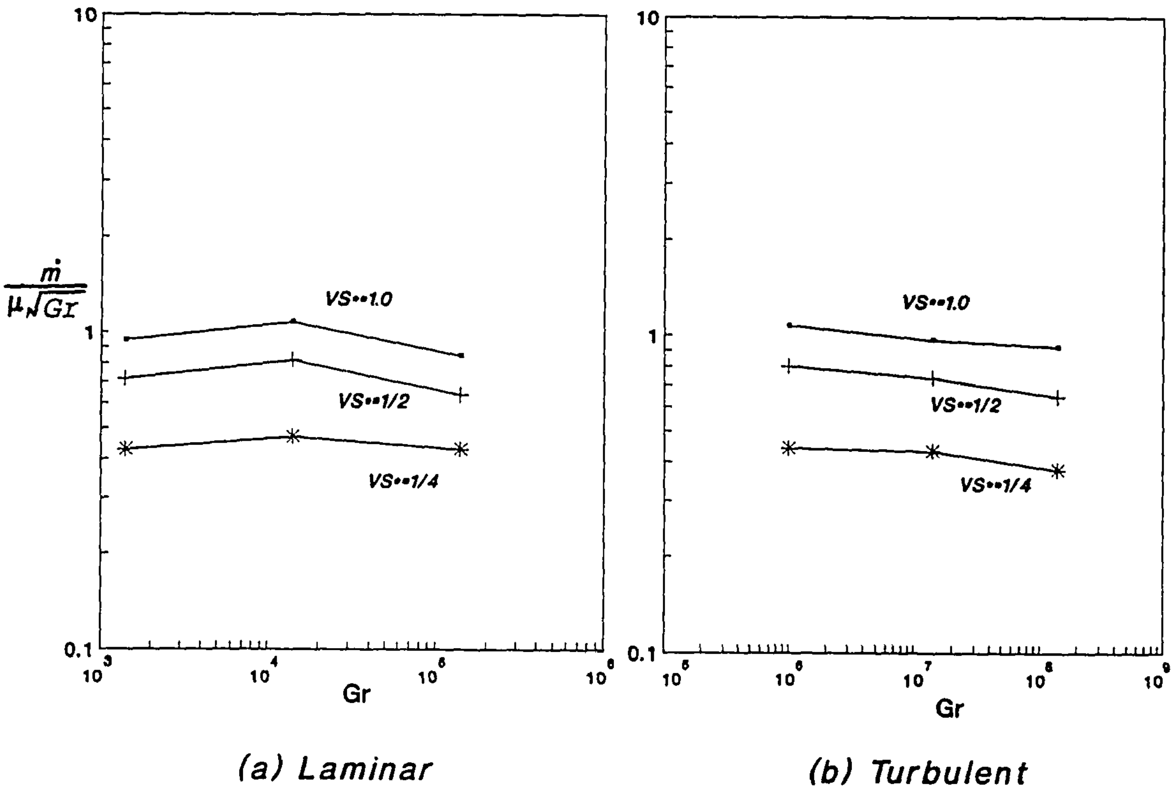

Fig. 5.31 Non-dimensional mass flow rate as the function of *Gr* for different vent sizes

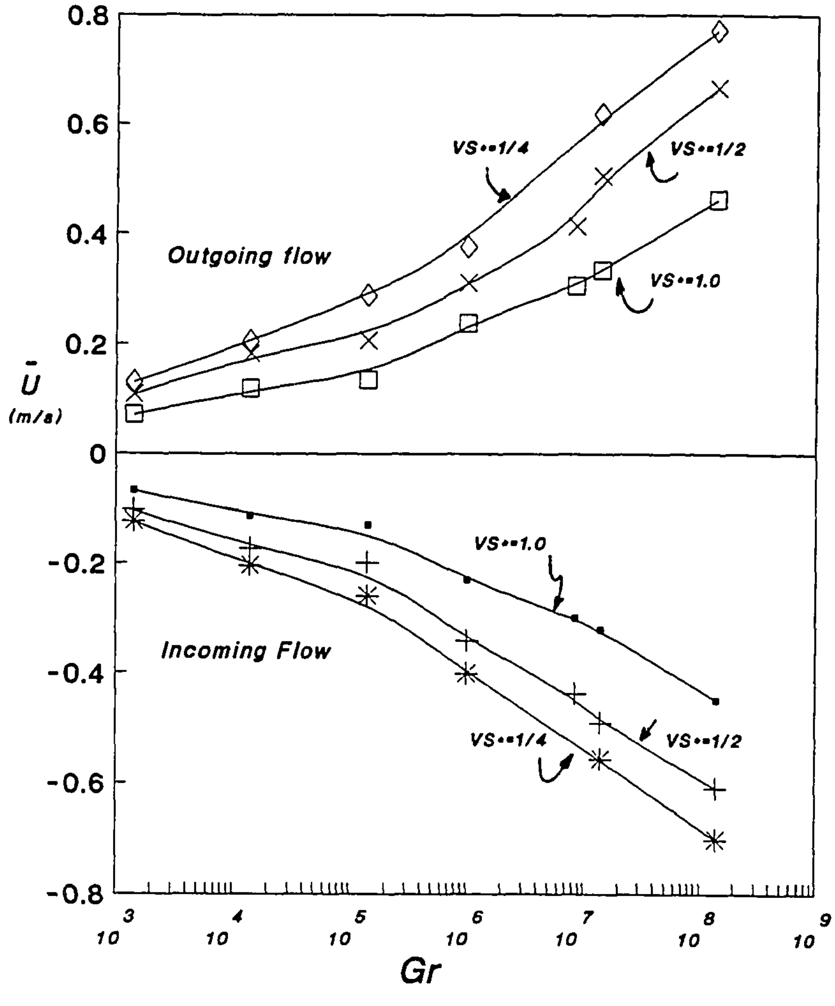

Fig. 5.32 Average u-velocity at inlet and exit for various of *Gr* and *Vs**

Figure 5.33 shows the variation of local Nusselt number on the heated wall for a typical turbulent case of $Gr = 1.0\times10^6$, $Pr = 0.71$ and $Ar = 20$. The recirculating region near the leading edge of heated wall causes a small peak in the local Nusselt number in that region. Results indicate a thermal entrance region followed by a nearly fully developed region where the local heat transfer coefficient is nearly uniform. Near the trailing edge of the heated wall, the Nusselt number increases slightly. Figure 5.34 shows the variation of averaged Nusselt number on heated wall as a function of Grashof number and vent size for the aspect ratio of 20. Results indicate that the average Nusselt number on heated wall increases significantly as Grashof number increases. The Nusselt number also increases as the vent size is increased from $Vs^* = 0.25$ to 1.0. However, we note that the effect of vent size on the Nusselt number is not very pronounced as shown in Fig. 5.34. In contrast, as noted from Fig. 5.31, the effect of vent size on the mass flow rate is very significant while the effect of Grashof number is somewhat weaker.

Figure 5.35 shows the variation of non-dimensional net energy delivery rate of a side-vented cavity as the function of Grashof number and dimensionless vent size for the channel aspect ratio of 20. The net energy delivery rate increases as vent size and Grashof number are increased.

5.6 Vent Losses at Channel Inlet and Exit Sections

Figures 5.36–5.40 show the pressure variation in the system for Grashof number ranging from 1.4×10^3 to 1.4×10^8 for the dimensionless vent side of unity. These figures clearly show two-dimensional pressure field near the inlet and exit sections of the channel, and stratified (one-dimensional) pressure distribution in the rest of the channel. For the present coordinate system, this means that in the middle region the pressure is a function of only x-coordinate where as in the inlet/exit sections it is a function of x and y

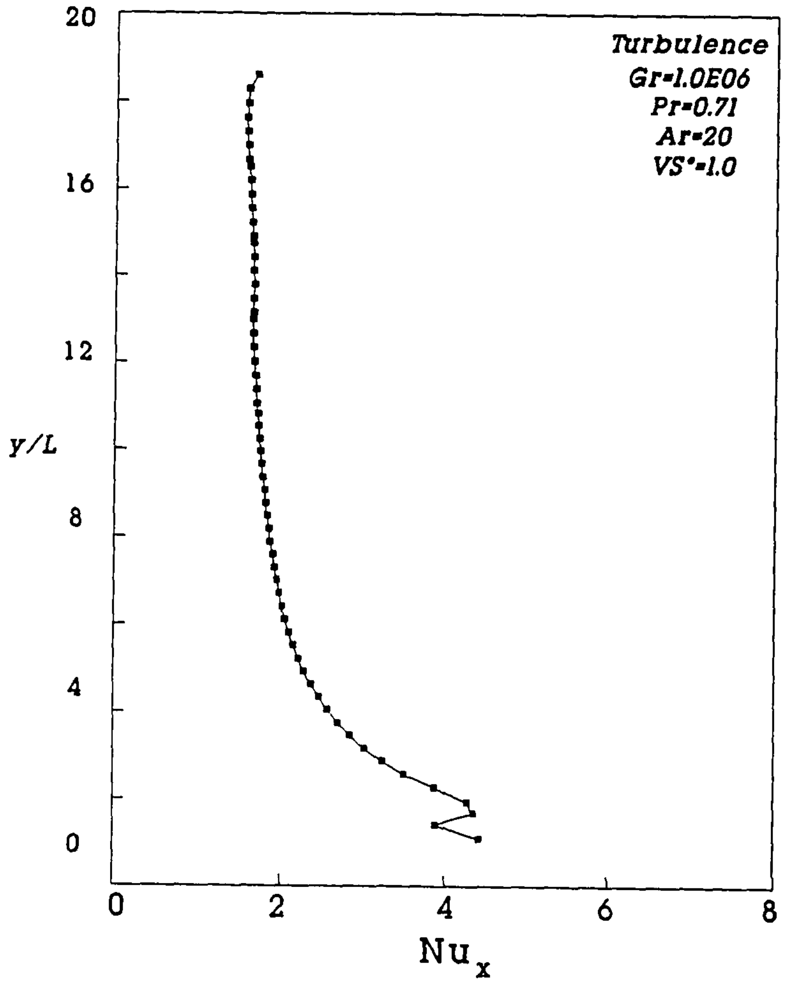

Fig. 5.33 Typical local Nusselt number on heated wall for $Gr = 1.0 \times 10^6$, $Pr = 0.71$, $Ar = 20$, $Vs^* = 1.0$

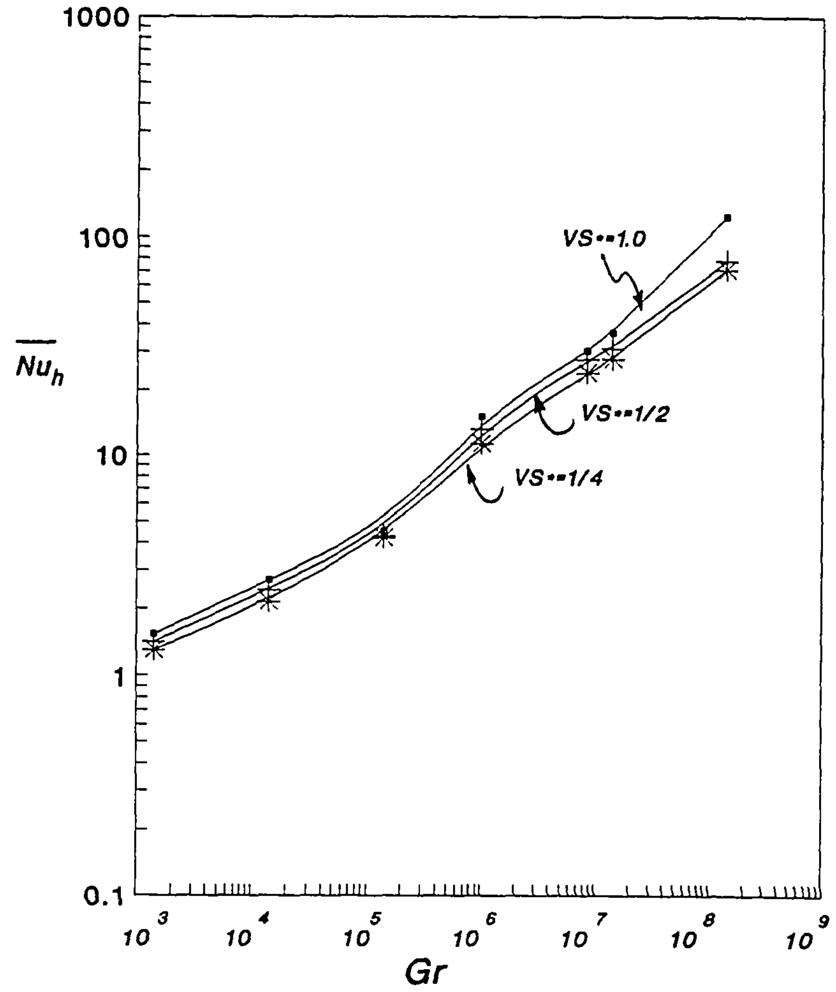

Fig. 5.34 Average Nusselt number on heated wall as the function of *Gr* for different vent sizes.

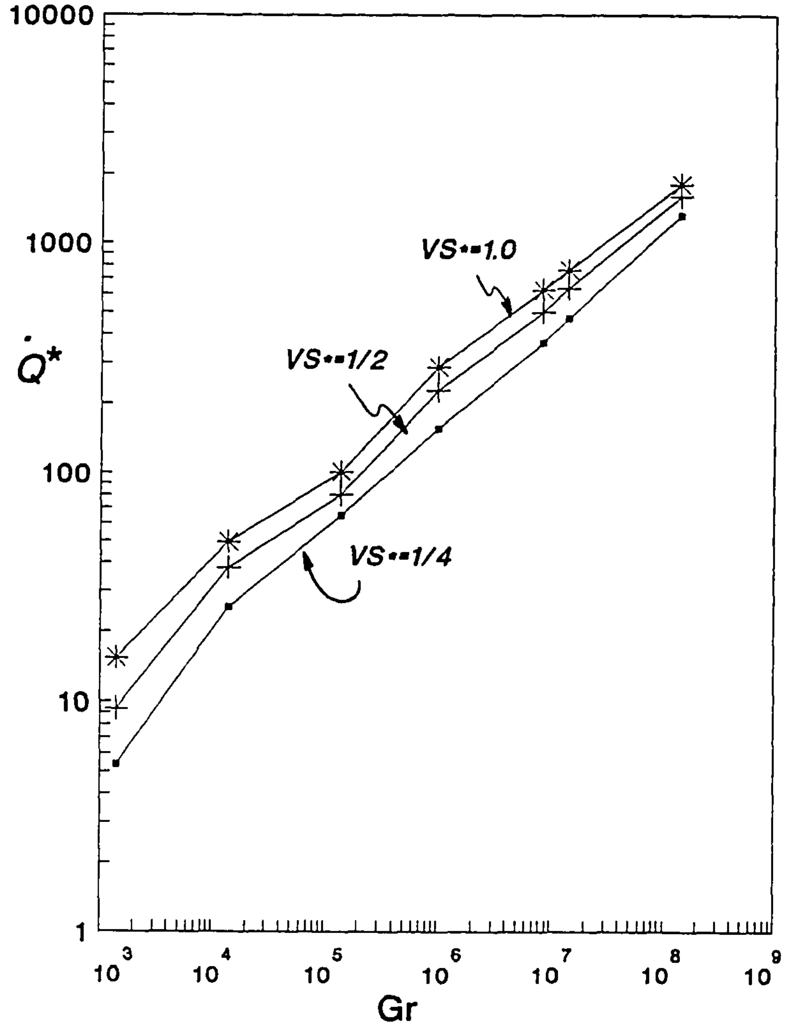

Fig. 5.35 Dimensionless energy rate as the function of *Gr* for different vent sizes.

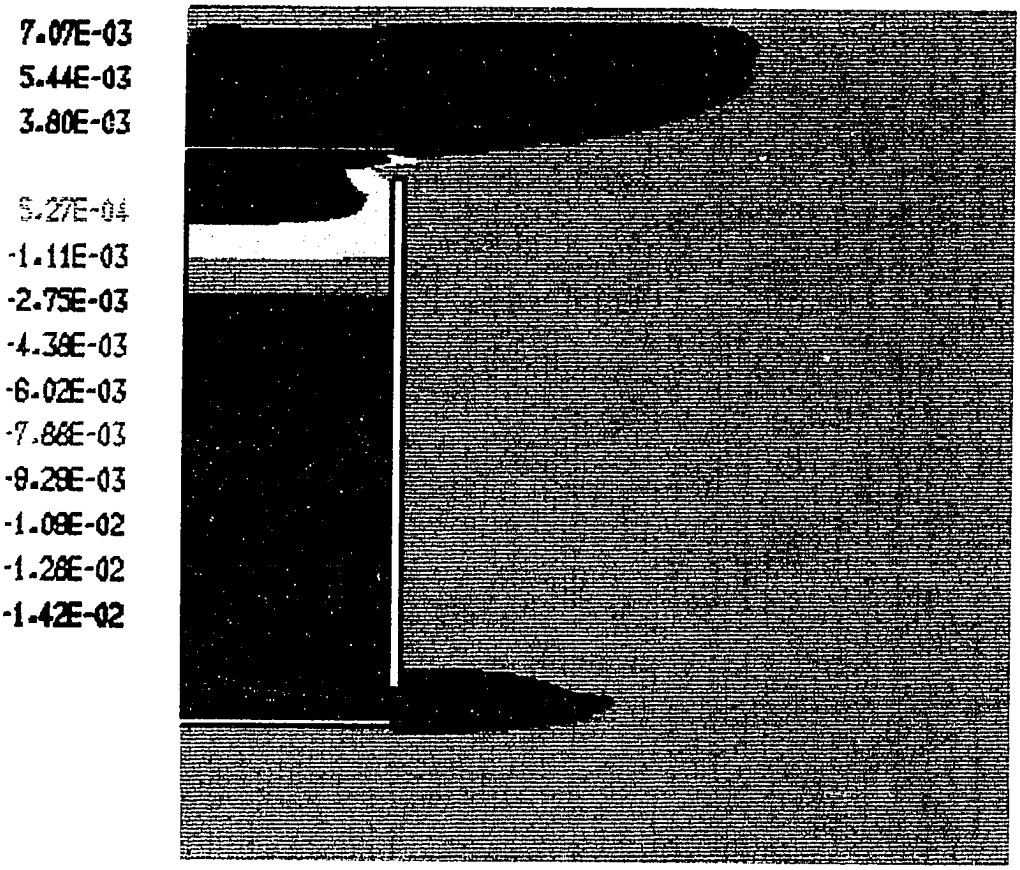

Fig. 5.36 Pressure field for laminar case with $Gr = 1.4\times10^3$, $Pr = 0.71$, $Ar = 20$ and $Vs^* = 1.0$

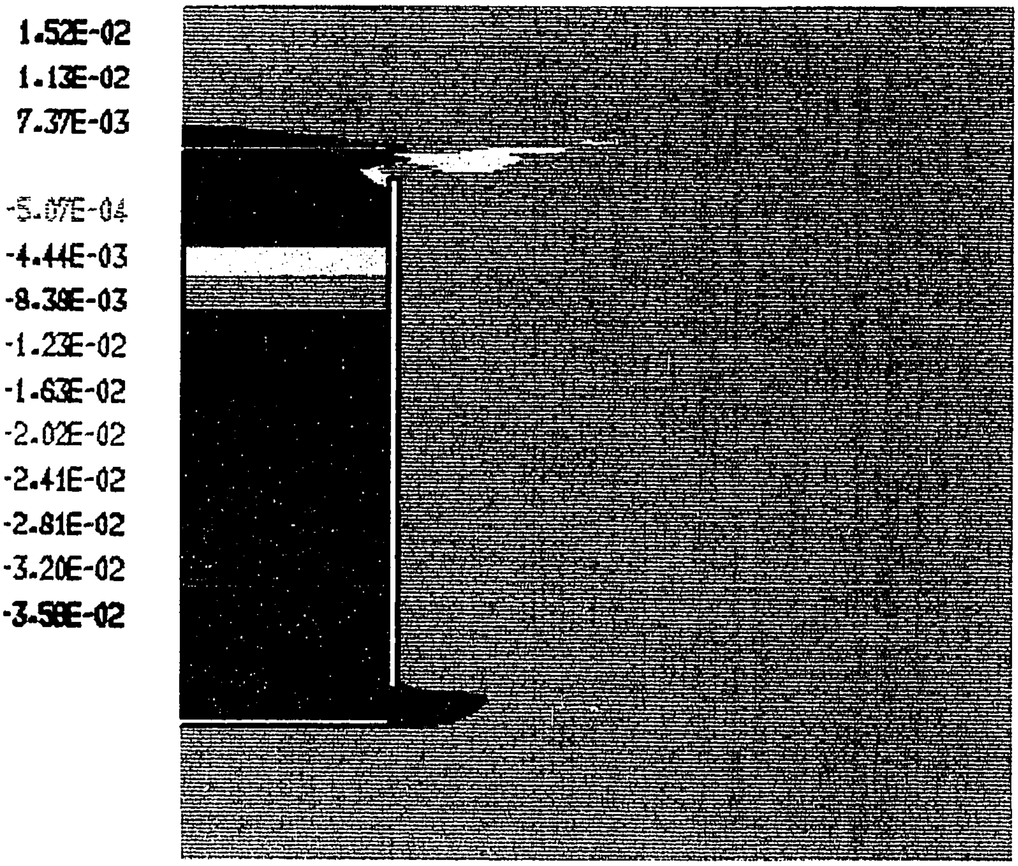

Fig. 5.37 Pressure field for laminar case with $Gr = 1.4\times10^4$, $Pr = 0.71$, $Ar = 20$ and $Vs^* = 1.0$

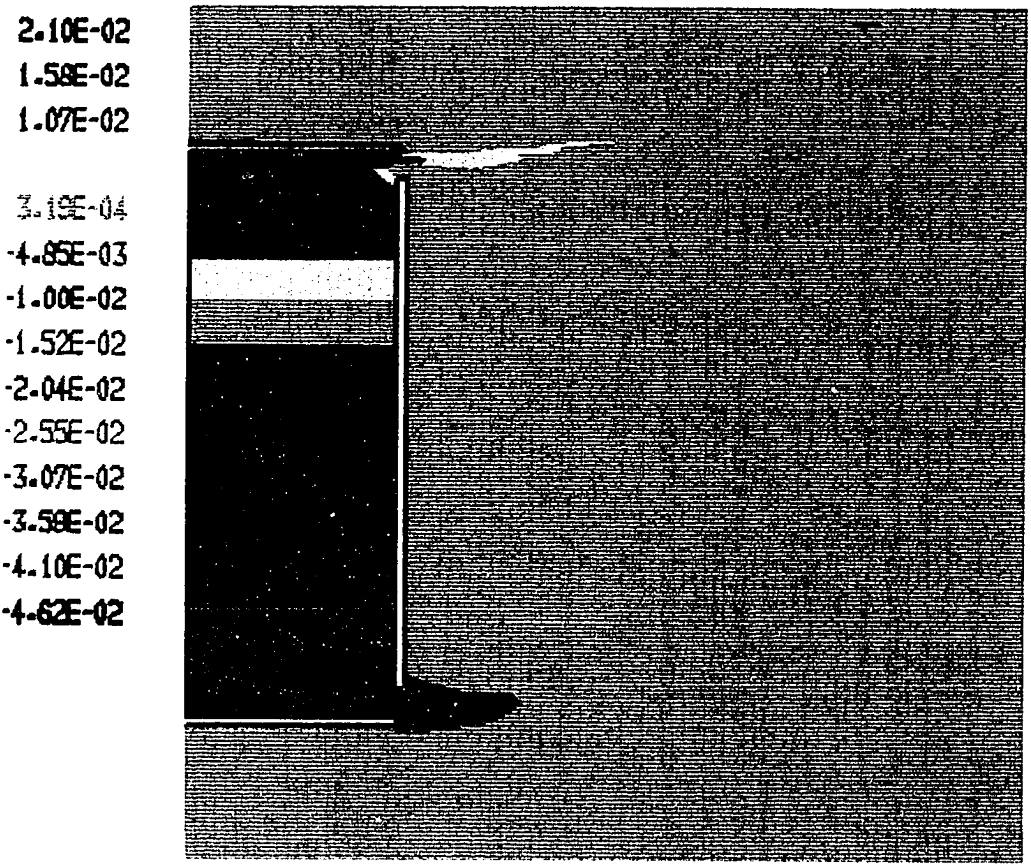

Fig. 5.38 Pressure field for laminar case with Gr = 1.4×10^5, Pr = 0.71, Ar = 20 and Vs^* = 1.0

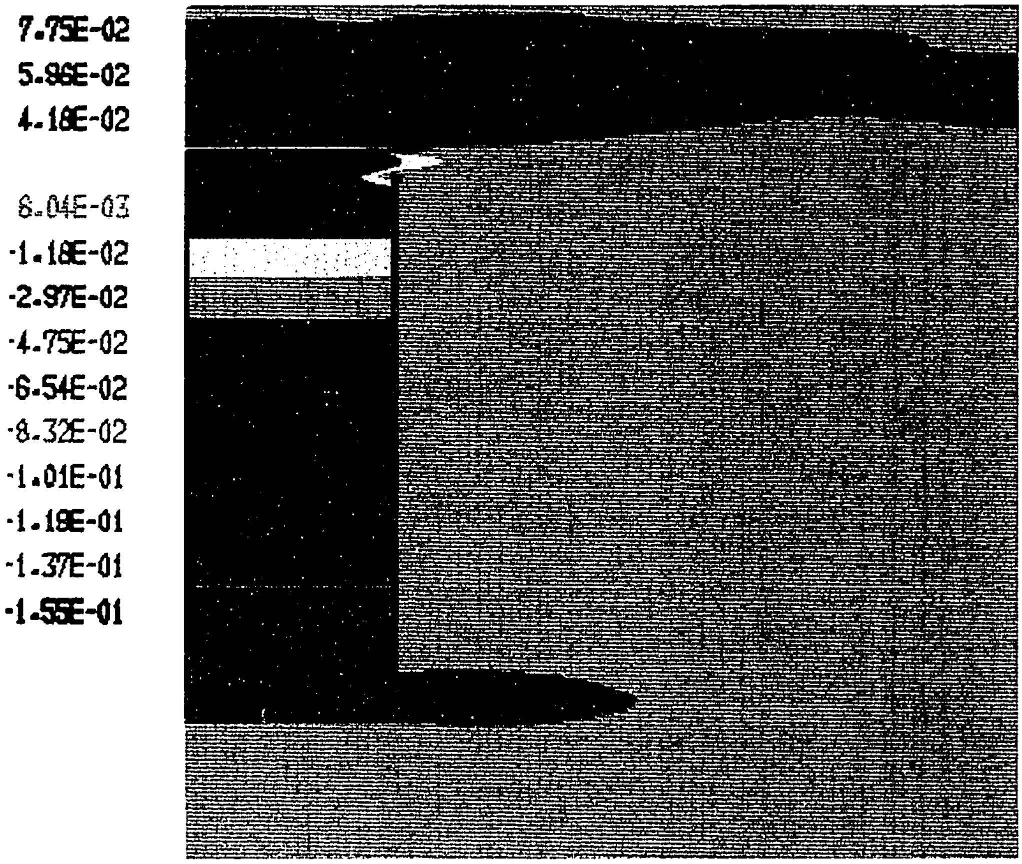

Fig. 5.39 Pressure field for turbulent case with $Gr = 1.0\times10^6$, $Pr = 0.71$, $Ar = 20$ and $Vs^* = 1.0$

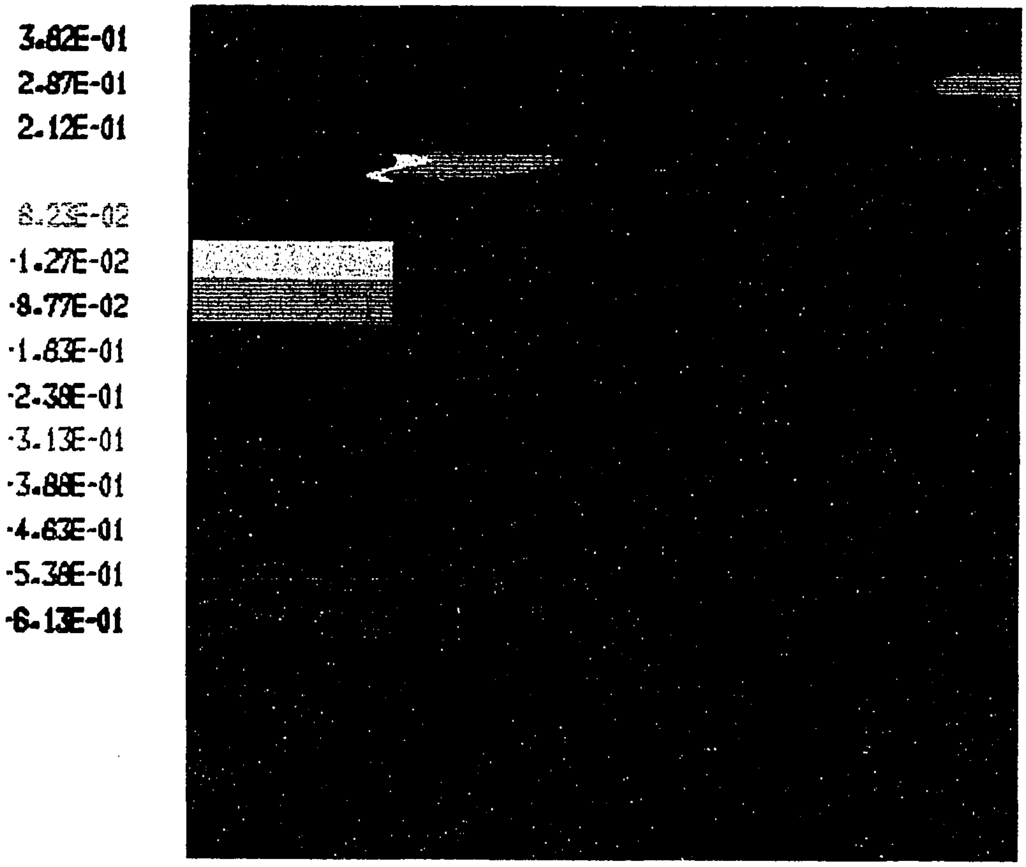

Fig. 5.40 Pressure field for turbulent case with $Gr = 1.4\times10^8$, $Pr = 0.71$, $Ar = 20$ and $Vs^* = 1.0$

coordinates. The present calculation procedure using elliptic equations can capture both trends as shown in Figs. 5.36–5.40. We note here that the boundary layer procedures such as the one used by Akbari and Borger [8] can not predict the inlet and exit pressure values due to vent losses. The vent loss coefficient (or pressure defect constant), K_x, is defined as

$$K_x = \frac{P_x}{\frac{1}{2}\rho_x(u_x)^2} + 1 \tag{5.3}$$

where x indicates location which could be inlet or exit. Figure 5.41 shows the inlet and exit vent loss coefficient (K_i and K_e) as a function of Grashof number. From these results, it is noted that the outlet vent loss is substantially higher than the inlet vent loss. The K_i value decreases slightly while K_e increases slightly as Gr is increased from 1.4×10^3 to 1.4×10^5. It is interesting to note that the total vent loss coefficient $K_T(\equiv K_i + K_e)$ shows a minimum at $Gr = 1.4\times10^4$ for which the mass flow rate also shows a maximum value in Fig. 5.31. The minimum value of K_T equal to 2.20 is within 6 percent of its maximum value of 2.35. It is to be noted that all previous boundary layer analyses have either assumed the values of K_T as zero [8] or have used assumed values of K_T to examine its effect on natural convective flow in a parametric type analysis [11]. Other studies [10–12] for a somewhat different geometry have calculated the value of K_T from the Navier-Stokes type analysis but these analyses do not calculate K_i and K_e separately.

Table 5.2 summarizes the vent loss coefficient at inlet and exit sections of the side-vented cavity for all laminar and turbulence cases considered in the present study. Figure 5.42 shows the variation of total vent loss coefficient K_T as the function of Gr and vent sizes. Unlike the laminar case, the total vent loss coefficient for the turbulent case increases with Gr, without showing a maximum point for either $Vs^* = 0.5$ or 1.0.

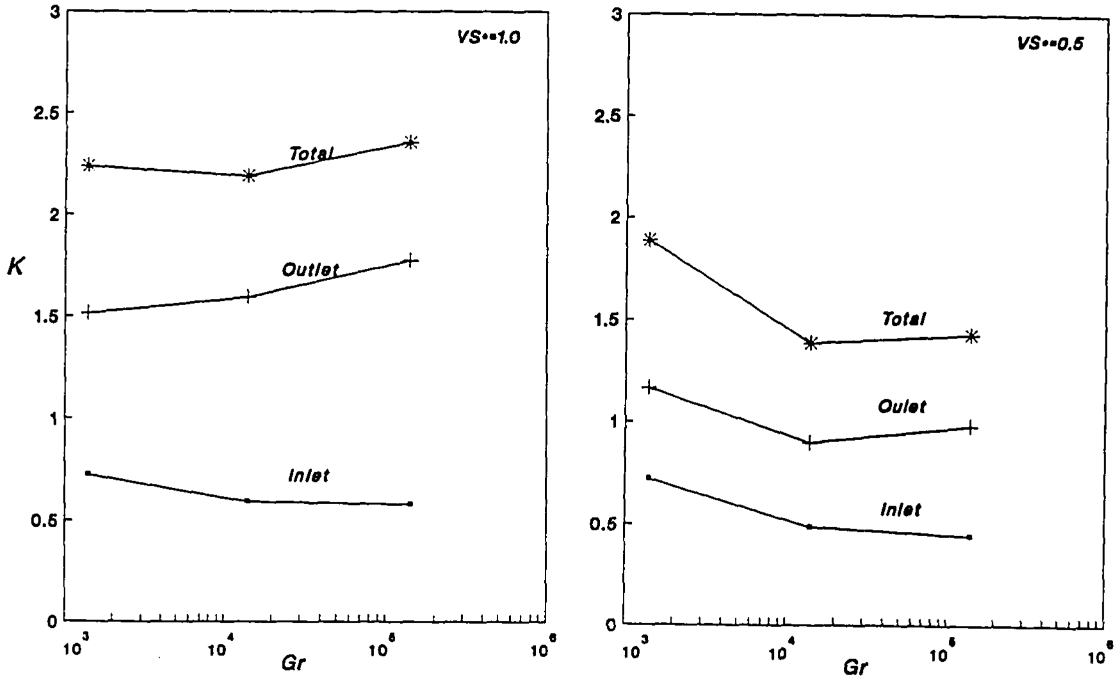

(a)

(b)

Fig. 5.41 Comparison of vent losses constant as the function of Gr and vent sizes. (a) Vs^* = 1.0, (b) Vs^* = 0.5

Table 5.2 Vent loss coefficient at inlet and exit of a side-vented cavity with full and half vent sizes for all cases

Gr/Vs^*	Inlet K_i	Exit K_e	Total K_T
1.4×10^3			
$Vs^* = 1.0$	0.725	1.514	2.239
$Vs^* = 1/2$	0.721	1.166	1.887
1.4×10^4			
$Vs^* = 1.0$	0.595	1.594	2.198
$Vs^* = 1/2$	0.487	0.900	1.387
1.4×10^5			
$Vs^* = 1.0$	0.582	1.774	2.356
$Vs^* = 1/2$	0.444	0.983	1.427
1.0×10^6			
$Vs^* = 1.0$	0.856	1.633	2.489
$Vs^* = 1/2$	0.672	1.244	1.916
1.4×10^7			
$Vs^* = 1.0$	0.982	1.550	2.532
$VS^* = 1/2$	1.395	1.464	2.859
1.4×10^8			
$Vs^* = 1.0$	1.198	1.687	2.885
$Vs^* = 1/2$	0.747	1.177	1.924

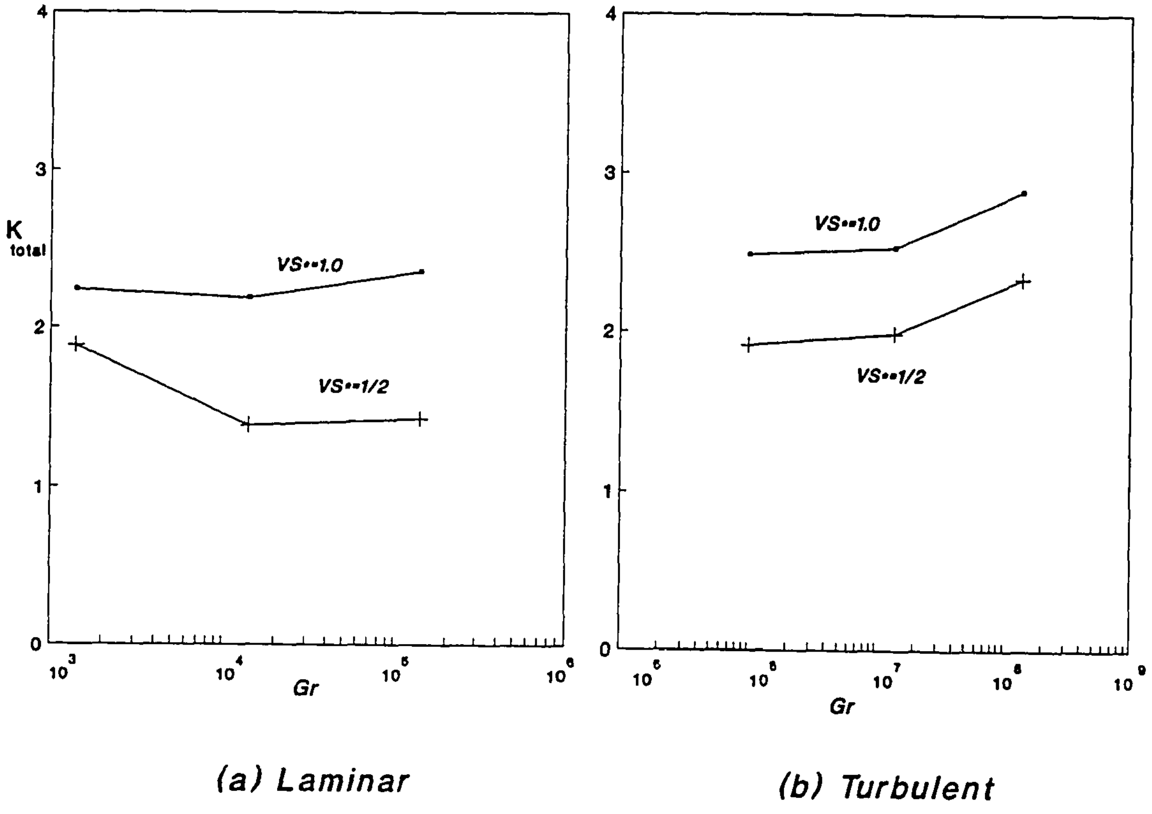

Fig. 5.42 Variation of total vent loss coefficient K as the function of Gr and vent sizes.

5.7 Effect of Cooled Wall Temperature

Two cases, one laminar and one turbulent have been investigated in the present study to examine the effect of cooled wall temperature on the local Nusselt number, mass flow rate and net energy delivery rate. Three different non-dimensional cooled wall temperature, namely $T_c^* = -0.72$, 0.15 and 0.55 have been studied. Figures 5.43 and 5.44 show the comparison of local Nusselt number on cooled wall for three different temperatures for a laminar case of $Gr = 1.4\times10^5$ and a turbulent case of $Gr = 1.0\times10^6$ respectively.

For the case of negative cooled wall temperature, $T_c^* = -0.72$, the secondary recirculating flow occupies almost three quarters of the channel space. As a result, the amount of heat loss to the ambient through cooled wall is substantial. Figures 5.45 and 5.46 show the flow field and temperature field respectively of a typical negative cooled wall temperature case of $T_c^* = -0.72$. Although the average Nusselt number on cooled wall does not clearly illuminate heat transfer phenomenon, the heat flux results indicate this effect quite clearly. As shown in Table 5.3, heat flux increase substantially as cooled wall temperature increases. Results also show that dimensionless mass flow rate has a similar trend as the net energy delivery rate, as the cooled wall temperature increases. Figures 5.47 and 5.48 show this effect of cooled wall temperature on dimensionless mass flow rate and net energy delivery rate respectively.

5.8 Effect of Aspect Ratio

The total average Nusselt number and non-dimensional net energy rate results as the function of Grashof number for a side-vented cavity of aspect ratio of 20 have been shown in Figs. 5.34 and 5.35 respectively. Two typical turbulent cases, $Gr = 1.4\times10^7$ and Gr

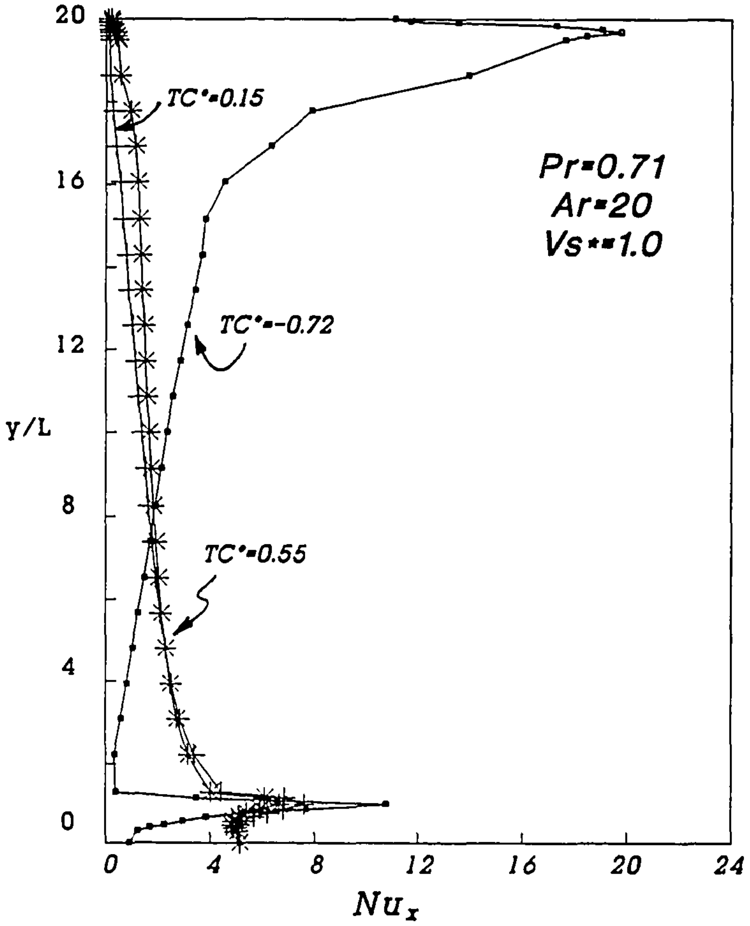

Fig. 5.43 Comparison of local Nusselt number on cooled wall for $Gr = 1.4\times10^5$ (laminar case)

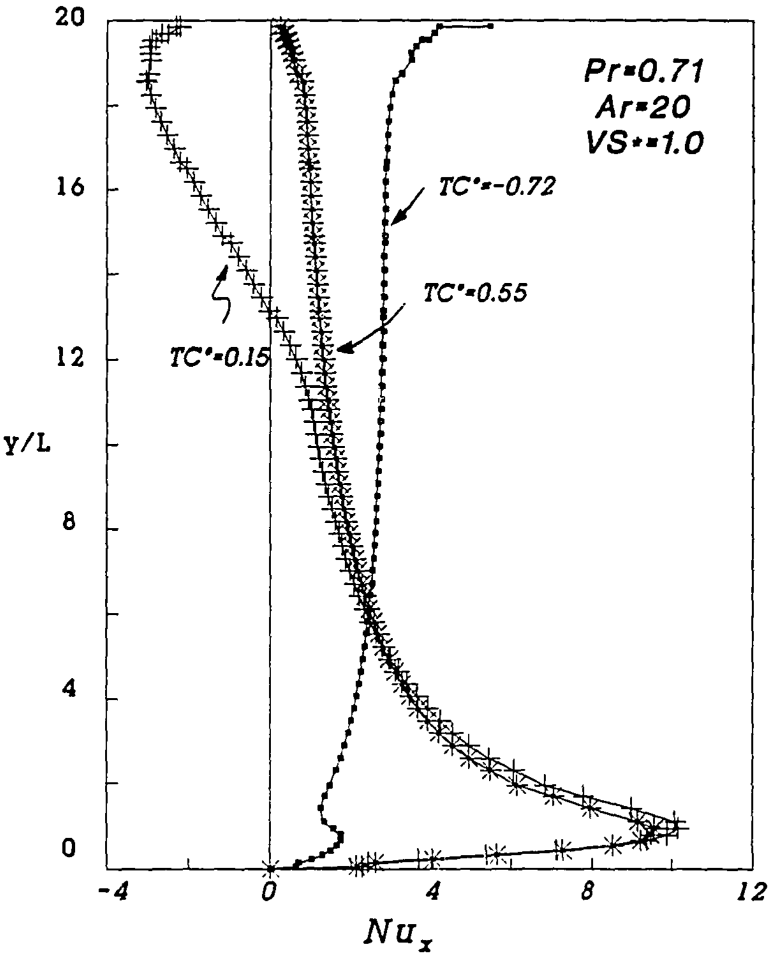

Fig. 5.44 Comparison of local Nusselt number on cooled wall for $Gr = 1.0 \times 10^6$ turbulent case

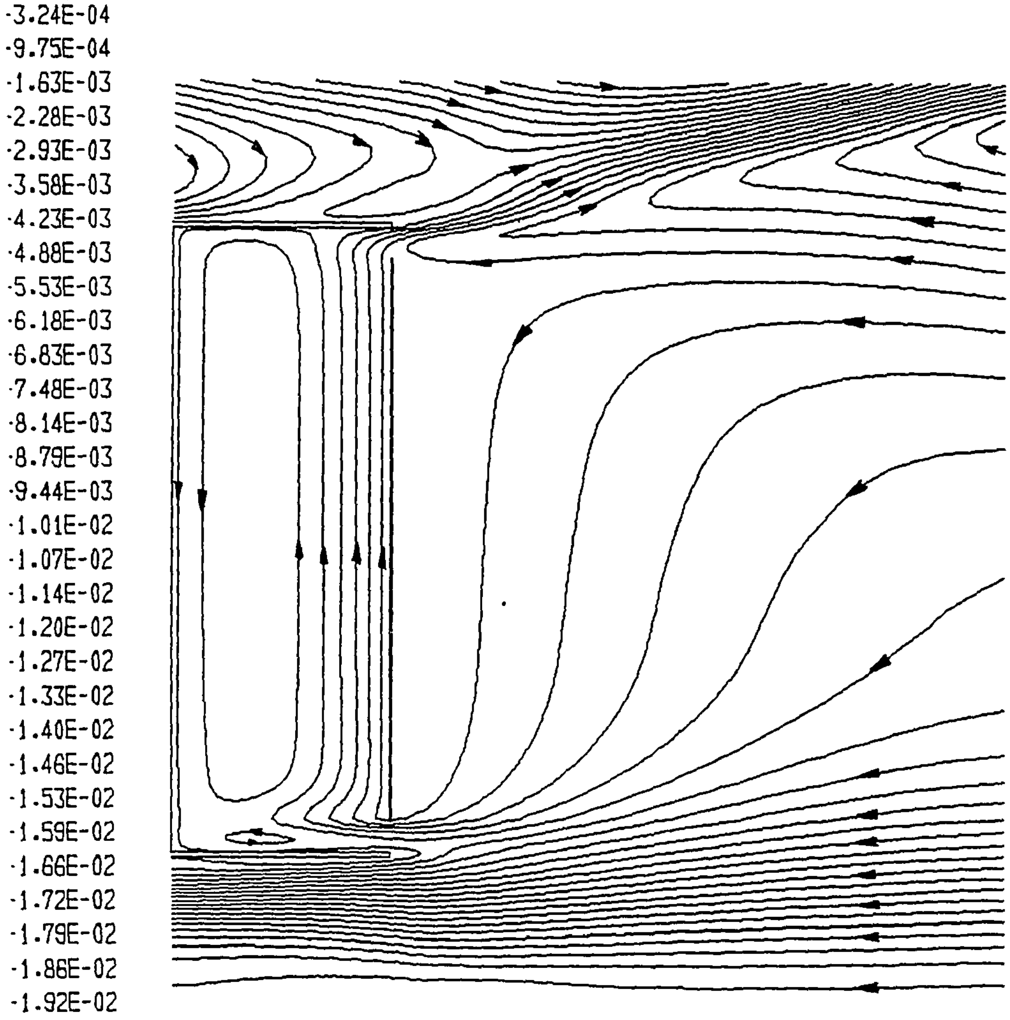

Fig. 5.45 Streamline contours for turbulent case with $Gr = 1.0\times10^6$, $Pr = 0.71$, $T_c^* = -0.72$, $Ar = 20$ and $Vs^* = 1.0$

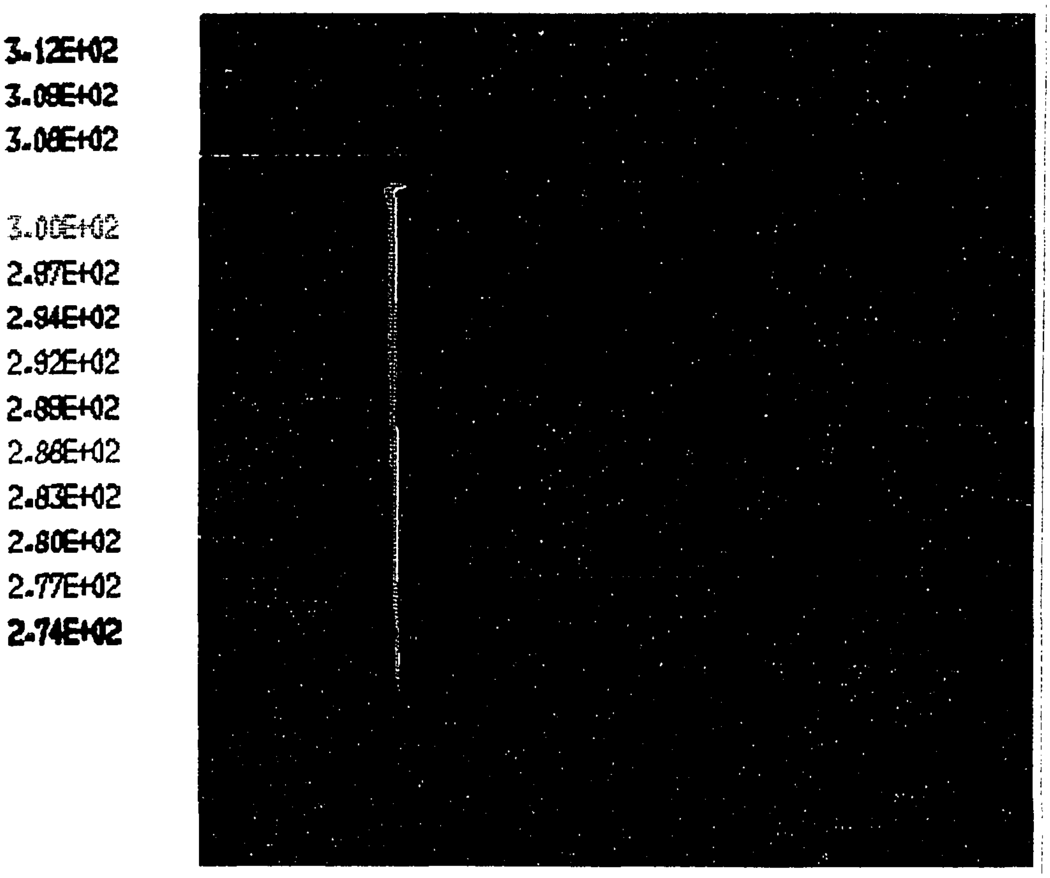

Fig. 5.46 Temperature distribution for turbulent case with $Gr = 1.0\times10^6$, $Pr = 0.71$, $T_c^* = -0.72$, $Ar = 20$ and $V_s^* = 1.0$

Table 5.3 Effect of cooled wall temperature on net energy delivery rate of two cases of vented cavity with $Vs^* = 1.0$

G_r	Area (m^2)		Average Nusselt Number		Heat Flux (W/m^2)		Mass Flow Rate (kg/s)	Mean Fluid Temp. (K)	Net Energy Rate (W)
	Cold	Hot	$\overline{Nu}_c$	$\overline{Nu}_h$	Cold	Hot			
Laminar $G_r=1.4\times10^5$									
$T_c^*=-0.72$	0.6434	0.5791	6.707	5.293	-62.83	108.2	1.554×10^{-3}	285.7	22.229
0.15	0.6434	0.5791	3.830	4.528	6.287	73.76	4.983×10^{-3}	291.3	46.75
0.55	0.6434	0.5791	4.554	4.554	34.90	72.91	6.938×10^{-3}	291.6	64.66
Turbulence $G_r=1.0\times10^6$									
$T_c^*=-0.72$	1.244	1.1196	16.942	15.835	-113.0	139.8	2.782×10^{-3}	290.2	15.948
0.15	1.244	1.1196	12.472	15.035	6.878	122.2	16.88×10^{-3}	296.0	144.7
0.55	1.244	1.1196	16.039	16.080	62.70	127.4	20.99×10^{-3}	292.6	219.9

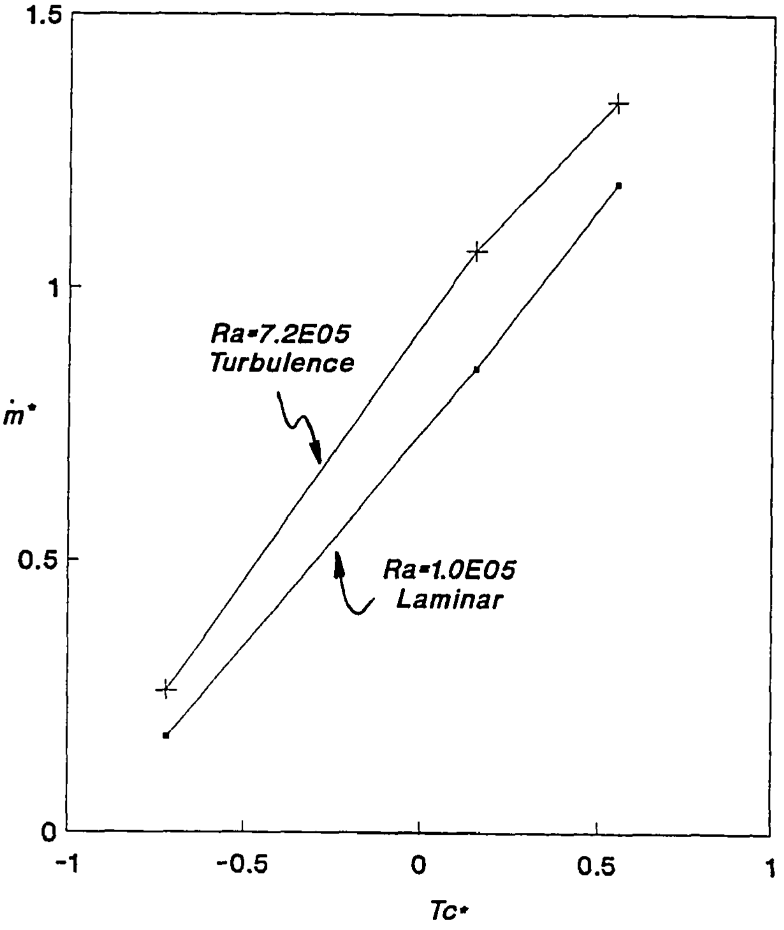

Fig. 5.47 Non-dimensional mass flow rate as function of cooled wall temperature for $Pr = 0.71$, $Ar = 20$, $Vs^* = 1.0$ cases

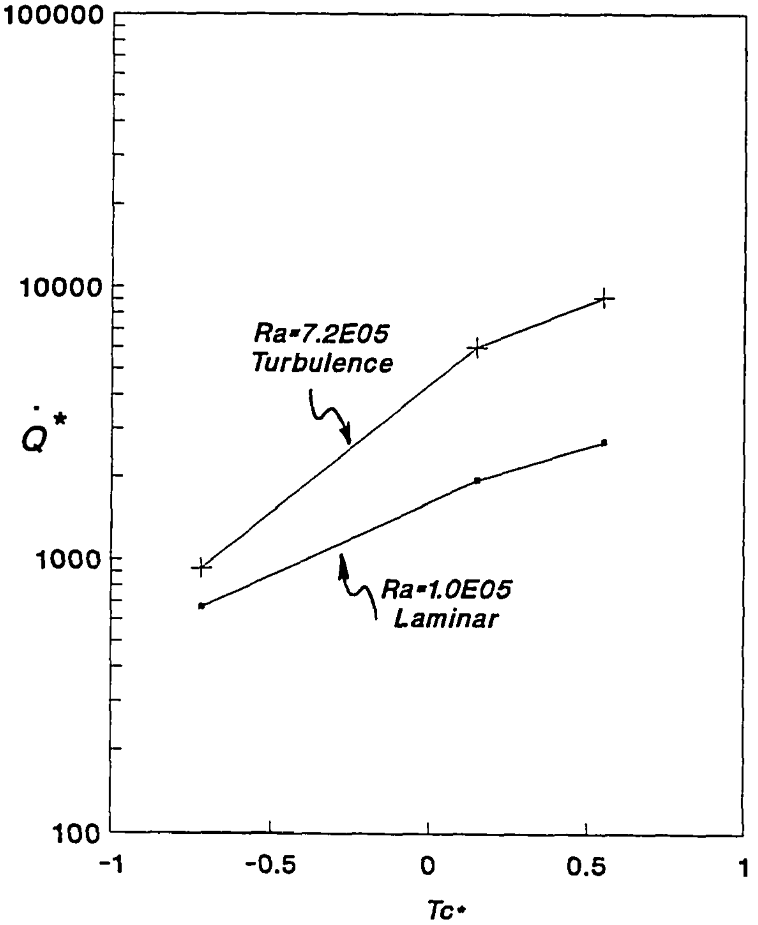

Fig. 5.48 Non-dimensional net energy delivery rate as function of cooled wall temperature for $Pr = 0.71$, $Ar = 20$, $Vs^* = 1.0$ cases

$= 1.4\times10^8$ with aspect ratio of 10 have also been investigated in the present study in order to compare and determine the effect of aspect ratio on the net energy delivery rate.

Figures 5.49 and 5.50 show the streamline contours for a side-vented cavity with Ar, and $Vs^* = 1.0$ and for $Gr = 1.4\times10^7$ and $Gr = 1.4\times10^8$ respectively. These results should be compared with Figs. 5.12 and 5.13 for corresponding cases of aspect ratio of 20. It is noted that in the lower aspect ratio cases, the thermal plume discharged from the channel exit is stronger than those in the higher aspect ratio cases, and in the upper left corner a secondary flow cell is formed for $Ar = 10$ cases.

Temperature distribution of these two cases have been depicted in Figs. 5.51 and 5.52. These figures along with Table 5.4 showed that for higher aspect ratio, buoyancy effect is stronger than that for lower aspect ratio. This trend can be seen not only from the mean fluid temperature on Table 5.4, but it can also be seen from the heat flux and the net energy delivery rate. Although the heat transfer area for $Ar = 20$ case is almost two times as large as in the case of $Ar = 10$, the net energy delivery rate is not linearly proportional to the heat transfer area, and is more than two times. Nusselt number correlations for vent size, $Vs^* = 1.0$ are as follows:

Laminar: $(1.4\times10^3 \leq Gr < 1.4\times10^5)$

$$\overline{Nu} = 0.174(Gr)^{1/4}(Ar)^{-1/9} \tag{5.4}$$

Turbulent: $(1.0\times10^6 \leq Gr \leq 1.4\times10^8)$

$$\overline{Nu} = 0.126(Gr)^{1/3}(Ar)^{-1/9} \tag{5.5}$$

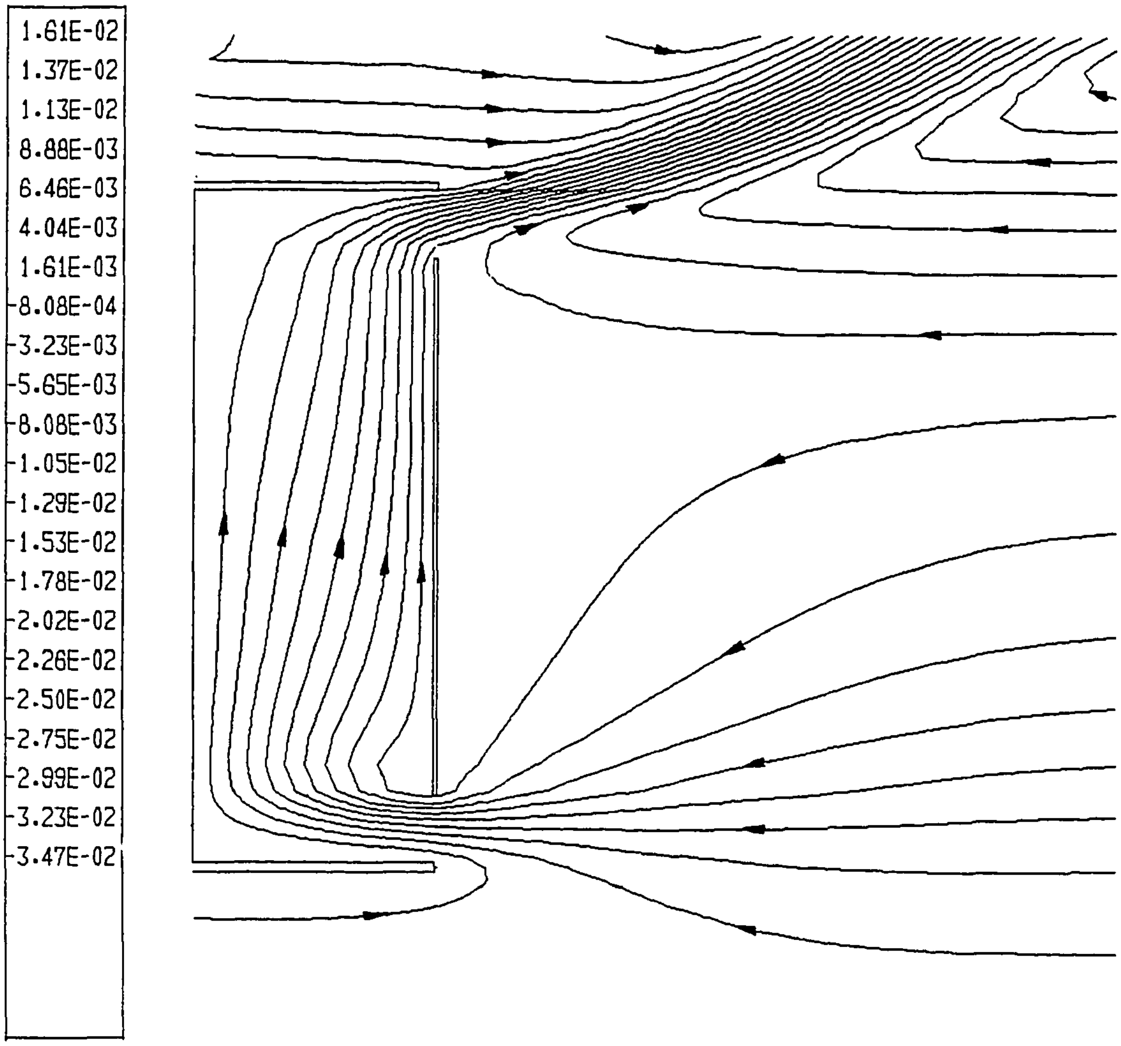

Fig. 5.49 Streamline contours for turbulent case with $Gr = 1.4\times10^7$, $Pr = 0.71$, $Ar = 10$ and $Vs^* = 1.0$

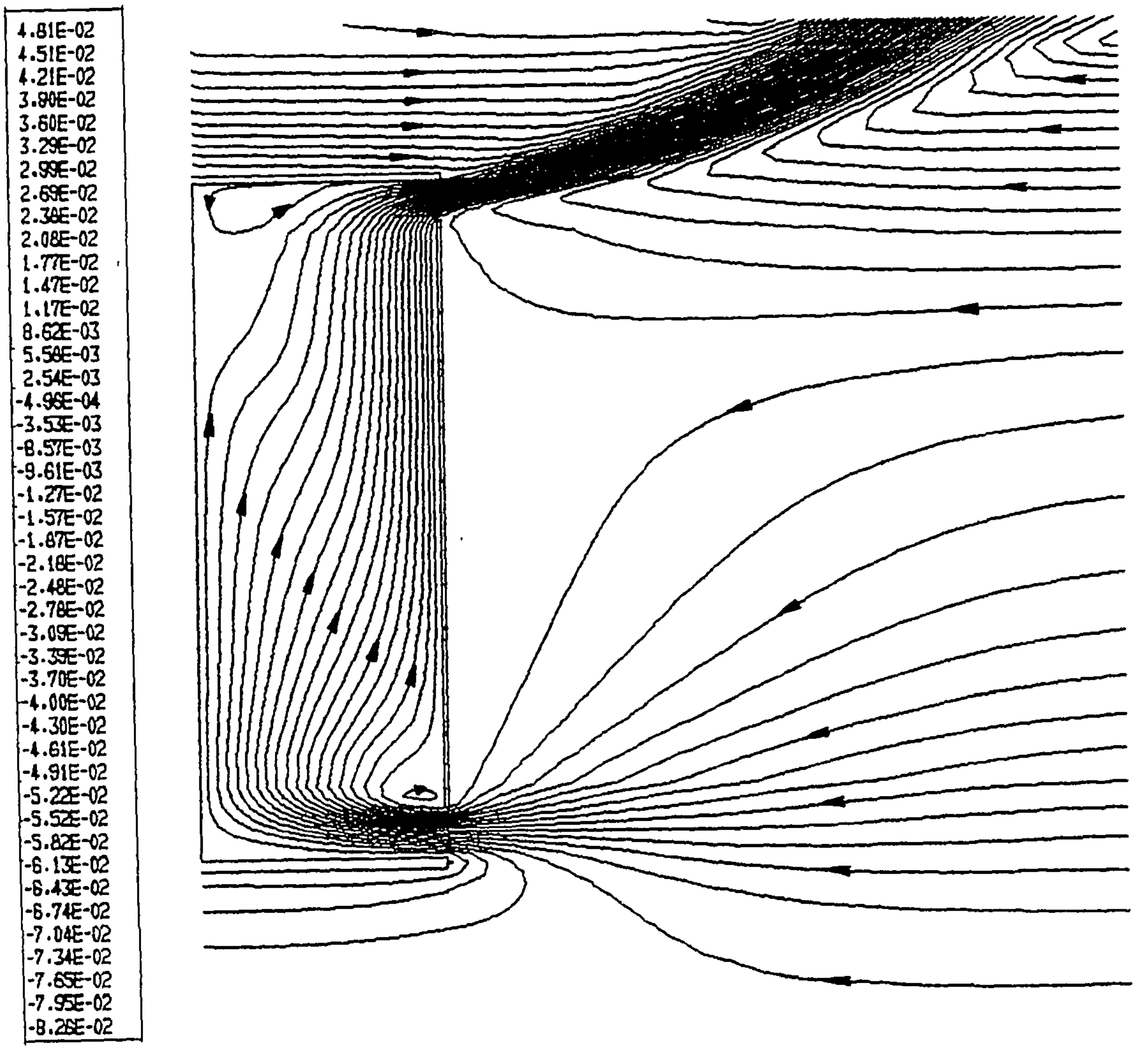

Fig. 5.50 Streamline contours for turbulent case with $Gr = 1.4\times10^8$, $Pr = 0.71$, $Ar = 10$ and $Vs^* = 1.0$

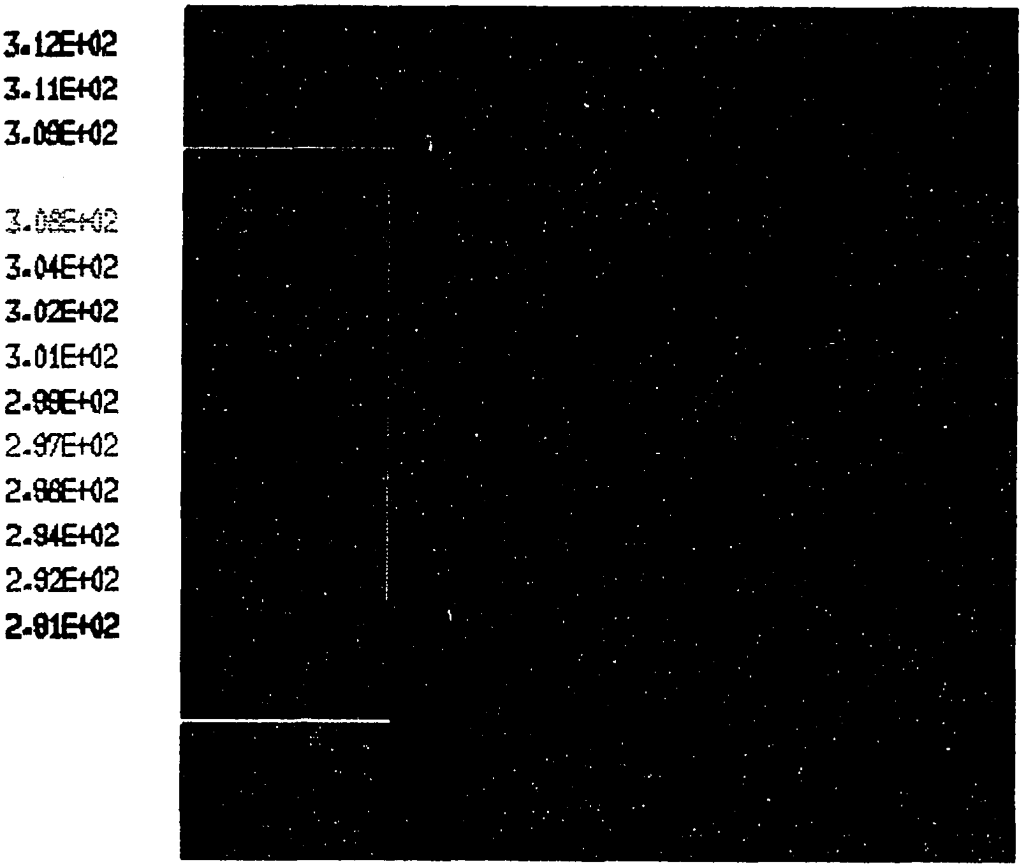

Fig. 5.51 Temperature distribution for turbulent case with *Gr* = 1.4×10^7, *Pr* = 0.71, *Ar* = 10 and *Vs** = 1.0

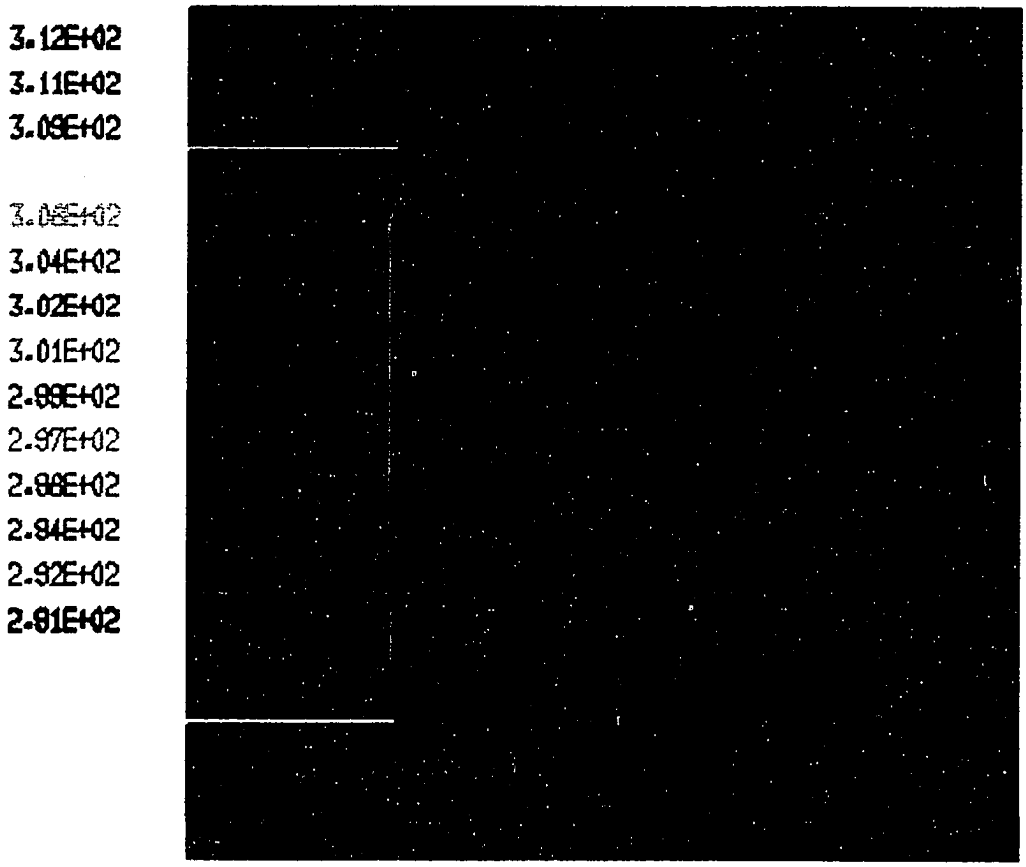

Fig. 5.52 Temperature distribution for turbulent case with $Gr = 1.4\times10^8$, $Pr = 0.71$, $Ar = 10$ and $Vs^* = 1.0$

Table 5.4 Effect of aspect ratio on net energy delivery rate for two typical turbulent cases with $Vs^* = 10$

Grashof Number	Aspect Ratio	Mean Fluid Temp. (K)	Mass Flow Rate (kg/s)×100		Heat Flux (W/m^2)		Area (m^2)		Net Energy (W)
			In	Out	Cold	Hot	Cold	Hot	
1.4×10^7	10	290.7	-2.759	2.81	10.87	112.3	1.4933	1.1946	150.39
	20	290.9	-5.635	5.720	10.79	130.8	2.9866	2.6879	383.80
1.4×10^8	10	290.5	-6.469	6.506	8.778	11.7	3.2172	2.5738	315.73
	20	290.6	-17.06	17.16	14.66	141.2	6.4344	5.7910	912.02

Overall, for side-vented cavities with vent size equal to the channel width, the average Nusselt number for turbulent flow as a function of Gr and Ar in the present study can be correlated in the following form for any aspect ratio of turbulence cases,

$$\overline{Nu} = 0.0920(Ra)^{1/3} \tag{5.6}$$

The above correlation gives higher values than those obtained by Markatos et al. for closed cavity ($\overline{Nu} = 0.060(Ra)^{1/3}$) [17].

5.9 Effect of Vent Size

The effect of vent size on total average Nusselt number in the side-vented cavities is shown in Figure 5.53. The larger the vent size, the higher the heat transfer rate. The total average Nusselt number increases as the dimensionless vent size, Vs^*, increases from 0.25 to 1.0. This trend can be seen in both laminar and turbulent flow regimes.

To conclude the above discussion of all the efforts on the total average Nusselt number, we would like to add the factor of dimensionless vent size to the correlation of the overall average Nusselt number as follow (for all cases of Ar = 20):

$$\overline{Nu} = 0.136(Gr)^{1/3}(Vs^*)^{1/4} \tag{5.7}$$

5.10 Effect of Prandtl Number

Different medium such as water has also been considered in the present study for natural convective flows in a side-vented cavities. The Prandtl number of 6.78 has been used for these cases. Figure 5.54 shows the streamline contours of water flow in a side-vented cavity of Ar = 20, for the turbulent case of Gr = 1.4×10^{10}. The flow moves uniformly and slowly upward along the channel due to its high viscosity. The mass flow

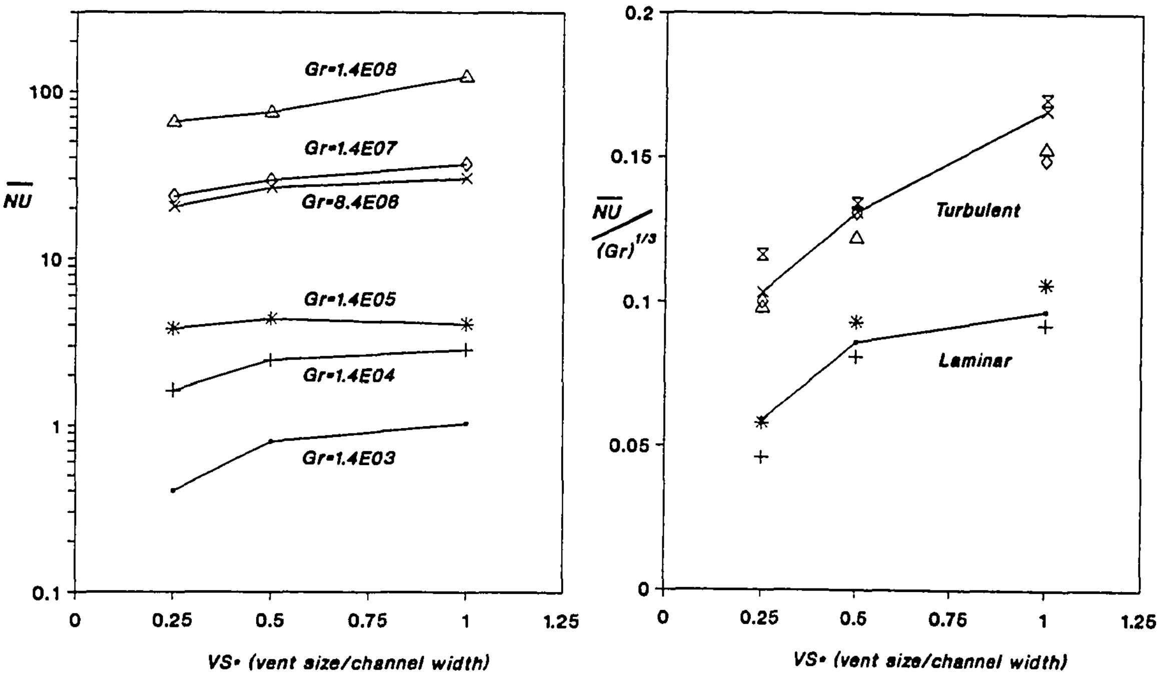

Fig. 5.53 Effect of vent size on total averaged Nusselt number for various Gr with $Pr = 0.71$, $Ar = 20$

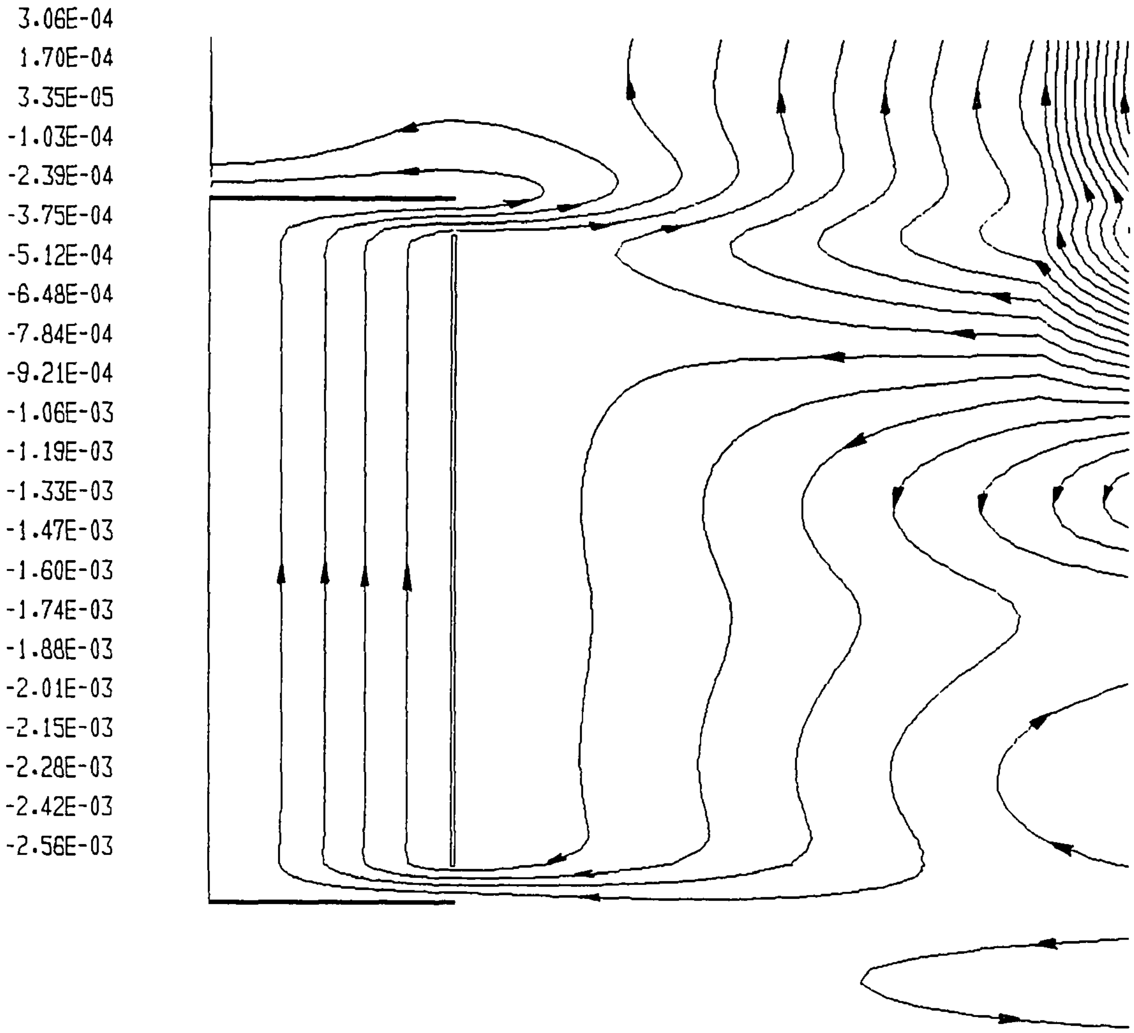

Fig. 5.54 Streamline contours for turbulent case with $Gr = 1.4 \times 10^{10}$, $Pr = 6.78$, $Ar = 20$ and $Vs^* = 1.0$

rate of 4.32×10^{-4} kg/sec for this case of $Gr = 1.4\times10^{10}$, is relatively small compared to the same case of air (1.567×00 kg/sec).

Figure 5.55 shows the comparison of the development of the axial velocity profiles with distance for air and water flow in a side-vented cavity. Both cases have the same Grashof number of 1.4×10^{7} in the turbulent flow regime, and have the same aspect ratio of 20, dimensionless vent size of 1.0 and dimesionless cooled wall temperature of 0.15. Figure 5.56 shows the development of the temperature profiles for the cases described above. These two figures clearly show the influence of Prandtl number for these two fluids. For higher Prandtl number fluid such as water, the velocity boundary layer develops faster towards its fully developed shape than the thermal boundary layer. On the other hand, in the case of air flow, the development of velocity and thermal boundary layer are almost at same order of magnitude.

Table 5.5 shows the comparison of net energy delivery rate in a side-vented cavity for air and water flow for two turbulent cases, namely $Gr = 1.4\times10^{7}$ and 1.4×10^{10}. The buoyancy effect increases as Grashof number increases, and much more heat is discharged to the reservoir via the channel exit. Although, water has higher heat capacity, the mass flow rate is so small that it extracts only a small amount of heat from the heated cavity when compared to the same Grashof number case of air.

5.11 Comparison of Mass Flow Rate Results from Present Study and Other Calculations

To complete the present study of flow in a side-vented cavity, the comparison of mass flow rate obtained in the present study and Akbari and Borger's boundary layer calculation [8,9] is presented here. The only difference between these two studies is that Akbari and Borger's physical model has openings at top and bottom end whereas the present geometry has side vents. The comparison of result of mass flow rate tabulated in

Table 5.5 Comparison of net energy rate in side-vented cavity between air and water in two turbulence cases with $Ar = 20$, $Vs^* = 10$

Grashof Number	Prandtl Number	Mean Fluid Temp (K)	Mass Flow Rate (kg/sec)		Heat Flux (W/m^2)		Area (m^2)		Net Energy (W)
			In	Out	Cold	Hot	Cold	Hot	
1.4×10^{7}	0.71(Air)	290.7	-5.635×10^{-2}	$5..720\times10^{-2}$	10.79	130.8	2.9866	2.6879	383.803
	6.78 (Water)	292.5	-4.757×10^{-7}	4.755×10^{-7}	4079	-3457	0.0031	0.00279	0.348
1.4×10^{10}	0.71(Air)	*	*	*	*	*	*	*	*
	6.78(Water)	292.8	-4.319×10^{-4}	4.323×10^{-4}	426.2	-345.1	0.031	0.0279	4.880

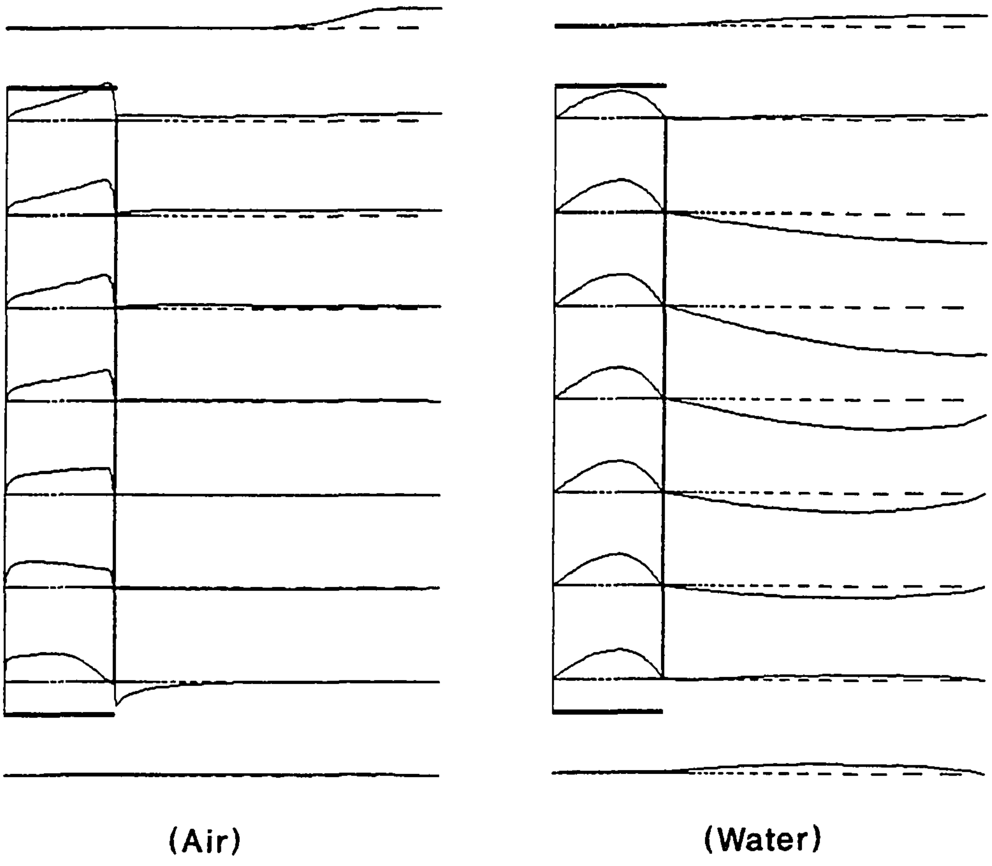

Fig. 5.55 Comparison of the development of axial velocity profiles with distance between air and water at $Gr = 1.4\times10^7$, $T_c^* = 0.15$ $Pr = 6.78$, $Ar = 20$ and $Vs^* = 1.0$

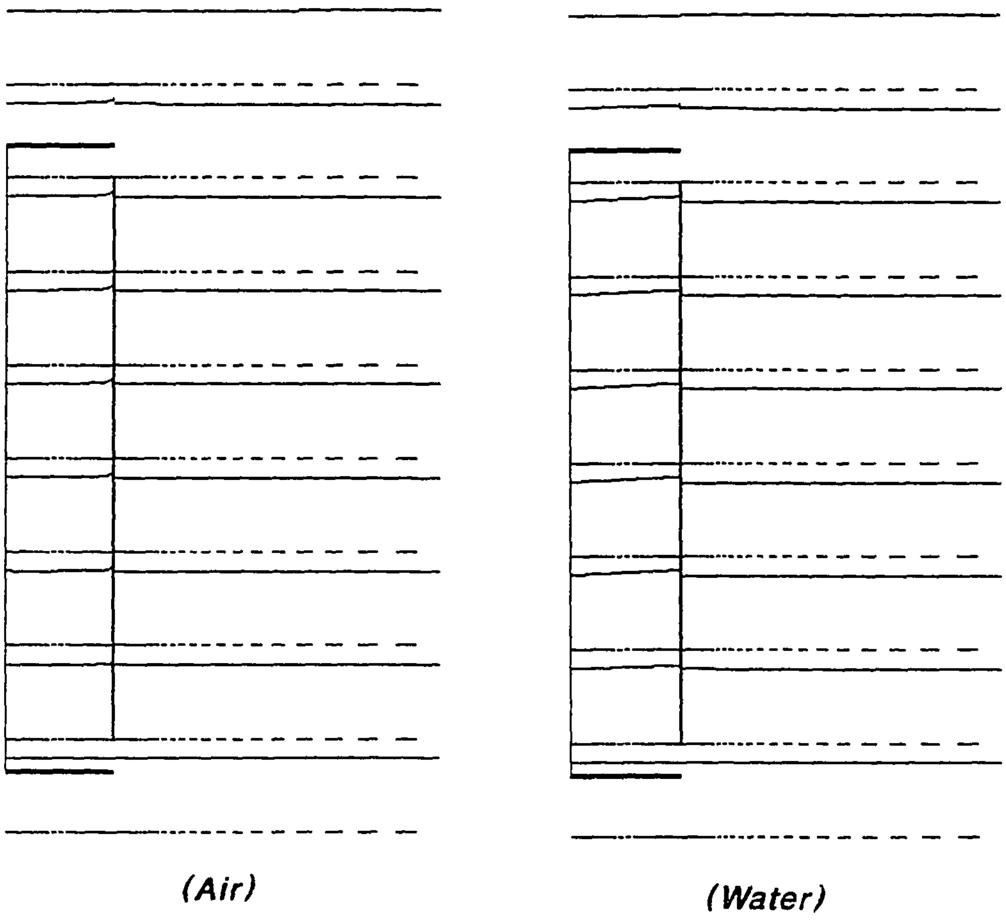

Fig. 5.56 Comparison of the development of temperature profiles with distance between air and water at $Gr = 1.4\times10^7$, $T_c^* = 0.15$ $Pr = 6.78$, $Ar = 20$ and $Vs^* = 1.0$

Table 5.6 shows that Akbari and Borger's correlations overestimate the values of mass flow rate by about 25% in the laminar regime, and underestimates the values of mass flow rate by about 30% in the turbulent flow regime. We note here that good match between the two results is not to be expected due to two major differences in the two models. The Akbari and Borger's model does not take into account the inlet and exit bent losses, and it is based on boundary layer analysis. The present study, on the other hand, takes into account the inlet and exit vent losses by using an elliptic procedure.

Table 5.6 Comparison of mass flow rate between present study and Akbari's calculation

Gr	Channel Width (m)	Channel Height (m)	Mass Flow Rate (Akbari's Cal.) (kg/sec)	Mass FlowRate (Present Study) (kg/sec)
Laminar				
Gr=1.4×10^3	0.006932	0.13864	6.96×10^{-4}	5.55×10^{-4}
1.4×10^3	0.014933	0.29866	2.28×10^{-3}	2.00×10^{-3}
1.4×10^5	0.032172	0.64344	6.31×10^{-3}	4.98×10^{-3}
Turbulent				
1.0×10^6	0.0622	1.244	1.36×10^{-2}	1.68×10^{-2}
1.4×10^7	0.14933	2.9866	3.83×10^{-2}	5.68×10^{-2}
1.4×10^8	0.32172	6.4344	1.18×10^{-1}	1.71×10^{-1}

Chapter 6

RESULTS FOR TROMBE WALL CHANNEL COUPLED TO THE ROOM

6.1 Introduction

In this chapter, results are presented for a more realistic Trombe wall geometry, simulating a 4m×4m×1m passive solar house, with a 3.8m×0.5m storage block placed at a distance of 0.1m (channel width) to the right of the glazing wall. Both heating and cooling (or ventilation) modes are investigated in this study. In the heating mode, the system forms a closed thermo-syphon loop, with room air circulating clockwise through the Trombe wall channel by the action of buoyancy force inside the channel. In the cooling mode, two vents are provided for fresh air circulation. One of them is located at the top section of the Trombe wall channel with its size being exactly equal to the channel width of 0.1 m. The second vent with 0.5m opening is located on the farthest vertical wall of the room. The main objective is to draw fresh air from outside to cool the conditioned space. The storage block essentially acts as a heater that creates a strong chimney effect by generating a low pressure region inside the Trombe wall channel. This allows cooler air to come in from the ambient through the room vent and the heated air to be discharged through the channel exit vent.

6.2 Heating Mode

6.2.1 Physical Model

A schematic of the Trombe wall configuration, simulating a passive solar house, is shown in Fig. 6.1. The left surface of the room is a clear glass wall which allows solar

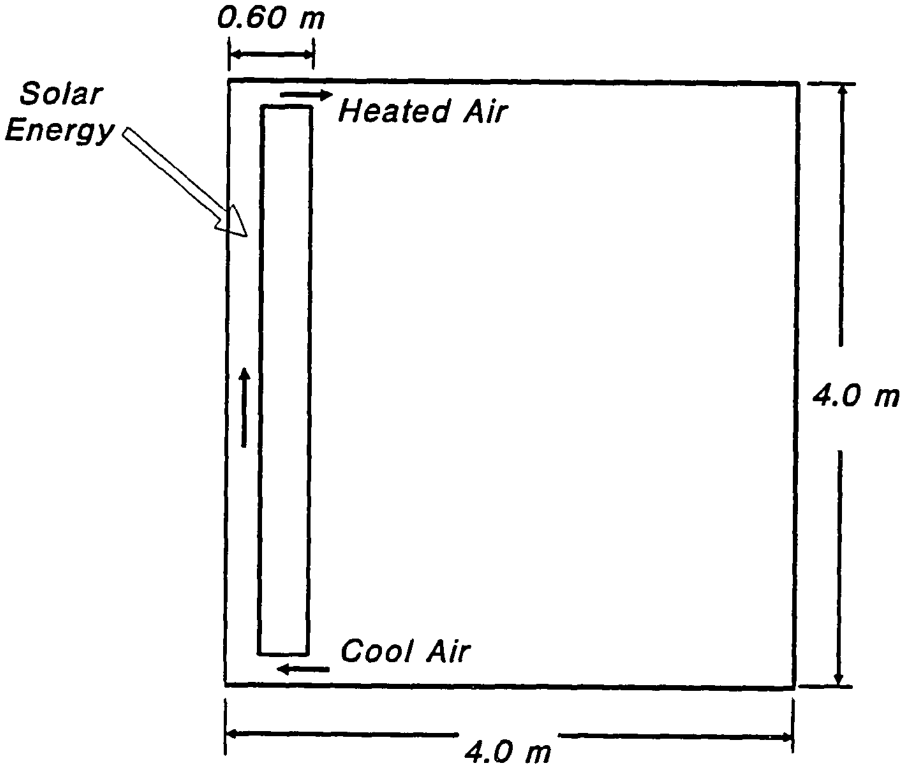

Fig. 6.1 Schematic of the Trombe wall channel coupled to the room operating in heating mode

radiation to enter the room and heat up the black painted storage wall. The energy then irradiates to the opposite wall and also diffuses to air in the channel formed by two differentially heated walls. Collected energy is then carried by the buoyancy driven flow to the room.

The characteristics times for heat conduction in the wall are typical 100 to 1000 times larger than the characteristics times for natural convection in the channel. Consequently, as the wall temperature condition changes due to changing solar radiation and ambient conditions, the natural convection in the channel adjusts quickly to these changes and as a result in can be analyzed as a quasi-steady process. The wall in the meantime also undergoes changes, albeit at a much slower pace. In the present analysis, the emphasis is on the energy transfer through the natural convective loop. As a result, the conductive heat transfer through the wall is not considered. However, it is important to note that the conductive heat transfer analysis provides a thermal boundary conditions at the solid-fluid interface. In absence of such analysis here, we have assumed certain plausible boundary conditions at the solid-fluid interfaces. The temperature of the walls in the conditioned space are maintained at 300 K, and the storage block surface facing the room side is set at a constant value of 300 K. The temperature of heated wall has been set at 320 K, and the temperature of cooled wall is varied from 270 K to 300 K in the present study, to investigate the effect of cooled wall temperature on the net energy rate delivered to the room.

6.2.2 Grid Independence of Results

In the present study, a numerical grid with 111×61 grid points has been used for all the cases, simulating the Trombe wall coupled to the room. The effect of grid size on the local heat transfer coefficient in the channel was also examined by using a finer grid with

151×91 grid points. The results obtained from this grid are compared with the standard 111×61 grid. Figure 6.2 shows the comparison of local heat transfer obtained from two calculations using different grid. It is noted that with the exception of slight deviation in the entrance region, results from the two cases are almost identical to one another. This indicates that the results presented here with the 111×61 grid are essentially grid independent.

6.2.3 Flow Field

Four different cooled wall temperatures have been investigated in the heating mode case, namely 270 K, 280 K, 290 K and 300 K. The heated wall temperature is kept fixed at 320 K for these four cases. The principal objective is to investigate the effect of cooled wall temperature on the mass flow rate induced through the channel.

Figures 6.3 to 6.6 show the streamline contours of air flow in the Trombe wall channel coupled to the room for cooled wall temperature values of 270 K, 280 K, 290 K and 300 K respectively. In these cases, the heated air emerges from the channel and flows close to the walls of the conditioned room and returns back to the channel, thus competing the thermo-syphon loop. For the lowest cooled wall temperature case, a minuscule amount of heated air is discharged to the room. As a result of weak natural convection in the channel, the natural convection in the room also very weak.

Figure 6.7 shows the streamline contours inside the Trombe wall channel for the case of 270 K cooled wall temperature. At this low temperature, there is a large recirculating flow pattern inside the channel as seen from an enlarged view of the channel presented in Fig. 6.7. The heat loss to the cooled side wall of the channel is high and this indicates a negative buoyancy force on the cooled wall. This causes the fluid to sink near the cooled wall, thus leading to the recirculating flow pattern. As cooled wall temperature

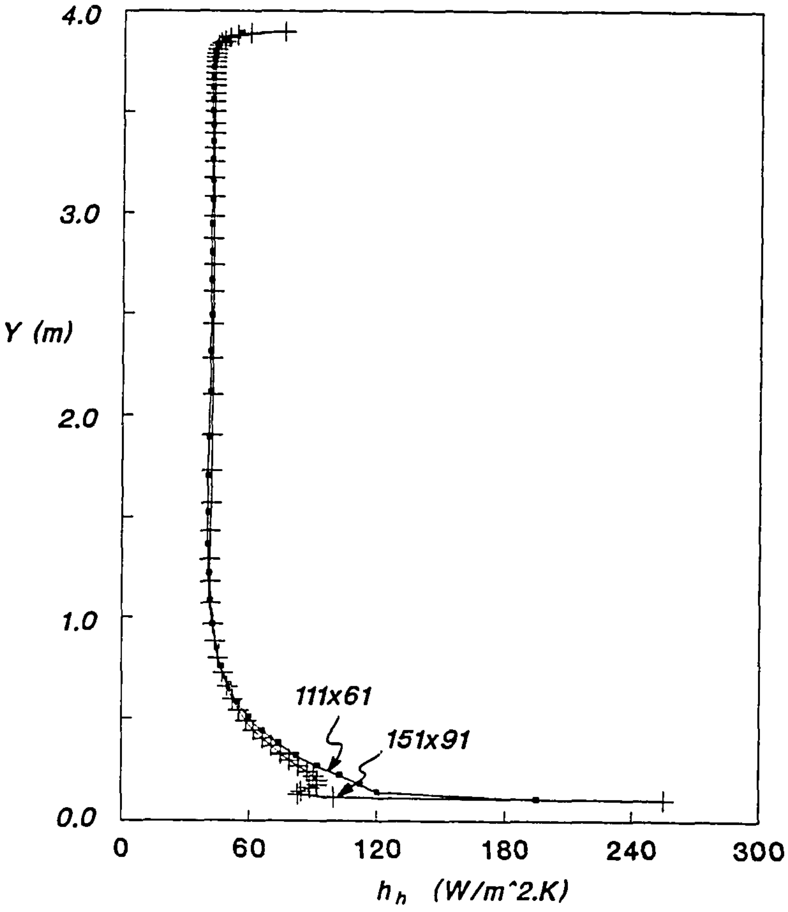

Fig. 6.2 Comparison of local heat transfer coefficient on heated wall between two calculations with different grid points

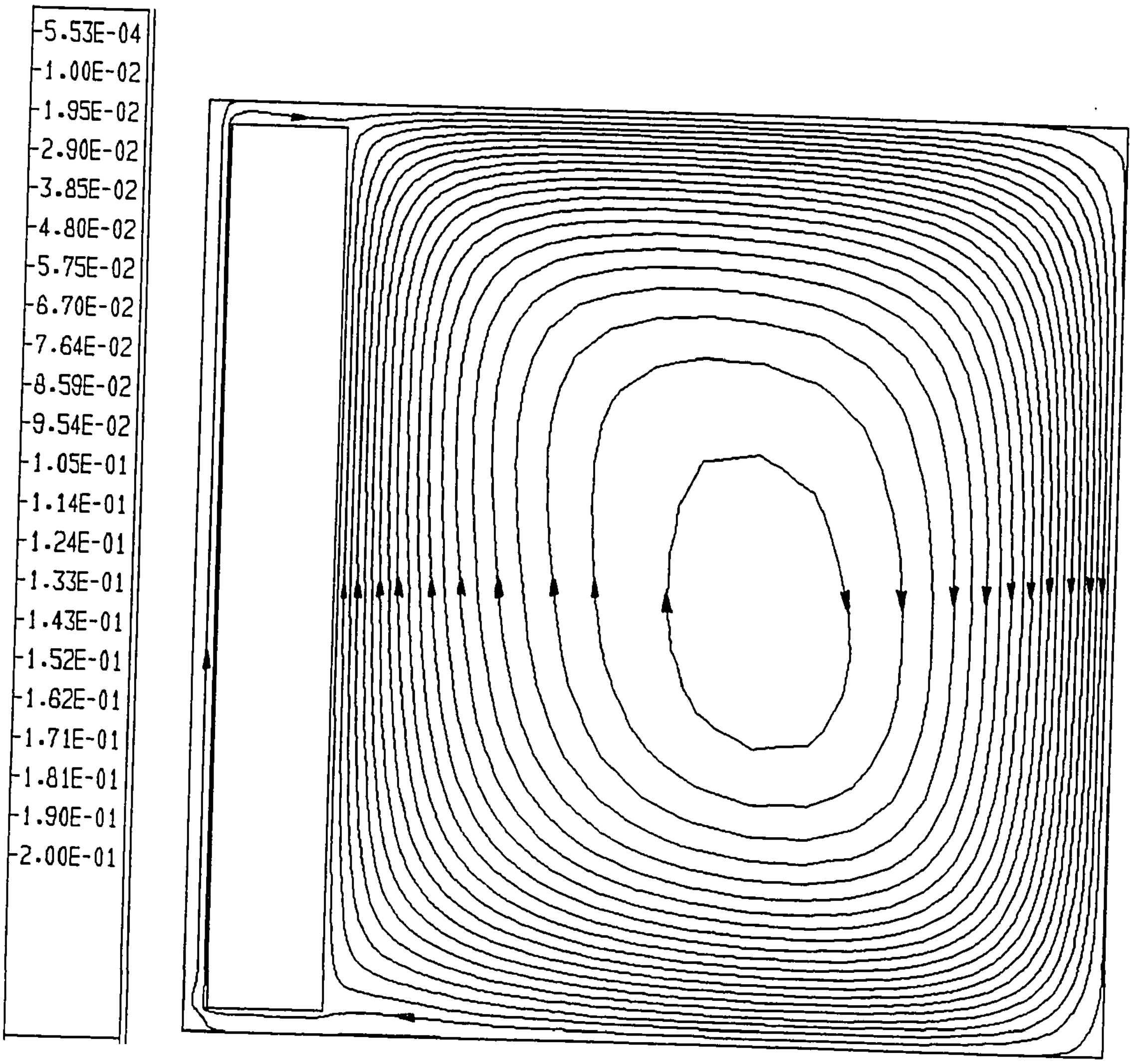

Fig. 6.3 Streamline contours for air flow in a Trombe wall channel coupled to the room at T_c = 270 K

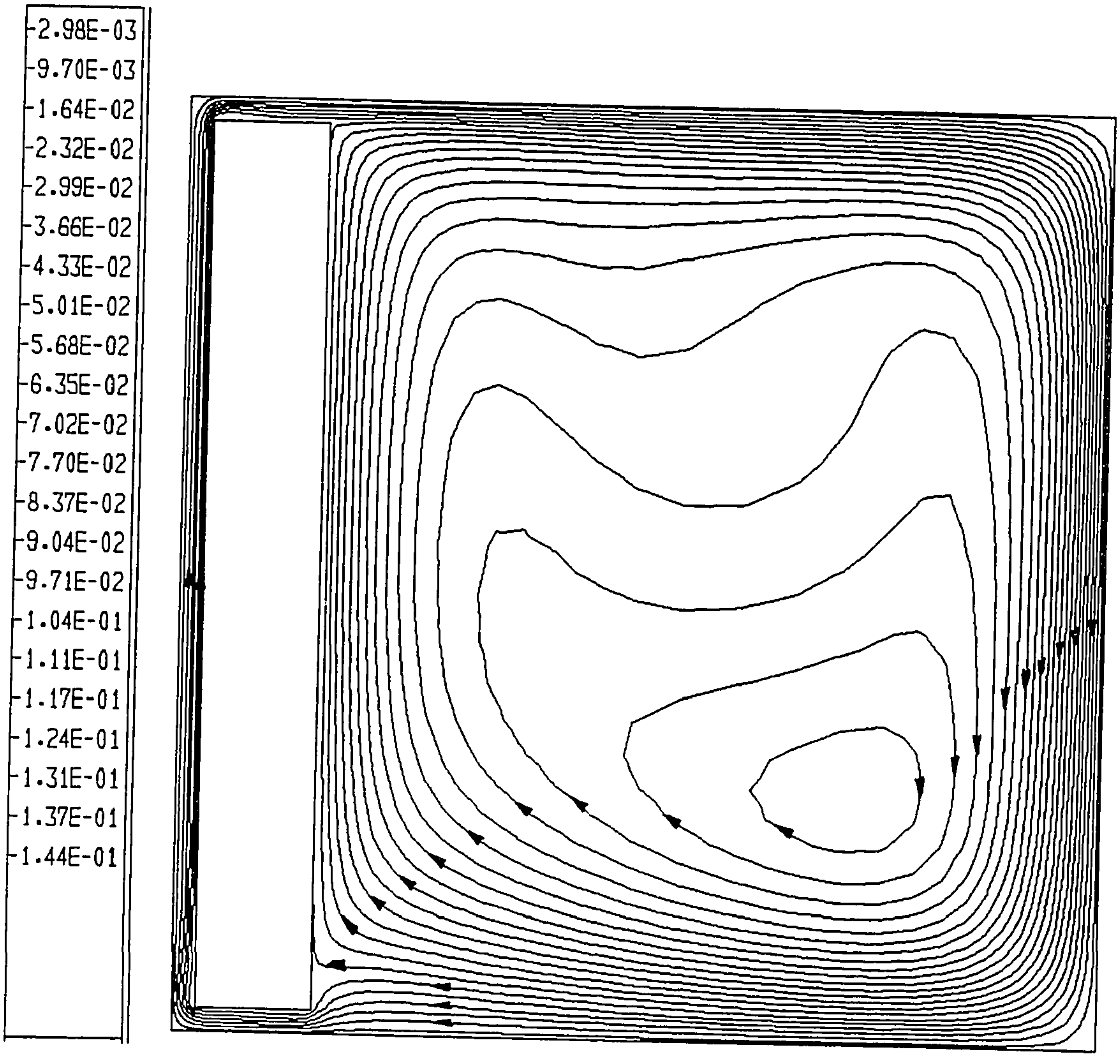

Fig. 6.4 Streamline contours for air flow in a Trombe wall channel coupled to the room at T_c = 280 K

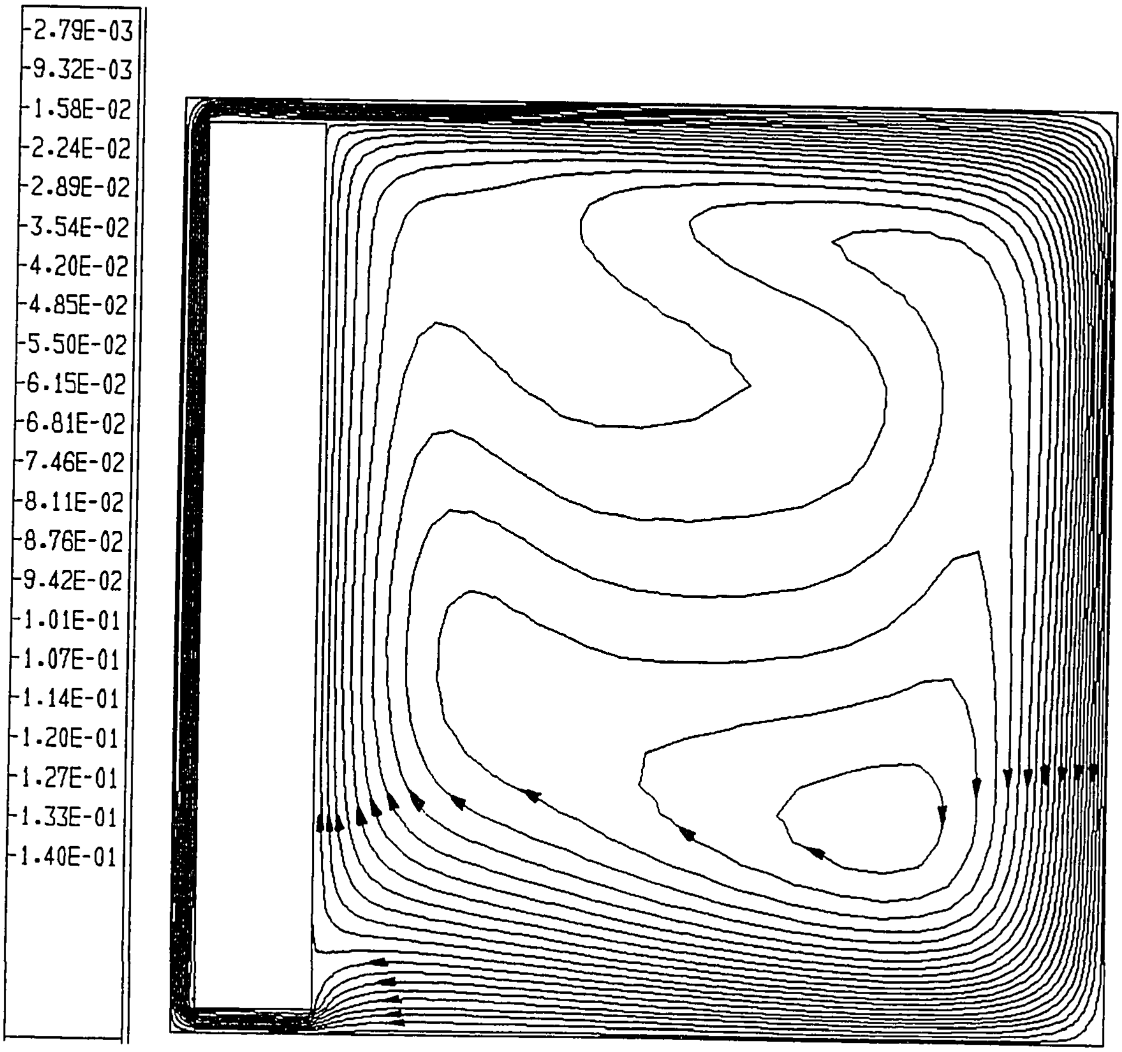

Fig. 6.5 Streamline contours for air flow in a Trombe wall channel coupled to the room at T_c = 290 K

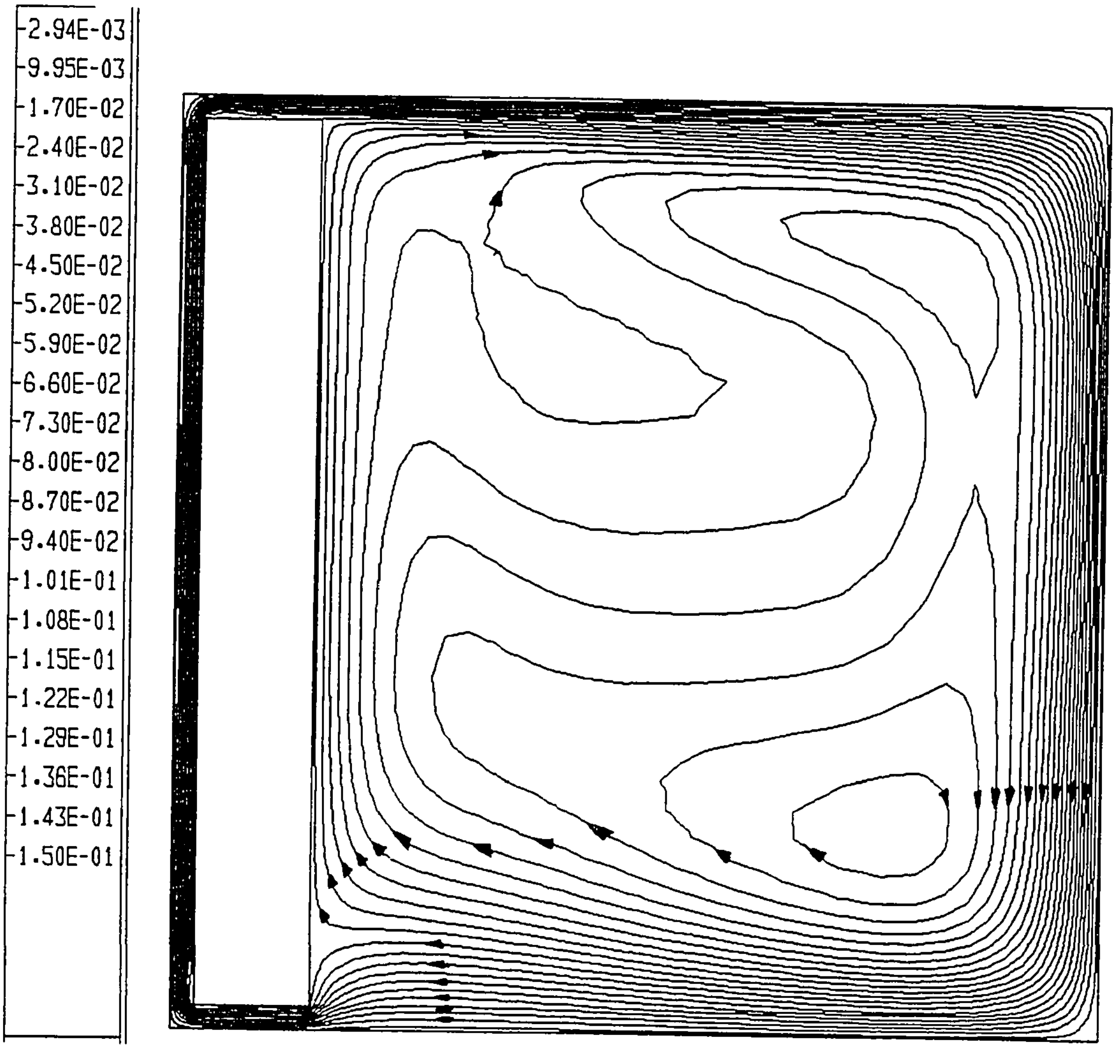

Fig. 6.6 Streamline contours for air flow in a Trombe wall channel coupled to the room at T_c = 300 K

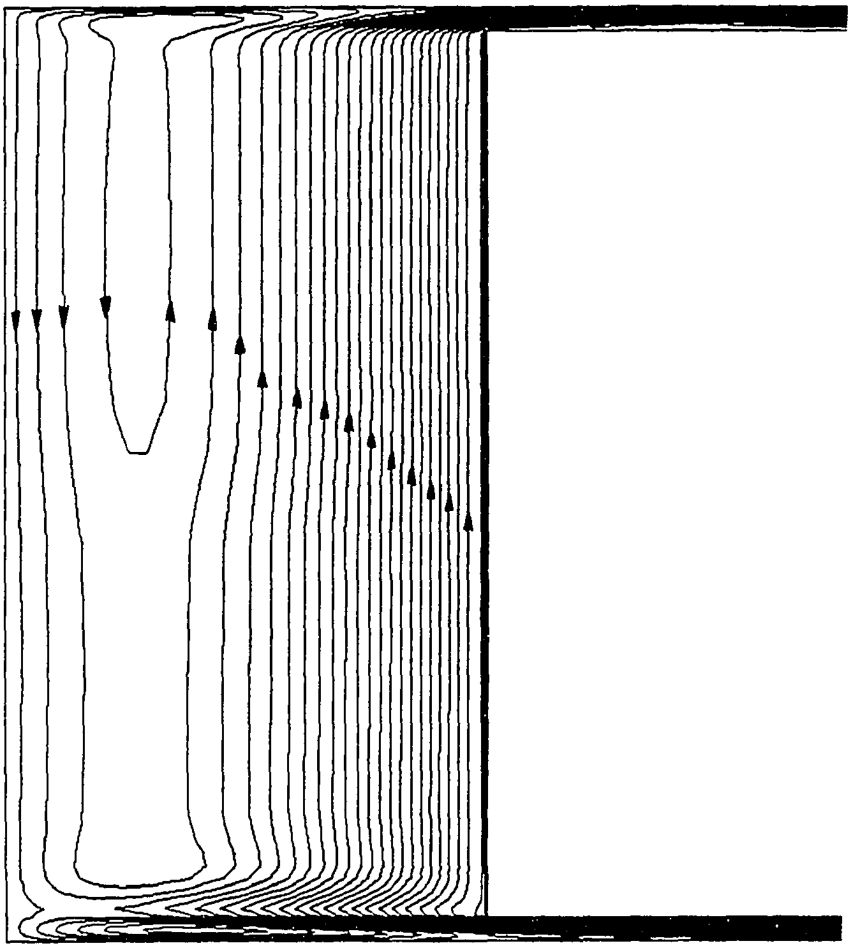

Fig. 6.7 Streamline contours inside the Trombe wall channel of the 270 K cooled wall temperature case

increases, the amount of air delivered to the room increases, the amount of air delivered to the room increases significantly. This results in shifting of the center of the room vortical motion from the room center to a location closer to the right lower corner. At higher cooled wall temperature multi-cellular flow patterns appear.

6.2.4 Temperature Distribution

Figures 6.8–6.11 show the temperature distribution in the Trombe wall channel coupled to the room in the heating mode for cooled wall temperature ranging from 270 K to 300 K respectively. The stratification of the temperature field in the room has been observed in all cases of cooled wall temperature higher than 280 K. The thermal stratification is most pronounced for the 300 K cooled wall temperature case. It is to be noted that although thermal stratification occurs naturally, it is undesirable since it causes cooler temperatures in the occupied space as compared to relatively warmer temperature in regions closer to the ceiling.

6.2.5 Mass Flow and Energy Delivery Rate Results

Table 6.1 shows the comparison of air flow and energy delivery rates to the room for different cooled wall temperatures. The mean air temperature in the room, the mass flow rate and the net energy rate delivered to the room all increase with the increasing cooled wall temperature. For example, the mean air temperature in the room increases from 291.5 K to 295.7 K. The net energy delivery rate increases even more dramatically from 25.5 W to 518.9 W, when cooled wall temperature is increased from 270 K to 300 K. It is to be noted that the response time for temperature changes in the room resulting from wall temperature changes have been estimated to be less than 30 minutes. As a result, the quasi-steady equations have been used to analyze these cases.

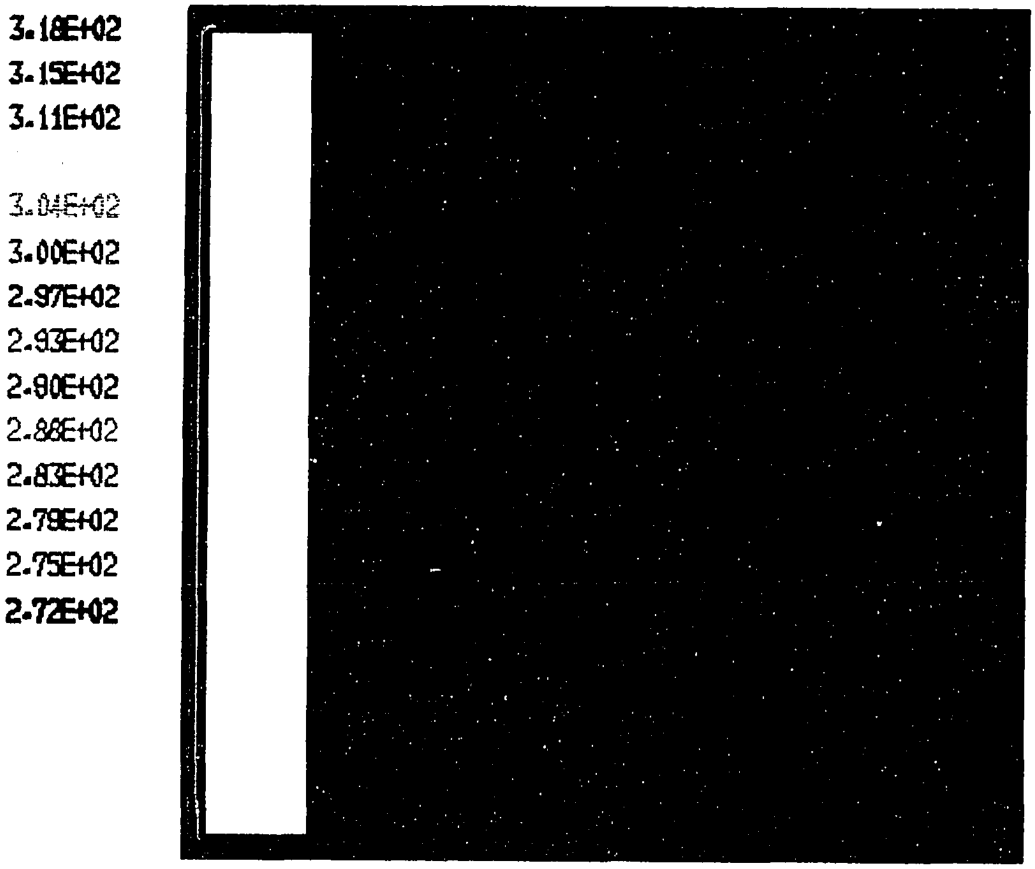

Fig. 6.8 Temperature distribution for air flow in a Trombe wall channel coupled to the room at T_c = 270 K

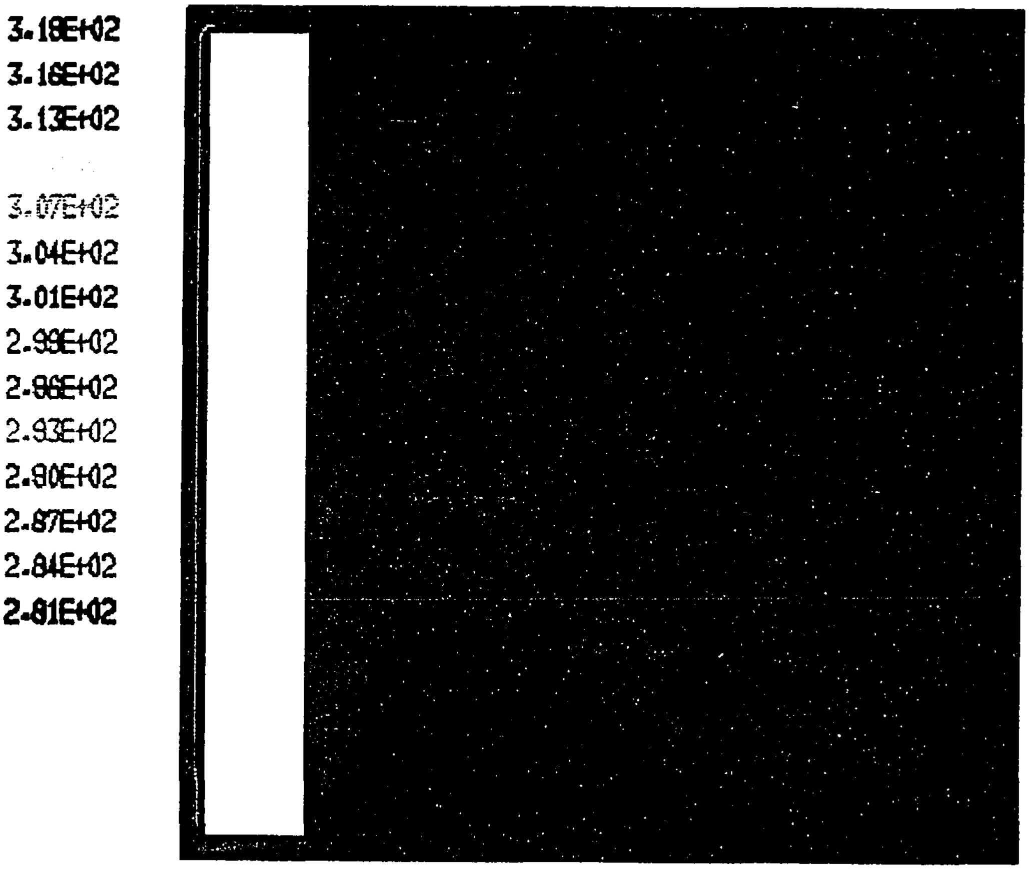

Fig. 6.9 Temperature distribution for air flow in a Trombe wall channel coupled to the room at T_c = 280 K

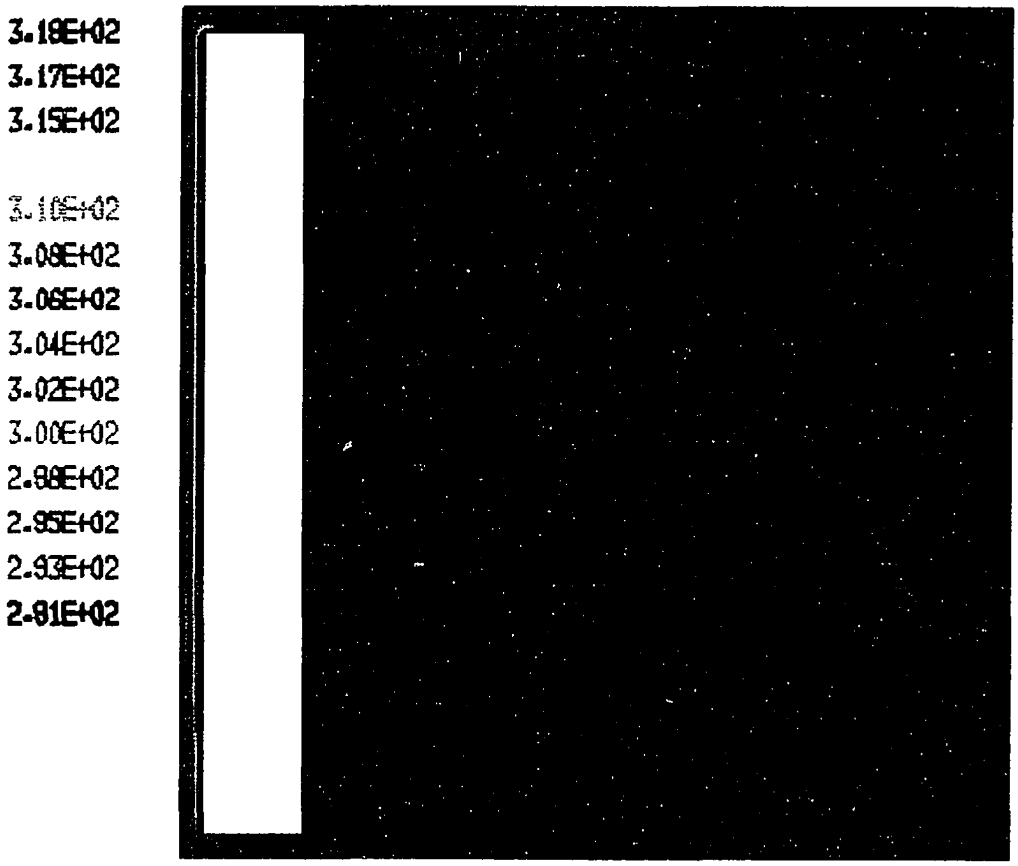

Fig. 6.10 Temperature distribution for air flow in a Trombe wall channel coupled to the room at T_c = 290 K

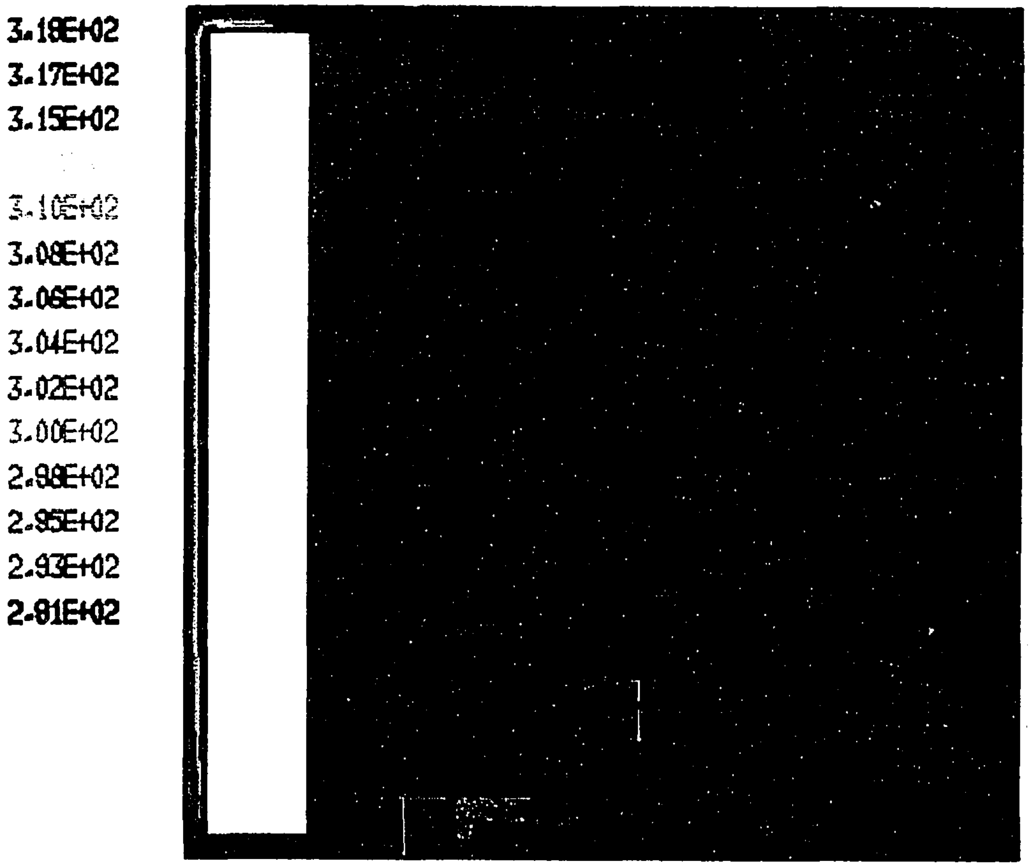

Fig. 6.11 Temperature distribution for air flow in a Trombe wall channel coupled to the room at T_c = 300 K

Table 6.1 Comparison of total energy rate delivered to the room (Heating) among different cooled wall temperatures

Cooled Wall Temp. (K)	Area (m^2)		Mass Flow Rate (kg/sec)		Heat Flux (W/m^2)		Overall Mean Fluid Temp	Net Energy
	Cold	Hot	In	Out	Cold	Hot	(K)	(W)
270	4.0	3.8	-1.685×10^{-2}	1.703×10^{-2}	-2103	2176	291.5	25.5
280	4.0	3.8	-5.317×10^{-2}	5.227×10^{-2}	-1467	1657	292.7	143.0
290	4.0	3.8	-7.416×10^{-2}	7.435×10^{-2}	-906.1	1227	294.2	313.4
300	4.0	3.8	-9.025×10^{-2}	9.076×10^{-2}	-409.2	895.2	295.7	518.9

Figures 6.12 and 6.13 show the comparison of local heat transfer coefficients for four different cooled wall temperature cases on heated and cooled walls respectively. In Fig. 6.12, the average heat transfer coefficient on heated wall decreases from about 75 W/m^2K to about 35 W/m^2K as cooled wall temperature increases from 270 K to 300 K. Meanwhile, the temperature difference between the heated wall and mean fluid (as indicated in Table 6.1) decreases from about 28.5 K to 24.3 K, as the cooled wall temperature increases from 270 K to 300 K. This result indicates that the heat transfer rate from heated wall to the air flow for the lower cooled wall temperature case is higher than for the higher cooled wall temperature case. Similar trend has been observed on the cooled wall, when cooled wall temperature increases from 270 K to 290 K. The difference between average inlet temperature and average exit temperature increases from –0.34 K to 12.34 K, indicating significantly that no heat loss to the ambient.

6.2.6 Calculation of Pressure Losses

The pressure losses at inlet and exit section of the Trombe wall channel coupled to the room case occur in a manner similar to side-vented cavity case, except that there are additional frictional losses due to the horizontal segments. The friction of the lower horizontal segment causes the static pressure at inlet to be higher than that of the dynamic pressure at the channel entrance location, thus, negative pressure loss coefficients are shown in Table 6.2 at the inlet section for all different cooled wall temperature cases due to more frictional loss to the entrance section of the channel. This trend is exactly opposite to the side-vented cavity case. However, the pressure losses at exit section are all positive, has the same trend as the side-vented cavity case, except the value of K at exit is not decreasing regularly as the cooled wall temperature increases. Figures 6.14–6.17 show the pressure distribution for all four cases. For lower cooled wall temperature cases of 270 K and 280 K, the pressure fields on the room side are uniformly distributed

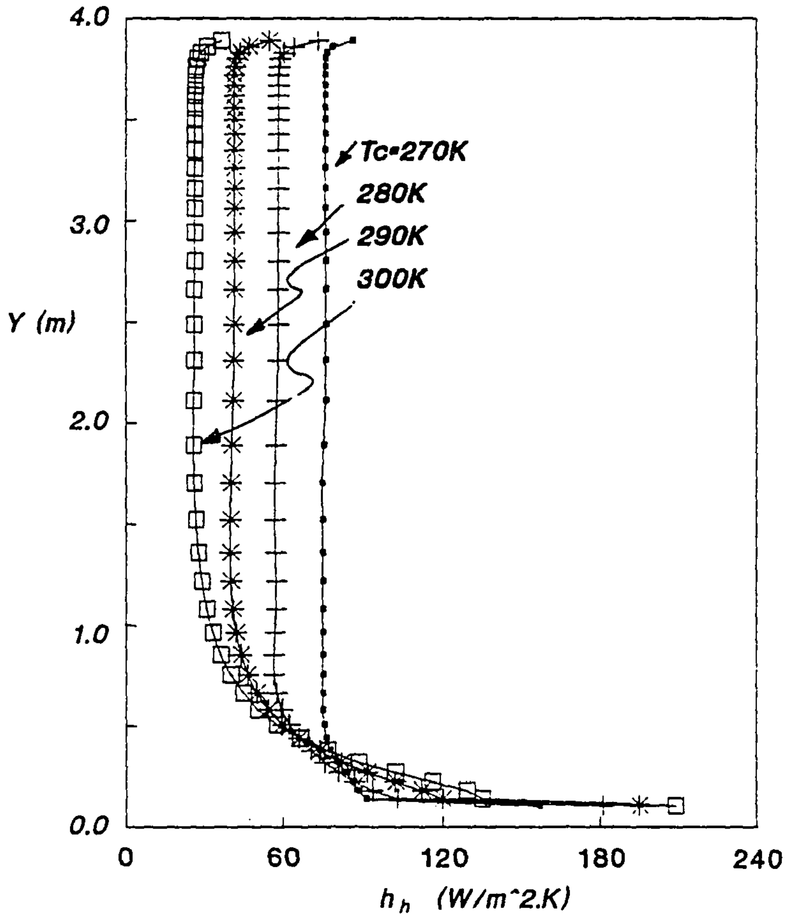

Fig. 6.12 Comparison of local heat transfer coefficient on heated wall for four cooled wall temperatures

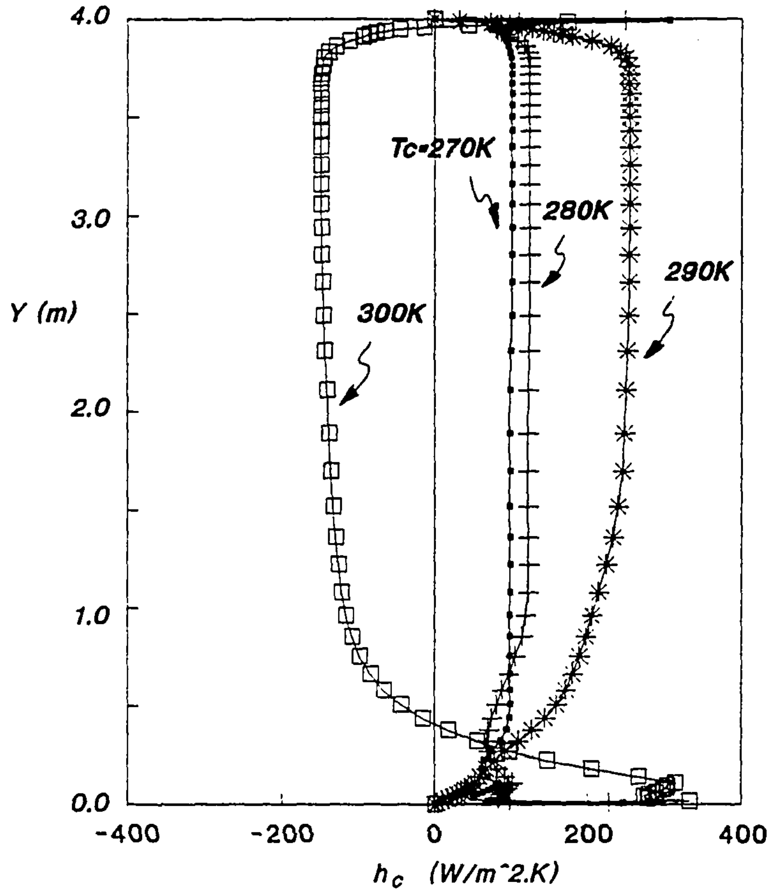

Fig. 6.13 Comparison of local heat transfer coefficient on cooled wall for four cooled wall temperatures

Table 6.2 Pressure losses at the horizontal inlet and exit of the Trombe wall channel operating in heating mode

Cooled Wall Temp. (K)	Density (kg/m^3)		Averaged Velocity (m/sec)×10		Static Pressure (Pa)×10		Dynamic Pressure (Pa)×10		Pressure Loss Constant	
	In	Out	In	Out	In	Out	In	Out	In	Out
270	1.207	1.207	-1.40	1.46	0.258	36.50	0.118	0.128	-3.197	286.29
280	1.212	1.180	-4.38	4.52	-0.838	21.37	1.162	1.204	-0.279	18.744
290	1.210	1.162	-6.12	6.51	-2.101	7.990	2.263	2.464	-0.072	4.242
300	1.210	1.150	-7.45	8.09	-3.318	-4.372	3.389	3.760	-0.012	2.163

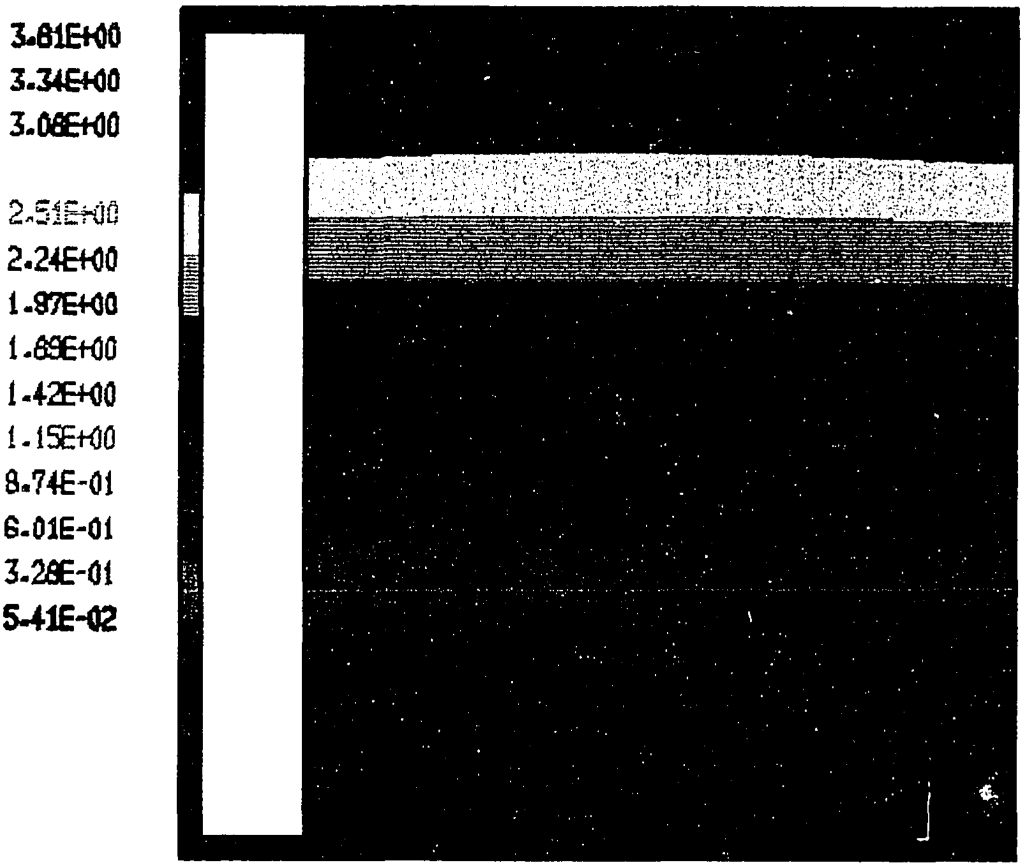

Fig. 6.14 Pressure field for air flow in a Trombe wall channel coupled to the room in the heating mode with T_c = 270 K

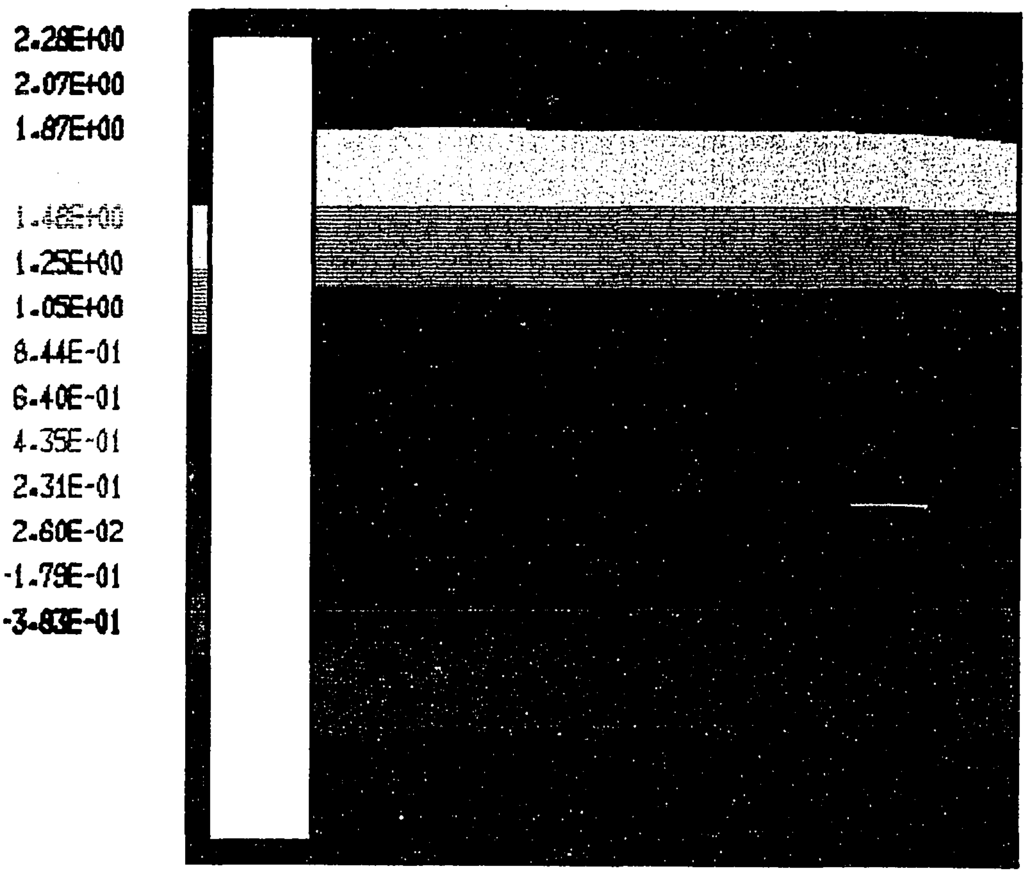

Fig. 6.15 Pressure field for air flow in a Trombe wall channel coupled to the room in the heating mode with T_c = 280 K

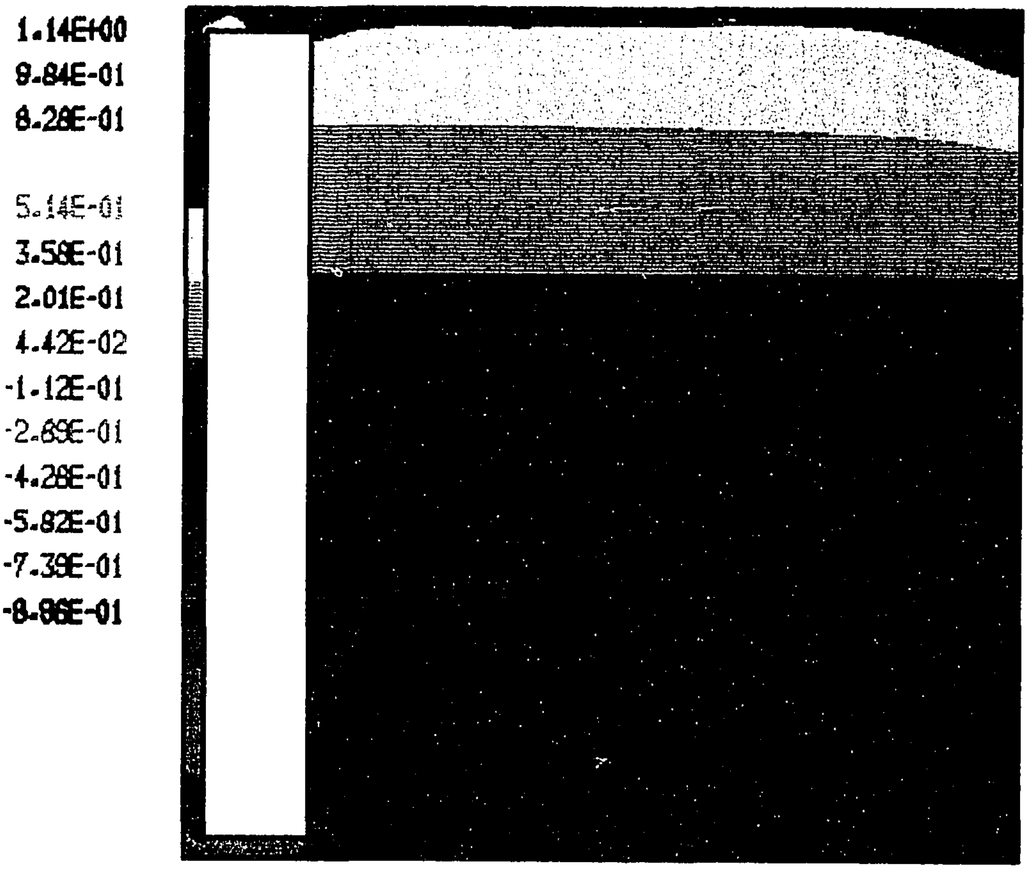

Fig. 6.16 Pressure field for air flow in a Trombe wall channel coupled to the room in the heating mode with T_c = 290 K

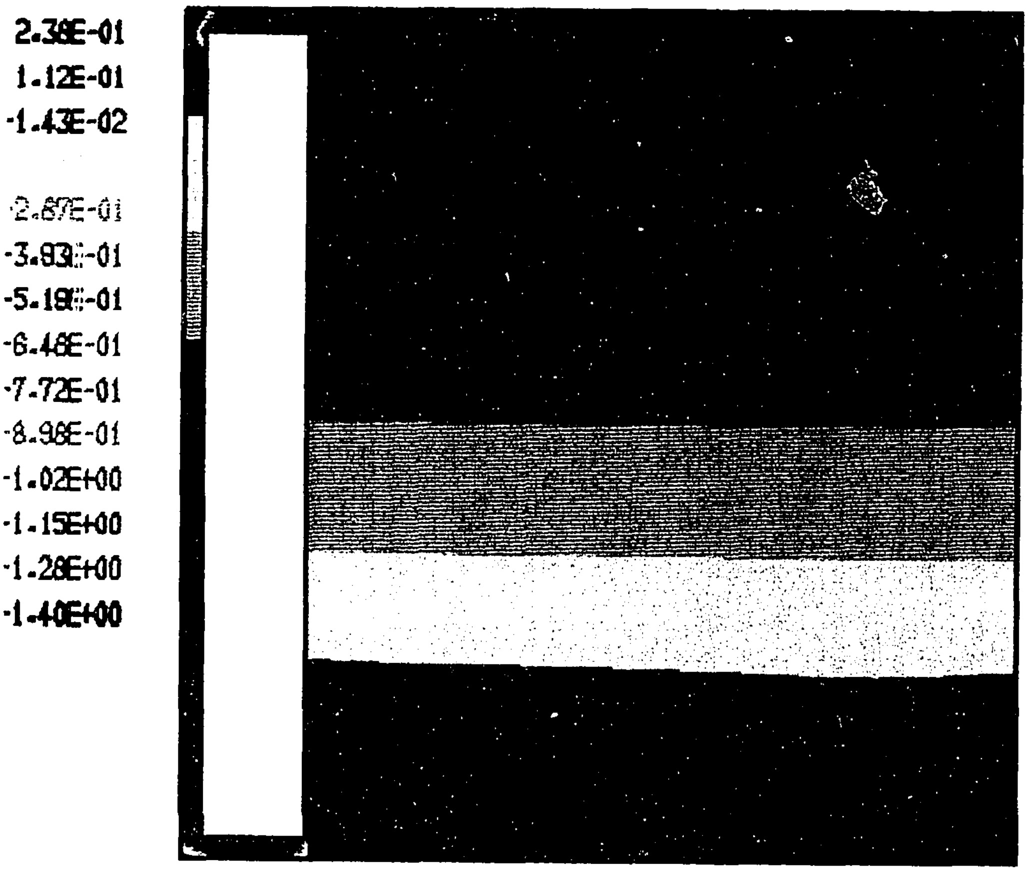

Fig. 6.17 Pressure field for air flow in a Trombe wall channel coupled to the room in the heating mode with T_c = 300 K

throughout the room without much distribution from the incoming heated air via the channel exit. In the higher cooled wall temperature case of 300 K. The buoyancy effect is much stronger in the channel and much more heated air has been discharged to the room, which pressed the positive but low value of pressure field down toward the channel entrance region. This phenomena can be seen very clear from both Figs. 6.16 and 61.7. If we compare the local $(P - P_\infty)$ values horizontally from inlet to exit of the channel, we will find out that these values change from near zero to +0.3 Pa for the 270 K cooled wall temperature case, and from –0.7 Pa to +0.7 Pa for the 300 K cooled wall temperature case. This simple comparison fully supports the phenomena we discussed earlier in this section.

6.2.7 Truncated Trombe Wall Geometries

Three different Trombe wall geometries have been investigated in the present study. This first case is the standard case involving the Trombe wall channel coupled to the room. This geometry requires substantial computational effort. As a result, we have also investigated certain truncated Trombe wall geometries to see if accurate results can be obtained with fewer grid points and consequently with lesser computational effort. In the second case, a truncated Trombe wall geometry shown in Fig. 6.18 is considered. In this case, a full room geometry is replaced with a truncated room geometry. The line of truncation is set at X = 1.25 m. This represents a free boundary on which one must apply new set of boundary conditions. Since velocity conditions are not known on this boundary, a zero pressure boundary condition is applied. From previous discussion on the full scale geometry, it is evident that this condition can at best be regarded as an approximation. Also, the x-derivative of temperature is assumed to be zero on the boundary. In the third case, the free boundary is located at X = 0.6 m where the horizontal segments end. The reason for doing this investigation is to not only reduce the calculation domain and to save the computational time, but also to establish the influence of the location of the free pressure boundary condition on the heat transfer phenomena inside the Trombe wall channel as well as the net energy rate discharged to the room via the channel exit. Figures 6.18–6.21 show the streamline contours and temperature field for the second and third cases respectively. Table 6.3 shows the comparison of mass flow rate and net energy delivery rate for these three cases. For the second case, i.e, truncated geometry at the halfway position, results for heat transfer coefficient inside the channel, as well as the net energy rate discharged to the room closely approximate the results for the standard full room size case. By putting pressure boundary condition right at inlet and exit section of the channel, one overestimates both the heat transfer coefficient inside the channel and the net energy delivered to the room by bout 9%. This can be observed from Fig. 6.22 and Table 6.3. Figure 6.22 shows the comparison of local heat transfer coefficient on the heated wall for the above three cases. In conclusion, it can be stated that if one is willing to tolerate about 9% uncertainty in estimation of the energy delivery and mass flow rates, then a truncated geometry of the type discussed here can be adopted. The advantage, of course, would be that the computational effort will be significantly reduced. For 3–D geometries, not considered here, this may be an important factor in numerical simulation.

6.2.8 Channel Gap Effect

The effect of channel width on mass flow rate and energy rate delivered to the room has also been investigated in the present study. Five other values of channel width, namely L = 0.05 m, 0.2 m, 0.3 m, 0.4 m and 0.5 m have been employed besides the previous case of L = 0.1 m width. Figure 6.23 shows the effect of channel gap on both mass flow rate and energy delivery rate. It is noted that the mass flow rate in the

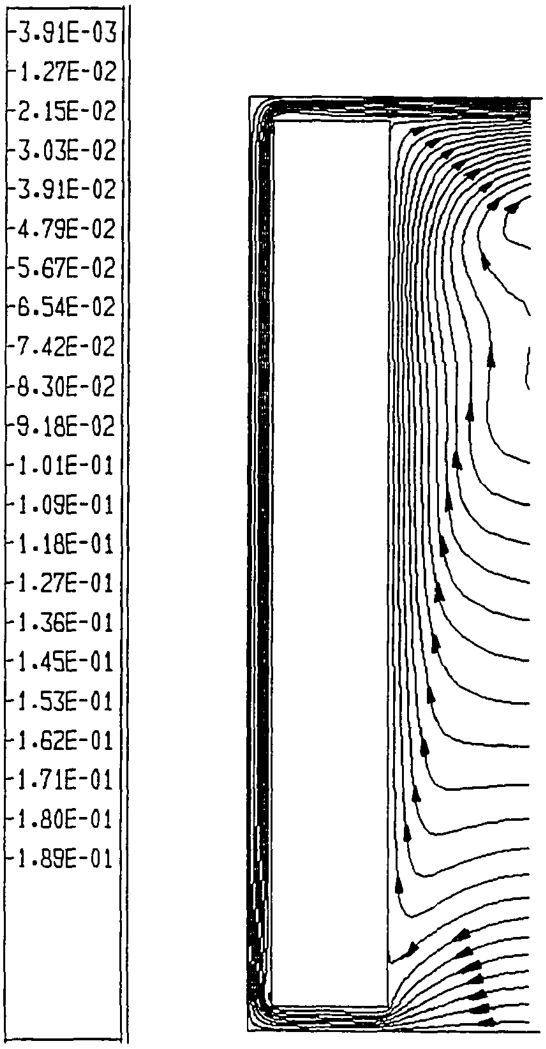

Fig. 6.18 Streamline contours for air flow in a Trombe wall channel coupled to the room at T_c = 290 K, X = 1.25 m

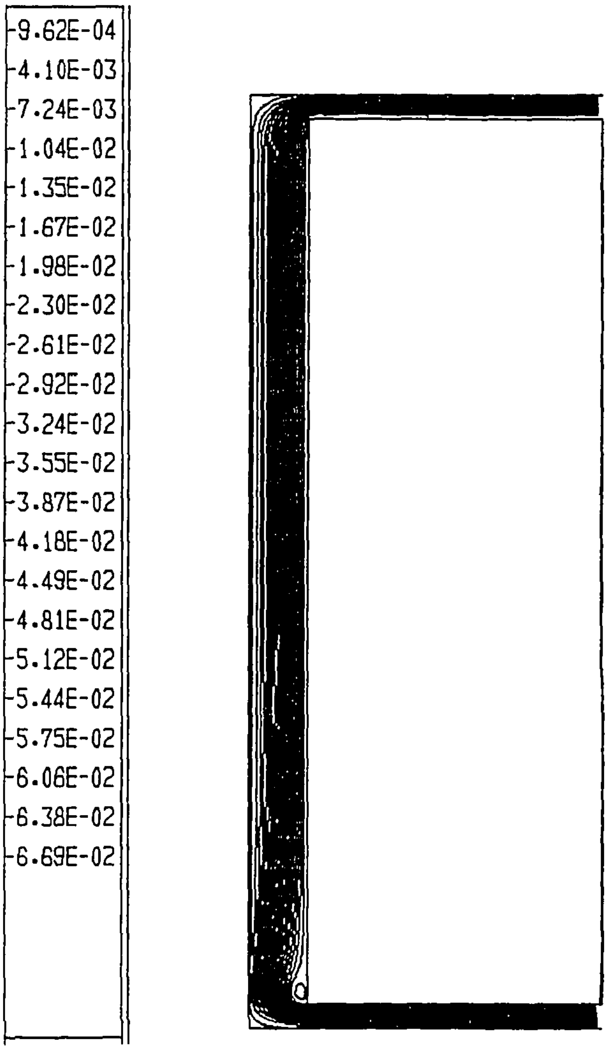

Fig. 6.19 Streamline contours for air flow in a Trombe wall channel coupled to the room at T_c = 290 K, X = 0.60 m

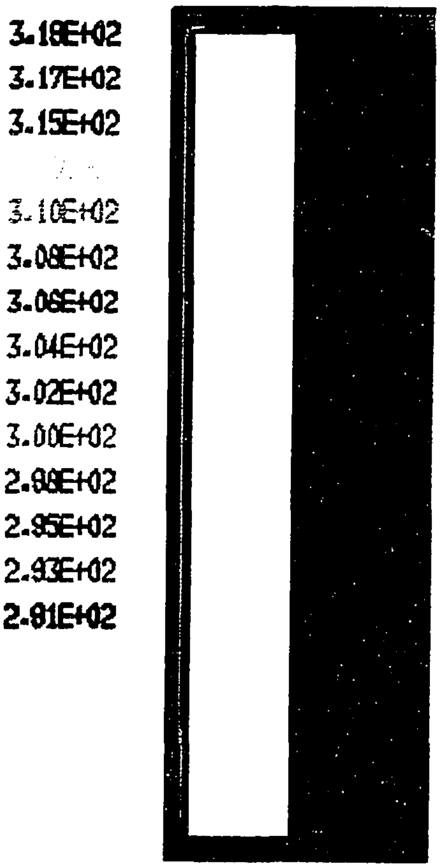

Fig. 6.20 Temperature distribution for air flow in a Trombe wall channel coupled to the room at T_c = 290 K, X = 1.25 m

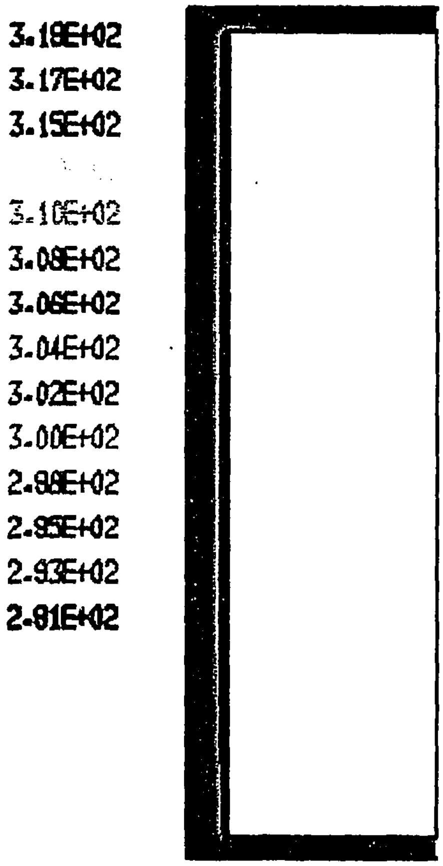

Fig. 6.21 Temperature distribution for air flow in a Trombe wall channel coupled to the room at $T_c = 290$ K, X = 0.60 m

Table 6.3 Comparison of mass flow rate and net energy rate among three different locations of boundary condition

Free Boundary Location (m)	Area (m^2)		Mass Flow Rate (kg/sec)		Heat Flux (W/m^2)		Mean Fluid Temp (K)	Net Energy (W)
x^-	Cold	Hot	In	Out	Cold	Hot		
4.0	4.0	3.8	-7.416×10^{-2}	7.435×10^{-2}	-906.1	1227	294.2	313.4
1.25	4.0	3.8	-7.858×10^{-2}	7.869×10^{-2}	-902.1	1231	294.3	339.8
0.6	4.0	3.8	-7.943×10^{-2}	7.989×10^{-2}	-890.5	1168	294.3	344.2

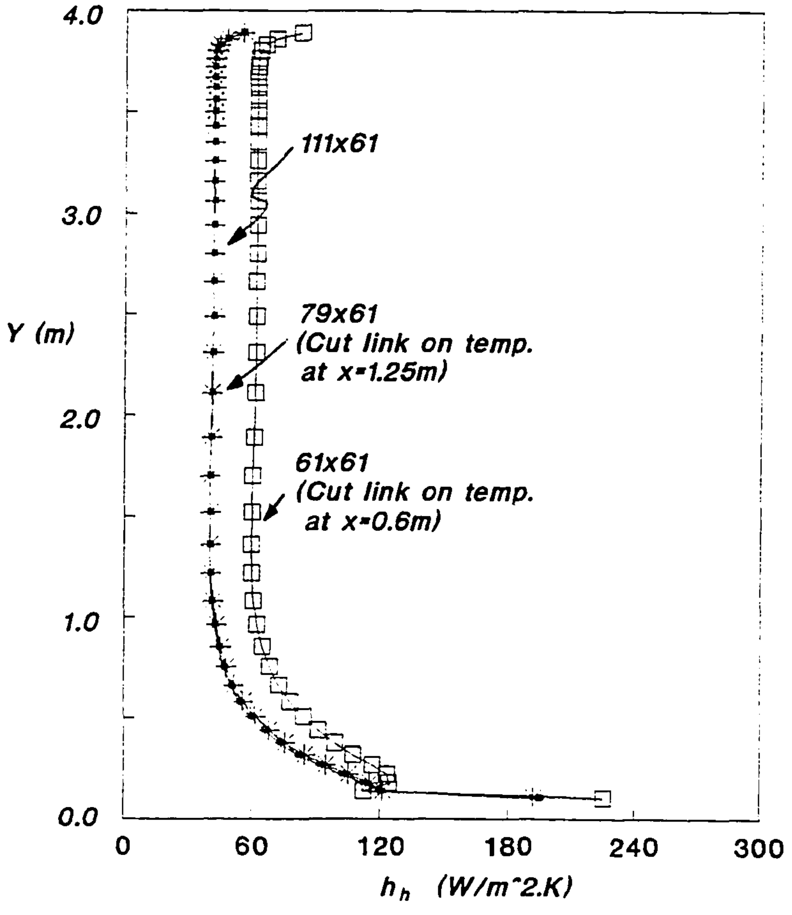

Fig. 6.22 Comparison of local heat transfer coefficient on heated wall among different locations of pressure boundary condition

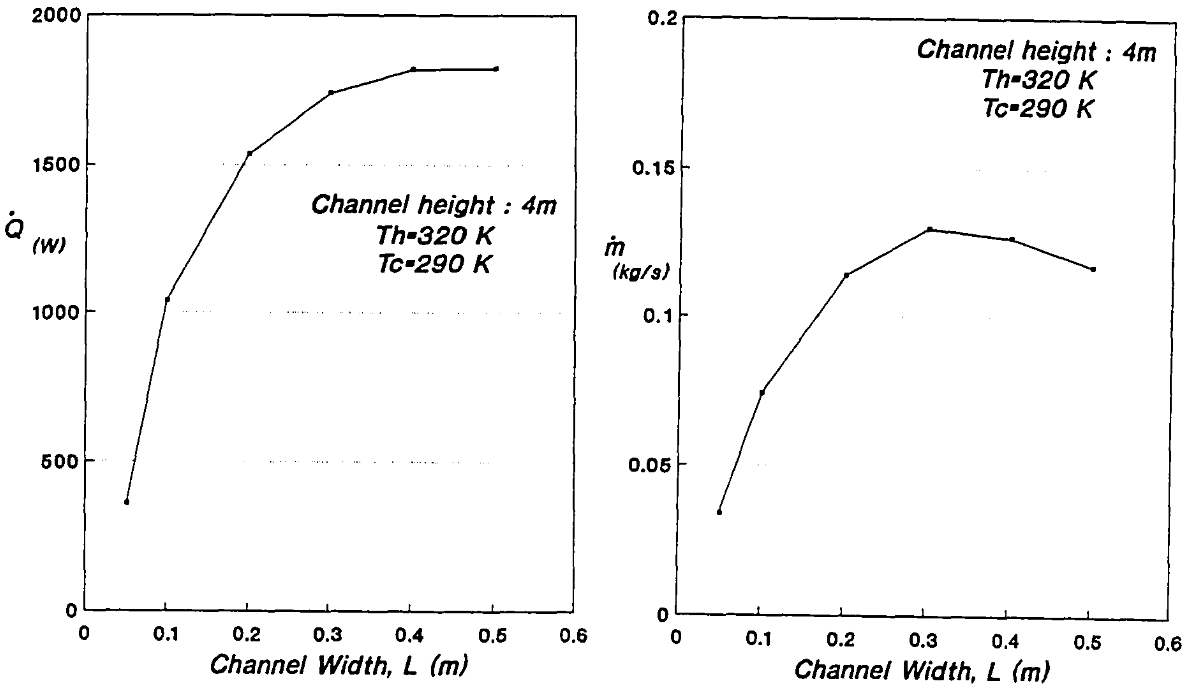

Fig. 6.23 Mass flow rate and energy delivery rate as the function of channel width

Trombe wall channel reaches a maximum value when the channel gap is about 0.3 m wide. However, the energy delivery rate reaches its maximum value at L = 0.5 m. These results show that there is an optimal channel gap for delivering the maximum amount of convective heat to the conditioned space. This type of information is considerable importance in the design of Trombe wall type solar passive systems.

6.2.9 Effect of the Room-Side Storage Block Surface Temperature

Simulation of Trombe wall channel coupled to the room operating in heating mode, has also been conducted by changing the surface temperature of the storage block on the room side from 290 K to 305 K. While the cooled wall and heated walls are maintained at temperatures of 290 K and 310 K respectively.

Figure 6.24 shows the mass flow rate and energy delivery rate as the function of storage block surface temperature facing the room. Since, buoyancy force is the major factor in the study of natural convective heat transfer in the Trombe wall channel geometries, and is a function of temperature difference between the air in the Trombe wall channel and the air in the room. Therefore, the higher the surface temperature of the storage block on the room side, the higher the room air temperature, the less the buoyancy force in the Trombe channel. Thus, less air mass and its energy delivered to the room

6.3 Ventilation Mode Results

6.3.1 Physical Model

Trombe wall channel can also be used for building ventilation during the summer months. The heated wall on south side is used as a heat source to create low pressure inside the channel. This in turn causes the fresh outdoor air to be drawn into the room, thus creating ventilation as well as cooling effect. Figure 6.25 shows the schematic of a Trombe wall system operating in the cooling or ventilation mode. Cool air is pulled

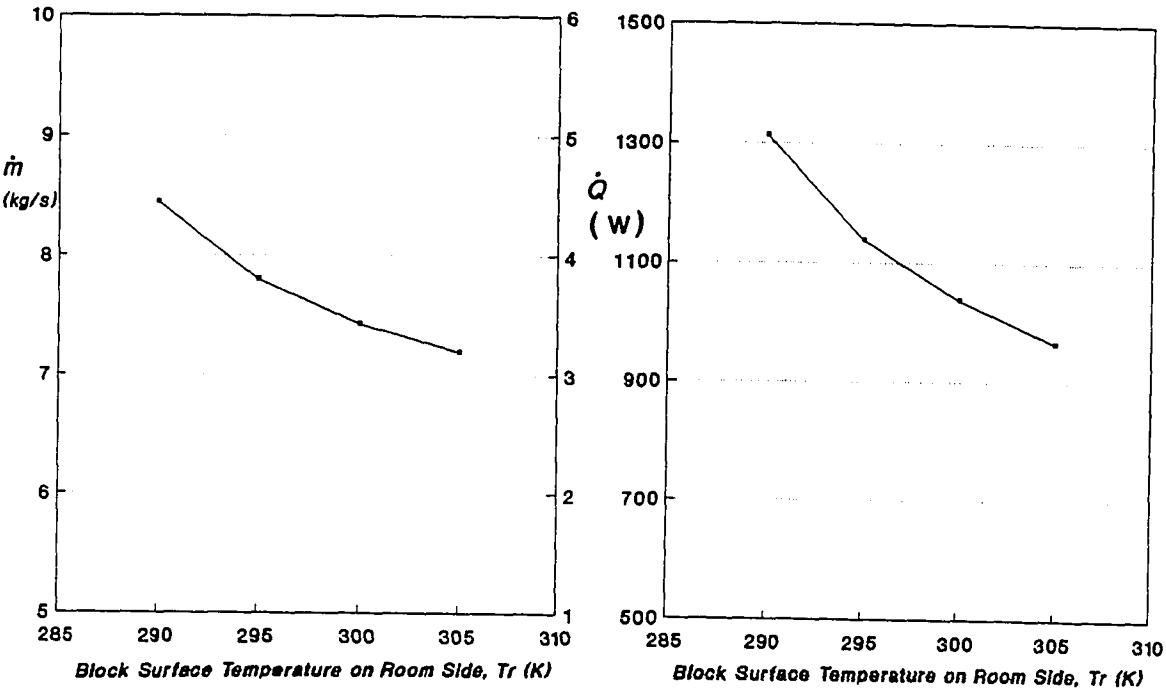

Fig. 6.24 Mass flow rate and energy delivery rate as the function of room wall temperature

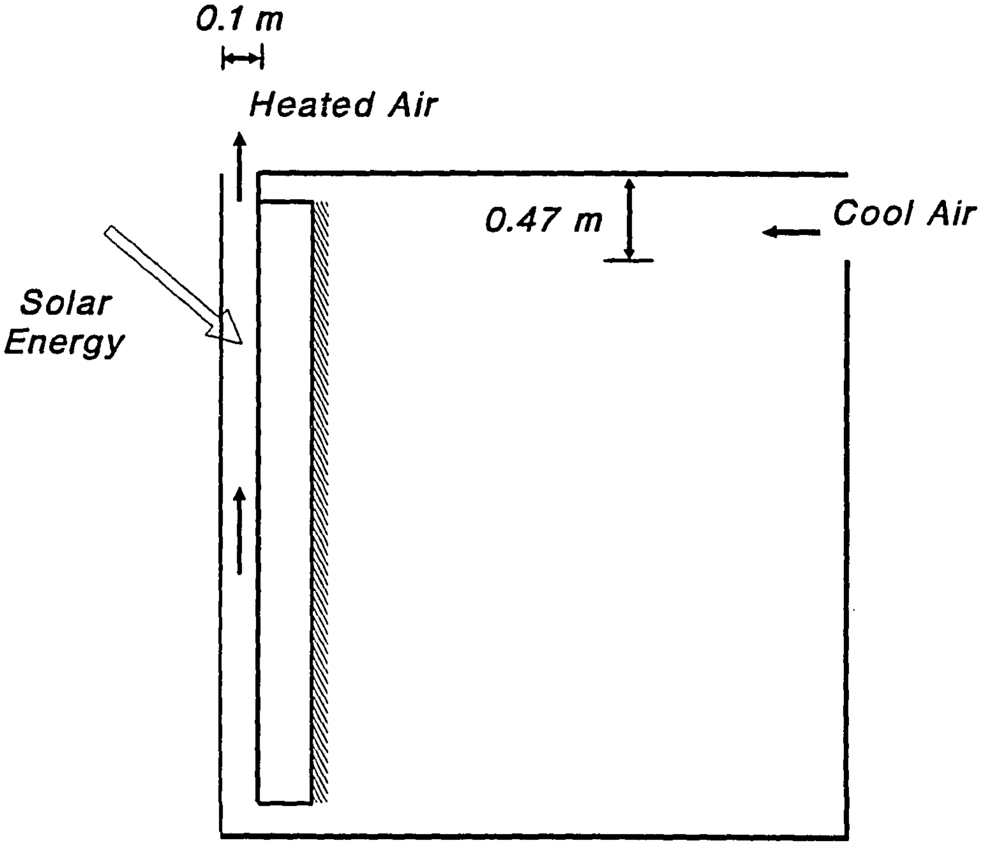

Fig. 6.25 Schematic of the Trombe wall channel coupled to the room operating in cooling mode

from the vent at the right-hand upper corner of the room, since the Trombe wall channel acts like a chimney due to very strong buoyancy effect created by the hot wall surface. The hot air rises due to its buoyancy and is ejected from the open vent located at the top of the channel. The main objective here is to explore the ventilation and cooling potential of this system. The effect of room vent location and the ventilation characteristics of the system are further investigated.

6.3.2 Flow Field

Three cases have been analyzed for the Trombe wall operation in the cooling mode. These case arise from three different locations of the room vent, namely near top, mid and bottom sections of the right room wall. The storage block wall surface on the room side is kept insulated for all three cases. The cooled wall and heated walls are maintained at 310 K and 330 K respectively. Other room walls are maintained at temperature of 310 K for all three cases.

6.3.3 Streamline Contours

Figures 6.26–6.28 show the streamline contours for the three positions of the room vent on the right wall, namely top, middle and low level locations. In the top-vent case, the cool air flow is drawn in from outside and is squeezed along the right vertical face of the Trombe wall by a strong secondary flow due to the buoyancy effect from the hot floor and side wall. In the case of bottom vent, as we can see from Fig. 6.27, two recirculating flow patterns coexit with the incoming cool air flow. The cool air flows only in a very narrow portion of the room near the floor. In the central-vent case, the cool air also flows along the right wall and the bottom floor. Despite differences in above three cases, it has been demonstrated that Trombe wall channel can act as a chimney, by the pulling in

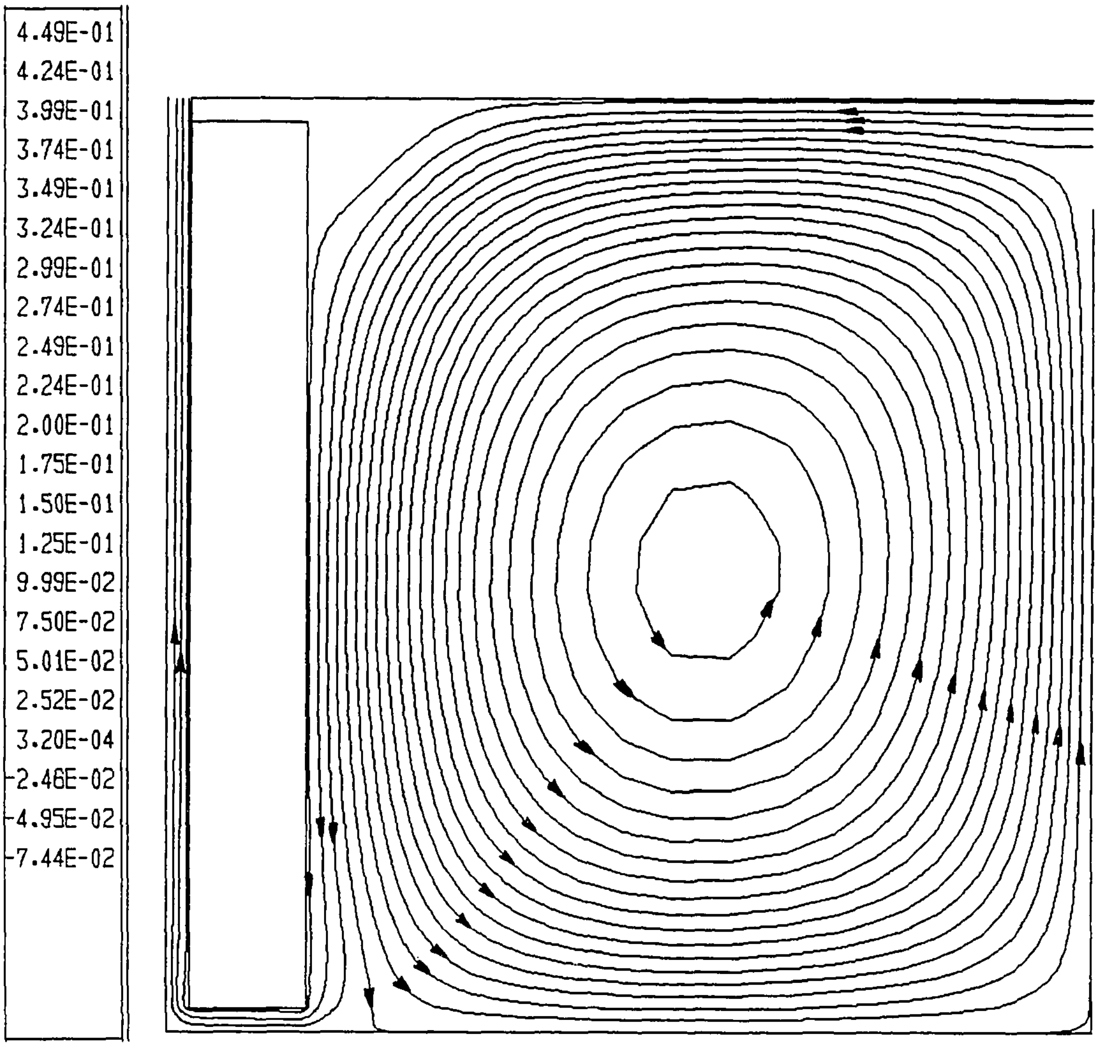

Fig. 6.26 Streamline contours for air flow in a Trombe wall channel coupled to the room in the cooling mode with top vent

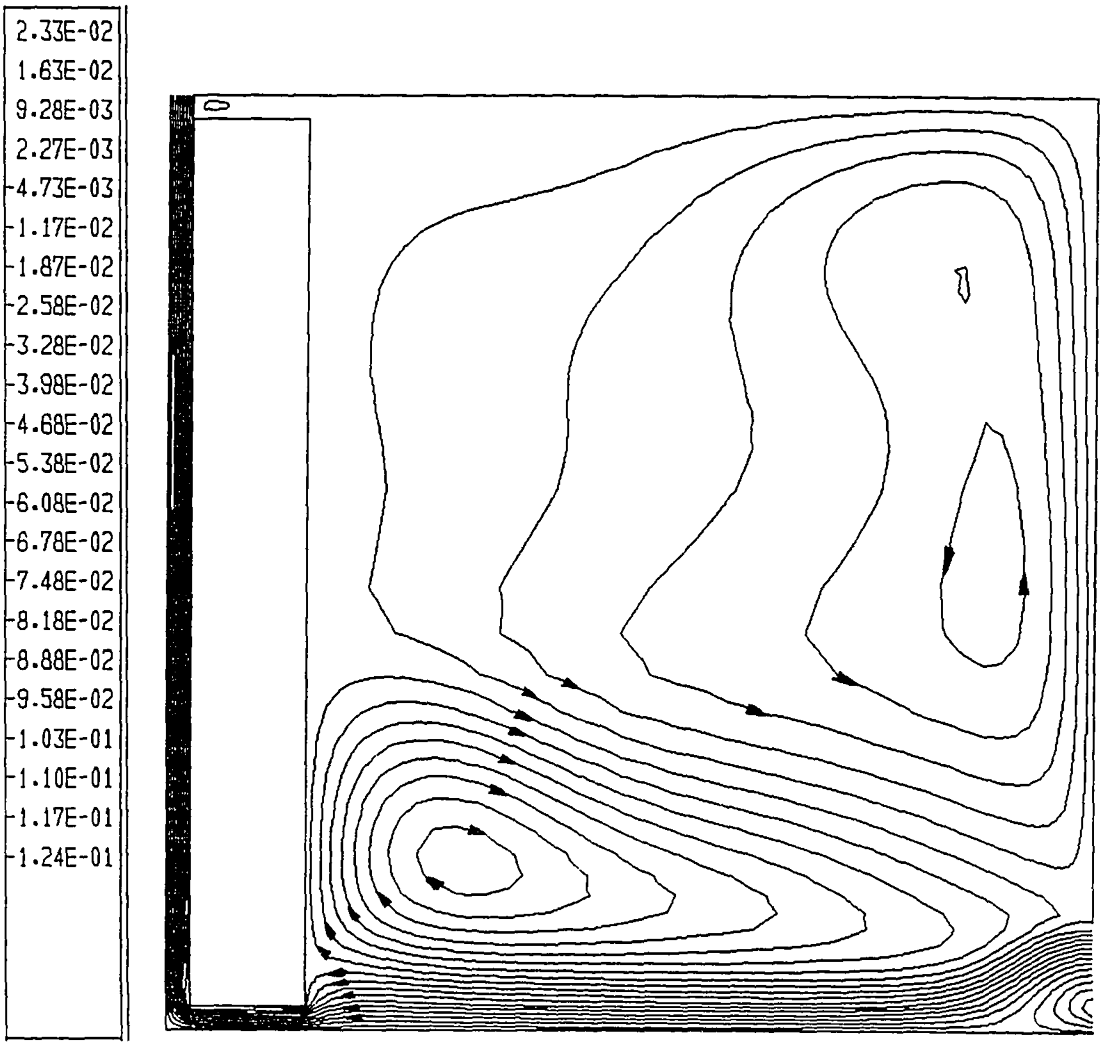

Fig. 6.27 Streamline contours for air flow in a Trombe wall channel coupled to the room in the cooling mode with bottom vent

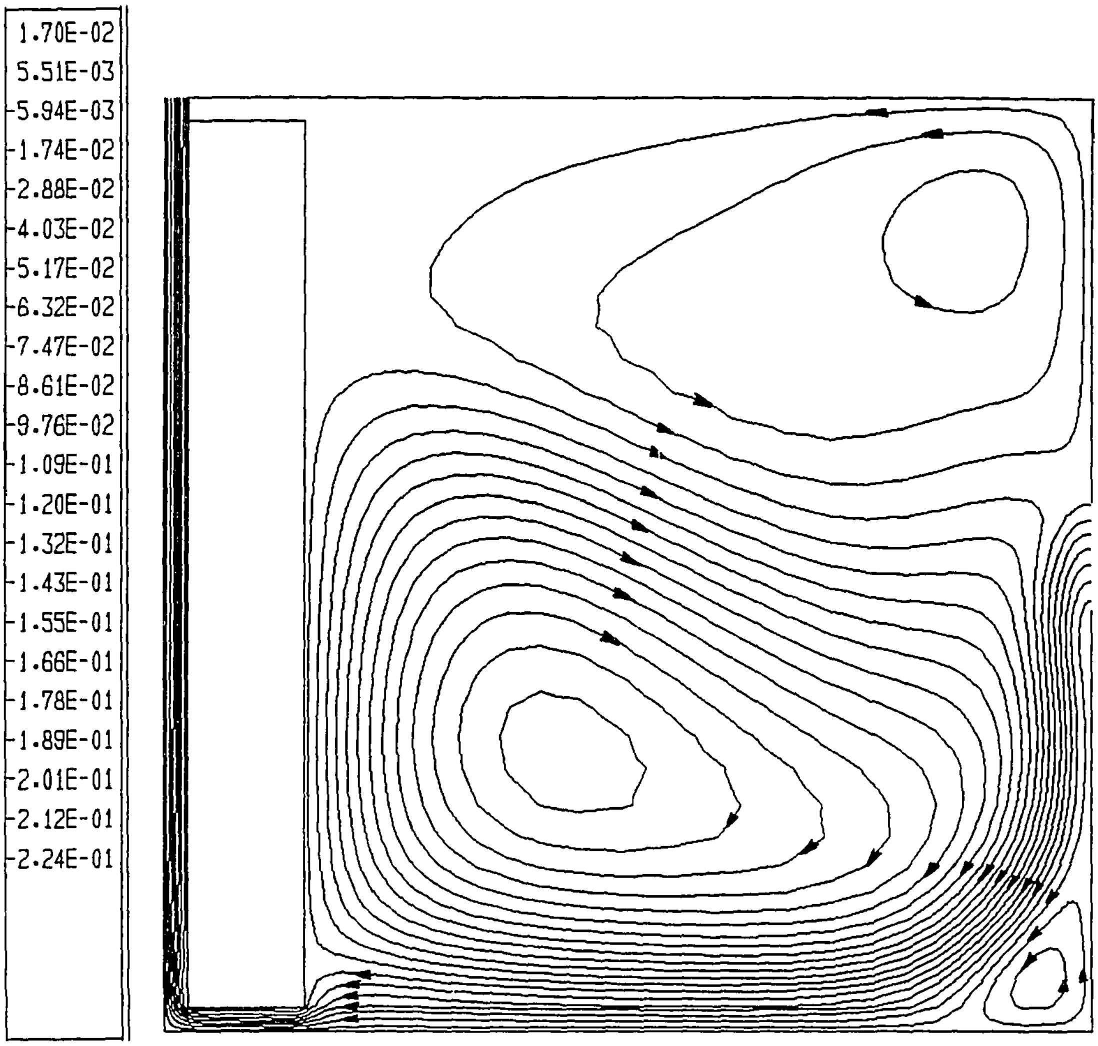

Fig. 6.28 Streamline contours for air flow in a Trombe wall channel coupled to the room in the cooling mode with central vent

fresh outside air. The problem in these cases is that the fresh air flows mainly along the room walls and floor, and this limits the capability of air to cool the room.

6.3.4 Temperature and Pressure Fields

Figures 6.29–6.31 show the temperature distributions for the three vent location cases. The mean air temperature inside the room is about 306.3 K for the top-vent case, which is 3.7 lower than the initial room (air) temperature of 310 K. The mean air temperature is about 308.5 K and 307.2 K for bottom-vent and central-vent respectively, as shown in Table 6.4. The limited simulation indicates that based on high mass flow rate and energy delivery rate, the top-vent appears to be the best choice for locating the room vent. Figure 6.32 shows the pressure distribution for the top-vent case. In the entrance region near the top vent, the pressure has negative values, which allows cool air to come inside the room.

6.3.5 Mass Flow and Energy Delivery Rates

Table 6.4 shows the comparison of mass flow rate, mean air temperature inside the room and total energy rate extracted from the room for the three cases with different vent location and two cases with top vent location and different room wall temperature. Results show that the central vent case has the strongest mass flow rate among the three cases discussed in the previous section of this chapter. However, it has a lower degree of cooling, which makes the total energy rate extracted from the room not as great as for the case with top-vent. The bottom-vent case is the worst design if one judges it by the total energy expelled from the room.

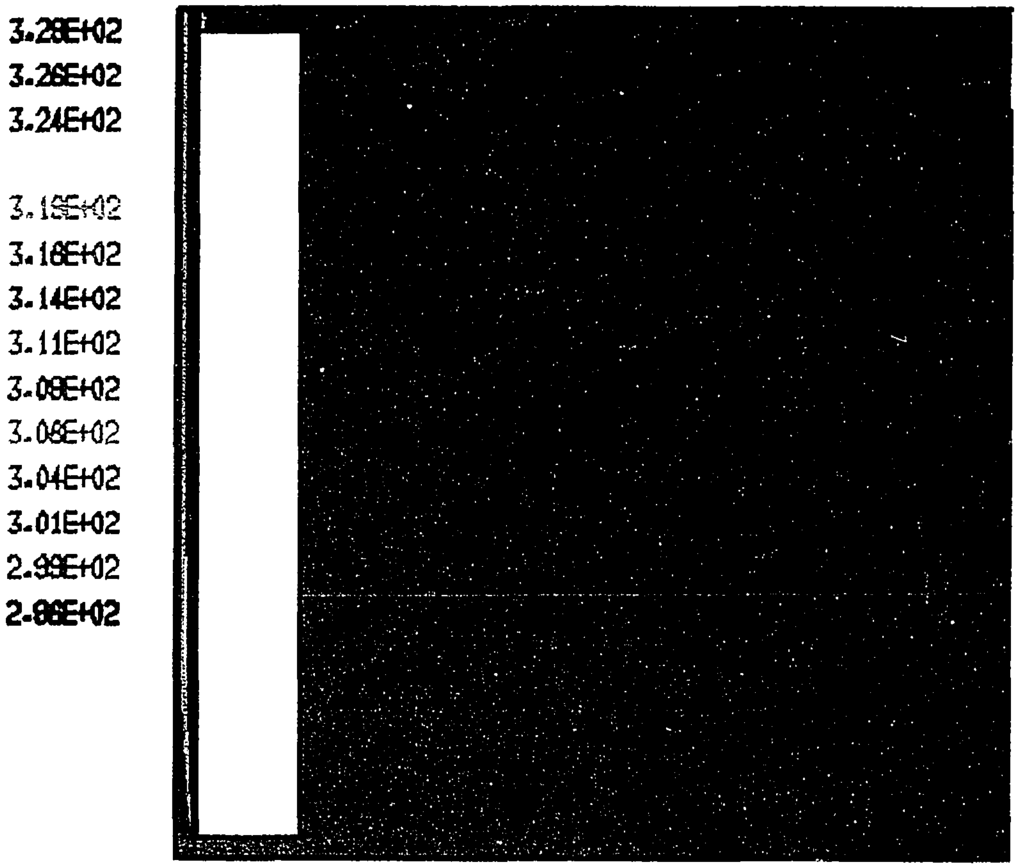

Fig. 6.29 Temperature distribution for air flow in a Trombe wall channel coupled to the room in the cooling mode with a top vent

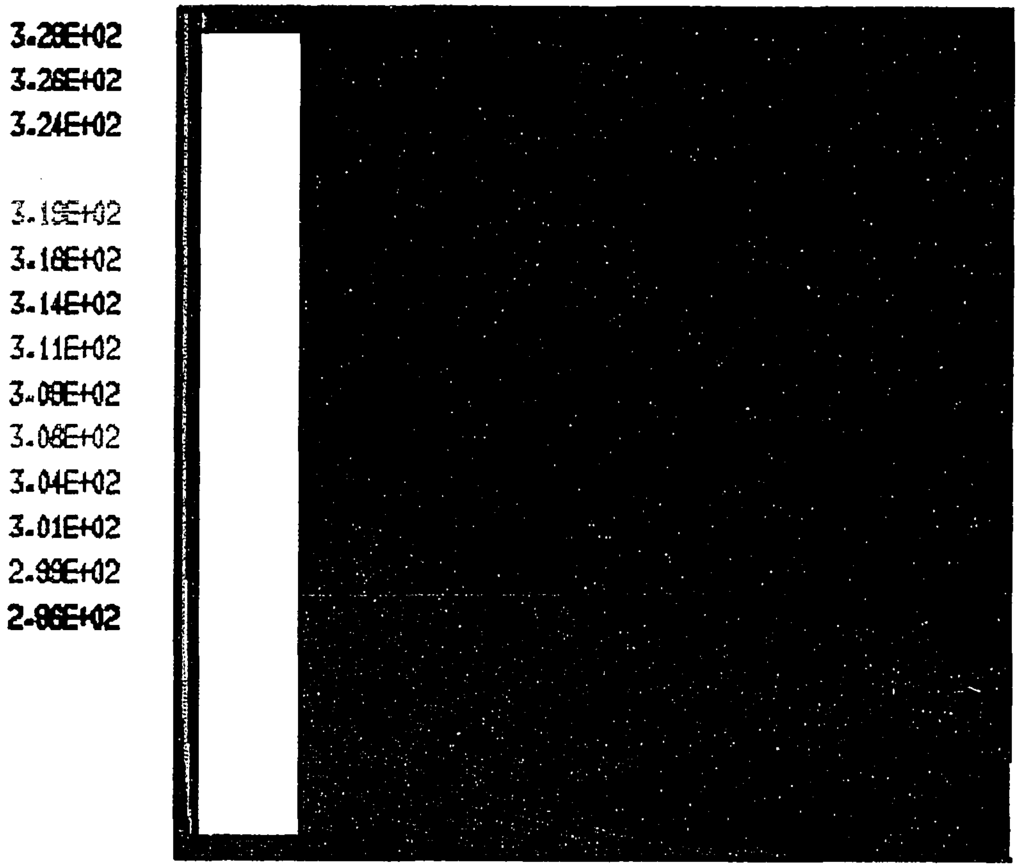

Fig. 6.30 Temperature distribution for air flow in a Trombe wall channel coupled to the room in the cooling mode with a bottom vent

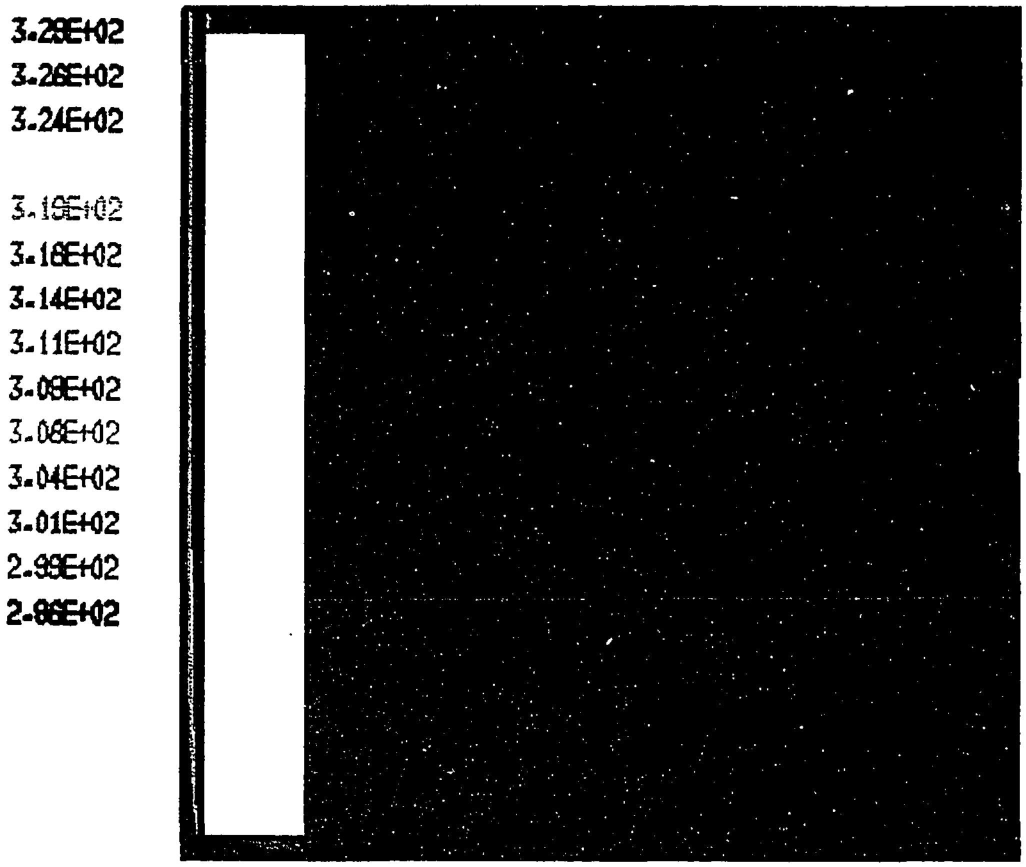

Fig. 6.31 Temperature distribution for air flow in a Trombe wall channel coupled to the room in the cooling mode with a central vent

Table 6.4 Comparison of total energy rate extracted from the room (Cooling) among different room wall temperatures and locations of vent

Room Wall Temp.	Vent Size (m^2)		Vent Location	Mass Flow Rate (kg/sec)		Heat Flux (W/m^2)		Mean Fluid Temp.	Net Energy (W)
(K)	In	Out		In	Out	Cold	Hot	(K)	
310	0.47	0.10	Top	-8.898×10^{-2}	9.66×10^{-2}	-505.1	858.7	306.3	346.7
310	0.47	0.10	Bottom	-8.298×10^{-2}	8.78×10^{-2}	-532.1	823.3	308.5	128.7
310	0.46	0.10	Center	-9.111×10^{-2}	9.954×10^{-2}	-515.9	845.3	307.2	277.8
305	0.46	0.10	Center	-9.857×10^{-2}	1.097×10^{-1}	-442.1	932.7	302.8	230.2
305	0.47	0.10	Top	-1.105×10^{-1}	1.194×10^{-1}	-421.0	973.9	302.6	277.6
300	0.47	0.10	Top	-1.233×10^{-1}	1.315×10^{-1}	-352.7	1048.0	299.9	226.6

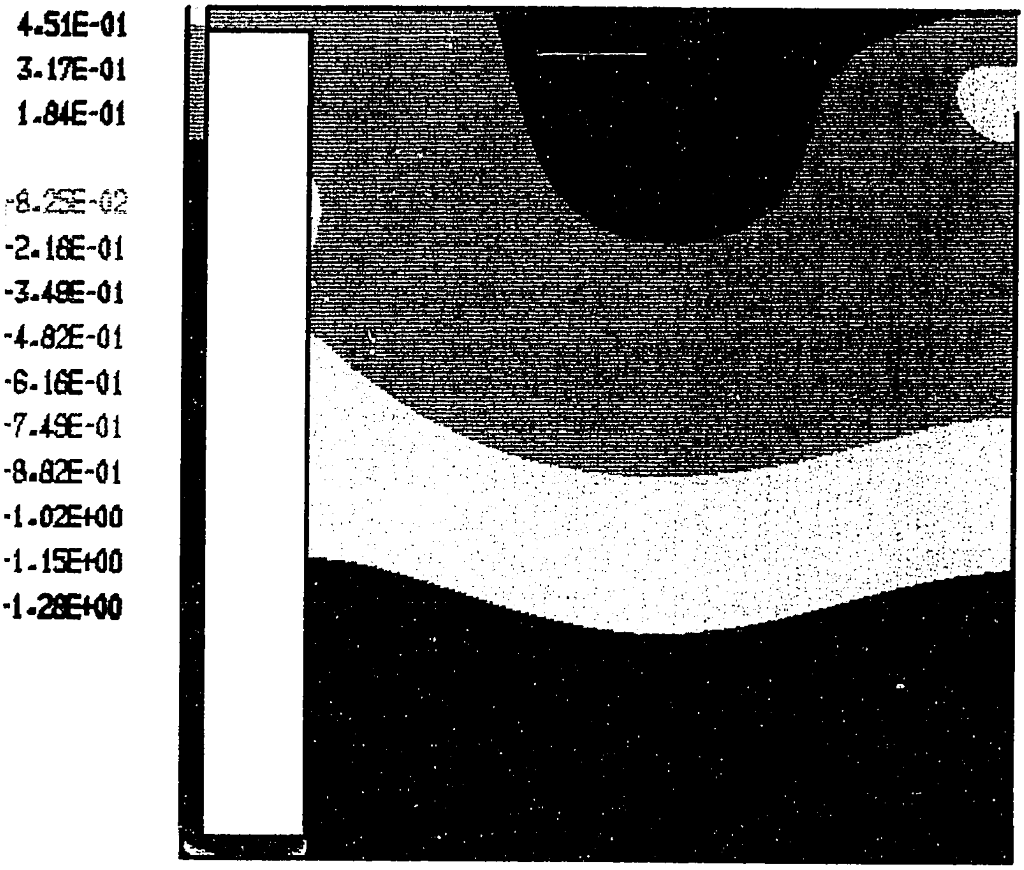

Fig. 6.32 Pressure field for air flow in a Trombe wall channel coupled to the room in the cooling mode with a top vent.

6.3.6 The Effect of Room Wall Temperature

In order to explore the passive cooling mode further, three additional cases have been investigated by using different temperatures on the room walls, ceiling and floor. The first case involves a central-vent, and room wall, ceiling and floor temperatures are all set at 305 K, 5 K lower than previous cases. The second case is a top-vent case with same thermal boundary conditions as in the first case. The third case involves the top-vent. The ceiling temperature is set at 305 K and side-wall and floor temperatures are set at 300 K. It is noted that the rest of the boundary conditions are the same for all these three cases, namely T_c = 310 K and T_h = 320 K.

Figures 6.33–6.35 show the streamline contours for these three cases. It is noted that room wall temperature has a pronounced effect on the flow pattern in the room. In the case of different ceiling and floor temperature as shown in Fig. 6.35, cool air flow comes-in via the top-vent, across the room diagonally, ejecting a large amount of energy through the Trombe wall channel to the ambient. From the point of view of mass flow rate induced and energy expelled point of view, this case yields the best result. In the case of central-vent as shown in Fig. 6.33, the cool air flow comes-in via the central-vent has been restricted in the lower portion of the room, this caused by a strong recirculating flow cell from the top and left-hand side of the room due to large buoyancy force.

Figures 6.36–6.38 show the temperature distribution for these three cases. As seen from Table 6.4, results still show that top-vent to be the best design for passive cooling. The net energy expelled decreases as the room wall temperature decreases, while, the mass flow rate increases as the room wall temperature decreases.

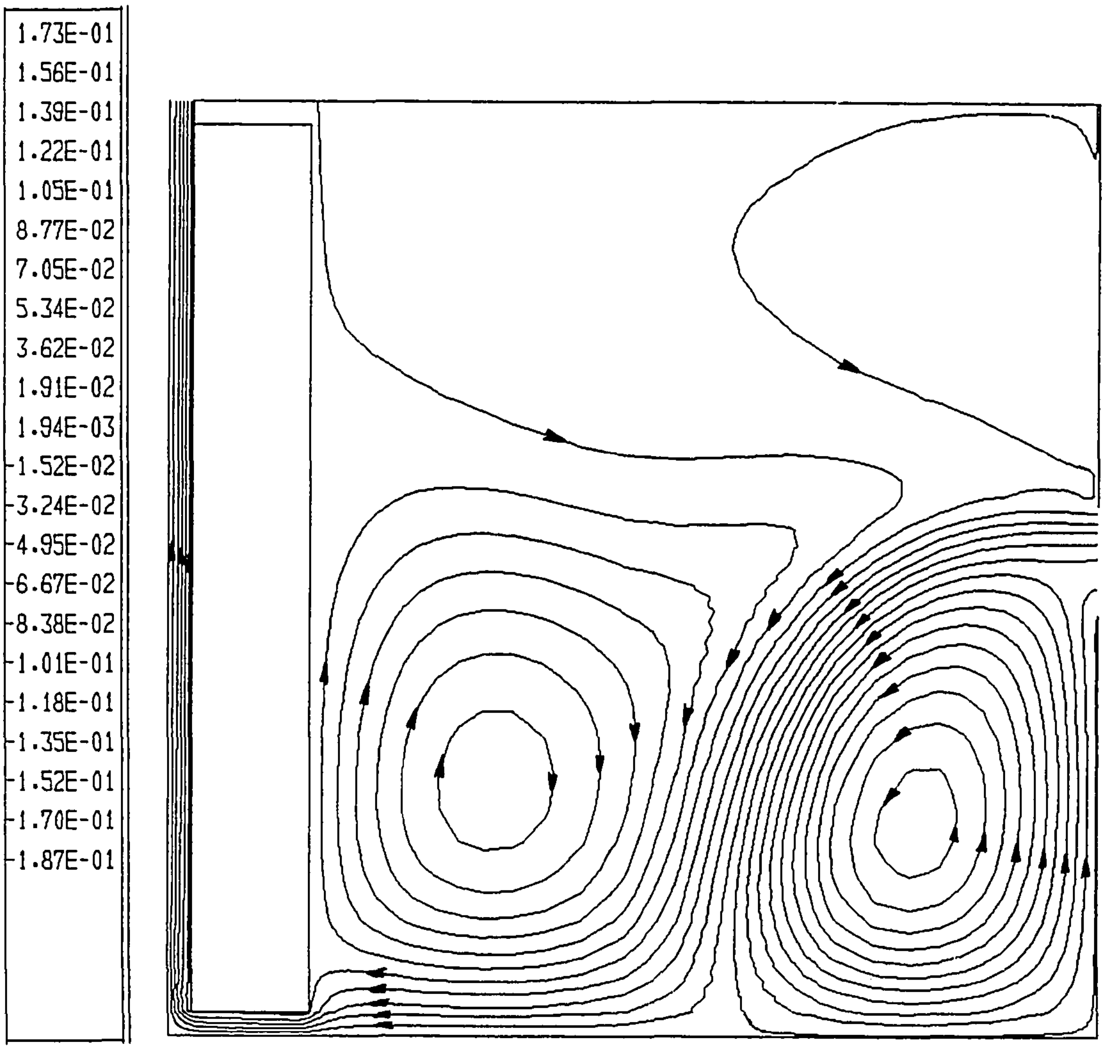

Fig. 6.33 Streamline contours for air flow in a Trombe wall channel coupled to the room in the cooling mode with a central vent, Tr = 305 K

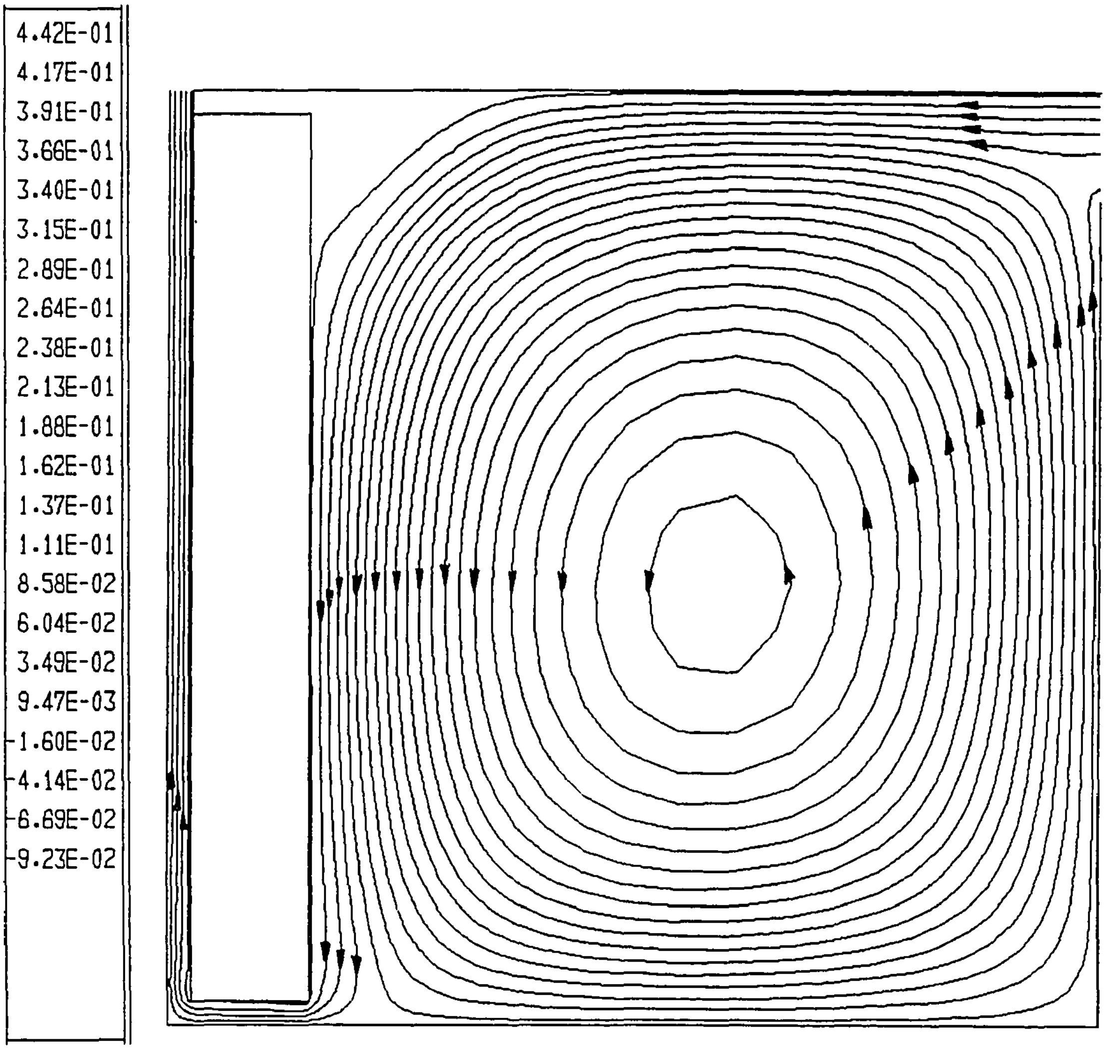

Fig. 6.34 Streamline contours for air flow in a Trombe wall channel coupled to the room in the cooling mode with a top vent, Tr = 305 K

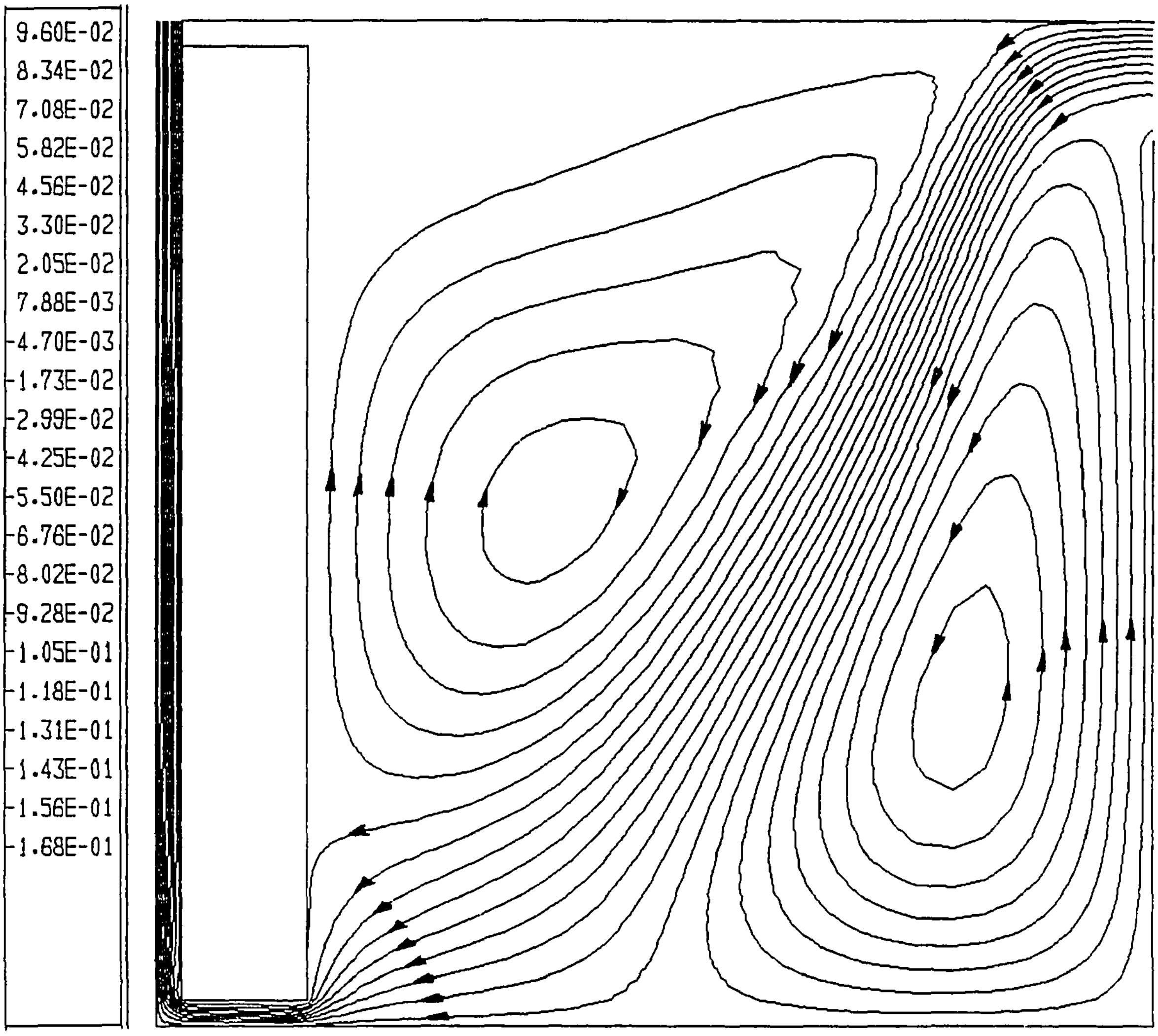

Fig. 6.35 Streamline contours for air flow in a Trombe wall channel coupled to the room in the cooling mode with a top vent, $T_r = 305$ K, $T_f = 300$ K

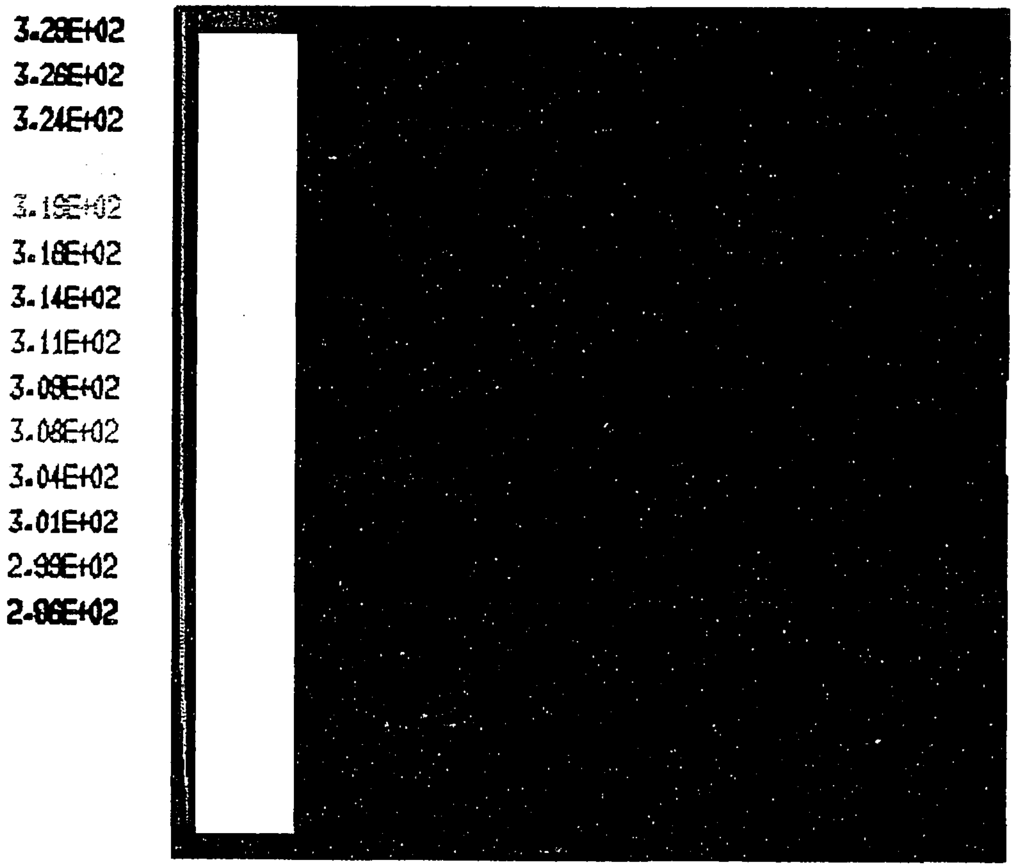

Fig. 6.36 Temperature distribution for air flow in a Trombe wall channel coupled to the room in the cooling mode with a central vent, T_r = 305 K

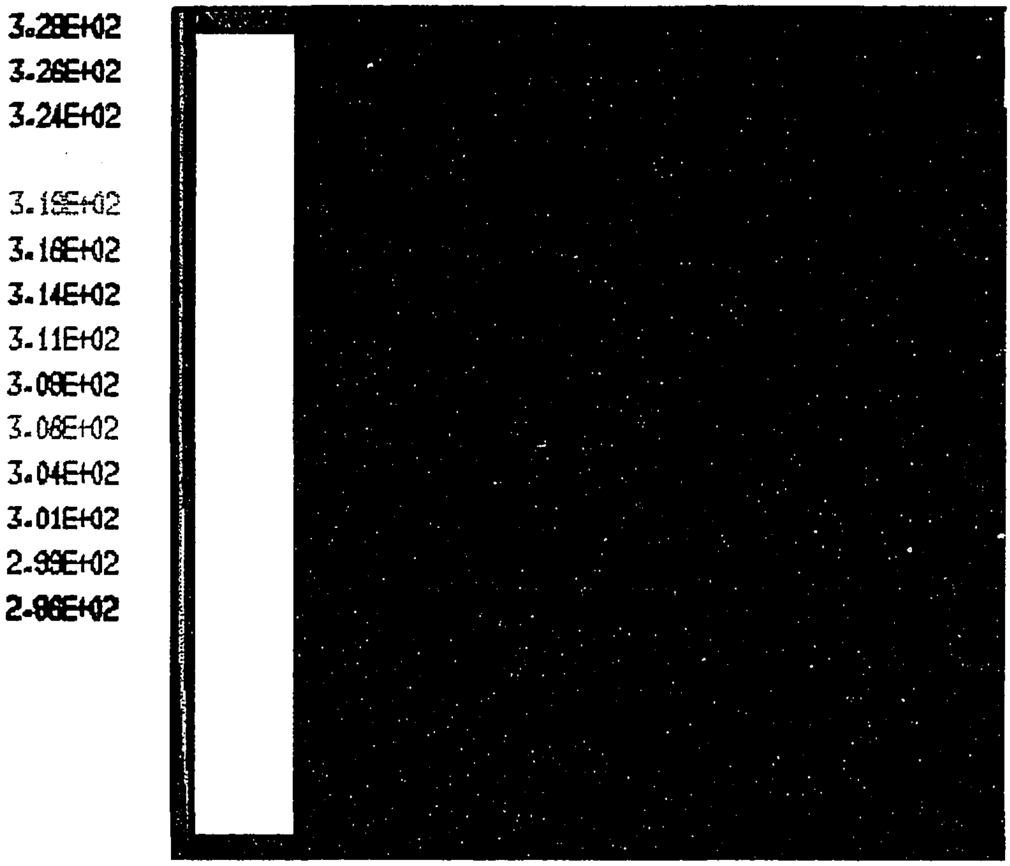

Fig. 6.37 Temperature distribution for air flow in a Trombe wall channel coupled to the room in the cooling mode with a top vent, T_r = 305 K

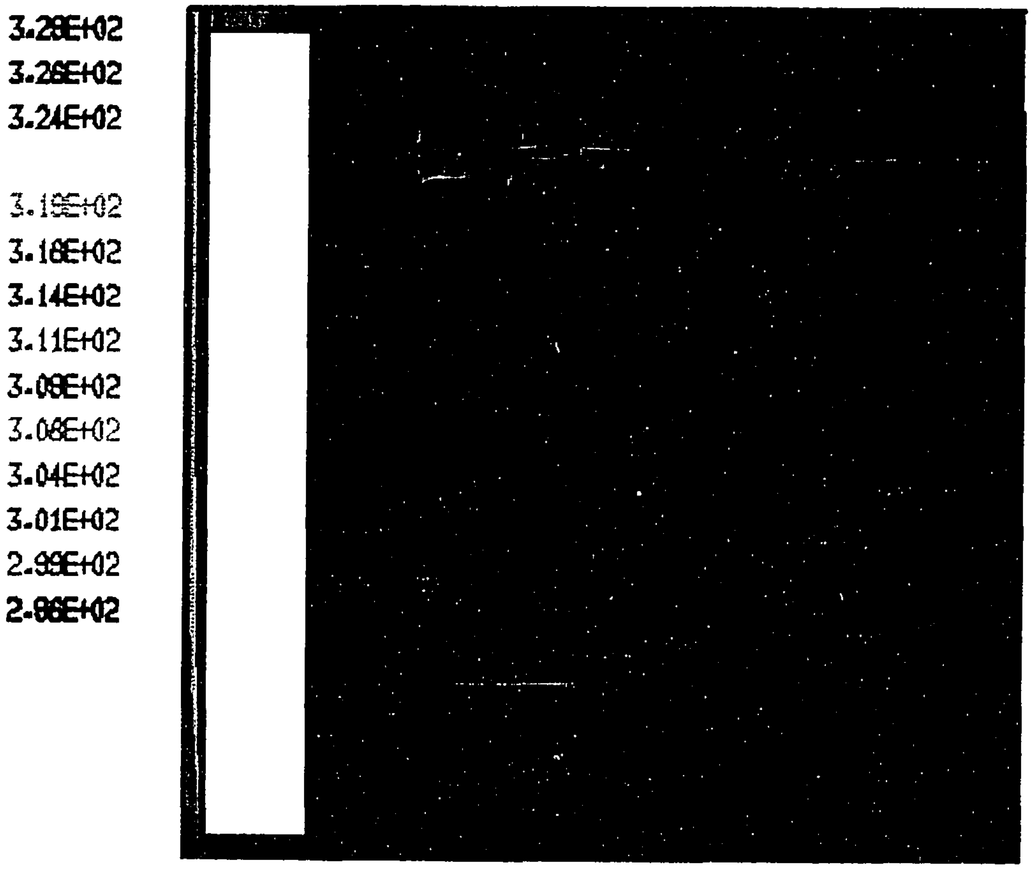

Fig. 6.38 Temperature distribution for air flow in a Trombe wall channel coupled to the room in the cooling mode with a top vent, T_r = 305 K, T_f = 300 K

Chapter 7

CONCLUSIONS AND RECOMMENDATIONS

A comprehensive energy analysis of the Trombe wall solar passive system using analytical and computational techniques has been made.

For laminar natural convective flow in the parallel wall channel, the application of momentum-integral method, and Oseen's linearization model for non-linear convective terms, led to a second order ordinary differential equations for pressure defect variable. For an optimized value of the convective parameter $\alpha = 1.3$, the pressure profiles are found to be in reasonable agreement with the results of Akbari and Borger [8]. Using the value of $\alpha = 1.3$, other parameters such as mass flux induced and the overall heat transfer coefficient are also found to be in good agreement with previously reported results for air. The momentum-integral theory is also extended to predict results for high and low Prandtl number fluids such as water and sodium. The momentum-integral method presents a relatively simple way of predicting the mass flow and energy delivery rates induced by the buoyancy force in the channel. Due to analytical solution procedure, it can easily be adopted in a more comprehensive program for energy analysis of these systems.

The results predicted for the case of side-vented cavities demonstrate that the flow patterns are strongly influenced by both Grashof number and vent size. Increasing Grashof number for a given aspect ratio and vent size enlarges and intensifies the recirculatory motion in the vertical channel. The peak velocity is found to shift toward the heated wall as Grashof number is increased. Its value also increased with increasing the vent size. The energy delivery to the atmosphere is strongly governed by both Grashof number and vent size. As Grashof number increases, the energy convected to the atmosphere increased substantially. The total vent loss coefficient for the laminar case shows a minimum at $Gr = 1.4 \times 10^4$ for which the dimensionless mass flow rate also shows a maximum value.

Results for the side-vented channel case also demonstrated the need to consider an outer free boundary to set the undisturbed ambient pressure condition.

Interestingly enough the pressures boundary condition applied at the channel vents could not predict the flow phenomenon correctly. Extension of the calculation domain to a certain distance from the physical boundaries yielded good results. The application of pressure boundary condition, at locations away from physical vent locations, yielded pressures at inlet and exit sections from which inlet and exit pressure losses can be calculated. This procedure is recommended for future natural convective flow studies involving inlet and exit vents. Results also showed that the energy delivery rate and mass flux increase with increasing Grashof number and the vent size.

For comprehensive geometry, both heating and ventilation modes have been investigated. In the heating mode, the result of the effect of Trombe wall channel width on mass flow and energy delivery rates shows that L = 0.3 m is the best channel width for delivering most mass to the conditioned space. Results also show that the truncated Trombe wall geometries could not be less than X = 1.25 m since a lower value underestimate the actual mass flow rate. In the ventilation mode, several different vent locations have been studied, preliminary results point to the fact that the top vent location may be the best for cooling effect.

REFERENCES

1. Robert, J.F., Peube, J. L., and Trombe, F., "Experimental Study of Passive Air-Cooled Flat-Plate Solar Collectors: Characteristics and Working Balance in the Obeillo Solar Houses," Energy Conversion in Heating and Cooling and Ventilation Buildings, Hemisphere Publishing Corp., Washington, Vol. 2, 1978, pp. 761–782.

2. Catton, I., "Natural Convection in Enclosures," Proceedings of the 6th International Heat Transfer Conference, Toronto, Vol. 6, 1978, pp. 13–43.

3. Ostrach, S., "Natural Convection Heat Transfer in Cavities and Cells," Proceedings of the 7th International Heat Transfer Conference, Vol. 1, 1982, pp. 365–379.

4. Chang, L., C., Yang, K. T. an Lloyd, J. R., "Radiation-Convection Interaction in Two-Dimensional Complex Enclosures," ASME Paper No. 82-HT-49, 1982.

5. Yao, L. S., "Free and Forced Convection in the Entry Region of a Heated Vertical Channel," International Journal of Heat and Mass Transfer, Vol. 26, No. 1, 1983, pp. 65–72.

6. Aihara, T., Maruyama, S. and Choi, J. S., "Laminar Free Convection with Variable Fluid Properties in Vertical Ducts of Different Cross-Sectional Shapes," Proceedings of 8th International Heat Transfer Conference, Vol. 4, 1986, pp. 1581–1586.

7. Aihara, T., "Heat Transfer Due to Natural Convection from Parallel Vertical Plates," Trans. Japan Soc. Mech. Engrs., Vol. 29, 1963, p. 903.

8. Akbari, H. and Borgers, T. R., "Free Convection Laminar Flow within the Trombe Wall Channel," Solar Energy, Vol. 22, 1979, pp. 165–174.

9. Borgers, T. R. and Akbari, H., "Free Convective Turbulent Flow within the Trombe Wall Channel," Solar Energy, Vol. 33, 1984, pp. 253–264.

10. Aihara, T., "Effects of Inlet Boundary-Conditions on Numerical Solution of Free Convection between Vertical Parallel Plates," Rep. Inst. High Speed Mech., Tohaka University, Vol. 28, 1973, pp. 1–27.

11. Kettleborough, C. F., "Transient Laminar Free Convection between Entrance Effects," International Journal of Heat and Mass Transfer, Vol. 15, 1972, pp. 883–896.

12. Nakamura, H., Asako, Y. and Naitou, T., "Heat Transfer by Free Convection between Two Parallel Flat Plates," Numer. Heat Transfer, Vol. 5, 1982, pp. 95–106.

13. Chaturvedi, S. K., Mohieldin, T. O. and Huang, G. C., "Mixed Laminar Convection in Trombe Wall Channels," Journal of Solar Energy Engineering, Vol. 110, 1988, pp. 31–37.

14. Wilkes, J. O. and Churchill, S. W., "The Finite-Difference Computation of Natural Convection in a Rectangular Enclosure," American Institute of Chemical Engineering Journal, Vol. 12, No. 1, January 1966, pp. 161–166.

15. De Vahl Davis, G., "Natural Convection of Air in a Square Cavity — A Bench Mark Numerical Solution," International Journal of Numerical Methods in Fluids, Vol. 3, 1983, pp. 249–264.

16. Fraikin, M. P., Portier, J. J. and Fraikin, C. J., "Application of a k-ϵ Turbulence Model in an Enclosed Buoyancy Driven Decirculating Flow," Chem. Engr. Commun., Vol. 13, pp. 289–314, 1982.

17. Markatos, N. C. and Periculeous, K. A., "Laminar and Turbulent Natural Convection in an Enclosed Cavity," International Journal of Heat and Mass Transfer, Vol. 27, No. 5, 1984, pp. 755–772.

18. Nicolette, V. F. and Yang, K. T., "Transient Cooling by Natural Convection in a Two-Dimensional Square Enclosure," International Journal of Heat and Mass Transfer, Vol. 28, No. 9, 1985, pp. 1721–1732.

19. Berkovsky, B. M. and Polevikov, V. K., "Heat Transfer and Turbulent Buoyant Convection," International Center for Heat and Mass Transfer, Dubrvink, Vol. 2, August 1976, pp. 443–455.

20. Patankar, S. V., Numerical Heat Transfer and Fluid Flow, Hemisphere Publishing Co., 1985.

21. FLUENT Manual, TN-369 Rev. 3, Creare Inc., 1987, Hanover, NH.

22. Boussinesq, J., "Essai Sur La Theorie Des Eaux Courantes," Mem. Presentes Acad. Sci., Vol. 23, Paris, 1977, p. 46.

23. Daly, B. J. and Harlow, F. H., "Transport Equations in Turbulence," Physics of Fluids, Vol. 13, 1970, pp. 2634–2649.

24. Harlow, F. H. and Nakayama, P. I., "Transport of Turbulence Energy Decay Rate," Los Alamos Scientific Laboratory Report, LA-3854, 1968, Los Alamos, New Mexico.

25. Prandtl, L., "Ueber die ausgebildete Turbulenz," Proceedings of the 2nd International Congress for Applied Mechanics, Zurich, 1926, pp. 62–74.

26. Yang, K. T. and Lloyd, J. R., "Turbulent Buoyant Flow in Vented Simple and Complex Enclosures," Natural Convection Fundamental and Application, Hemisphere Publishing Co., 1985, pp. 303–329.

27. Tichy, J. A., "The Effect of Inlet and Exit Losses on Free Convective Laminar Flow in the Trombe Wall Channel," Journal of Solar Energy Engr., Vol. 105, 1983, pp. 187–193.

28. Eugel, R. K. and Mueller, W. K., "An Analytical Investigation of Natural Convection in Vertical Channels," ASME Paper No. 67–HT-16, 1967.

29. Oseen, C. W., Neure Method und Ergebnisse in der Hydrodynamik, Leipzig: Akademische Verlag, 1927.

30. Anderson, D. A., Computational Fluid Mechanics and Heat Transfer, Hemisphere Publishing Co., 1984.

31. Harlow, F. H. and Welch, J. E., "Numerical of Time-Dependent Viscous Incompressible Flow of Fluid with Free Surfaces," Physics of Fluids, Vol. 8, 1965, p. 2187.

32. Patankar, S. V. and Spalding D. B., "A Calculation Procedure for Heat Mass and Momentum Transfer in 3–D Parabolic Flows," International Journal of Heat and Mass Transfer, Vol. 15, 1972, pp. 1787–1806.

33. Jones, W. P. and Launder, B. E., "The Prediction of Laminarization with a Two-Equation Model of Turbulence," International Journal of Heat and Mass Transfer, Vol. 15, 1972, p. 301.

34. Plumb, O. A. and Kennedy, L. A., "Application of a k-ϵ Turbulence Model to Natural Convection from a Vertical Isothermal Surface," Journal of Heat Transfer, February 1977, pp. 79–85.

35. Lin, S. J. and Churchill, S. W., "Turbulent Free Convection from a Vertical Isothermal Plate," Numerical Heat Transfer, Vol. 1, 1978, pp. 129–145.

36. Mohieldin, T. O., "Computation of 2–D and 3–D Natural Convection Heat Transfer in Closed and Vented Cavities," Master's Thesis, Mechanical Engineering Dept., Old Dominion University, Norfolk, Virginia.

APPENDICES

Appendix A

A CLOSED FORM SOLUTION — THE SECOND ORDER VELOCITY PROFILE FOR MOMENTUM-INTEGRAL APPROACH

The solution of problem of flow in a parallel channel can be determined analytically in closed form. This is done by adopting a second order velocity profile in the momentum-integral method. In the present study, we let

$$u^* = A\left(y^* - {y^*}^2\right) \tag{A.1}$$

Since, the volumetric flow rate is defined as

$$Q = \int_0^1 u^* dy^* \tag{A.2}$$

Substituting Eq. (A.1) into Eq. (A.2), we get

$$u^* = 6Q\left(y^* - {y^*}^2\right) \tag{A.3}$$

Apply this assumed axial velocity profile to the momentum-integral equation, and integrate from 0 to L and from 0 to 1, we get

$$\begin{aligned} \int_0^1 {u^*}^2 dy^* \Big|_{x^*=L} - \int_0^1 {u^*}^2 dy^* \Big|_{x^*=0} &= -\frac{\partial p^*}{\partial x^*} + \Bigg[\frac{\partial u^*}{\partial y^*}\Bigg)\Bigg|_{y^*=1} - \frac{\partial u^*}{\partial y^*}\Bigg)\Bigg|_{y^*=0}\Bigg] \\ + \int_0^L \int_0^1 T^* dy^* dx^* &= [P_L - P_o] - 12QL + \int_0^L \int_0^1 T^* dy^* dx^* \end{aligned} \tag{A.4}$$

$$\begin{aligned} 36Q^2\left[\int_0^1 \left({y^*}^2 - 2{y^*}^3 + {y^*}^4\right) dy^*\right] - Q^2 = -\left[0 + \frac{1}{2}Q^2\right] - 12QL \\ + \int_0^L \int_0^1 T^* dy^* dx^* \end{aligned}$$

or

$$\frac{7}{10}Q^2 = -12QL + \int_0^L \int_0^1 T^* dy^* dx^* \tag{A.5}$$

where

$$P_L = 0 \tag{A.6}$$

$$P_0 = -\frac{1}{2}Q^2 \tag{A.7}$$

$$\left.\frac{\partial u^*}{\partial y}\right)\Bigg|_{y^*=1} = -6Q \tag{A.8}$$

$$\left.\frac{\partial u^*}{\partial y}\right)\Bigg|_{y^*=0} = 6Q \tag{A.9}$$

with the known temperature field,

$$T^*(x^*, y^*, Q) = T_c^* + (1 - t_c^*)y^* + \sum_{n=1}^{\infty} A_n e^{-\frac{n^2\pi^2 x^*}{PrQ}} \sin(n\pi y^*) \tag{A.10}$$

Equation (A.5) can be rewritten in the following form

$$\frac{7}{10}Q^2 \left[-12Q + \frac{1+T_c^*}{2}\right] L + \sum_{n=1}^{\infty} \frac{A_n PrQ}{n^3\pi^3} [(-1)^n - 1] \left[e^{-\frac{n^2\pi^2 L}{PrQ}} - 1\right] \tag{A.11}$$

For high Q limit,

$$e^{-\frac{n^2\pi^2 L}{PrQ}} \simeq 1 - \frac{n^2\pi^2 L}{PrQ} \tag{A.12}$$

Thus, Eq. (A.11) can be further manipulated as follows:

$$\begin{aligned} \frac{7}{10}Q^2 &= \left[-12Q + \frac{1+T_c^*}{2}\right] L + \frac{A_1 PrQ}{\pi^3}(-2)\left(-\frac{\pi^2 L}{PrQ}\right) \\ &= \left[-12Q + \frac{1+T_c^*}{2}\right] L - \left[\frac{4}{\pi^4}(1+T_c^*)PrQ\left(e^{-\frac{\pi^2 L}{PrQ}} - 1\right)\right] \end{aligned} \tag{A.13}$$

or

$$L = \frac{\frac{7}{10}Q^2 - \left[\frac{4}{\pi^4}(1+T_c^*)PrQ\left(e^{-\frac{\pi^2 L}{PrQ}} - 1\right)\right]}{\left(-12Q + \frac{1+T_c^*}{2}\right)} \tag{A.14}$$

Equation (A.14) is an implicit equation of L, can be solved by any numerical method, for example, the Newton's method.

Appendix B

QUADRATIC SCHEME

B.1 Quadratic Upstream Interpolation for Convective Kinematics (QUICK)

The problems associated with both central and upstream differencing techniques can be interpreted in terms of the method of estimating wall values of the dependent variables in a control-volume formulation. For central differencing the estimation is based on linear (or first-order) interpolation, which, although intuitively reasonable and involving only second-order truncation error, has the unfortunate geometrical property that $\Phi_r - \Phi_l$ is independent of Φ_c, thus leading to stability problems in the convective sensitivity. Upstream differencing is equivalent to zeroth-order interpolation with the choice of direction depending of the sign of u. The directional dependence gives very stable convective sensitivity; however, this advantage is strongly offset by the first-order truncation error.

The formulation of the "QUICK" algorithm is conveniently illustrated using constant grid spacing [32]. Φ_r can be formulated as follows when u_r is positive to the right

$$\Phi_r = \frac{1}{2}(\Phi_c + \Phi_R) - \frac{1}{8}(\Phi_L + \Phi_R - 2\Phi_c) \tag{B.1}$$

which may be interpreted as a linear interpolation corrected by a term proportional to the upstream-weighted curvature. For modelling the gradient $\left(\frac{\partial\Phi}{\partial x}\right)_r$, it is a geometric property of the parabola that the slop half way between two points is equal to that of the chord joining the points, i.e.

$$\left(\frac{\partial\Phi}{\partial x}\right)_r = \frac{\Phi_r - \Phi_c}{\Delta x_r} \tag{B.2}$$

which is valid in the variable-grid case as well, as indicated by notation. This, of course, is independent to the central difference formula.

Similarly, the construction for Φ_l and $\left(\frac{\partial\Phi}{\partial x}\right)_l$ when u_l is also positive to the right. The corresponding formulas are

$$\Phi_l = \frac{1}{2}(\Phi_L + \Phi_c) - \frac{1}{8}(\Phi_{FL} + \Phi_c - 2\Phi_L) \tag{B.3}$$

and

$$\left(\frac{\partial\Phi}{\partial x}\right)_l = \frac{\Phi_c - \Phi_L}{\Delta x_l} \tag{B.4}$$

Because of the consistent quadratic interpolation used in modelling both the convective and diffusive terms, the overall truncation error in a solution obtained by the "QUICK" algorithm is third-order in the spatial grid size. Thus, highly accurate solutions can be obtained using practical grid spacing.

Appendix C

COMPUTER PROGRAM — CALCULATION OF FLOW IN A PARALLEL CHANNEL BY USING MOMENTUM-INTEGRAL METHOD

```
      PROGRAM MODEL13
      DIMENSION X (202) ,Y (1002) ,DPX (202) ,DPP (202) ,USQ (202) ,R1 (202) ,
     *          TSQ (202) ,U1 (202) ,U2 (202) ,U3 (202) ,U4 (202) ,V (202,1002) ,
     *          ATS (202) ,T (202,1002) ,U (202,1002) ,P (202) ,R (202) ,DUY (202)
      PI=3.14159
      PR=0.71
      TH=1.0
      TL=1.0
      Q=0.02
      ALPH=1.3
      WRITE (6,1)
    1 FORMAT('4TH ORDER U-PROFILE')
      WRITE (6,2) PR,TH,TL,Q,ALPH
    2 FORMAT ('PR=',F4.2/,'TH=',F4.2/,'TL=',F4.2/,'Q=',F6.4/,
     *        'ALPH=',F4.2/)
      A1=-1./12
      B1=TL/12.+5*Q
      A2=1./2
      B2=-TL/2.
      A3=-5./6
      B3=5*TL/6.-10*Q
      A4=5./12
      B4=5*Q-5*TL/12.
      D1=2*A2+3*A3+4*A4
      D2=2*B2+3*B3+4*B4
      G1=PI**2/ (PR*ALPH*Q)
      MT=111
      M=7
  888 DX=0.0019932/100
      X (1) =0.0
      X (M) = (M-1) *DX
      DO 777 N=2,1000
      DY=0.001
      Y (1) =0.0
      Y (1001) =1.0
      Y (N) =Y (N-1) +DY
      T (M,1) =TL
      T (M,1001) =TH
      G=2.* (1+TL) /PI
      H=2.* (1-TL) /PI
      G16=160.
```

```
      T(M,N)=TL+(1-TL)*Y(N)
     *        -G*EXP(-G1*X(M))*SIN(PI*Y(N))
     *        +H*EXP(-4*G1*X(M))*SIN(2*PI*Y(N))/2
     *        -G*EXP(-9*G1*X(M))*SIN(3*PI*Y(N))/3
     *        +H*EXP(-16*G1*X(M))*SIN(4*PI*Y(N))/4
     *        -G*EXP(-25*G1*X(M))*SIN(5*PI*Y(N))/5
     *        +H*EXP(-36*G1*X(M))*SIN(6*PI*Y(N))/6
     *        -G*EXP(-49*G1*X(M))*SIN(7*PI*Y(N))/7
     *        +H*EXP(-64*G1*X(M))*SIN(8*PI*Y(N))/8
     *        -G*EXP(-81*G1*X(M))*SIN(9*PI*Y(N))/9
     *        +H*EXP(-100*G1*X(M))*SIN(10*PI*Y(N))/10
 777  CONTINUE
      DPX(6 )=-0.2527
      DPX(M)=DPX(M-1)
 102  U1(M)=A1*DPX(M)+B1
      U2(M)=A2*DPX(M)+B2
      U3(M)=A3*DPX(M)+B3
      U4(M)=A4*DPX(M)+B4
      S1=0.0
      S=0.0
      DO 333 N=2,1000
      U(M,1)=0.0
      U(M,N)=U1(M)*Y(N)+U2(M)*Y(N)**2+U3(M)*Y(N)**3+U4(M)*Y(N)**4
      U(M,1001)=0.0
      S1=S1+U(M,N)*T(M,N)
 333  S=S+U(M,N)**2
      S1=(S1+U(M,1001)*T(M,1001)/2.)*DY
      S=(S+U(M,1001)**2/2.)*DY
      D1=(U(M,2)-U(M,1))/DY
      USQ(6 )=0.4275E-03
      USQ(M)=S
      DPP(M)=((USQ(M)-USQ(M-1))/DX-D2-(1+TL)/2
     *        +4*(1+TL)*(EXP(-G1*X(M))
     *        +EXP(-9*G1*X(M))/9
     *        +EXP(-25*G1*X(M))/25
     *        +EXP(-49*G1*X(M))/49
     *        +EXP(-81*G1*X(M))/81
     *        +EXP(-121*G1*X(M))/121
     *        +EXP(-169*G1*X(M)+160)*EXP(-G16)/169
C    *        +EXP(-225*G1*X(M)+160)*EXP(-G16)/225
C    *        +EXP(-289*G1*X(M)+320)*EXP(-G16)**2/289
C    *        +EXP(-361*G1*X(M)+320)*EXP(-G16)**2/361
     *         )/(PI**2))/(D1-1)
      IF(ABS(DPP(M)-DPX(M)).GE.5.E-4)THEN
      DPX(M)=(DPX(M)+DPP(M))/2
      GO TO 102
      ELSE
      END IF
      R1(M)=S1
      R(M)=S
      DUY(M)=D1
```

```
      U(1,N)=Q
      U(M,1)=0.0
      U(M,1001)=0.0
      V(1,N)=0.0
      V(M,1)=0.0
      V(M,1001)=0.0
      DO 331 N=2,500
      V(M,N)=V(M,N-1)-DY*(U(M,N)+U(M,N-1)-U(M-1,N)-U(M-1,N-1))/(2*DX)
  331 CONTINUE
      DO 332 N=1000,502,-1
      V(M,N)=V(M,N+1)+DY*(U(M,N)+U(M,N+1)-U(M-1,N)-U(M-1,N+1))/(2*DX)
  332 CONTINUE
      V(M,501)=(V(M,500)+V(M,502))/2.
      M=M+1
      IF(M.LE.MT )GO TO 888
      P(6 )=-0.2305E-03
      DO 108 M=7 ,MT
      P(M)=P(M-1)+DPX(M)*(X(M)-X(M-1))
      WRITE(6,107)M,DPX(M),M,P(M),M,R(M),M,R1(M),M,DUY(M)
  107 FORMAT('DPX(',I3,')=',F8.4,3X,'P(',I3,')=',E11.4,3X,
     *       'R(',I3,')=',E11.4/,'HX(',I3,')=',F12.6,5X,
     *       'DUY(',I3,')=',F11.6)
  108 CONTINUE
      M=2
      DO 111 N=1,1001,100
      WRITE(6,105)N,Y(N),M,N,T(M,N),U(M,N),V(M,N)
  111 CONTINUE
      DO 112 I=2,(MT-1)/10+1
      M=(I-1)*10+1
      DO 110 N=1,1001,100
      WRITE(6,105)N,Y(N),M,N,T(M,N),U(M,N),V(M,N)
  105 FORMAT('Y(',I4,')=',F7.3,3X,'T(',I3,',',I4,')=',F10.5,3X
     *       ,'U=',F7.5,3X,'V=',F9.5)
  110 CONTINUE
      WRITE(6,113)
  113 FORMAT(/)
  112 CONTINUE
      STOP
      END
```